令和 2 年度

長岡技術科学大学 大学院工学研究科 博士後期課程

エネルギー・環境工学専攻

博士論文

論 文 題 目

Study on Synthesis of Luminescent Hydroxyapatite Nanoparticles and Their Surface Functionalization for Cell Labeling Applications

(発光性ハイドロキシアパタイトナノ粒子の合成と細胞標識応用のための表面機能化に関する研究)

申請者：Takuya Kataoka

(片岡 卓也)

学籍番号：12101990

Acknowledgments

I wish to express my deepest gratitude to Prof. Dr. Motohiro Tagaya of the Department of Material Science and Technology, Nagaoka University of Technology (NUT), for his continuous and kindly support, supervision, guidance and encouragement throughout my study during the period from 2014 when I was assigned to the Nanobiomaterials laboratory.

In carrying out this study, I received great support from the Japan Society for the Promotion of Science (JSPS) Research Fellowships for Young Scientists. This study was partially supported by a grant from JSPS KAKENHI (Grant-in-Aid for JSPS Fellows, Grant No. 18J20271).

I deeply appreciate Prof. Dr. Hiroshi Matsubara, Prof. Dr. Tomoichiro Okamoto and Prof. Dr. Kiyoshi Ohnuma of NUT and Prof. Dr. Shoichi Kubo of Tokyo Institute of Technology for giving instructions and helpful comments on this thesis review. I am grateful that Analytical Measurement Center in NUT, which has allowed me to use many analyzers for my study.

Prof. Dr. Takaomi Kobayashi of NUT is deeply grateful for his valuable comments throughout study of my undergraduate research and scholarly activity. I would like to thank Dr. Kota Shiba of the National Institute for Materials Science (NIMS), who gave me many guidance and advice, from bachelor study to the present study. Prof. Dr. Yuichi Otsuka of NUT is deeply grateful for his valuable comments throughout study of my doctoral course. I would like to thank Dr. Sadaki Samitsu of NIMS and Prof. Dr. Mitsuhiro Okuda of CIC nanoGUNE for their valuable comments and analysis regarding sample morphology. I would like to thank Prof. Dr. Daisuke Kawagoe of Oyama College, Prof. Dr. Shigeaki Abe of Nagasaki University and Prof. Dr. Tania Guadalupe Peñaflor Galindo of Nagaoka College for their useful comments regarding publication papers.

I would like to express an incredibly special thanks to my colleagues in the Nanobiomaterials laboratory for their help, suggestions and teachings, and especially express my gratitude to Mr. Shota Yamada, Mr. Chai, Mr. Iori Yamada, Mr. Ikeda and Mr. Hashimoto for their advising and help every day. The other younger students of the laboratory made an environment that I could focus on the experiment. I am deeply grateful to everyone who took care of me.

Thanks to everyone's cooperation, I was able to finish doctoral course. At the end, I am deeply grateful to my parents (Mr. Toshiyuki Kataoka and Ms. Akemi Kataoka) who warmly watched and supported my life in doing university life and study.

Takuya Kataoka
March 2021

Contents

Chapter 1. General Introduction

1.1 Cell labeling nanomaterials 1
1.1.1 Labeling mechanism 1
1.1.2 Conventional nanomaterials 3
1.1.2.1 Organic molecules 3
1.1.2.2 Inorganic nanoparticles 4
1.2 Application of hydroxyapatite for cell labeling nanomaterials 5
1.2.1 Hydroxyapatite 5
1.2.1.1 Features 5
1.2.1.2 Hybrid systems with organic molecules *in vivo* 8
1.2.2 Incorporation into cells as the particle shape 10
1.2.3 Possibility of labeling by photofunctionalization 10
1.3 Europium (III) ion 11
1.3.1 Photochemical properties 11
1.3.2 Doping systems in hydroxyapatite 13
1.3.3 Organic complex systems 14
1.3.3.1 Types and photochemical properties 14
1.3.3.2 Tris (2,2,6,6-tetramethyl-3,5-heptanedionato) europium (III) (EuTH) 15
1.3.3.3 Possibility of synthesis for EuTH-interacted hydroxyapatite 16
1.4 Molecule that specifically binds to a cancer cell 16
1.4.1 Receptor expressed on cell surface 16
1.4.2 Types of molecules that specifically bind to receptors 17
1.4.3 Immobilization technique of specific binding molecule to solid surface 18
1.5 Cancer cell growth inhibitory drug molecules 21
1.5.1 Representative molecules and their functions 21
1.5.2 Citric acid 22
1.5.3 Possibility of synthesis for citric acid coordinated hydroxyapatite 23
1.6 Purpose of this study 23

1.7 Contents of this thesis 25
References 27

Chapter 2. Synthesis of Luminescent Europium(III) Complex-interacted Hydroxyapatite Nanoparticles and Their Rapid Cell Labeling by Folic Acid Immobilization

2.1 Introduction 36
2.2 Experimental Section 40
2.2.1 Chemicals 40
2.2.2 Materials and preparation 41
2.2.3 Characterization 42
2.2.3.1 Characterization of Eu(III) complex-interacted hydroxyapatite nanoparticles 42
2.2.3.2 Analysis of the amino-functionalized groups on Eu(III) complex-interacted hydroxyapatite nanoparticles 48
2.2.3.3 Analysis of the folate N-hydroxysuccinimidyl ester (FA-NHS)-immobilized nanoparticles 53
2.2.3.4 Characterization of the nanoparticles dispersed in phosphate buffer saline 54
2.2.3.5 Cytotoxic evaluation of the nanoparticles against NIH3T3 fibroblasts 56
2.2.3.6 Evaluation of cytotoxicity and cell labeling ability against HeLa cancer cells by the nanoparticles 57
2.3 Results and Discussion 59
2.3.1 Characterization of the Eu(III) complex-interacted nanoparticles 59
2.3.2 Characterization of the FA-NHS-immobilized nanoparticles 71
2.3.3 Size distributions of the nanoparticles in phosphate buffer saline 80
2.3.4 Cytotoxicity of the nanoparticles against fibroblasts 82
2.3.5 Cytotoxicity and cell labeling ability of the nanoparticles against cancer cells 83
2.4 Conclusion 89

References.....90

Chapter 3. Synthesis of Luminescent Hydroxyapatite Nanoparticles Coordinated with Citric Acid for Their Bifunctional Cell Labeling and Cytostatic Properties

3.1 Introduction.....98

3.2 Experimental Section.....102

3.2.1 Chemicals 102

3.2.2 Materials and preparation 102

3.2.3 Characterization 105

3.2.3.1 Characterization of europium(III) ion-doped hydroxyapatite nanoparticles coordinated with citric acid.....105

3.2.3.2 Characterization of the nanoparticles in phosphate buffer saline 109

3.2.3.3 Cytotoxic evaluation of the nanoparticles against NIH3T3 fibroblasts 110

3.2.3.4 Evaluation of cell labeling and cytostatic ability of the nanoparticles against HeLa cancer cells 110

3.3 Results and Discussion.....111

3.3.1 Characterization of the nanoparticles 111

3.3.2 Size distributions of the nanoparticles in phosphate buffer saline 131

3.3.3 Cytotoxicity of the nanoparticles 133

3.3.4 Cell labeling and cytostatic ability of the nanoparticles against cancer cells 134

3.4 Conclusion.....139

References.....141

Chapter 4. Summary.....147

Chapter 1

General Introduction

Chapter 1

General Introduction

1.1 Cell labeling nanomaterials

1.1.1 Labeling mechanism

Pathological diagnosis and noninvasive therapy have been extensively investigated so far by means of a variety of techniques. Among them, nanomaterials that can bind to the surface of cells and fluoresce by light irradiation with a specific wavelength are well-known as cell labeling nanomaterials and have been widely utilized for various purposes [1–4]. Many different types of cell labeling technologies have been developed for the diagnosis of cancer cells including radioisotopes for single-photon emission computed tomography (SPECT), positron emission tomography (PET) [5], iron-nanoparticles for magnetic resonance imaging (MRI) [6], and antibody-mediated labeling with optical probes [7]. However, the application of these techniques to early-stage cancer cells is still a grand challenge in this field. In order to overcome various difficulties, one of the keys would be to develop diagnostic techniques using a fluorescence endoscope to detect epithelial cancer cells.

Other important features that are demanded of the cell labeling nanomaterials are that they can safely label and visualize the cancer cells for diagnosis and inspection *in vivo* and *in vitro*. To realize such cell labeling nanomaterials, nanomaterial itself has to be biocompatible, efficiently fluoresce in the visible light range (400–800 nm) as well as effectively interact with the cells. For the early-stage detection of the cancer cells *in vivo*, the surface layer of the cells is stained to be observed with a fluorescence endoscope. Then, the cells are diagnosed on the basis of autofluorescence which is known as fluorescence emitted by cell constituents. A previous study reported that clear luminescence peaks were observed at approximately 500 nm and 630 nm when excited at a wavelength of 437 nm [8]. However, the luminescence intensity of autofluorescence is too weak to confirm with our naked eyes, limiting the practical use of this phenomenon to various applications. For this reason, many researchers have started from *in vitro* studies to achieve luminescence that can sufficiently be observed with a fluorescent endoscope, probably leading to the cell diagnosis *in vivo* afterward. Although the detection limit of a confocal laser scanning microscope in the z-direction is known to

be approx. 500 nm [9], some holographic microscopes can observe almost 30 μm in depth from the cellular top surface. Taking advantage of these techniques, cell labeling nanomaterials can be utilized for immunoassay or tissue biopsy to diagnose early-stage cancer in the visible light region.

To further develop and optimize nanomaterials with desired cell labeling properties, a possible mechanism on how the nanomaterials are captured by cells is considered in relation to the basic structure of cells. Endocytosis is known as one of the representative processes in which the nanomaterial is taken into the cell from the outside via the cell membrane [10]. There are two types of endocytosis: phagocytosis and pinocytosis. Phagocytosis is a mechanism that cells take up foreign substances (bacteria, viruses, parasites) and abnormal metabolites into the cell (tissue, blood, *etc*.) and decompose them. Phagocytosis occurs only in a specific type of cells such as phagocytic cells, monocytes, dendritic cells, NK cells and neutrophils. Pathogens, dead cells and cell debris (1 μm or more) are also included. On the other hand, pinocytosis refers to the phenomenon that cells take up nanomaterials as vesicles regardless of their permeability. Internalization of substances with a size less than 300 nm [11] and 50 to 80 nm [12] into cells have been reported. No clear consensus has been obtained so far with respect to the mechanism of nanomaterial uptake into cells. The surface physical properties are regarded as one of the important factors, while the uptake behavior also varies depending on the types of cells. Since proteins and nanomaterials *in vivo* bind to each other and agglutinate, the cellular uptake mechanism does not depend only on the size of the nanomaterials. Pinocytosis depends on the size, composition and structure of the nanomaterial surface.

Figure 1-1 shows an outline of the labeling mechanism (endocytosis). Based on the interaction between a nanomaterial surface and cell membrane (receptor), endocytosis is classified into two behaviors: passive and active. The former is a weak liquid phase interaction such as hydrogen bonding, a hydrophobic effect and van der Waals force. In such cases, the nanomaterials are easily taken into the cells since surface energy is the same as that of cell surfaces. The latter is a strong liquid phase/solid phase interaction such as ionic bonding, metal bonding and covalent bonding, *etc*. In the case of the strong interaction, the catalytic effect at the interaction point inhibits cellular uptake because of the high surface tension. The nanomaterial taken up by the cell is carried to the lysosome, then hydrolyzed and digested by enzymes. Likewise, the cell labeling nanomaterial is taken into the cell through the interaction with the receptor present on the surface of the cell membrane, and fluorescence is emitted by the excitation of visible light. The luminescence emitted from cells *in vitro* can be detected with a fluorescence microscope and used for diagnosis. Similarly, *in vivo*, it is detected with a fluorescence endoscope and used for diagnosis under the visible light excitation.

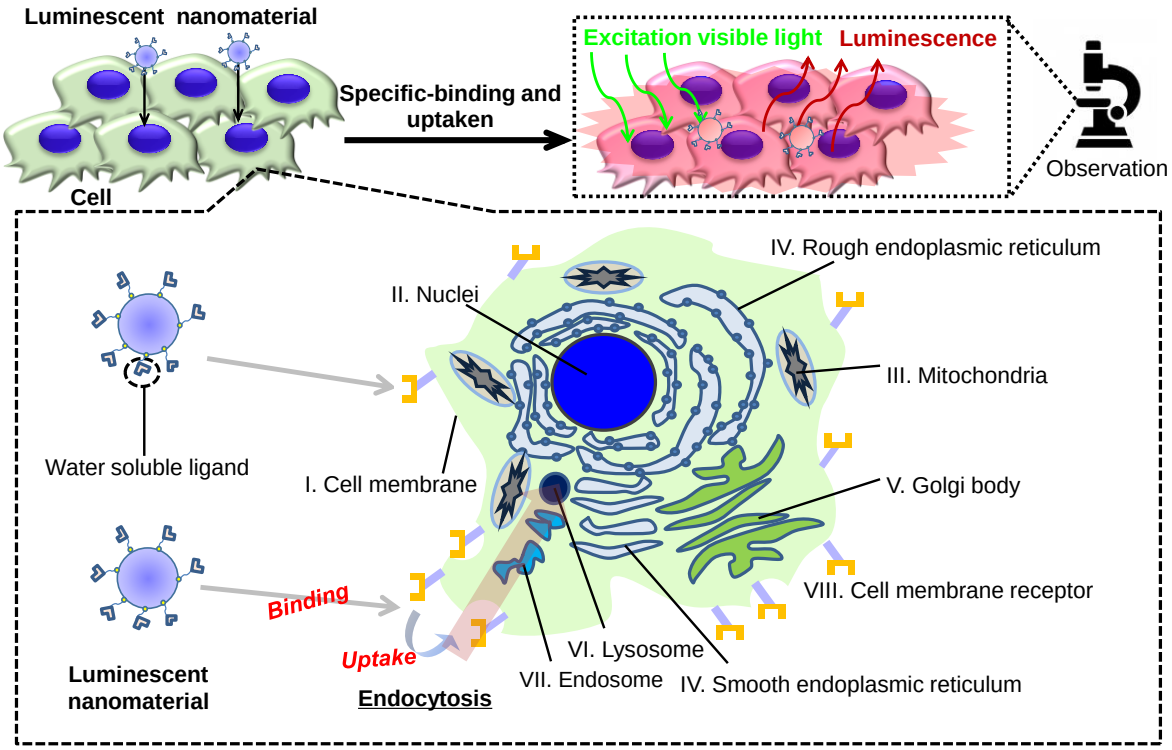

Figure 1-1. Illustration of the possible cell labeling mechanism for diagnosis. The site to be taken into the cell is different depending on the particle size as described in the text.

1.1.2 Conventional nanomaterials

1.1.2.1 Organic molecules

Organic molecules and inorganic nanoparticles have been used as cell labeling nanomaterials. Depending on the nanomaterial, there are some problems such as fast color degradation which is due to ultraviolet light excitation, damaging the living tissue (influence of active oxygen generated by photochemical reaction, damage of biomolecules due to electron transfer reaction, *etc.*). A variety of nanomaterials have been synthesized so far; however, there are still no suitable nanomaterials to solve such problems. Some examples of cell labeling nanomaterials already reported and known problems are shown in **Table 1-1**. For the organic molecules, a fluorescent protein (excitation wavelength: 400 nm) [13], temperature-responsive polymers (excitation wavelength: 456 nm) [14] and pH-responsive dye (excitation wavelength: 532 nm) [15] have been reported. Such cell labeling nanomaterials are not cytotoxic and do not affect cell function and cell growth behavior. Fluorescent proteins are less toxic to living bodies and emit luminescence through visible light excitation. However, the protein can be decomposed by light irradiation, affecting the function of cell labeling. In the case of fluorescent organic low molecules, their fluorescence properties are affected by the molecular size

which frequently causes steric hindrance. Although no such drawbacks are seen with the temperature-responsive and pH-responsive dyes, some other difficulties including water insolubility and aggregate formation limit their usage in cell labeling applications. For this kind of application, it is necessary to synthesize nanomaterials that have sufficient stability in their color and luminescence properties even under continuous/strong light excitation.

Table 1-1. Conventional cell labeling nanomaterials of organic molecular state solved in solution and inorganic particle state dispersed in solution, and their problems [13–22].

	Luminescent nanomaterial	Problem	Reference
Organic molecular state solved in solution	Fluorescent proteins	Decomposition and denaturation of protein by excitation light irradiation	[13]
	Temperature-responsive polymers	Aqueous insolubility by an easy aggregation	[14, 15]
	pH-responsive dyes		
Inorganic particle state dispersed in solution	Semiconductor quantum dots	Containing biotoxic elements such as Cd and Hg	[16–18]
	Lanthanide (Ln) ion-doped oxides	Low quantum efficiency	[19–22]

1.1.2.2 Inorganic nanoparticles

Among various inorganic nanoparticles, semiconductor quantum dots (excitation wavelength: 260 nm) have been mainly utilized for cell labeling applications [16] because of their strong luminescence and stable color. However, a problem has been also reported in terms of biotoxicity which is induced by compositional Cd, Hg, *etc*. (biotoxic element) [16–18]. These heavy metals are known to affect cell function and reduce cell viability, possibly leading to undesirable and/or unexpected results *in vivo* experiments. Besides, since the quantum dots are usually excited by UV light irradiation, potential damage to the cells is also concerned. To solve this problem, a Ln ion-doped oxide that is excited by the light with a longer wavelength has been reported as the cell labeling nanomaterial [19–22], while its luminescent properties and safety to cells are unknown yet (**Table 1-1**).

In order to overcome these barriers, a Ln ion-doped hydroxyapatite (HA) would be one of the model nanomaterials. HA has an excellent affinity with cells so that it can be used as a cell label. It is possible to synthesize cell labeling HA-based nanomaterials with an excellent cell affinity by doping Ln ions that have low toxicity to living bodies and are capable of being excited by a low energy light in the visible range. Needless to say, the luminescent species (Ln ions) have to be

incorporated into the HA structure in such a way that their amount, spatial distribution and so on are controlled.

1.2 Application of hydroxyapatite for cell labeling nanomaterials

1.2.1 Hydroxyapatite

1.2.1.1 Features

The HA ($Ca_{10}(PO_4)_6(OH)_2$) with a Ca/P ratio of 1.67 is an inorganic component contained in living tissues (bones and teeth), the crystal system is hexagonal, the space group is P63/m, and the unit cell is 0.94 nm × 0.94 nm × 0.68 nm [23]. As a crystal structure, the four columnar Ca (*i.e.*, Ca (I) site) is aligned parallel to the *c* axis, and the six screw axis Ca (*i.e.*, Ca (II) site) surround the *c*-axis. Also, hydroxyl groups are present in the part surrounded by the screw Ca. The crystal structure of HA is shown in **Figure 1-2**. The high biocompatibility due to having a composition close to the

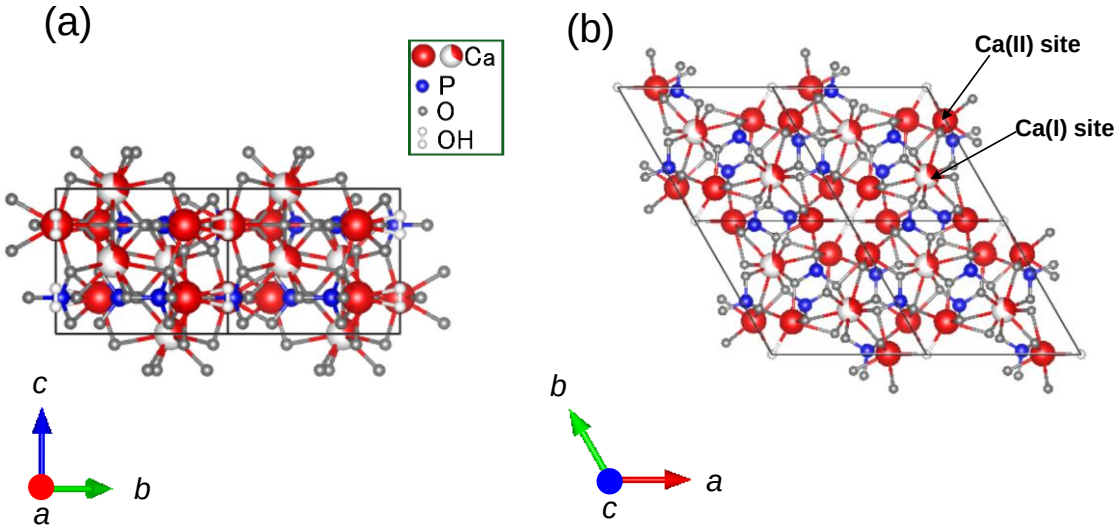

Figure 1-2. Crystalline structures of HA viewed from the (a) *a*- and (b) *c*-axis directions.

hard tissues *in vivo* is an advantage, and applied study as a biomaterial is proceeding. The reported particle size of HA is around 20–300 nm [24,25], and it has excellent light resistance. The uptake of the HA nanoparticles with a size of 50–200 nm by the osteoblasts has been investigated, exhibiting excellent uptake efficiency without cytotoxicity [26]. The Ca ions in the HA can be easily substituted with the other metal ions, and by substituting Ln ions, a luminescence property can be imparted. By

using the HA matrix, it is possible to achieve cell labeling nanomaterials that are safe for the living body and do not affect the color degradation and luminescence properties due to the light excitation. Furthermore, since it is possible to impart the other functions (e.g., drug delivery carrier) for achieving the multi-functional particles, it is important to design the cell labeling nanomaterials as nanoparticle shapes.

In general, the nanoparticle growth involves the process for the precipitation of a solid from solution. An understanding of the precipitation process is important for the growth of nanoparticles to the desired size and shape. For nanoparticle nucleation, the solution must be supersaturated either by adding the required reactants to produce a supersaturated solution during the reaction or by dissolving the solute at a high temperature and then cooling to low temperatures [27,28]. In general, the process for the precipitation consists of a nucleation and nanoparticle growth [27,28]. Homogeneous nucleation occurs by combining solute molecules to form nuclei. This nucleation occurs due to the thermodynamic driving force because the energy of supersaturated solution is not stable. The overall free energy change (ΔG) is the sum of the free energy by the formed new surface and the free energy by the formation of a new volume, using the following Equation (1) (**Eq. (1)**) [27,28].

$$\Delta G = -\frac{4}{V}\pi k_B T ln(Sr) + 4\pi r^2 \gamma \quad (1)$$

For spherical nanoparticles, where V is the molecular volume of the precipitated species, k_B is the Boltzmann constant, T is temperature, Sr is the saturation ratio, r is the radius of the nuclei and γ is the surface free energy per unit surface area. ΔG has a positive maximum value at a critical radius (r^*) when $Sr > 1$. The nuclei larger than the r^* decrease the free energy for growth and form stable nuclei that grow to form nanoparticles. The r^* defined by the following **Eq. (2)** can be obtained by setting $d\Delta G/dr = 0$ [27,28].

$$r^* = \frac{2V\gamma}{3k_B T ln(Sr)} \quad (2)$$

For a given value of Sr, the nanoparticles with $r > r^*$ will grow. After the nucleation are occurred in the solution, the nanoparticles grow by molecular addition. Nucleation stops when the precursor concentration drops below the critical concentration [27,28]. Then, the formed nanoparticles continue to grow by the addition of molecules until they reach the equilibrium concentrations. They grow by hybridizing with smaller unstable nuclei after the nanoparticles grow to a stable size. The nanoparticles are not thermodynamically stable for growth kinetically. To form stable nanoparticles during the reaction, the nanoparticles must be added surface protecting agents, such as capping agents [27,28]. **Figure 1-3** shows the nanoparticle nucleation and growth processes with adding the capping agent. The nucleation plays a key role in

determining the size/shape of the resulting nanoparticles as shown in **Figure 1-3(a)**. The critical nuclei can be smaller than the ones for the synthesis of nanoparticles. Thermodynamically, nanoparticles will grow toward the nanoparticle shape having the lowest energy state at equilibrium, which is based on the classic LaMer model [27–29]. Even spherical or rod-shaped nanoparticles are not thermodynamically stable unless they are capped by the capping agents. It is true in the case of most nanoparticle systems. In the previous report, it was showed that the use of the capping agents during the synthesis of HA nanoparticles affected the average nanoparticle sizes of HA [30]. It suggests that capping agents during synthesis are strongly dependent on the mechanism of HA nucleation and growth [30]. When there is no interaction between the HA nanoparticles and the capping agents, the growth rate of each plane of the HA is different, resulting in anisotropically-shaped nanoparticles. When there is an interaction between a specific plane of HA nanoparticles and the capping agents, the specific plane of the HA on which the capping agent is not adsorbed grows, resulting in anisotropically-shaped nanoparticles. When there is the interaction between the entire surface of the HA nanoparticles and the capping agents, HA nanoparticles reach a stable thermodynamic critical radius, as the nuclei of the nanoparticle is surrounded by the cappinng agents. And the HA nanoparticles have an isotropic nanoparticle shape. **Figure 1-3(b)** shows three dimensional curves of LaMer model based on Stöber process that is proposed here to describe homogeneous nucleation and growth of the nanoparticles based on aggregation mechanism. An mechanism of LaMer model [30], which incorporated the conceptual separation of nucleation and growth, have been proposed to describe the formation of HA nanoparticles. When the reaction starts, the precursor concentration increases with reaction time. Saturation solubility in **Figure 1-3(b)** is the equilibrium solubility of the precursor under the given conditions. In a homogenous nucleation in which no nuclei or nanoparticles are initially present, an energy barrier exists for nuclei generation. In this case, it requires that the precursor concentration is higher than a value defined as critical supersaturation. When this is achieved, the nucleation starts, and precursors can either react with each other to generate new nuclei or adsorb to the surface of existing nuclei, leading to growth of the nuclei. Both nucleation and growth consume precursors, leading to a decrease of precursor concentration during the synthesis of nanoparticles. The presence of capping agents plays a role in the kinetics during the synthesis of nanoparticles. As shown in the curve of **Figure 1-3(b)**, the decay rates of the precursor concentration changes depending on the presence or absence of the capping agents. It is associated with the growth of HA controlled by the presence of capping agents [30]. Due to the instability of the nuclei, the aggregation also occurs during the nucleation. The particle number first increases and then decreases during nucleation. It is only when aggregation stops at

the end of the nucleation stage that the particle number becomes constant. And this particle number is maintained throughout the nanoparticle growth stage. Therefore, capping agents may be used to determine the shape of HA nanoparticles.

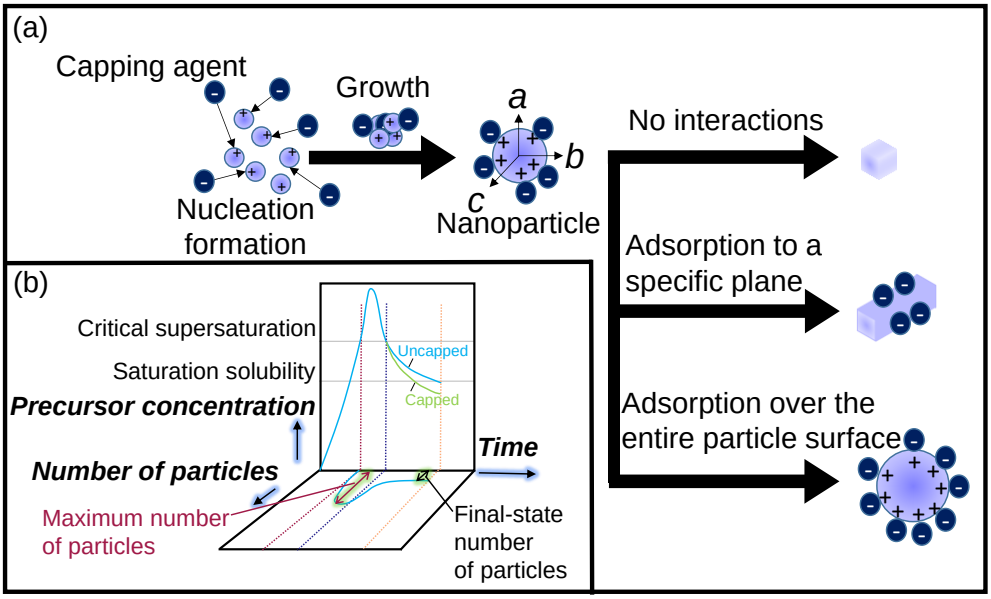

Figure 1-3. (a) Possible nanoparticle nucleation and growth processes with adding the capping agent, which can be classified into three types based on the interactions between the agent and the particle. (b) Three dimensional curves based on LaMer model to Stöber process, representing homogeneous nucleation and growth of the nanoparticles based on aggregation mechanism.

1.2.1.2 Hybrid systems with organic molecules *in vivo*

Figure 1-4 shows examples of inorganic/organic hybrids. **Figure 1-4(a** and **b)** shows the hierarchical structure of the chiton. The chiton is known to concentrate as much as 100,000 ppm of iron in teeth. In general, although organisms often use calcium as the main component when forming hard tissues such as teeth, there are a few organisms that form teeth with magnetite (Fe_2O_3) as the main component. The hydroxyl group of lepidocrocite (α-, γ-FeOOH) is exposed on the surface and exists as an inorganic/organic hybrid by interacting with α-chitin and proteins [31–33]. This inorganic/organic hybrid is achieved by the chemical bond of the Fe^{2+} ion of α- and γ-FeOOH with the carboxyl group and hydroxyl group in the α-chitin and proteins.

The bone tissue *in vivo* is also the same. **Figure 1-4(c** and **d)** is a schematic diagram of bone tissue *in vivo*. HA is the main component of bone *in vivo*, and it forms a chemical bond at the interface with collagen and exists as the inorganic/organic hybrid. This hybrid was achieved by

the chemical bonding of Ca^{2+} ions in HA and carboxyl groups in collagen fibril on the interface. The action of organisms to form minerals is called biomineralization and it is known to also occur *in vivo*. In order to understand the nucleation of HA *in vivo*, the studies have been conducted to synthesize HA in simulated body fluids (SBF) to evaluate the physicochemical properties at the interfaces. The several functional groups to induce the HA nucleation in SBF have been reported, and (Ti, Zr, Ta, Nb)–OH, $–PO_3H_2$, $–SO_3H$, $–CONH_2$ and –COOH have beeen candidated as the preferential nucleation sites [34–38]. The study on the synthesis of the other functional nanoparticles has also been conducted using biomineralization [39,40]. Therefore, the possibility of the development of the novel cell labeling nanoparticles by mimicking biomineralization is expected.

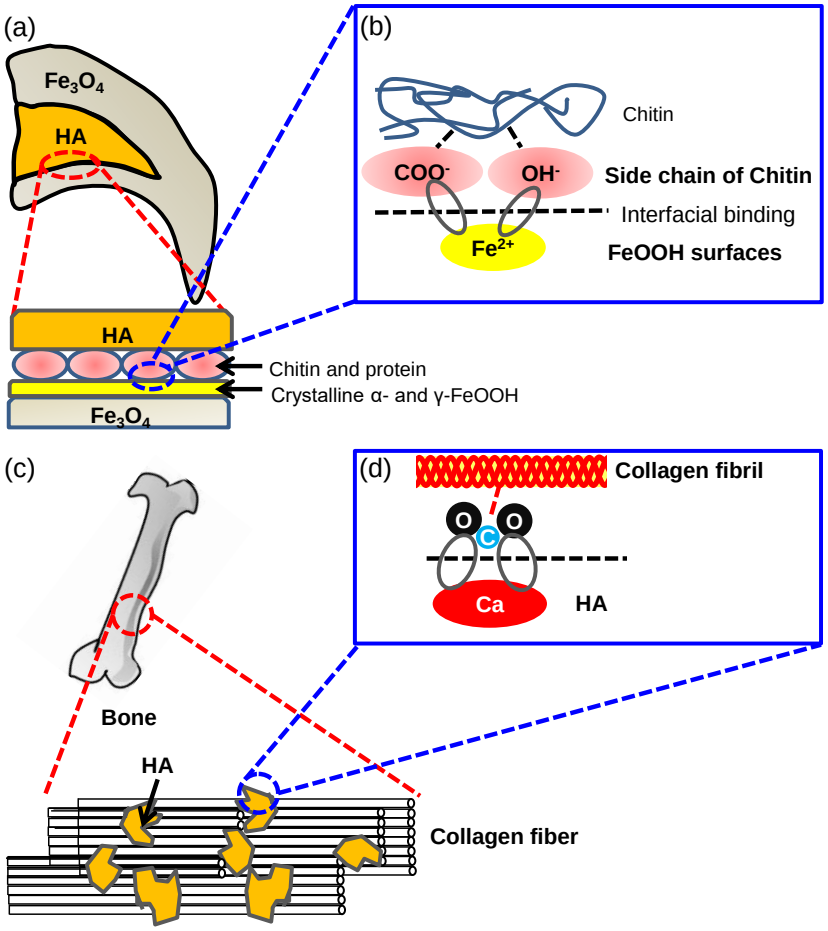

Figure 1-4. (a, c) Hieratical structures of inorganic/organic hybrids at (a, b) teeth of chiton and (c, d) cancellous bone tissue, and their (b, d) interfacial interactions in the binding state at the molecular level.

1.2.2 Incorporation into cells as the particle shape

The interaction between cytophilic nanoparticles and cells depends on the particle size, surface structure, chemical composition, solubility and aggregation. These are important for circulation in the body, invasiveness to lesions and accumulation, and can be expected to improve the effects of diagnosis and therapy.

The substances diffuse into the cells due to the concentration gradient. The transport of the substances inside and outside the cell membranes by the concentration gradient without chemical change is called passive transport [41]. In passive transport, the substance is transported by the concentration gradient. On the other hand, transporting the substances against the concentration gradient is called active transport [42]. The active transport is performed by a pump in the cell using the hydrolysis energy of adenosine triphosphate. However, selective intracellular targeting is difficult to be done using these intracellular transports. Therefore, the selective cellular uptake through endocytosis can be achieved by designing the surface immobilization states of the nanoparticles. Since several endocytosis-mediated cellular uptake mechanisms have been proposed, the size of the nanoparticle to be incorporated is also an important factor in cellular uptake. As previously mentioned, the uptake of HA nanoparticles with a size of 50–200 nm (100 μg/mL) has been reported in osteoblasts [43]. In particular, the particle size of about 80 nm for HA particles has been reported to be good for cellular uptake. Specifically, the cells taking up the HA nanoparticles showed the same growth behavior as non-incorporated cells, and the cell affinity with the particles alone was confirmed. It has already been defined that there is toxicity to cells when the cell growth rate is less than 130 % in 6 h of culture [44]. As an international standard, the nanoparticle is defined as non-cytotoxicity, if the decrease rate in the cell viability during the cell culture is 30% or less as compared with the case in the cells without the nanoparticle [45]. The HA particles can be judged to be non-cytotoxic in the size range of 50–200 nm [43] according to previous reports [44,45]. Thus, if the HA with the size range of 50–200 nm can be synthesized, it can be judged that HA is suitable as a matrix for cell labeling nanoparticles.

1.2.3 Possibility of labeling by photofunctionalization

Hybrids with functional low molecular compounds such as 8-hydroxyquinoline (8Hq) [46,47] and glucosamine [48] on a nanoscale have already been reported. For example, in the HA/8Hq system, the 8Hq molecules were chemically bonded to the Ca^{2+} ions on the HA by applying mechanical forces. The photofunction of the hybrids has been studied by evaluating the light absorption and luminescence through the metal-ligand charge transfer complex formation. In the HA/glucosamine

system, glucosamine molecules were bound with HA due to the hydrogen-bonding interactions between the amino and hydroxyl groups of glucosamine and the hydroxyl groups on the surface of HA. No study has been done yet to contain a photofunctional dye (visible light-responsive) and HA and use them as cell labels. Several studies of the europium (III) ion (Eu^{3+}) doped HA have been reported [49,50]. However, the low internal quantum efficiency is a problem when compared to existing cell labeling nanoparticles.

Thus, a detailed understanding of the photophysicochemical driving force at the interface between HA and functional molecules is considered to be important for the design of novel cell labeling nanoparticles.

1.3 Europium (III) ion

1.3.1 Photochemical properties

In the case of Ln ions, most of the luminescence transitions in the infrared to the near-ultraviolet region are due to transitions between the split 4*f* orbital levels [51,52]. The electric dipole transition between energy levels belonging to the same electron configuration becomes a forbidden transition by the selection rule of evenness and oddity. When atoms or ions are in a solid or in a solution, the 5*d* level mixes with the 4*f* level due to the crystal field effect, resulting in an allowable transition. The crystal-field effect is caused by the interactions between the *4f* electrons and the electrons of the ligands. The transition probability changes depending on the symmetry of the ligand field and the electronic state of the Ln ion. The 4*f* orbitals of the Ln ions are shielded by the 5*s* and 5*p* orbitals [53], which increases the fluorescence lifetime. The 6 electrons in the 4*f* shell can be placed in seven 4*f* orbitals. The degeneracy of a 4*f*n electronic configuration is given by the binomial coefficient using the following Equation (3) (**Eq. (3)**).

$$\binom{14}{n} = \frac{14!}{n!\,(14-n)!} \tag{3}$$

where *n* is the number of 4*f* electrons. And the *n* of Eu^{3+} is 6. The energy diagram of the Eu^{3+} ion was shown in **Figure 1-5**. All the peaks correspond to the transitions from the metastable orbital singlet state of $^5D_0$ to the spin–orbital states of ^7F_J (J = 0, 1, 2, 3, 4) of the Eu^{3+} ion. J represents the total angular momentum. These transitions are assigned to the $^5D_0$ to $^7F_0$ at about 575 nm, $^7F_1$ at about 590 nm, $^7F_2$ at about 616 nm, $^7F_3$ at about 653 nm and $^7F_4$ at about 698 nm, respectively. In particular, the transition of $^5D_0$ to $^7F_1$ is called magnetic dipole transition, and the transitions of $^5D_0$ to $^7F_{0,\,2,\,3,\,4}$ are called electric dipole transition. In the case of Eu^{3+}, the electric dipole transition from the excited state $^5D_0$ to the $^7F_{0,\,2,\,3,\,4}$ level is forbidden if the substitution site has

an inversion symmetry. On the other hand, it is known that the occurrence probability of the magnetic dipole transition is irrelevant to symmetry. When an atom or crystal is in the molecule, electrons belonging to the atom of interest undergo a Coulomb interaction from the charge in the surrounding ions. The Coulomb potential due to such a surrounding charge is called the crystal field potential. Due to this crystal field potential, the energy levels of atoms that degenerate in the free atom state split. The degeneracy of the $^4f_6$ configuration is partly or totally lifted by several perturbations acting on the Eu^{3+} ion. Therefore, for cell labeling applications of the Eu^{3+} ions, it is important to change the symmetry and enhance the luminescence.

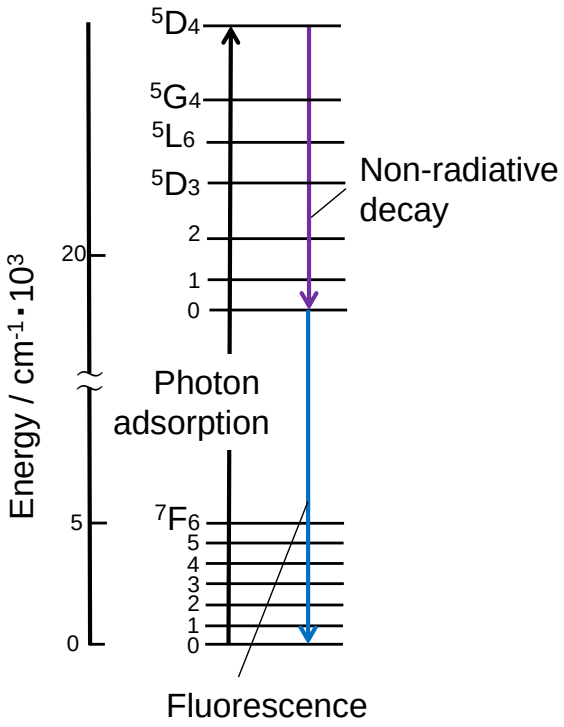

Figure 1-5. Energy diagram of Eu^{3+} and the possible excitation and relaxation processes. The excitation processes consist of $^7F_0 \rightarrow {}^5D_4$, $^7F_0 \rightarrow {}^5G_4$, $^7F_0 \rightarrow {}^5L_6$, $^7F_0 \rightarrow {}^5D_2$ and $^7F_0 \rightarrow {}^5D_1$, and the relaxation processes corresponded to the transitions from the metastable orbital singlet state of $^5D_0$ to the spin–orbital states of ^7F_J (J=0, 1, 2, 3 and 4) of Eu^{3+}.

1.3.2 Doping systems in hydroxyapatite

There are many ions *in vivo* that play important roles in the expression of various biological functions. The HA can be given various functions by the substitution of ions in the crystal structure. The studies of ion substitution in the HA crystal structure have been conducted [54–56]. In particular, it is known that the Ca^{2+} can be substituted by various metal ions. **Table 1-2** shows some reports on the doping of Eu^{3+} ions into the HA structure which is considered to be useful as a cell label. Among

Table 1-2. Synthetic temperatures, approximate sizes of primary particles and excitation and luminescence wavelengths of the Eu^{3+}-doped HA in the previous reports [56–58].

Synthetic temperature (°C)	Approximate size of primary particle (nm)	Excitation wavelength (nm)	Luminescence wavelength (nm)	Remarks	Reference
180	40–190	393	614	2.1 % (internal quantum yield @ excitation wavelength at 393 nm)	[56]
40, 120	10–60	393	618	0.7–2.0 ms (luminescence lifetime)	[57]
60	50–200	394	613	–10.6 ± 4.2 mV (zeta potential)	[58]

the Ln ions, the Eu^{3+} ion is known to have low cytotoxicity. The synthesis temperature has been controlled to synthesize the Eu^{3+} ion-doped HA. Excitation and luminescence spectra measurements were performed in the range of the excitation wavelength of 392–394 nm and luminescence wavelength of 612–618 nm [56–58]. The internal quantum efficiency, fluorescence lifetime and zeta potential were reported as other evaluation remarks in the references. The internal quantum efficiency of 2.1 % was achieved by the excitation light irradiation of 394 nm [56], the fluorescence lifetime of about 0.7–2.0 ms was achieved [57], and the zeta potential of about –10.6 mV was reported [58]. It is required to improve the internal quantum efficiency, elucidate the existence state of Eu^{3+} ion by the fluorescence lifetime, and improve the water dispersibility of Eu^{3+} ion-doped HA by increasing the zeta potential. **Figure 1-6** shows a diagram of the coordination structure of oxygen to the Ca site in HA. The Ca (I) site has a coordination number of 9, and C_3 symmetry, and the Ca (II) site has a coordination number of 7, and C_s symmetry. The transition from $^5D_0$ to $^7F_0$ is known to indicate the presence of Eu^{3+} ions at the Ca (I) and Ca (II) sites in HA. The $^5D_0$ to $^7F_0$ transition peak appears at a maximum fluorescence wavelength of 572 nm at the Ca (I) site and 577 nm at the Ca (II) site [59]. By separating the peak of these two wavelengths, it is possible to evaluate the ratio of Eu^{3+} ions present at the Ca site. The photofunctionalization of HA using the Eu^{3+} ion is the subject of study. However, due to the low internal quantum efficiency, almost no study has been reported on its application in the cell labeling. Thus, the state of Eu^{3+} ions in the HA is important regarding the luminescence behavior.

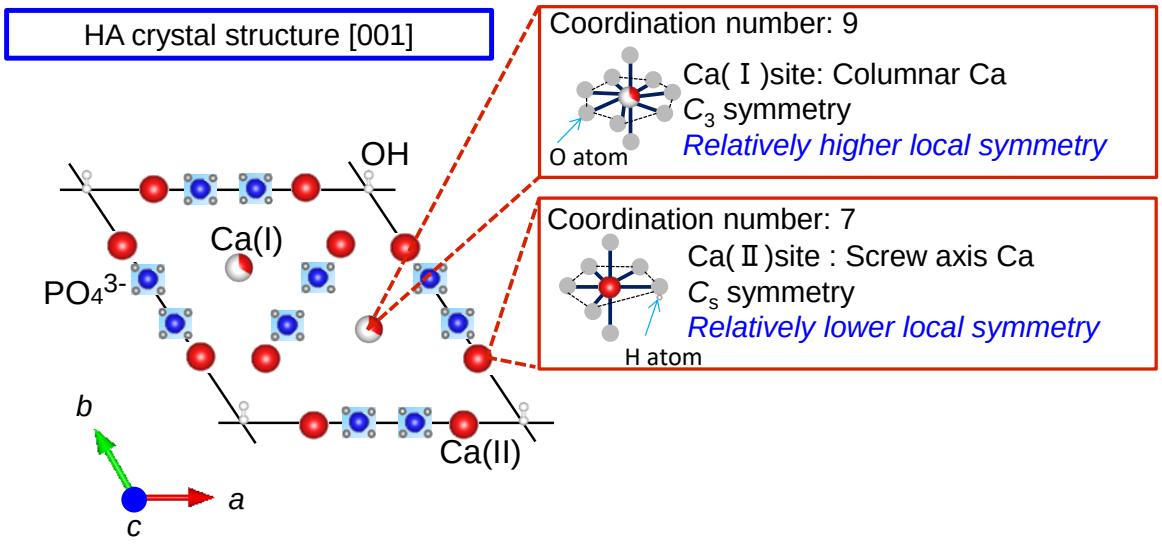

Figure 1-6. Coordination states of Ca (I) and Ca (II) sites in the HA structure.

1.3.3 Organic complex systems

1.3.3.1 Types and photochemical properties

As functional low molecular weight compounds, the Eu (III) complexes having a ligand are interesting because of their luminescent properties and have been studied in the biofield and the electronics field. The Eu (III) complexes have characteristic narrow luminescence spectrum lines and long-lived excited states. The ligands effectively increase light absorption. Although the spectral shape depends on the electronic environment, due to the spatially shielded *f-f* transition, the Eu^{3+} ion alone has a low light absorption ability. It is known that a strong luminescence is observed in the Eu (III) complex in which various ligands are bound to the Eu^{3+} ion. The ligand absorbs the ultraviolet light, and the energy is transferred to the Eu^{3+} ion and finally observed as luminescence. The effect of the ligand is called the antenna effect. When electrons in a singlet ground state molecule are excited to a high energy state by light absorption, they become an excited singlet state (S_1) or an excited triplet state (T_1). The S_1 is a molecular state in which all the electron spins are paired, and the spins of excited electrons become the opposite direction to the ground state electrons. In the T_1, the spins of the excited electrons become the same direction as that of the ground state electrons. Since the excitation to the T_1 includes the inversion of spin, which is a forbidden transition, the probability of the molecule forming the T_1 by light absorption is low. The processes of non-radiatively changing from the S_1 to T_1 or T_1 to S_1 are called intersystem crossing. When the vibrational levels of the two excited states overlap, the probability of intersystem crossing increases because the change in energy

due to the transition is low. **Figure 1-7** shows examples of Eu (III) complexes that have been reported for cell labeling. Some β-diketonato Eu (III) complexes have been used for cell labeling [60,61]. These reports describe that the Eu (III) complex was dissolved in phosphate buffered saline, then cell labeling was performed. In the case of the β-diketonato Eu (III) complex of **Figure 1-7(a)**, the excitation/luminescence spectrum was measured at the excitation wavelength of 402 nm and the luminescence wavelength of 614 nm, and the internal quantum efficiency was 41 % [60]. In the case of the β-diketonato Eu (III) complex of **Figure 1-7(b)**, the excitation/luminescence spectrum was measured at the excitation wavelength of 405 nm and the luminescence wavelength of 612 nm, and the internal quantum efficiency was 23 % [61]. However, these available Eu (III) complex luminescent probes have the problem of color degradation, when the probes are exposed to a continuous and intense excitation light for monitoring the biological processes. By introducing an asymmetric coordination field into the Eu (III) complex, the forbidden transition is broken to allow the *f-f* transition, and the light absorption coefficient can be increased to improve the luminescence intensity. If the symmetry of the ligand can be lowered, application as a cell labeling probe can be expected.

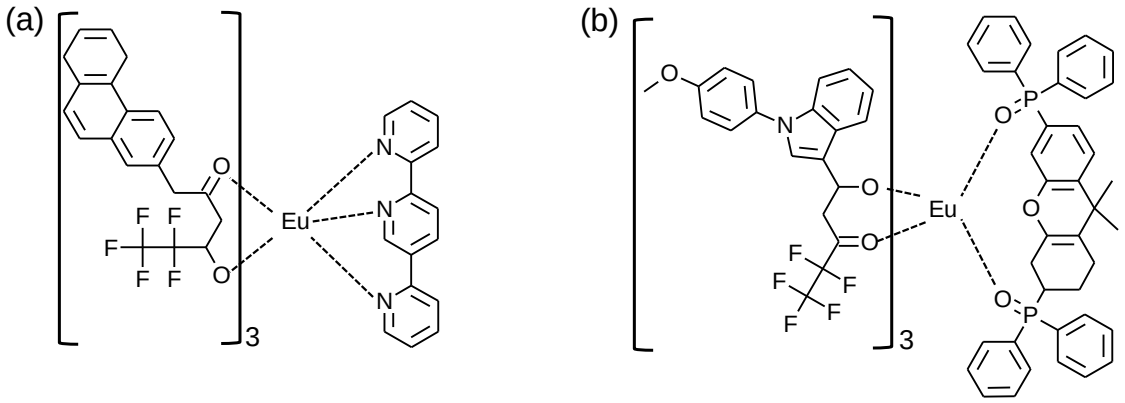

Figure 1-7. Eu^{3+} complexes of (a, b) β-diketonate ligand [60,61]. Internal quantum efficiency of (a) is 41 % (λ_{ex}= 402 nm, λ_{em}= 614 nm), and (b) is 23 % (λ_{ex}= 405 nm, λ_{em}= 612 nm). The Eu^{3+} complexes have been studied for biological labelling applications.

1.3.3.2 Tris (2,2,6,6-tetramethyl-3,5-heptanedionato) europium (III) (EuTH)

The molecular model of tris(2,2,6,6-tetramethyl-3,5-heptanedionato) europium (III) (EuTH) as a complex having the β-diketonato ligand is shown in **Figure 1-8**. This complex has a highly-symmetrical molecular structure and is insoluble in water but soluble in ethanol. Due to the high symmetry of the ligand, the luminescence intensity is low.

In the EuTH, it is known that the distance between the Eu–O and the ligand and the coordination structure affect the electron transition [62]. Different electronic transition states are observed by the coordination symmetry structural change, and the electric dipole transition is strongly observed in the luminescence spectra. Since it can be dissolved in ethanol, the synthesis of a homogeneous nanoparticle with HA can be expected.

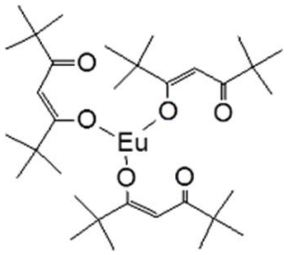

Figure 1-8. Chemical structures of EuTH molecule at the 2-dimensional view.

1.3.3.3 Possibility of synthesis for EuTH-interacted hydroxyapatite

Ln complexes incorporated into an inorganic porous matrix, such as zeolite or mesoporous silica, that forms an inorganic/organic nanoparticle have been reported [63,64]. The confinement of the Ln complex within the inorganic porous structure not only improves its stability but also reduces the quenching due to aggregation between the Ln complexes. However, the nanoparticle with luminescent properties based on the inorganic/organic interface of highly biocompatible HA nanoparticles has not been reported. It is expected that the electron localization between the ligand of the Ln complex and the central metal can be used as a nucleation site of the HA crystals. It was also possible that a high luminescence behavior can be achieved. The nucleation of HA in the electron localization of EuTH may lead to the construction of the HA/EuTH interface.

1.4 Molecule that specifically binds to a cancer cell

1.4.1 Receptor expressed on cell surface

Receptors are present in all cells. The receptor is a substance and is present on the cell membrane, which specifically binds to a substance outside the cell membrane and is usually a protein. Cells can identify specific substances by receptors and receive information from outside the cells. The binding of the receptor to the substance triggers a variety of responses in the cell. **Table 1-3** shows the types of receptors expressed on the surface of epithelial cancer cells that can be treated with an endoscope [65–70].

The types of overexpressed receptors differ depending on the type of cancer. It is known that specific recognition of these receptors enables particle uptake into the cells.

Table 1-3. Classifications of epithelial cancer cells that can be treated with an endoscope, excess expression receptor on the cells and their binding molecules [65–70].

Classification of cancer	Excess expression receptor	Classification of binding molecule	Reference
Epithelial-derived tumor	α-Folate receptor	α-Folate	[65]
Breast cancer	Estrogen receptor	Estrogen	[66]
Breast cancer or endometrial cancer	Progesterone receptor	Progesterone	[67]
Gastric cancer, breast cancer, ovarian cancer	HER2 receptor	HER2	[68]
Skin cancer	Insulin receptor	Insulin	[69]
Metastatic tumor and drug resistant tumor	Transferrin receptor	Transferrin	[70]

1.4.2 Types of molecules that specifically bind to receptors

Table 1-3 also shows the molecules that recognize and specifically bind to the receptors. For example, folic acid (α-folic acid) binds approximately perpendicular to folate receptor groove formed by helices (protein) [71]. The N and O atoms of hydrophilic pterin ring form hydrogen bonds with the receptor residues. The N atoms of pterin in the folic acid form strong hydrogen bonds with the side-chain carboxyl group and hydroxyl group of receptor [71], and then van der Waals forces provide the final strong binding interaction [72]. The high binding affinity (1.0–10 $\times 10^9$ M^{-1}) of the folate receptor for folic acid has led to the development of drug conjugates with the folic acid [73]. The benefits of using folic acid are manifold. In particular, it has high stability and can be easily immobilized to various types of organic molecules, antibodies and nanoparticles. The folate receptors are overexpressed on cancer cells. The folate receptors on human cervical cancer-derived (HeLa) cells are overexpressed 3.5 times as much as in normal cells (NIH swiss mouse embryo-derived (NIH3T3) fibroblasts) [74]. Moreover, folate receptors on HeLa cells are more than twice as overexpressed as other cancer cells (such as adenocarcinomic human alveolar basal epithelial cells and human breast adenocarcinoma cells) [75]. The recognition of organic molecules or proteins corresponding to the receptor allows the particle uptake into the cells. The binding affinity between folate receptors and folic acid molecule, and the number of receptors on

the surface of cancer cells allow the selective uptake of the cell labeling nanoparticles into the cancer cells [73]. In order to be used as the cell labeling nanoparticles, the molecules should be present in the dispersed state on the particle surfaces. The aggregation of the molecules may make it difficult for the receptor to recognize the molecules. Thus, the efficient uptake of HA nanoparticles into the cells becomes possible by immobilizing the cell-binding (ligand) molecules on the HA surface.

1.4.3 Immobilization technique of specific binding molecule to solid surface

By immobilizing a specific binding molecule on a solid surface, it is possible to impart new properties such as *in vivo* stability, tissue targeting, cell tropism, *etc*., to the nanoparticle. In order to maximize the properties of the nanoparticles *in vivo*, it is necessary to achieve surface immobilization techniques that consider the interaction between the cells and particles. The surface immobilization techniques are both chemical (covalent bond) and physical (non-covalent bond). One of the highly-stable chemical methods is reacting a functional group on the solid surface with a specific binding molecule. In this method, since the reactive groups of the molecules immobilized on the surface cause steric hindrance, the polymerization density decreases. Inorganic particles having a hydroxyl group on the surface can be easily made into a functional surface by the method. As an example, hydrophilic amorphous silica particles are negatively charged (≡Si–OH), because the oxygen present in the skeleton of $–SiO_4–$ is partially deficient. When the hydroxyl group on the surface of the amorphous silica is reacted with 3-aminopropyltriethoxysilane (APTES, $H_2N(H_2C)_3Si(OCH_2CH_3)_3$), trimethoxy (2-carboxyethyl) silane ($HOOC(CH_2)_2Si(OCH_3)_3$) and the methylphosphonic acid 3-(trivinylxylsilyl) propyl salt ($NaPO_3(CH_2)_3Si(OH)_3$), *etc*., it becomes positively or negatively charged by the covalent bond. Specifically, the hydroxyl group of the silicon alkoxide and the hydroxyl group of the solid surface form a hydrogen bond, and the covalent bond is formed by dehydration condensation. Thereby, reactive functional groups, such as amino groups ($–NH_2$) and carboxyl groups (–COOH) can be present on the solid surface. **Figure 1-9** showed an example of the immobilization of molecules already reported. **Figure 1-9(a)** showed the immobilization process of APTES on a solid surface. By bonding an amino group-terminated silane coupling agent to the solid surface, the OH group on the solid surface is bonded to Si. The following is an example of the reaction process of APTES.

Formation of silanol group by hydrolysis (**Eq. (4)**) ;

$$H_2N(H_2C)_3-Si(OC_2H_5)_3 + 3H_2O \rightarrow H_2N(H_2C)_3-Si(OH)_3 + 3C_2H_5OH \quad (4)$$

Self-assembly reaction of hydrolyzed silanes (**Eq. (5)**) between the molecules occurs.

$$\begin{aligned} &H_2N(H_2C)_3-Si(OH)_3 + H_2N(H_2C)_3-Si(OH)_3 \\ &\rightarrow H_2N(H_2C)_3-Si(OH)_2-O-Si(OH)_2-(CH_2)_3NH_2 \end{aligned} \quad (5)$$

Dehydration condensation on the solid surface (**Eq. (6)**) occurs between the molecule and solid surface.

$$\begin{aligned} &H_2N(H_2C)_3-Si(OH)_3 + HO-\bullet \\ &\rightarrow H_2N(H_2C)_3-Si(OH)_2-O-\bullet + H_2O \end{aligned} \quad (6)$$

where ● is a solid surface.

Figure 1-9(b-1 and **b-2)** showed the immobilization processes of molecules on the solid surface. These are examples of the immobilization of a molecule via the APTES [76,77]. The following is an example of the reaction process (reaction of **Figure 1-9(b-1)**) **Eq. (7)**.

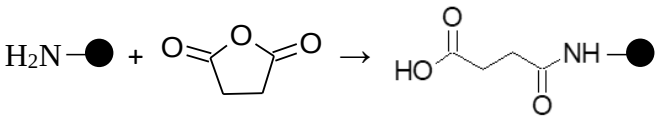

(7)

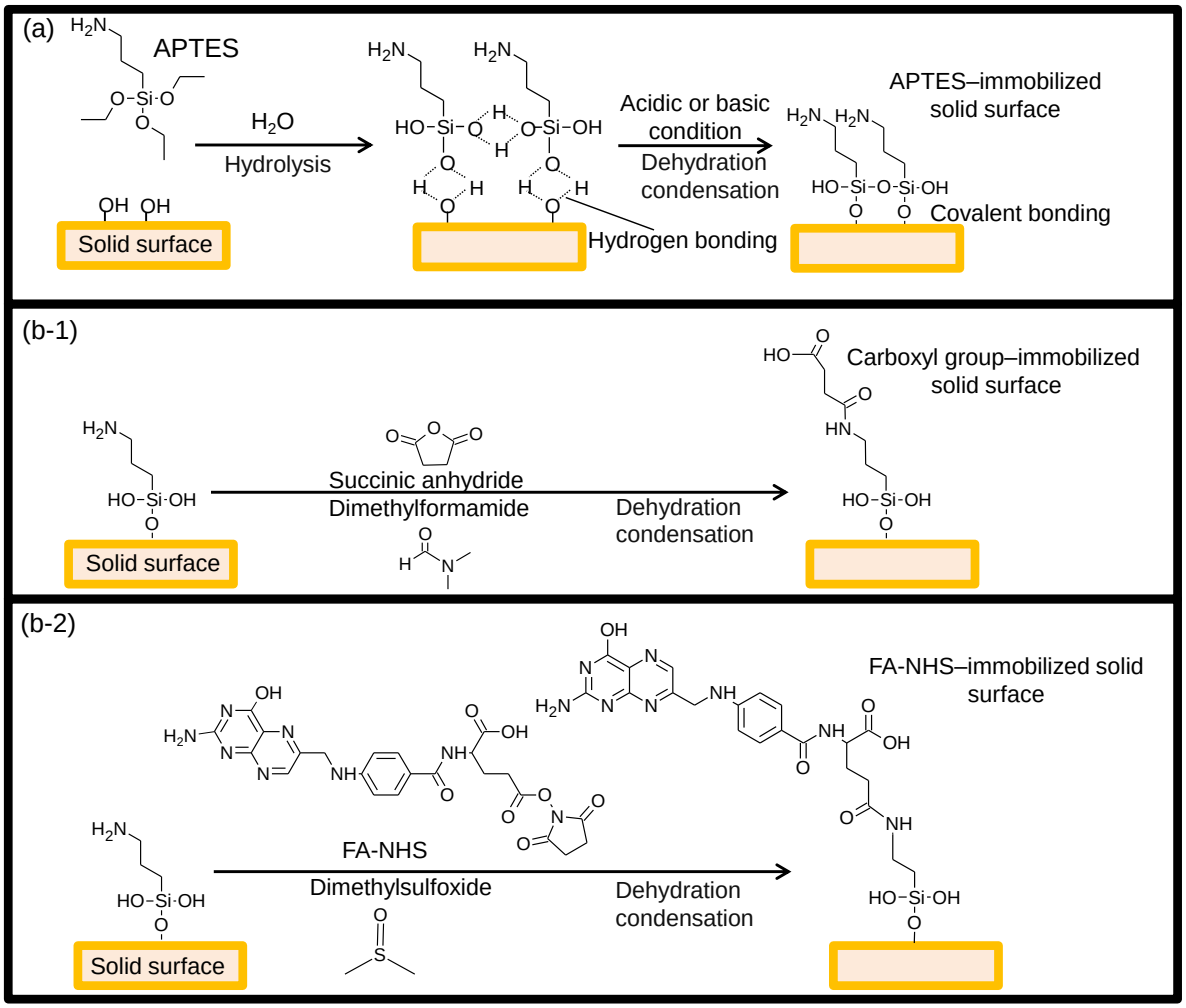

Figure 1-9. Immobilization processes of (a) APTES, (b-1) carboxyl group and (b-2) FA-NHS on the solid surface. In this case, the representative APTES-immobilized solid surface changed from an amine to (b-1) carboxyl group and (b-2) FA-NHS were shown.

The surface amino group stably immobilizes the molecule through the peptide (–HN–CO–) bond. Specifically, APTES is bonded to the solid surface by a liquid phase reaction, the solid surface is coated with the –Si–O–Si– bond, and the amino group is exposed to the surface. Next, the molecule is formed via a covalent bond to the solid surface by a dehydration condensation reaction ($–NH_2$ + –COOH → –NH–CO–) of an amino group and a carboxylic acid in the molecule. Such a reaction mechanism makes it possible to immobilize folate derivatives (folate *N*-hydroxysuccinimidyl ester (FA-NHS)), which are known to specifically bind to cancer cells, on the solid surfaces [78]. As the report of the physical surface immobilization technique, the immobilization of ferritin by an electrostatic interaction was achieved on the solid surface [79]. The uptake of the ferritin-immobilized particles into cells was also observed. Thus, for the solid surface, various surface states can be designed.

1.5 Cancer cell growth inhibitory drug molecules

1.5.1 Representative molecules and their functions

Table 1-4 shows examples of cytostatic drug molecules. Vitamin C exerts a strong antioxidant action and generates a large amount of hydrogen peroxide [80]. Although normal

Table 1-4. Mechanism and function of cytostatic drug molecules in the previous reports [80–85].

Cytostatic drug molecules	Mechanism	Function	Reference
Vitamin C	Damage of tumor cell due to high dosage	Damage of tumor cells by generation of hydrogen peroxide	[80]
Fucoidan	Induction of apoptosis of cancer cells	Anti-tumor function by modulating endoplasmic reticulum stress cascades	[81]
Caffeine	Induction of apoptosis by activating the caspase-9/caspase-3 pathway	Function as a sustained anticancer agent by activating the caspase-9/caspase-3 pathway	[82]
Citric acid	Suppression of tumor cell growth both in glycolysis and tricarboxylic acid cycles *in vitro*	Suppression of lung cancer cell growth by dosage	[83–85]

cells can neutralize hydrogen peroxide, cancer cells cannot neutralize it, causing cell death. Fucoidan has been shown in basic studies to have the function of transmitting stress signals to the endoplasmic reticulum and inducing cell death [81]. Caffeine has been reported to inhibit cancer cell DNA repair and suppress the growth of cancer cells. It has also been reported that the caspase-9/caspase-3 pathway, which is one of the signal transduction pathways causing cell death, functions as a persistent anticancer agent by activation [82]. Citric acid is known to induce cell death by inhibiting the function of proteins involved in cell growth by forming a chelate in the cell with minerals such as iron and calcium [83,84]. It has also been reported that the glycolytic system of the cell is inhibited to suppress proliferation [85]. If these drug molecules can be contained with the HA, they may be applied as nanoparticles for cancer therapy.

1.5.2 Citric acid

Figure 1-10 shows the molecular structure of citric acid (**Figure 1-10(a)**), dissociation state in solution (**Figure 1-10(b)**) and mechanism of suppression of cancer cell growth by citric acid in the cancer cells (**Figure 1-10(c)**). When the amount of citric acid is increased in the cancer

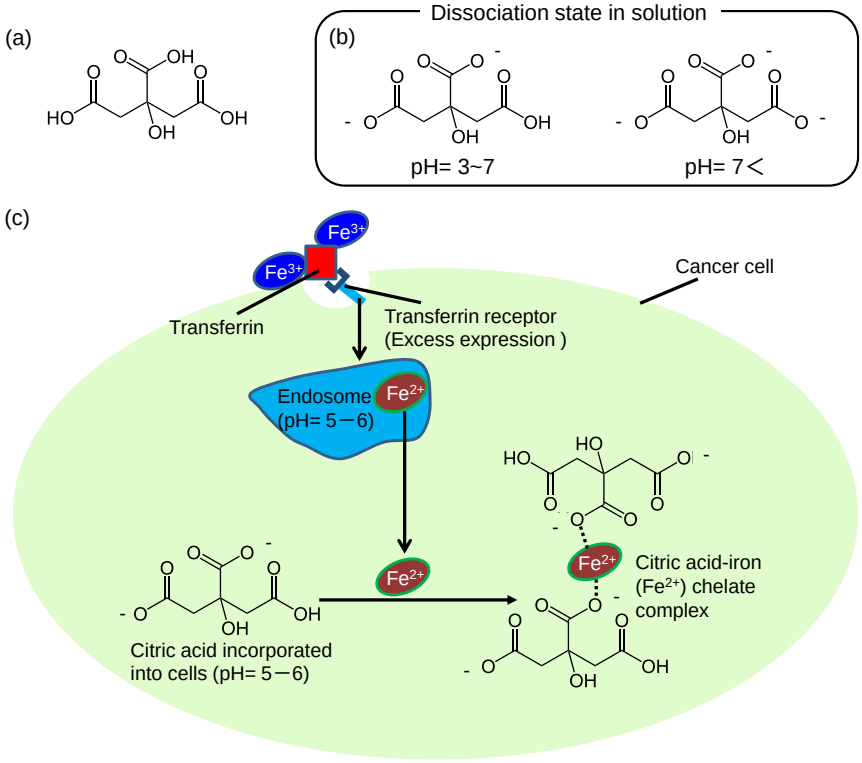

Figure 1-10. (a) Chemical structure of citric acid and (b) dissociated state in solution at the different pH (pK_{a1}= 3.12, pK_{a2}= 4.76, pK_{a3} = 6.39). (c) Cytostatic mechanism by citric acid. Citric acid and Fe^{2+} ions can form a chelate complex, and the depletion of Fe^{2+} ions in the cytoplasm can suppress the cancer cell proliferation. The binding affinity between citric acid and iron (II) is about 5.0×10^{19} M^{-1}, and the binding affinity between citric acid and Ca^{2+} is about 2.0×10^{4}. In the cells, stable chelates are formed between $Fe^{2+}$and citrate.

cells, chelates are formed with calcium, iron, copper and zinc, which inhibit the action of proteins and antioxidant enzymes involved in cell growth. As a result, it has been reported to suppress the growth of cancer cells and induce cell death. In the blood, iron (III) ions (Fe^{3+}) bind to transferrin and are transported into the cells. Two Fe^{3+} ions bind to one transferrin. Transferrin binds to the transferrin receptor located on the cell membrane and is taken up by endocytosis. When it becomes an acidic environment in the lysosome (endosome), Fe^{3+} ions are then dissociated into iron (II) ions (Fe^{2+}). It then forms the chelate complex with citric acid, depletes Fe^{2+} ions in the cytoplasm, and inhibits the growth of the cells [86]. The binding affinity between citric acid and Fe^{2+} ion is about 5.0×10^{19} M^{-1} [87], and the binding affinity between citric acid and Ca^{2+} ion is

about 2.0×10^4 M^{-1} [88]. In addition, some concentrations of Fe^{2+} ion and Ca^{2+} ion in normal cells and cancer cells have been reported. The Fe^{2+} ion in mouse-derived fibroblasts (BALB/3T3) as one of the normal cells has been reported to be about 1.0 pg/L [89], and the Fe^{2+} ion in human-derived cancer cells (THP-1) as one of the cancer cells has been reported to be about 0.1–0.5 pg/cell [90]. It is known that both Ca^{2+} ion in normal and cancer cells maintain the concentratiat the several tens of nM regardless of the cell types [91]. In the cells, stable chelates are formed between the Fe^{2+} ions and citric acid. In normal cells (e.g., prostatic epithelium cells) [92], it is known that the addition of citric acid does not affect cellular activity.

1.5.3 Possibility of synthesis for citric acid coordinated hydroxyapatite

The citric acid molecule is used to control the form of HA and is known to exist as the carboxyl ion of $–COO^-$ in alkaline solution and as a dimer by hydrogen bonding in the form of $(–COOH)_2$ in an acidic solution [93]. Since HA has Ca sites in the *a*-axis direction and phosphate sites in the *c*-axis direction, it has been thought that citric acid molecule adsorbs on the Ca sites and affects the formation of the HA nanoparticles. During HA formation in alkaline solution, it has been suggested that the carboxyl ion of the citric acid molecule and Ca^{2+} ions of HA chemically bond perpendicular to *a*-plane (100) on the HA. The citric acid molecule easily forms the chelate with the Ca^{2+} ions of the HA. The citric acid is stably present on the particle surface by coordinating with Ca^{2+} ions on the outermost surface of HA. On the basis of these results, it has been considered that the competitive reaction between the HA formation and chelate formation enables the synthesis of nanoparticles. The synthesis of nanoparticles can be achieved by utilizing the interaction between ions present at the Ca sites in the HA and carboxyl ions of the citric acid molecule. Therefore, by coordinating the citric acid to HA nanoparticles for cancer cell labeling, it may be possible to impart cytostatic ability. When the citric acid coordinated HA nanoparticles are added to cells collected by tissue biopsy containing cancer cells and normal cells and cultured, normal cells may be able to grow preferentially. By binding luminescent HA nanoparticles to cancer cells and removing the luminescent cancer cells, only normal cells can be taken out and transplanted *in vivo*, which may contribute to regenerative medicine.

1.6 Purpose of this study

Cancer cell labeling nanomaterials have been developed that stain specific cells for visualization without cytotoxicity. However, significant problems are known such as color degradation and toxicity in conventional nanomaterials. HA is one of the excellent options to

overcome the barriers based on its high biocompatibility, HA is present as the main component of hard tissues *in vivo*, making it possible to be utilized as a biomaterial. When aiming at the cell labeling application of HA, it is important to bind a photofunctional molecule with HA in the nucleation process and to synthesize nanoparticles as a form of inorganic/organic nanoparticles. Moreover, a study to develop theranostic nanoparticles with fluorescence and therapeutic properties toward applications in such a field as biomedicine is important. In order to design novel theranostic nanoparticles, one of the keys would be to control interfacial interactions between HA and functional molecules. To explore the combination of HA and various functional molecules will lead to a large number of multifunctional nanoparticles that advance the frontier technologies of bio-related fields. A rapid cell labeling and easily observable luminescence intensity by HA/functional molecule nanoparticles were aimed. Moreover, it was also proposed to design the theranostics HA nanoparticles with therapeutic functions by selecting appropriate functional molecules. Specifically, This study focused on the "ion–polar interaction" and the " ion–ion interaction" between HA and functional molecules. (**Figure 1-11**).

The targets to be achieved in this study are shown below:

I Extreme biosafety for normal cells

- ✓ The ratio of N_1 (which means the normal cell adhesion density with adding nanoparticles at the culture time of 24 h) to N_0 (which means the normal cell adhesion density without adding nanoparticles at the culture time of 24 h)) (N_1/N_0) is 0.7 or more [45]
- ✓ Average particle size of 20–200 nm in biological fluid (coefficient of variation: 30 % or less) [43]
- ✓ Excitation/luminescence visible light at 400–800 nm region in the observation

II Efficient luminescence

- ✓ Strong luminescence intensity that can be visually confirmed
- ✓ Internal quantum efficiency of more than 7 % [94]

III Construction of particle surface that is rapid binding with cancer cells and taken up into the cells at high concentration

- ✓ High concentration of binding and uptake into cells by immobilization of cell-binding molecules [78]
- ✓ Short-term labeling of tumor cells within 3 h after the adding nanoparticles [95,96]

IV Achievement of both cancer cell labeling and suppression of cell growth

- ✓ Growth suppression (N_1/N_0 ratio of 0.7 or less) while labeling cancer cells [45]

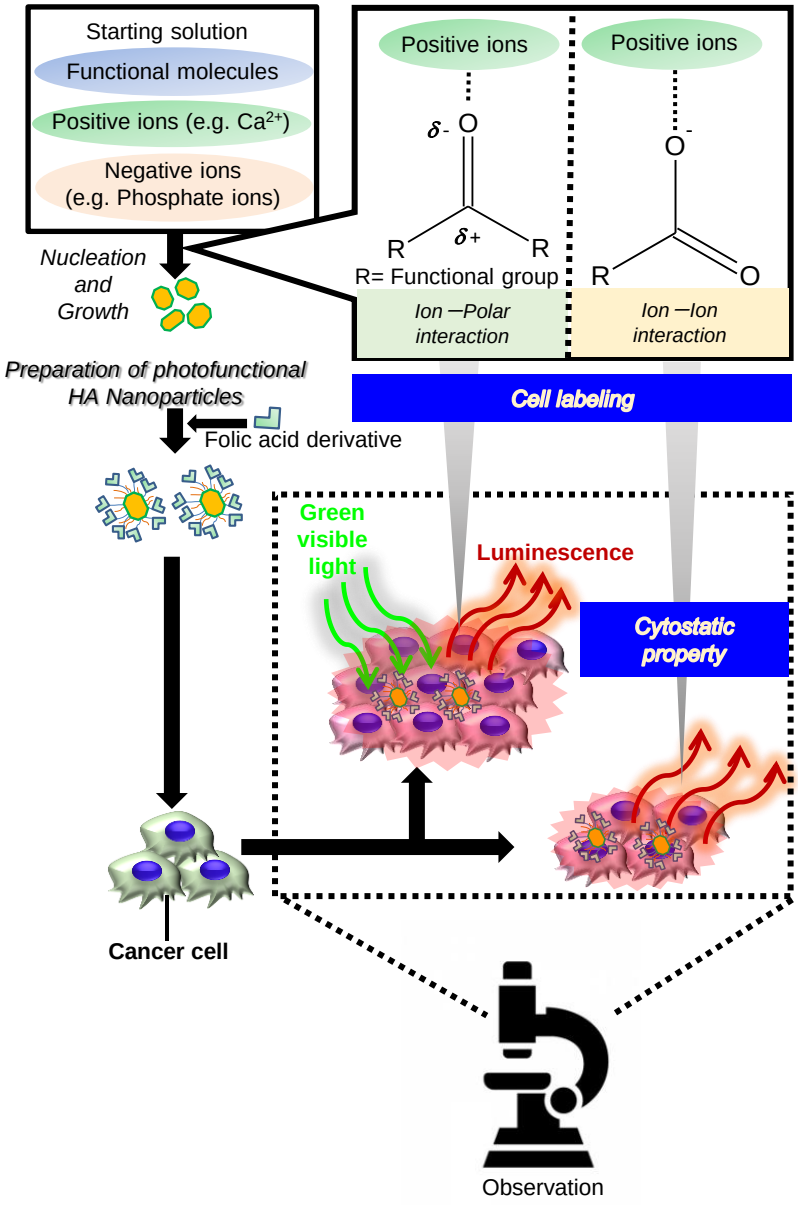

Figure 1-11. Scheme of the purpose of this study.

1.7 Contents of this thesis

In this thesis, it was investigated about “Study on Synthesis of Luminescent Hydroxyapatite Nanoparticles and Their Surface Functionalization for Cell Labeling Applications”. It was found a technology for photofunctionalization and surface functionalization of hydroxyapatite (HA) nanoparticles, which are the main components of hard tissues in the living body, and evaluated and clarified the cell labeling properties. This thesis consists of four chapters. (**Figure 1-12**)

In ***Chapter 1***, "*General Introduction*", the problems of cell labeling technology were

explained by giving examples of conventional cell labeling nanomaterials. Furthermore, the photophysical chemistry properties of Eu (III) ion were described. Moreover, the importance of the Ca site of HA and the inorganic/organic interface structure between HA and functional molecules to realize photofunctionalization and cell selectivity *in vivo* were proposed, and the control of the interface state was outlined. Then, focusing on the inorganic/organic interface of photofunctional HA and functional molecules, the strategy for photofunctionalization of HA was proposed. Furthermore, It described cell-binding molecule immobilization technology to particle surface for specific binding or uptake to cancer cells and showed the significance and purpose of this study.

In ***Chapter 2***, "*Synthesis of Luminescent Europium(III) Complex-interacted Hydroxyapatite Nanoparticles and Their Rapid Cell Labeling by Folic Acid Immobilization*", EuTH with β-diketonato ligand was contained at the particle growth stage of HA, and the effect of EuTH concentration was discussed. Then, folic acid derivative molecules were immobilized on the nanoparticle surface via 3-aminopropyltriethoxysilane (APTES), and the cell-binding property was discussed. Furthermore, it was evaluated the cytocompatibility to NIH swiss mouse embryo-derived (NIH3T3) fibroblasts and binding or uptake behavior to human cervical cancer-derived (HeLa) cells.

In ***Chapter 3***, "*Synthesis of Luminescent Hydroxyapatite Nanoparticles Coordinated with Citric Acid for Their Bifunctional Cell Labeling and Cytostatic Properties*", luminescent Eu^{3+} ion-doped HA nanoparticles coordinated with citric acid were synthesized by substituting Ca site of HA with less toxic Eu^{3+} ion in the presence of citric acid. The physicochemical properties based on the interfacial interactions between Eu^{3+} ion-doped HA and citric acid at the nanoparticle surfaces were discussed. Then, folic acid derivative molecules were immobilized on the nanoparticle surface via APTES, and the binding or uptake behavior of cells was examined. Specifically, the cytocompatibility using NIH3T3 fibroblasts and cell labeling properties against HeLa cells were evaluated to investigate the effect of the nanoparticles on the suppression of HeLa cell growth.

In ***Chapter 4***, "*Summary*", it was summarized the usefulness of the luminescent HA nanoparticles of this study as cell labeling nanoparticles. Furthermore, it was mentioned the synthesis of luminescent HA nanoparticles in the presence of functional molecules and the photofunctional interfaces between HA and functional molecules achieved by nanoparticles of HA and functional molecules.

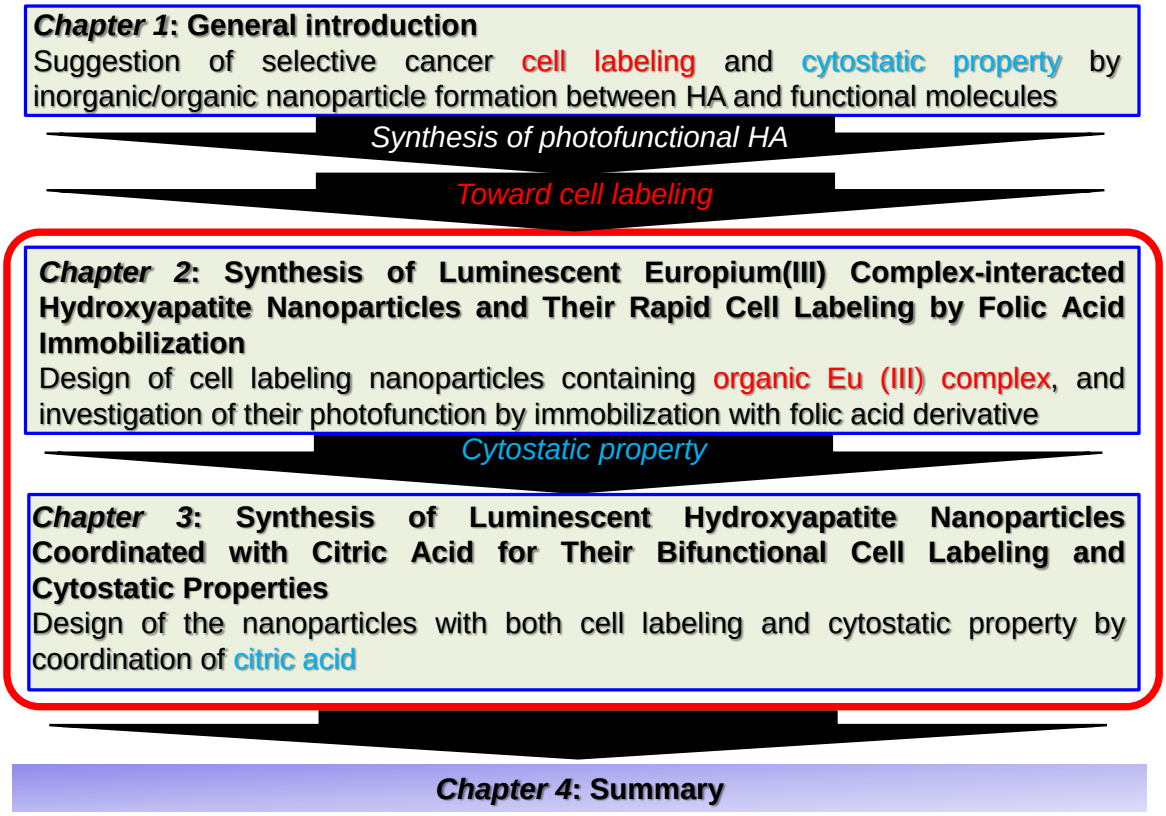

Figure 1-12. Chapter contents and their constructions of this thesis.

References

[1] M. Zhang, M. Yu, F. Li, M. Zhu, M. Li, Y. Gao, L. Li, Z. Liu, J. Zhang, D. Zhang, T. Yi, C. Huang, A highly selective fluorescence turn-on sensor for cysteine/homocysteine and its application in bioimaging, J. Am. Chem. Soc. 129 (2007) 10322–10323.

[2] S. Zhu, Q. Meng, L. Wang, J. Zhang, Y. Song, H. Jin, K. Zhang, H. Sun, H. Wang, B. Yang, Highly photoluminescent carbon dots for multicolor patterning, sensors, and bioimaging, Angew. Chemie. 125 (2013) 4045–4049.

[3] Y. Yang, Q. Zhao, W. Feng, F. Li, Luminescent chemodosimeters for bioimaging, Chem. Rev. 113 (2013) 192–270.

[4] S.C. Ray, A. Saha, N.R. Jana, R. Sarkar, Fluorescent carbon nanoparticles: Synthesis, characterization, and bioimaging application, J. Phys. Chem. C. 113 (2009) 18546–18551.

[5] C. Müller, K. Zhernosekov, U. Köster, K. Johnston, H. Dorrer, A. Hohn, N.T. Van Der Walt, A. Türler, R. Schibli, A unique matched quadruplet of terbium radioisotopes for PET and SPECT and for α- and β--radionuclide therapy: An in vivo proof-of-concept study with a new receptor-targeted folate derivative, J. Nucl. Med. 53 (2012) 1951–1959.

[6] C.G. Hadjipanayis, M.J. Bonder, S. Balakrishnan, X. Wang, H. Mao, G.C. Hadjipanayis, Metallic iron nanoparticles for MRI contrast enhancement and local hyperthermia, Small. 4 (2008) 1925–1929.

[7] S. Achilefu, Lighting up tumors with receptor-specific optical molecular probes, Technol. Cancer Res. Treat. 3 (2004) 393–409.

[8] U. Noriya, I. Ryu, I. Hiroyasu, Diagnosis of upper gastrointestinal diseases using autofluorescence imaging videoendoscopy system, Nippon Laser Igakkaishi. 30 (2009) 37–40.

[9] S. Masuda, Y. Yanase, E. Usukura, S. Ryuzaki, P. Wang, K. Okamoto, T. Kuboki, S. Kidoaki, K. Tamada, High-resolution imaging of a cell-attached nanointerface using a gold-nanoparticle two-dimensional sheet, Sci. Rep. 7 (2017) 1–10.

[10] N.M. Zaki, N. Tirelli, Gateways for the intracellular access of nanocarriers: A review of receptor-mediated endocytosis mechanisms and of strategies in receptor targeting, Expert Opin. Drug Deliv. 7 (2010) 895–913.

[11] T.F. Roth, K.R. Porter, Yolk protein uptake in the oocyte of the mosquito aedes aegypti. l, J. Cell Biol. 20 (1964) 313–32.

[12] S. Monier, R.G. Parton, F. Vogel, J. Behlke, A. Henske, T. V Kurzchalia, VIP21-caveolin, a membrane protein constituent of the caveolar coat, oligomerizes in vivo and in vitro., Mol. Biol. Cell. 6 (1995) 911–27.

[13] A. Miyawaki, Y. Niino, Molecular spies for bioimaging-fluorescent protein-based probes, Mol. Cell. 58 (2015) 632–643.

[14] K. Okabe, N. Inada, C. Gota, Y. Harada, T. Funatsu, S. Uchiyama, Intracellular temperature mapping with a fluorescent polymeric thermometer and fluorescence lifetime imaging microscopy, Nat. Commun. 3 (2012) 1–9.

[15] A. Fukazawa, S. Suda, M. Taki, E. Yamaguchi, M. Grzybowski, Y. Sato, T. Higashiyama, S. Yamaguchi, Phospha-fluorescein: a red-emissive fluorescein analogue with high photobleaching resistance, Chem. Commun. 52 (2016) 1120–1123.

[16] J. Shen, Y. Zhu, X. Yang, C. Li, Graphene quantum dots: emergent nanolights for bioimaging, sensors, catalysis and photovoltaic devices, Chem. Commun. Chem. Commun. 48 (2012) 3686–3699.

[17] A. Kumari, A. Sharma, U. Malairaman, R.R. Singh, Proficient surface modification of CdSe quantum dots for highly luminescent and biocompatible probes for bioimaging: A comparative experimental investigation, J. Lumin. 199 (2018) 174–182.

[18] L. Wang, W. Li, M. Li, Q. Su, Z. Li, D. Pan, M. Wu, Ultrastable amine, sulfo cofunctionalized graphene quantum dots with high two-photon fluorescence for cellular imaging, ACS Sustain. Chem. Eng. 6 (2018) 4711–4716.

[19] T. Zako, H. Nagata, N. Terada, M. Sakono, K. Soga, M. Maeda, Improvement of dispersion stability and characterization of upconversion nanophosphors covalently modified with PEG as a fluorescence bioimaging probe, J. Mater. Sci. 43 (2008) 5325–5330.

[20] H. Wang, M. Uehara, H. Nakamura, M. Miyazaki, H. Maeda, Synthesis of well-dispersed Y_2O_3:Eu nanocrystals and self-assembled nanodisks using a simple non-hydrolytic route, Adv. Mater. 17 (2005) 2506–2509.

[21] A. Escudero, C. Carrillo-Carrión, M. V. Zyuzin, S. Ashraf, R. Hartmann, N.O. Núñez, M. Ocaña, W.J. Parak, Synthesis and functionalization of monodisperse near-ultraviolet and visible excitable multifunctional Eu^{3+}, Bi^{3+}:$REVO_4$ nanophosphors for bioimaging and biosensing applications, Nanoscale. 8 (2016) 12221–12236.

[22] Z. Li, H. Miao, Y. Fu, Y. Liu, R. Zhang, B. Tang, Fabrication of $NaYF_4$:Yb,Er nanoprobes for cell imaging directly by using the method of hydrion rivalry aided by ultrasonic, Nanoscale Res. Lett. 11 (2016) 1–10.

[23] S.Koutsopoulos, Synthesis and characterization of hydroxyapatite crystals: A review study on the analytical methods, J. Biomed. Mater. Res. 62 (2002) 600–612.

[24] J.P. Fabiola Vázquez-Hernández, Salvador Mendoza-Acevedo, Claudia Oliva Mendoza-Barrera Mendoza-Álvarez, Julio Luna-Arias, Antibody-coupled hydroxyapatite nanoparticles as efficient tools for labeling intracellular proteins, Mater. Sci. Eng. C. 71 (2017) 909–918.

[25] H.-W.J. Jeremy B. Vines, Dong-Jin Lim, Joel M. Anderson, Hydroxyapatite nanoparticle reinforced peptide amphiphile nanomatrix enhances the osteogenic differentiation of mesenchymal stem cells by compositional ratios, Acta Biomater. 8 (2012) 4053–4063.

[26] Z. Shi, X. Huang, Y. Cai, R. Tang, D. Yang, Size effect of hydroxyapatite nanoparticles on proliferation and apoptosis of osteoblast-like cells, Acta Biomater. 5 (2009) 338–345.

[27] X. Peng, J. Wickham, A.P. Alivisatos, Kinetics of II-VI and III-V colloidal semiconductor nanocrystal growth: “Focusing” of size distributions, J. Am. Chem. Soc. 120 (1998) 5343–5344.

[28] C. Burda, X. Chen, R. Narayanan, M.A. El-Sayed, Chemistry and properties of nanocrystals of different shapes, Chem. Rev. 105 (2005) 1025–1102.

[29] Y. Huang, J.E. Pemberton, Synthesis of uniform, spherical sub-100nm silica particles using a conceptual modification of the classic LaMer model, Colloids Surfaces A Physicochem. Eng. Asp. 360 (2010) 175–183.

[30] V.C. Dumont, A.A.P. Mansur, S.M. Carvalho, F.G.L. Medeiros Borsagli, M.M. Pereira, H.S. Mansur, Chitosan and carboxymethyl-chitosan capping ligands: Effects on the nucleation and growth of hydroxyapatite nanoparticles for producing biocomposite membranes, Mater. Sci. Eng. C. 59 (2016) 265–277.

[31] J.L. Kirschvink, H.A. Lowenstam, Mineralization and magnetization of chiton teeth: paleomagnetic, sedimentologic, and biologic implications of organic magnetite, Earth Planet. Sci. Lett. 44 (1979) 193–204.

[32] L.R. Brooker, A.P. Lee, D.J. Macey, W. Van Bronswijk, J. Webb, Multiple-front iron-mineralisation in chiton teeth (Acanthopleura echinata: Mollusca: Polyplacophora), Mar. Biol. 142 (2003) 447–454.

[33] L.M. Gordon, D. Joester, Nanoscale chemical tomography of buried organicg-inorganic interfaces in the chiton tooth, Nature. 469 (2011) 194–198.

[34] T. Miyazaki, Development of novel bone integrating materials inspired by medical glass, New Glas. 24 (2009).

[35] P. Zhu, Y. Masuda, K. Koumoto, The effect of surface charge on hydroxyapatite nucleation, Biomaterials. 25 (2004) 3915–3921.

[36] A. Takeuchi, C. Ohtsuki, T. Miyazaki, M. Kamitakahara, S.I. Ogata, M. Yamazaki, Y. Furutani, H. Kinoshita, M. Tanihara, Heterogeneous nucleation of hydroxyapatite on protein: Structural effect of silk sericin, J. R. Soc. Interface. 2 (2005) 373–378.

[37] M. Tanahashi, T. Matsuda, Surface functional group dependence on apatite formation on self-assembled monolayers in a simulated body fluid, J. Biomed. Mater. Res. 34 (1997) 305–315.

[38] Q. Liu, J. Ding, F.K. Mante, S.L. Wunder, G.R. Baran, The role of surface functional groups in calcium phosphate nucleation on titanium foil: A self-assembled monolayer technique, Biomaterials. 23 (2002) 3103–3111.

[39] S. Kim, C.B. Park, Bio-inspired synthesis of minerals for energy, environment, and medicinal applications, Adv. Funct. Mater. 23 (2013) 10–25.

[40] Y. Mikami, H. Tsuda, Y. Akiyama, M. Honda, N. Shimizu, N. Suzuki, K. Komiyama, Alkaline phosphatase determines polyphosphate-induced mineralization in a cell-type independent manner, J. Bone Miner. Metab. 34 (2016) 627–637.

[41] B. Simons, Passive transport and binding of lead by human red blood cells, J. Physiol. 378 (1986) 267–286.

[42] J.C. Skou, Enzymatic basis for active transport of Na^+ and K^+ across cell membrane, Physiol. Rev. 45 (1965) 596–617.

[43] K. Deshmukh, M.M. Shaik, S.R. Ramanan, M. Kowshik, Self-activated fluorescent hydroxyapatite nanoparticles: A promising agent for bioimaging and biolabeling, ACS Biomater. Sci. Eng. 2 (2016) 1257–1264.

[44] J. Guang, W. Haifang, Y. Lei, W. Xiang, P. Rongjuan, Y. Tao, Z. Yuliang, G. Xinbiao, Cytotoxicity of carbon nanomaterials: single-wall nanotube, multi-wall nanotube, and fullerene, Environ. Sci. Technol. 39 (2005) 1378–1383.

[45] ISO 10993-5, Biological evaluation of medical devices Part 5: Tests for in vitro cytotoxicity, 2009.

[46] Y. Matsuya, T.; Otsuka, Y.; Tagaya, M.; Motozuka, S.; Ohnuma, K.; Mutoh, Formation of stacked luminescent complex of 8-hydroxyquinoline molecules on hydroxyapatite coating by using cold isostatic pressing, Mater. Sci. Eng. C. 58 (2016) 127–132.

[47] S. Motozuka, M. Tagaya, An investigation into photofunctional interfaces of 8-hydroxyquinoline/hydroxyapatite hybrids, Opt. Mater. 66 (2017) 392–398.

[48] H. Luo, W. Li, D. Ji, G. Zuo, G. Xiong, Y. Zhu, L. Li, M. Han, C. Wu, Y. Wan, One-step exfoliation and surface modification of lamellar hydroxyapatite by intercalation of glucosamine, Mater. Chem. Phys. 173 (2016) 262–267.

[49] M. Ming, L. Wei-Peng, C. Xiao-Feng, M. Ke-Ya, G. Yan-Chuan, Luminescent and cytotoxic characteristics of an ellipsoidal and microsized europium (Eu)-doped hydroxyapatite, J. Inorg. Mater. 31 (2016) 890–896.

[50] Y. Han, X. Wang, H. Dai, S. Li, Synthesis and luminescence of Eu^{3+} doped hydroxyapatite nanocrystallines: Effects of calcinations and Eu^{3+} content, J. Lumin. 135 (2013) 281–287.

[51] D. Kouyate, J.-C. Ronfard-Haret, J. Kossanyi, Photo- and electro-luminescence of rare earth-doped semiconducting zinc oxide electrodes: Emission from both the dopant and the support, J. Lumin. 50 (1991) 205–210.

[52] K. Binnemans, Interpretation of europium(III) spectra, Coord. Chem. Rev. 295 (2015) 1–45.

[53] A.J. Freeman, R.E. Watson, Theoretical investigation of some magnetic and spectroscopic properties of rare-earth ions, Phys. Rev. 127 (1962) 2058–2075.

[54] K. Lin, P. Liu, L. Wei, Z. Zou, W. Zhang, Y. Qian, Y. Shen, J. Chang, Strontium substituted hydroxyapatite porous microspheres: Surfactant-free hydrothermal synthesis, enhanced biological response and sustained drug release, Chem. Eng. J. 222 (2013) 49–59.

[55] Q. Yuan, J. Wu, C. Qin, A. Xu, Z. Zhang, S. Lin, X. Ren, P. Zhang, Spin-coating synthesis and characterization of Zn-doped hydroxyapatite/polylactic acid composite coatings, Surf. Coatings Technol. 307 (2016) 461–469.

[56] A. Escudero, M.E. Calvo, S. Rivera-Fernández, J.M. de la Fuente, M. Ocaña, Microwave-assisted synthesis of biocompatible europium-doped calcium hydroxyapatite and fluoroapatite luminescent nanospindles functionalized with poly(acrylic acid), Langmuir. 29 (2013) 1985–1994.

[57] A. Al-Kattan, P. Dufour, J. Dexpert-Ghys, C. Drouet, Preparation and physicochemical characteristics of luminescent apatite-based colloids, J. Phys. Chem. C. 114 (2010) 2918–2924.

[58] Z. Yan-Zhong, H. Yan-Yan, Z. Jun, Z. Shai-Hong, L. Zhi-You, Z. Ke-Chao, Characteristics of functionalized nano-hydroxyapatite and internalization by human epithelial cell., Nanoscale Res. Lett. 6 (2011) 1–8.

[59] M. Long, F. Hong, W. Li, F. Li, H. Zhao, Y. Lv, H. Li, F. Hu, L. Sun, C. Yan, Z. Wei, Size-dependent microstructure and europium site preference influence fluorescent properties of Eu^{3+}-doped $Ca_{10}(PO_4)_6(OH)_2$ nanocrystal, J. Lumin. 128 (2008) 428–436.

[60] M.L.P. Divya, V. Sankar, V. Raghu, K.G. Reddy, A mitochondria-specific visible-light sensitized europium β-diketonate complex with red emission, Dalt. Trans. 42 (2013) 12317–12323.

[61] M.L.P. George, T.M. Krishna, M.S. Reddy, A lysosome targetable luminescent bioprobe based on a europium β-diketonate complex for cellular imaging applications, Dalt. Trans. 45 (2016) 18719–18729.

[62] B.N. Nelson, A.G. Caster, M.T. Berry, Gas-phase photoionization of tris(2,2,6,6-tetramethyl-3,5-heptanedionato) europium(III), Chem. Phys. Lett. 396 (2004) 256–260.

[63] Z.B. Yan. B, Two photoactive lanthanide (Eu^{3+}, Tb^{3+}) hybrid materials of modified β-diketone bridge directly covalently bonded mesoporous host (MCM-41), J. Photochem. Photobiol. A Chem. 195 (2008) 314–322.

[64] P. Li, Y. Wang, H. Li, G. Calzaferri, Luminescence enhancement after adding stoppers to europium(III) nanozeolite L, Angew. Chemie Int. Ed. 53 (2014) 2904–2909.

[65] A.R. Hilgenbrink, P.S. Low, Folate receptor-mediated drug targeting: From therapeutics to diagnostics, J. Pharm. Sci. 94 (2005) 2135–2146.

[66] A.M. Brzozowski, A.C.W. Pike, Z. Dauter, R.E. Hubbard, T. Bonn, O. Engström, L. Öhman, G.L. Greene, J.-Å. Gustafsson, M. Carlquist, Molecular basis of agonism and antagonism in the oestrogen receptor, Nature. 389 (1997) 753–758.

[67] K. Horwitz, W. McGuire, Estrogen control of progesterone receptor in human breast cancer. correlation with nuclear processing of estrogen receptor, J. Biol. Chem. 253 (1978) 2223–8.

[68] M. Scaltriti, F. Rojo, A. Ocana, J. Anido, M. Guzman, J. Cortes, S. Di Cosimo, X. Matias-Guiu, S. Ramon y Cajal, J. Arribas, J. Baselga, Expression of p95HER2, a truncated form of

the HER2 receptor, and response to anti-HER2 therapies in breast cancer, JNCI J. Natl. Cancer Inst. 99 (2007) 628–638.

[69] G.S. Hotamisligil, P. Peraldi, A. Budavari, R. Ellis, M.F. White, B.M. Spiegelman, IRS-1-mediated inhibition of insulin receptor tyrosine kinase activity in TNF-α-and obesity-induced insulin resistance, Science. 271 (1996) 665–668.

[70] H.A. Huebers, Y. Beguin, P. Pootrakul, D. Einspahr, C.A. Finch, K. Sasaki, M. Hirayama, T. Numata, T. Nishisato, I. Urushizaki, Intact transferrin receptors in human plasma and their relation to erythropoiesis., Blood. 75 (1990) 102–7.

[71] C. Chen, J. Ke, X. Edward Zhou, W. Yi, J.S. Brunzelle, J. Li, E.L. Yong, H.E. Xu, K. Melcher, Structural basis for molecular recognition of folic acid by folate receptors, Nature. 500 (2013) 486–489.

[72] M.A. Van Dongen, R. Rattan, J. Silpe, C. Dougherty, N.L. Michmerhuizen, M. Van Winkle, B. Huang, S.K. Choi, K. Sinniah, B.G. Orr, M.M. Banaszak Holl, Poly(amidoamine) dendrimer-methotrexate conjugates: The mechanism of interaction with folate binding protein, Mol. Pharm. 11 (2014) 4049–4058.

[73] M. Fernández, F. Javaid, V. Chudasama, Advances in targeting the folate receptor in the treatment/imaging of cancers, Chem. Sci. 9 (2018) 790–810.

[74] S. Chen, L. Rong, Q. Lei, P.X. Cao, S.Y. Qin, D.W. Zheng, H.Z. Jia, J.Y. Zhu, S.X. Cheng, R.X. Zhuo, X.Z. Zhang, A surface charge-switchable and folate modified system for co-delivery of proapoptosis peptide and p53 plasmid in cancer therapy, Biomaterials. 77 (2016) 149–163.

[75] Y. Yu, J. Wang, S.C. Kaul, R. Wadhwa, E. Miyako, Folic acid receptor-mediated targeting enhances the cytotoxicity, efficacy, and selectivity of withania somnifera leaf extract: In vitro and in vivo evidence, Front. Oncol. 9 (2019) 1–11.

[76] C.I. Olariu, H.H.P. Yiu, L. Bouffier, T. Nedjadi, E. Costello, S.R. Williams, C.M. Halloran, M.J. Rosseinsky, Multifunctional Fe_3O_4 nanoparticles for targeted bi-modal imaging of pancreatic cancer, J. Mater. Chem. 21 (2011) 12650–12659.

[77] V. Lebret, L. Raehm, J.-O. Durand, M. Smaïhi, M.H. V. Werts, M. Blanchard-Desce, D. Méthy-Gonnod, C. Dubernet, Folic acid-targeted mesoporous silica nanoparticles for two-photon fluorescence, J. Biomed. Nanotechnol. 6 (2010) 176–180.

[78] W. Sun, J. Fan, S. Wang, Y. Kang, J. Du, X. Peng, Biodegradable drug-loaded hydroxyapatite nanotherapeutic agent for targeted drug release in tumors, ACS Appl. Mater. Interfaces. 10 (2018) 7832–7840.

[79] K. Yamada, S. Yoshii, S. Kumagai, I. Fujiwara, K. Nishio, M. Okuda, N. Matsukawa, I. Yamashita, High-density and highly surface selective adsorption of protein–nanoparticle complexes by controlling electrostatic interaction, Jpn. J. Appl. Phys. 45 (2006) 4259–4264.

[80] C.M. Doskey, V. Buranasudja, B.A. Wagner, J.G. Wilkes, J. Du, J.J. Cullen, G.R. Buettner, Tumor cells have decreased ability to metabolize H_2O_2: Implications for pharmacological ascorbate in cancer therapy, Redox Biol. 10 (2016) 274–284.

[81] S. Chen, Y. Zhao, Y. Zhang, D. Zhang, Fucoidan induces cancer cell apoptosis by modulating the endoplasmic reticulum stress cascades, PLoS One. 9 (2014) 1–10.

[82] H. Liu, Y. Zhou, L. Tang, Caffeine induces sustained apoptosis of human gastric cancer cells by activating the caspase-9/caspase-3 signalling pathway, Mol. Med. Rep. 16 (2017) 2445–2454.

[83] S. Johnson, Do mitochondria regulate cellular iron homeostasis through citric acid and haem production? Implications for cancer and other diseases, Med. Hypotheses. 60 (2003) 106–111.

[84] H. Kozlowski, A. Janicka-Klos, J. Brasun, E. Gaggelli, D. Valensin, G. Valensin, Copper, iron, and zinc ions homeostasis and their role in neurodegenerative disorders (metal uptake, transport, distribution and regulation), Coord. Chem. Rev. 253 (2009) 2665–2685.

[85] J.G. Ren, P. Seth, H. Ye, K. Guo, J.I. Hanai, Z. Husain, V.P. Sukhatme, Citrate suppresses tumor growth in multiple models through inhibition of glycolysis, the tricarboxylic acid cycle and the IGF-1R pathway, Sci. Rep. 7 (2017) 1–13.

[86] H.C. Hann HW, Stahlhut MW, Effect of iron and desferoxamine on cell growth and in vitro ferritin synthesis in human hepatoma cell lines, Hepatology. 11 (1990) 566–569.

[87] J.L. Pierre, I. Gautier-Luneau, Iron and citric acid: A fuzzy chemistry of ubiquitous biological relevance, BioMetals. 13 (2000) 91–96.

[88] A. De Robertis, A. Gianguzza, S. Sammartano, Solubility of some calcium-carboxylic ligand complexes aqueous solution, Talanta. 42 (1995) 1651–1662.

[89] Y. Liu, W. Zhu, D. Ni, Z. Zhou, J.H. Gu, W. Zhang, H. Sun, F. Liu, Alpha lipoic acid antagonizes cytotoxicity of cobalt nanoparticles by inhibiting ferroptosis-like cell death, J. Nanobiotechnology. 18 (2020) 1–14.

[90] B. Janic, A.M. Rad, E.K. Jordan, A.S.M. Iskander, M.M. Ali, N.R.S. Varma, J.A. Frank, A.S. Arbab, Optimization and validation of FePro cell labeling method, PLoS One. 4 (2009) 1–8.

[91] R. Phengchat, H. Takata, K. Morii, N. Inada, H. Murakoshi, S. Uchiyama, K. Fukui, Calcium ions function as a booster of chromosome condensation, Sci. Rep. 6 (2016) 1–10.

[92] M.E. Mycielska, A. Patel, N. Rizaner, M.P. Mazurek, H. Keun, A. Patel, V. Ganapathy, M.B.A. Djamgoz, Citrate transport and metabolism in mammalian cells: Prostate epithelial cells and prostate cancer, BioEssays. 31 (2009) 10–20.

[93] T. Toyama, A. Oshima, T. Yasue, Hydrothermal synthesis of hydroxyapatite whisker from amorphous calcium phosphate and the effect of carboxylic acid, J. Ceram. Soc. Japan. 109 (2011) 232–237.

[94] A. V. Stavitskaya, A.A. Novikov, M.S. Kotelev, D.S. Kopitsyn, E. V. Rozhina, I.R. Ishmukhametov, R.F. Fakhrullin, E. V. Ivanov, Y.M. Lvov, V.A. Vinokurov, Fluorescence and cytotoxicity of cadmium sulfide quantum dots stabilized on clay nanotubes, Nanomaterials. 8 (2018) 391.

[95] K. Sano, M. Ohashi, K. Kanazaki, A. Makino, N. Ding, J. Deguchi, Y. Kanada, M. Ono, H. Saji, Indocyanine green-labeled polysarcosine for in vivo photoacoustic tumor imaging, Bioconjug. Chem. 28 (2017) 1024–1030.

[96] Y. Zhu, T. Ikoma, N. Hanagata, S. Kaskel, Rattle-type Fe_3O_4@SiO_2 hollow mesoporous spheres as carriers for drug delivery, Small. 6 (2010) 471–478.

Chapter 2

Synthesis of Luminescent Europium(III) Complex-interacted Hydroxyapatite Nanoparticles and Their Rapid Cell Labeling by Folic Acid Immobilization

Chapter 2

Synthesis of Luminescent Europium(III) Complex-interacted Hydroxyapatite Nanoparticles and Their Rapid Cell Labeling by Folic Acid Immobilization

2.1 Introduction

The specific cell labeling techniques using luminescent nanoparticles are important in the biomedical fields. The targeting through the specific ligand molecules is able to bind to the cell surface and achieve the receptor-mediated endocytosis [1]. The cell labeling technologies will be improved by the development of cytocompatible photoluminescence probes [2,3].

Lanthanide (Ln) ion-doped nanoparticles provide the several advantages such as lower cytotoxicity, photostability and sharp luminescence bands as compared with the conventional cell labeling materials such as organic dyes and quantum dots [4,5]. The Ln ions (Tb, Eu, Dy, etc.) can be doped in the host matrixes such as phosphates and glasses [6–8]. Thus, the Ln ions can easily endow the photoluminescence properties, and be used as the novel photoprobes for cell labeling applications [9]. The spectral shapes depend on the electronic environment structures, although the Ln ions alone have poor light absorption abilities due to the forbidden intraconfiguration *f-f* transition [10]. From the previous reports, the labeling of Eu(III) β-diketonate complex for the living cells was investigated [11–13], and the chemically-synthesized Eu (III) complex of dopamine and diethylenetriaminepentaacetic acid was applied to the cell labeling [14]. In addition, there have also been the report by dipicolinato-based Eu(III) complex [15]. However, there was the problems of the

color degradation during the cell observation, and it can be suggested that the design of the particulate (e.g., nanoparticle) formation with multifunction in addition of the suppression of color degradation is important. The luminescence properties are difficult to be not affected by the nanoparticle surfaces modification molecular states, and the main challenges for the nanoparticles are to improve the efficiency of the binding and labeling ability to the cells. For designing the novel cell labeling nanoparticles to rapidly, sensitively and safely visualize the cells, the improvement of targeting and photofunctional ability through the specific molecules, and dispersibility in biological solution is important.

In the important biomaterial material, hydroxyapatite (HA: $Ca_{10}(PO_4)_6(OH)_2$) has the excellent properties such as biocompatibility and biological activity [16–19]. The HA nanoparticles could be served as the useful host materials for doping Ln ions (e.g., Tb, Eu etc.) in the biomedical field [20–22]. However, the doping amount of the ions is limited because the luminescence quenching occurs by accompanying energy transfer between the neighboring ions [23]. On the other hand, HA exists as the main component of bone tissues *in vivo*, and the biological functions are dominantly attributed to the inorganic/organic interface states between HA and collagen; thus, the structural calcium(II) ion (Ca^{2+}) of HA forms the chemical bonds with the reactive oxygen atoms of biomolecules. In order to improve the photofunctions of Ln ions in HA, the construction of the interface states between HA and functional molecules based on the inorganic/organic interactions are important. Accordingly, the HA bonded with functional low-molecular compounds such as triethyl amine and 8-hydroxyquinoline have been reported as the luminescent nanomaterials [24–26]. Therefore, it is important to design the novel interface states between HA and organic luminescent Ln species to enhance the cell labeling functions based on the luminescence intensity as well as the internal quantum efficiency (η_{int}).

When the cell labeling is performed *in vivo*, the efficient interactions between the cells and nanoparticles without cytotoxicity is desired. The luminescent HA nanoparticles maintain their cytocompatibility in the biological solution [24]. The dispersibility in water is important for the biomedical applications such as drug delivery system [27]. Thus, it is important to develop the surface modification strategy for achieving the luminescence and cytocompatibility of the nanoparticles with the dispersibility in water. From these viewpoints, the surface modification of the HA nanoparticles has been reported. For example, the modification of folic acid (FA) via dehydration condensation of polyethyleneimine [28], and that of succinic anhydride via dehydration condensation of 3-aminopropyltriethoxysilane (APTES, $H_2N(CH_2)_3Si(OC_2H_5)_3$)[29] have been reported. In addition, the HA nanoparticles were ultrasonically dispersed in cyclohexane, and then n-propylamine and 3-(methacryloyloxy)propyltrimethoxysilane were added and stirred at 65 °C to obtain the silanized HA. Then, the modification of polymethyl methacrylate on the silanization HA has also been achieved

with the polymerization reaction [30]. Therefore, the surface functionalization of the luminescent HA nanoparticles can improve the physicochemical properties, and also control the elution of Ca and phosphate ions into biological solution.

The functionalization of folic acid (FA) receptor on the HA nanoparticles has received attention, as it is overexpressed in cancer cells, and can facilitate the uptake (i.e., endocytosis). The immobilization of FA molecules via dehydration condensation reaction of APTES on the HA nanoparticles at phosphate buffer (pH = 7.4) has been achieved [31]. The folate-derivatized colloidal gold particles have been found to enter human cervical cancer-derived (HeLa) cells, then and be transferred to multivesicular bodies and eventually move into the cytoplasm or lysosomal-like compartments [32]. Here, the FA molecular structure in solution was changed with the pH value [33]. When the solution is acidic (pH = 1), it becomes cationic type and the main luminescence band is centered at 485 nm (excitation light at 370 nm). When the solution is neutral (pH= 6), it becomes neutral type and the main luminescence band is centered at 445 nm (excitation light at 400 nm). When the solution is basic (pH= 13), it becomes anionic type and the main luminescence band is centered at 460 nm (excitation light at 400 nm). These luminescence are attributed to S_1–S_0 relaxation [34]. From so far, the studies on luminescent HA nanoparticles (i.e., synthesis of diagnosis) and surface immobilization molecules (i.e., targeting technique) for the cancer cell labeling have separately been designed and investigated. For designing the novel cell-labeling nanoparticles to rapidly, sensitively and safely visualize specific cells, the improvement of the targeting ability as well as the luminescence properties based on the interactions between luminescent substances and surface molecules is important. A graft copolymer having the polylysine main chain and side chain of amino group modified by polyethylene glycol and Cy5.5 was synthesized. The Cy5.5 molecules mutually associates within the graft copolymer to decrease the luminescence intensity [35]. The hybrids of the peptide-coated substrate of a kinase enzyme and pyrene was synthesized, indicating that pyrene was associated with the hydroxyphenyl group of the tyrosine residue side chain to induce the luminescence quenching [36]. In these reports, the luminescence based on the host–guest and guest–guest interactions were investigated with disregarding the targeting molecular behavior. In other words, there is no report on the investigation of photo-interactions and photofunctions at the interfaces between the targeting molecules and luminescent spices in host (i.e., HA). From the viewpoints, the designing of the nanoparticles with the cytocompatibility and photofunctional interfaces between the targeting molecules and luminescent spices in HA for the rapid cell targeting and labeling was proposed here.

In this study, the photofunctionalization strategy of the FA molecule immobilized on the luminescent HA nanoparticles investigated, and evaluated the physicochemical properties of the

nanoparticle surfaces. The cytocompatibility against the HeLa cells was also evaluated to verify whether the nanoparticle can be the candidate for the rapid cell labeling. Concretely, the synthesis and photofunctionalization of the nanoparticles between the HA and organic Eu(III) complex (EuTH: tris (2,2,6,6-tetramethyl-3,5-heptanedionato) europium(III)) (EHA) was investigated. It was considered that the EuTH can be stably present on the HA surface by working as a capping agent when synthesizing the nanoparticles. Then, folic acid derivative (FA-NHS: folate N-hydroxysuccinimidyl ester, $C_{23}H_{22}N_8O_8$) was immobilized on EHA. The cytotoxicity against the NIH3T3 fibroblasts and the cell labeling ability against the HeLa cancer cells were evaluated (**Scheme 2-1**). It proposed here that the novel photofunctions can be found by changing the molecular occupancy (i.e., modification density) of FA-NHS on EHA. Specifically, the photofunctional interfaces between the FA-NHS and EuTH were focused. The achievement of "(i) rapid targeting to the cancer cells" and "(ii) effective luminescent ability including η_{int} based on the photofunctional interfaces between the FA-NHS and EuTH " in one particle were aimed.

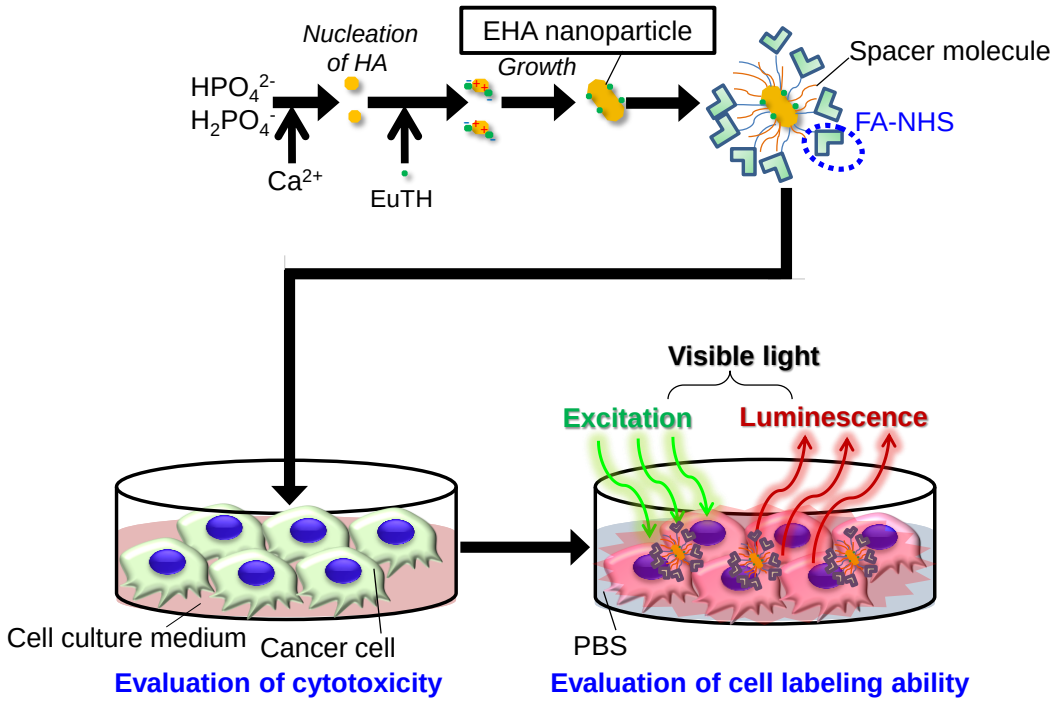

Scheme 2-1. Preparation of EHA nanoparticles and their cytotoxicity and cell labeling ability evaluation with the immobilization amount of FA-NHS on the surfaces.

2.2 Experimental Section

2.2.1 Chemicals

Dipotassium hydrogen phosphate (K_2HPO_4), tetramethylammonium hydroxide (TMAOH), calcium chloride dehydrate ($CaCl_2 \cdot 2H_2O$), EuTH (**Scheme 2-2(a)**), ethanol, dimethyl sulfoxide (DMSO), phosphate buffer (PB: pH = 7, phosphate ion concentration = 0.1 M) were purchased from Wako Chemical Co. Ltd. APTES and Methyltriethoxysilane (MTES, $CH_3Si(OC_2H_5)_3$) were purchased from Tokyo Chemical Industry Co., Ltd. FA-NHS (**Scheme 2-2(b)**) were purchased from Fujimoto Molechemical Co., Ltd. All the chemicals were used as received without further purification.

(a)

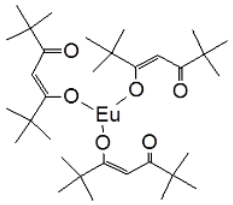

(b)

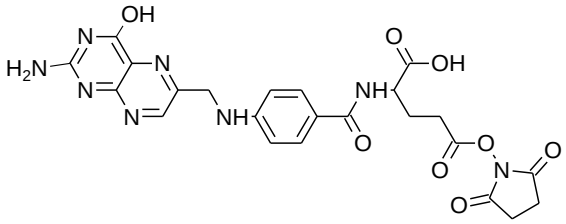

Scheme 2-2. Chemical structures of (a) EuTH and (b) FA-NHS molecule at the 2-dimensional views.

As the reagents for the characterization, phosphate buffered saline (PBS: pH = 7) with the ions (K^+: 4.15 mM, Na^+: 153 mM, HPO_4^{2-}: 9.57 mM, Cl^-: 139.57 mM), 2,4,6-trinitrobenzene sulfonate sodium dihydrate (TNBS-Na, $(O_2N)_3C_6H_2SO_3Na \cdot 2H_2O$), sodium dodecyl sulfate (SDS, $CH_3(CH_2)_{11}OSO_3Na$) and hydrochloric acid (HCl) were purchased from Wako Chemical Co., Ltd. Sodium carbonate and sodium bicarbonate of Wako Chemical Co., Ltd. were used for preparation of carbonic acid-bicarbonate buffer solution.

2.2.2 Materials and preparation

50 mL of ultrapure water containing 6 mmol of K_2HPO_4 was prepared and the pH was adjusted to be 12 by adding TMAOH. 30 mL of aqueous solution containing 9.9 mmol of $CaCl_2 \cdot 2H_2O$ was added to the K_2HPO_4 aqueous solution at the dropping rate of 1 mL/min to prepare HA solution. The HA solution was added into 20 mL of ethanol solution containing 0, 0.1, 0.25, 0.5 and 1.0 mmol of EuTH and refluxed at 80 °C for 3 h. The precipitation products were washed once with ethanol and ultrapure water, and lyophilized for 1 day. Here, the feed Eu concentration of Eu to (Ca+Eu) was 0, 1.0, 2.5, 5.0 and 10 mol%, which are denoted as ***X***EHA (***X***= the feed Eu concentration of Eu to (Ca+Eu) (mol%)). and fixed in this study, and the sample was abbreviated as EHA. The molar ratio of Ca to P was fixed at 1.65. As a reference, the neat EuTH powder was used.

5.0EHA (200 mg) was dispersed in 20 mL of ethanol and the pH was adjusted to be 12 by adding TMAOH. In the representative synthesis, APTES (0.064 mmol) and MTES (0.064 mmol) were added to the **5.0**EHA-dispersed solution and stirred at 40 °C for 1 h. The solid product was washed with ethanol and dried at 65 °C for 1 day to obtain the APTES-MTES modified **5.0**EHA (**0F**-A5.0EHA). As the comparison, the ratio of APTES to MTES (APTES : MTES) was varied. The ratio was set to be 0: 1 (MTES-5.0EHA), 1: 1 (**0F**-A5.0EHA), 1: 0 (APTES-5.0EHA). The theoretical occupancy with the modification on the **5.0**EHA based on the Brunauer-Emmett-Teller (BET) [37] surface area of the **5.0**EHA (196 m^2/g) was determined be 125 %, when all the feed molecules are immobilized on **5.0**EHA. The theoretical molecular occupancy of APTES or MTES was described in 2.2.3.2.

FA-NHS was immobilized on **0F**-A5.0EHA according to the previous report [31]. **0F**-A5.0EHA (150 mg) was mechanically dispersed into the mixture solution of 12 mL of DMSO and 25 mL of PB containing 0.0015, 0.003, 0.007, 0.015, 0.03, 0.045, 0.06 and 0.075 mmol of FA-NHS and the solution was stirred at 40 °C for 3 h (**Scheme 2-3**). The solid products were washed with ethanol and lyophilized. The theoretical occupancy of the immobilized FA-NHS on the **5.0**EHA based on the BET surface area was determined to be 5, 10, 25, 50, 100, 150, 200 and 250 %, respectively, when all the feed molecules are immobilized on **0F**-A5.0EHA. Here, the sample name is called as ***X*F**-A5.0EHA (***X***= the theoretical molecular occupancy of FA-NHS). The theoretical molecular occupancy of FA-NHS was described in 2.2.3.3.

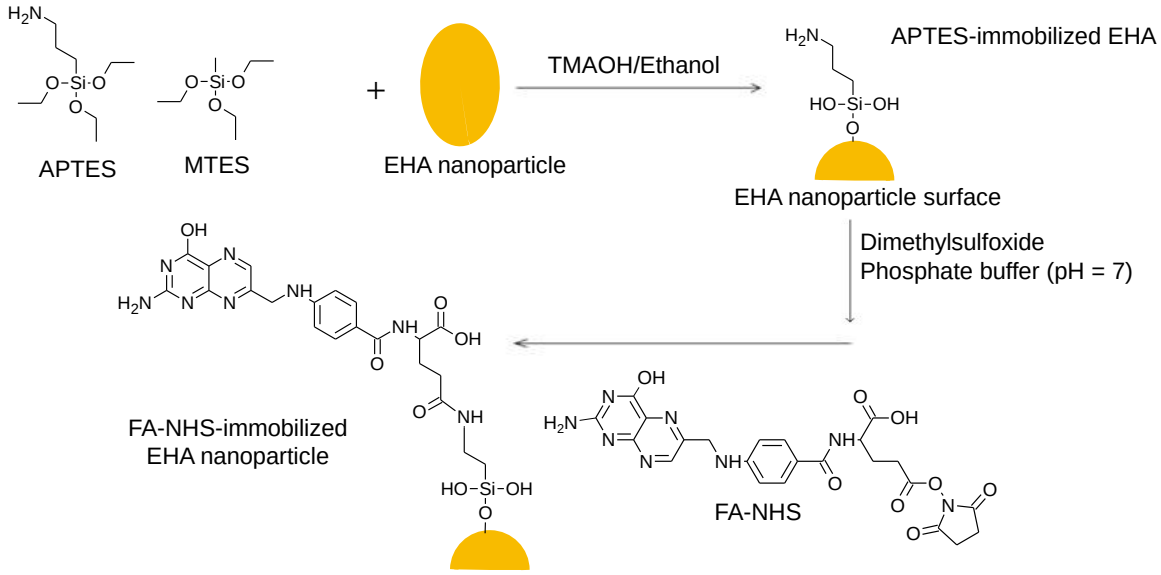

Scheme 2-3. Immobilization processes of FA-NHS on the EHA nanoparticle surfaces.

2.2.3 Characterization

2.2.3.1 Characterization of Eu(III) complex-interacted hydroxyapatite nanoparticles

The elemental compositions were characterized by X-ray fluorescence analysis (XRF; Rigaku Co., Ltd., ZSX Primus II). The XRF analysis was performed using a sample pellet, which was made by pressurizing the sample powder without any dilution. The fundamental parameter method was carried out using software (Rigaku Co., Ltd., EZ Scan Program) as a semi-quantitative analysis.

The prescribed amount of EuTH was dissolved in 10 mL of HCl aqueous solution (pH = 2) to prepare the calibration curve for the quantitative analysis. 10 mg of ***X***EHA was added to 10 mL of HCl aqueous solution (pH = 2) and completely dissolved. The HCl aqueous solution (pH = 2) was placed in the reference cell for the UV-Visible spectral measurement. The absorption spectra were measured to exhibit the maximum absorption wavelength at 278 nm and prepare the calibration curve as shown in **Figure 2-1(a)**. The correlation coefficient was 0.99804. The occupation molecular area of EuTH was assumed to be 0.65 × 0.65 × π nm^2 as the spherical shape **(Figure 2-1(b))**, and was calculated the concentration at which the theoretical occupancy of EuTH on ***X***EHA was 100 %. The theoretical occupancy of EuTH on ***X***EHA was calculated with dividing the occupation molecular area of EuTH by the BET surface area. The BET surface area was determined using a nitrogen (N_2)

adsorption and desorption instrument (BELSORP-mini, MicrotracBEL Co., Ltd.). 100 mg of each sample was subjected to pretreatment at 80 °C under vacuum for 1 h using the BELPREP-vac II, Microtrac Bell Co., Ltd. As a result, the BET surface areas of the **1.0**EHA, **2.5**EHA, **5.0**EHA and **10**EHA were 40, 70, 196 and 144 m^2/g, respectively. The resultant contained amounts of EuTH on ***X***EHA were measured. In the illustrative demonstration, the resultant molecular occupancy areas of EuTH on ***X***EHA and the intermolecular distance between EuTH molecules were calculated assuming monolayer-state adsorption from the above the theoretical occupancy of EuTH on ***X***EHA.

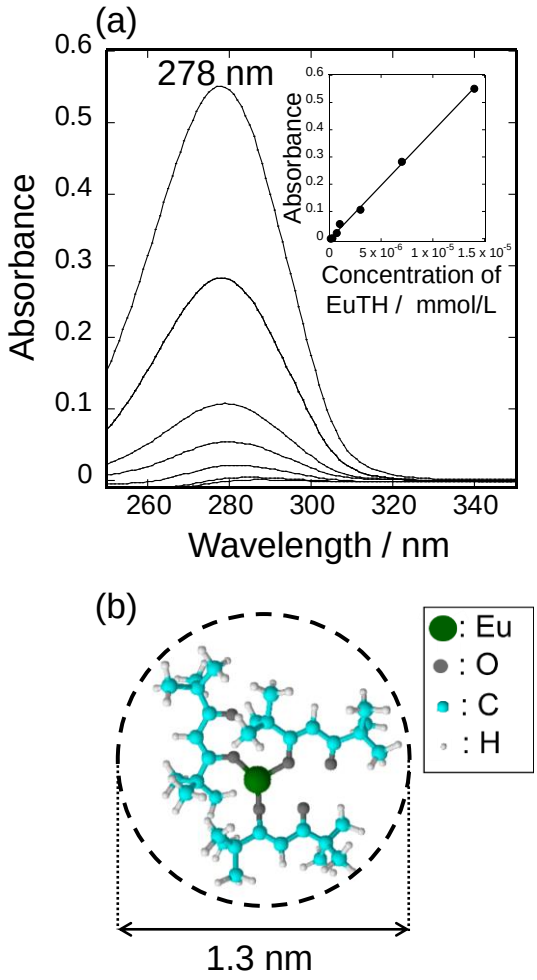

Figure 2-1. (a) UV-Vis absorption spectra of the EuTH solution at the pH of 2. (inset): the calibration curve between the EuTH concentration and absorbance (R^2= 0.99804). (b) Chemical structure of EuTH molecule at the 3-dimensional view.

X-ray diffraction (XRD) patterns were recorded with a powder X-ray diffractometer (Rigaku Co., Ltd., Smart Lab). The XRD patterns were measured with an X-ray source of CuKα line (λ = 0.15418 nm) and a voltage/current of 40 kV/30 mA. Using the Scherrer's equation (K=0.9), the crystallite sizes were estimated from the half width of the 002 and 300 diffractions and denoted as D_{002} and D_{300}. The D_{002}/D_{300} ratio was calculated.

Zeta potential measurements of the ***X***EHA nanoparticles dispersed in PBS at the particle concentration of 50 ng/mL were performed at room temperature using the nanoparticle multi-analyzer (qNano, Izon Science, Co., Ltd.). The relationship between the electrophoretic velocity (v_x) of the sample nanoparticle x and the zeta potential is expressed by the Smoluchowski approximation as shown in the following **Eq. (1)** [38].

$$\frac{(v_x)_{el\,S}}{(v_x)_{el\,C}} = \frac{\xi_{net\,S}}{\xi_{net\,C}} \tag{1}$$

where $(v_x)_{el\,S}$ and $(v_x)_{el\,C}$ are the electrophoretic mobility of the sample and CPC100 calibration nanoparticles, respectively. The $\xi_{net\,S}$ and $\xi_{net\,C}$ values are the net zeta potential of the sample and CPC100 calibration nanoparticles, respectively. The zeta potential value of the sample nanoparticles at an applied pressure ($\xi_{P\,S}$) can be expressed by summarizing the $\xi_{net\,S}$ and membrane zeta potential (ξ_m) by the following **Eq. (2)**.

$$\xi_{P\,S} = \xi_{net\,S} + \xi_m \tag{2}$$

The zeta potential (ξ_S^i) of each sample nanoparticle i is given by averaging the respective zeta potential values calculated at various positions (l_x) in a pore. The l_x is the position of the nanoparticle within the pore at t hour ($t = T_x$). The zeta potential of the sample nanoparticle is estimated by taking the average of l_x at several discrete points as shown in the following **Eq. (3)**.

$$\xi^i{}_S = \frac{\sum_x \xi^i_{x\,S}}{\sum_x} = \frac{\sum_x (v^i_{x\,S} - v^P_{x\,C}P)/(v^V_{x\,C}V)}{\sum_x}\xi_{net\,C} + \xi_m \tag{3}$$

where $v^i_{x\,S}$ is the sum of the time averaged electrokinetic and convection velocity components of the sample particulates at the position of l_x within the pore by the following **Eq. (4)**.

$$v^i_{x\,S} = \frac{l_x}{T^i_x} = \frac{\int_0^{T^i_x} v^i(t)dt}{T^i_x} \tag{4}$$

$v^P_{x\,C}$ is the convective velocity per unit pressure, $v^V_{x\,C}$ is the electro kinetic velocity per unit voltage, P is the applied pressure and V is the measurement voltage. P and V are parameters at the nanoparticle size measurement, and $v^P_{x\,C}$ and $v^V_{x\,C}$ are determined at nanoparticle size measurement. By measuring the CPC100 calibration nanoparticles in addition to the sample nanoparticles of this study, the zeta potential can be measured [39]. The $v^V_{x\,C}$ and $v^P_{x\,C}$ were calculated by averaging typically over more

than 500 CPC100 calibration nanoparticles.

The morphologies of the samples deposited on a carbon-coated Cu grid were observed by a transmission electron microscope (TEM; JEOL Co., Ltd., JEM-1400) at an accelerating voltage of 120 kV, and the short-axis sizes (*S*), long-axis sizes (*L*) and aspect ratio (*L*/*S*) distributions of the nanoparticles were estimated by counting 300 particles. The average particle size (*Ave.*) and coefficient of variation (*Cv.*) values were also calculated.

The dissolution rate of Ca^{2+} from the total Ca^{2+} content in the nanoparticles were investigated by the immersion in PBS for 48 h and 66 h under static condition. The Ca^{2+} concentration was measured using a D-73LAB equipped with an electrode (6583-10C, Horiba, Co., Ltd., Japan). The standard Ca^{2+} solution was prepared by mixing ultrapure water containing 1000 mg/L of $CaCl_2 \cdot 2H_2O$ and 0.1 M of KCl (support salt). 100, 10 and 1.0 mg/L of the Ca^{2+} solutions with KCl (0.1 M) were also used for drawing a calibration curve. The dissolved Ca^{2+} weight from the nanoparticles was measured at the particle concentration of 100 μg/mL in PBS. The value obtained with PBS was subtracted from that obtained with PBS containing the nanoparticle, and the dissolved Ca^{2+} weight was divided by the initial Ca^{2+} weight in the nanoparticles determined by the XRF result.

Infrared spectra were recorded on a Fourier transform infrared spectrometer (FT-IR; JASCO Co., Ltd., FT/IR-4600). The FT-IR spectra were measured using a KBr pellet and the weight ratio between the sample powder and KBr was set at 3: 7. All the spectra were recorded after subtracting the background spectrum of pristine KBr. In order to analyze the C–O and C=O bonding states in a HA structure [40,41], the peak positions of C–O and C=O stretching vibration were examined by the second derivative FT-IR spectra. Their baselines were drawn in the range between 1261 and 1239 cm^{-1} and 1585 and 1560 cm^{-1}. Their peak top positions of C–O and C=O stretching vibration were compared. The adsorption band in the region around 860 cm^{-1} corresponds to bending mode of the CO_3^{2-} ion group and stretching mode of the CO_3^{2-} ion group in addition to weak shoulder band at around 860 cm^{-1} resulted from symmetric stretching mode (ν_5) of P−O(H) of HPO_4^{2-} group ($\nu_s HPO_4^{2-}$). Due to the presence of CO_3^{2-} ion in these samples, bending mode of the CO_3^{2-} ion group and stretching mode of the CO_3^{2-} ion group may appear at 870 and 860 cm^{-1}, respectively [42]. The contained amount of CO_3^{2-} ion in the **0**EHA was estimated from the FT-IR spectra as the background of the spectrum shape of the KBr alone [43]. Based on the FT-IR spectra, the peak areas were calculated after a preliminary baseline correction of the complete 4000–400 cm^{-1} spectrum. As the vibrational domains were retained for the analysis, both the stretching vibration of $\nu_s(CO_3^{2-})$ for carbonate ions and ν_1 and ν_3 of the P−O bonds were simply used. In particular, the area of the $\nu_s(CO_3^{2-})$ band was performed at the wavenumbers between 1502–1475 cm^{-1}, and that of ν_1 and ν_3 by the P−O bond contributions was integrated at the wavenumbers between 1205–930 cm^{-1}. By the calculation

based on the previous report [43], the carbonation amount (mass %CO_3) of the nanoparticles was calculated by a validated FT-IR methodology using the **Eq. (5)** and **Eq. (6)**.

$$r_{c/p} = \frac{Area\ of\ the\ \nu_s(CO_3^{2-})\ band}{Area\ of\ the\ \nu_1 and\ \nu_3(P-O)\ bond\ contributions} \quad (5)$$

$$\text{Mass } \%CO_3 = 28.62 \times r_{c/p} + 0.0843 \quad (6)$$

In order to analyze the P–O bonding component, the P–O bonding states of ***X***EHA nanoparticles were investigated by the FT-IR spectral deconvolution technique at the wavenumber regions between 817–1210 cm^{-1}. The P–O stretching band was deconvoluted into six components at the absorption peak bands of 1135–1093, 1079–1028, 1025–1000, 958–950, 928–888 and 876–844 cm^{-1}, which are belonging to "[1a] triply degenerated asymmetric stretching mode (ν_{3a}) of the P−O bond ($\nu_{as}PO_4^{3-}$, $\nu_{as}HPO_4^{2-}$)", "[1b] triply degenerated asymmetric stretching mode (ν_{3b}) of the P−O bond ($\nu_{as}PO_4^{3-}$, $\nu_{as}HPO_4^{2-}$)", "[1c] triply degenerated asymmetric stretching mode (ν_{3c}) of the P−O bond ($\nu_{as}PO_4^{3-}$, $\nu_{as}HPO_4^{2-}$)", "[2] nondegenerated symmetric stretching mode (ν_1) of the P−O bond ($\nu_sPO_4^{3-}$)", "[3] characteristic peak of hydrogen phosphate group (nondistinguishable peak)", and "[4] symmetric stretching mode (ν_5) of the P−O(H) bond of the HPO_4^{2-} group", respectively (**Table 2-1**) [42,44]. All

Table 2-1. Assignments of phosphate groups of the EHA in the FT-IR spectra.

Area number	Assignments	Peak position (cm^{-1})
[1a]	Triply degenerated asymmetric stretching mode, ν_{3a}, of the P−O bond ($\nu_{as}PO_4^{3-}$, $\nu_{as}HPO_4^{2-}$)	1135–1093
[1b]	Triply degenerated asymmetric stretching mode, ν_{3b}, of the P−O bond ($\nu_{as}PO_4^{3-}$, $\nu_{as}HPO_4^{2-}$)	1079–1028
[1c]	Triply degenerated asymmetric stretching mode, ν_{3c}, of the P−O bond ($\nu_{as}PO_4^{3-}$, $\nu_{as}HPO_4^{2-}$)	1025–1000
[2]	Nondegenerated symmetric stretching mode, ν_1, of the P−O bond ($\nu_sPO_4^{3-}$)	958–950
[3]	Characteristic peak of hydrogen phosphate group (nondistinguishable peak)	928–888
[4]	Symmetric stretching mode, ν_5, of the P−O(H) bond of the HPO_4^{2-} group ($\nu_sHPO_4^{2-}$)	876–844

the deconvolutions were performed by fitting with the Gaussian functions using the SOLVER option in the software (Microsoft Excel 2016). In the SOLVER calculation, the generalized reduced gradient method was used until the satisfied states of all the constraints and optimization conditions. All the residual values by the deconvolutions were less than 3 %. From the separated spectra, the ratio of the mono-component area was calculated.

Photoluminescence properties were evaluated by luminescence spectroscopy and microscopy. The excitation and luminescence spectra were recorded on a FP-8500 spectrophotometer (PL; JASCO Co., Ltd.) with the monitored luminescence and excitation wavelengths at 615 nm and 464 nm, respectively, which were excited from a Xe lamp at room temperature (atmosphere: air, excitation /detection slit sizes: 2.5 nm/2.5 nm, measure time: 0.1 s, step width: 1.0 nm, sample weight: 20 mg, shape: pellet). All the spectra were recorded under the same resolution. Besides, the $^5D_0 \rightarrow {}^7F_1$ (between 583−603nm) and $^5D_0 \rightarrow {}^7F_2$ (between 603−636nm) transitions can be attributed to magnetic dipole and electric dipole transitions of ***X*F**-A5.0EHA, respectively [45]. The integrated luminescence intensities of the $^5D_0 \rightarrow {}^7F_1$ and $^5D_0 \rightarrow {}^7F_2$ were named as I_{590} and I_{615}, respectively. The intensity of the magnetic dipole transition exhibits very little variation with the crystal field strength acting on the Eu^{3+} ion. The electric-dipole transition is sensitive to the local structure surrounding the Eu^{3+} ion. Accordingly, the relative peak intensity ratio (i.e., I_{590}/I_{615}) indicates the spatial symmetry of the Eu^{3+} ion site [45].

The integrated luminescence intensities centered at the peak tops of $^5D_0 \rightarrow {}^7F_2$ transition (between 603–636nm at the samples) under the excitation wavelengths at 464 nm was calculated, and the integrated luminescence intensity (I) per 1 mol of the contained EuTH was calculated using the resultant EuTH molar concentration from XRF.

The fluorescent microscope images were obtained using a luminescence microscope (Olympus Co., Ltd., CKX41N-FL; excitation wavelength: 420−480 nm, dichroic mirror wavelength: >500 nm, emission wavelength: > 520 nm, sensitivity: ISO 400) with an emission source (Olympus Co., Ltd., U-RFLT50).

The internal quantum efficiency (η_{int}) was measured using an integrating sphere (ISF-834; internal diameter: φ 60 mm) shown in the **Scheme 2-4(a)**. The excitation and luminescence spectra were recorded by the above spectrophotometer at the same wavelengths. The scattering light by the excitation was measured by setting a standard barium sulfate white board instead of the sample inner the integrating sphere.

As shown in the **Scheme 2-4(b),** the incident, scattering, and luminescence light intensities, which were abbreviated as I_0, I_1, and I_2, respectively, were measured and calculated. The measured wavelength was in the range between 350–750 nm, and it was calculated by total fluorescence observed in the visible light region. The measured wavelengths for the I_0 and I_1 were in the range between 450–479 nm (excitation wavelength of 464 nm), and those for the I_2 at the excitation wavelengths of 464 nm was 479–750 nm, respectively. Then, η_{int} was calculated by **Eq. (7)**. For the EuTH, the η_{int} values were 0.37 at the excitation wavelengths of 464 nm, respectively.

$$\eta_{int} = \frac{I_2}{(I_0 - I_1)} \times 100 \quad (7)$$

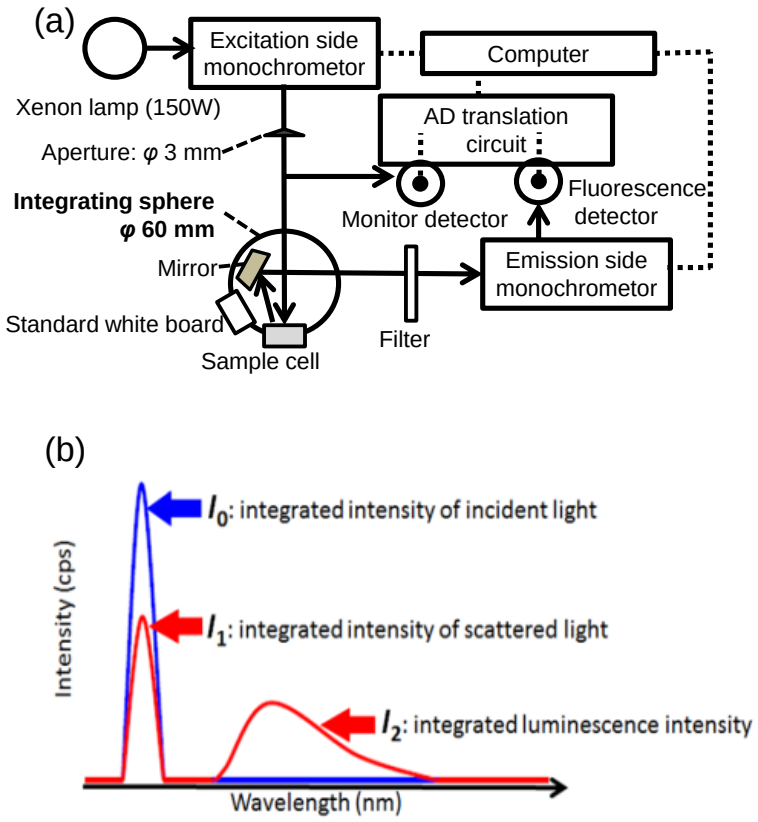

Scheme 2-4. (a) Schematic set-up diagram of optical system for measuring the quantum yield. (b) Scheme of the representative incident, scattering, and luminescence light intensity spectra for calculating the internal quantum efficiency. The integrated peak intensities attributed to the incident, scattering, and luminescence were abbreviated as I_0, I_1 and I_2, respectively.

2.2.3.2 Analysis of the amino-functionalized groups on Eu(III) complex-interacted hydroxyapatite nanoparticles

TNBS-Na is known as the binding reagent with an amino group. In weakly alkaline water, TNBS-Na specifically reacts with the amino groups in amino acids, peptides and proteins, giving a yellow trinitrophenyl (TNP) derivative (TNP derivative) [46]. The TNP derivatives are yellow and have the maximum absorption at 420 nm, and can be used for the detection of amino groups. The chemical scheme of the TNP derivative form between the amino group (primary amine) and the $NaSO_3^-$ site of TNBS-Na was shown in **Scheme 2-5(a)**. In this study, the amino group was

qualitatively analyzed by the maximum absorption wavelengths at 355 nm for TNBS-Na and at 420 nm for TNP derivatives.

For the preparation of the comparative reference samples of TNBS-Na, the predetermined amount of TNBS-Na aqueous solution (0.14 M) was added to 20 mL of carbonic acid-bicarbonate buffer (0.05 M) and stirred at a room temperature for 16 h. During the stirring, the aluminum foil was wrapped around the reaction vessel so as not to be affected by the external light. After the stirring, 1.25 mL of SDS solution (5 wt%) and 2.5 mL of HCl aqueous solution (1 N) were added to the solution. Here, the added amount of the TNBS-Na solution was 0.01, 0.02, 0.05, 0.1 and 0.2 mL, and the sample name was called as $\boldsymbol{Y_1}$TNBS-Na ($\boldsymbol{Y_1}$= the added amount of the TNBS-Na solution). Ultrapure water was measured (detection slit size: 2.5 nm, step width: 1.0 nm) in a reference cell for the UV-Visible spectrophotometer (UV-Vis, JASCO Co., Ltd. V-750).

For the preparation of the APTES-TNP derivative samples, 0.1 mL of TNBS-Na aqueous solution (0.14 M) was added to 20 mL of carbonic acid-bicarbonate buffer (0.05 M). Then, the predetermined amount of APTES was added and subsequent procedure was same as the mentioned above. Here, the addition amount of APTES was 0.001, 0.005, 0.01, 0.02 and 0.04 mL, and the sample name was called as $\boldsymbol{Y_2}$APTES-TNP ($\boldsymbol{Y_2}$= the added amount of APTES). The TNBS-Na aqueous solution without containing APTES was set to be in a reference cell for the UV-Visible spectrophotometer measurement under the same condition mentioned above.

0.1 mL of TNBS-Na aqueous solution (0.14 M) was added to 20 mL of carbonic acid-bicarbonate buffer (0.05 M), and 10 mg of the sample (**5.0**EHA, MTES-5.0EHA, **0F**-A5.0EHA and APTES-5.0EHA) was added and stirred and subsequent procedure was same as the mentioned above. The solid phase was washed with ethanol and ultrapure water and lyophilized for 1 day. The sample names are called as **5.0**EHA-TNP, MTES-5.0EHA-TNP, **0F**-A5.0EHA-TNP and APTES-5.0EHA-TNP, respectively. The evaluation was carried out by the UV-Visible diffuse reflection absorption spectrum with an integrating sphere (ISV-922, JASCO Co., Ltd.) using the UV-Visible spectrophotometer. A standard white board was placed inside the integrating sphere, and the baseline was measured. In the absorbance spectra, the peak areas attributed to TNBS-Na and TNP derivative was subtracted from the peak areas of the diffuse reflection absorption spectra of **5.0**EHA-TNP, MTES-5.0EHA-TNP, **0F**-A5.0EHA-TNP and APTES-5.0EHA-TNP to create difference spectra of the samples. In the difference spectra, in order to analyze the peak areas attributed to TNBS-Na and TNP derivative, the peak areas were investigated by the spectral deconvolution technique at the wavelength regions between 333–500 nm. The peak areas attributed to TNBS-Na and TNP derivative were deconvoluted into two components at the absorption peaks of 374–495 nm (S_1) and 333–379 nm (S_2), which belong to TNP derivative, and TNBS-Na molecule, respectively. All the

deconvolutions were performed by fitting with the Gaussian functions using the SOLVER option in the software (Excel). In the SOLVER calculation, the generalized reduced gradient method was used until satisfied all the constraints and optimization conditions. All the residual values by the deconvolutions were less than 4 %. From the separated spectra, the ratio of the mono-component area was calculated. The qualitative analysis of the amino group modified nanoparticle was carried out based on the peak area ratio (S_1/S_2) (detection slit size: 2.5 nm, step width: 1.0 nm, sample weight: 10 mg, shape: pellet).

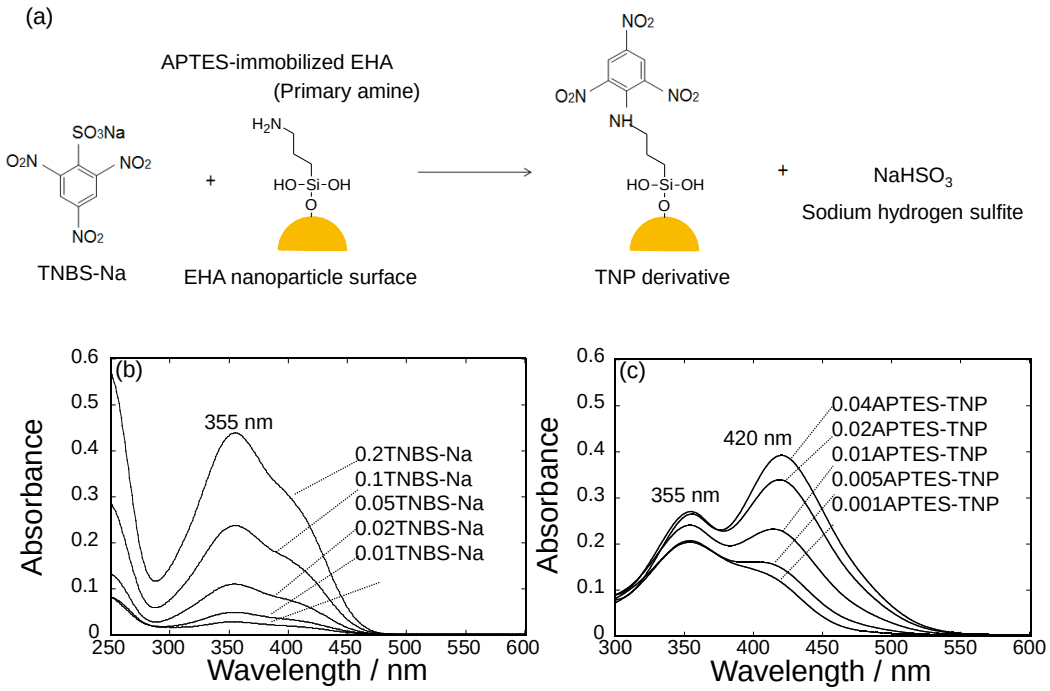

Scheme 2-5. (a) Reaction pathway of primary amine in NH_2–*R* (*R*=EHA nanoparticle) with TNBS-Na. UV-Vis absorption spectra of (b) TNBS solutions with the different concentrations and (c) the TNBS-stained APTES solutions with the different concentrations.

Scheme 2-5(b and **c)** shows the UV-Vis absorption spectra of the TNBS solution at different concentrations, the TNBS-stained APTES solutions at different concentrations, UV-Vis diffuse reflection absorption spectra of the TNBS-stained APTES-MTES-co-immobilized EHA nanoparticles, and the change in the area ratios. In the absorption spectra of the TNBS solution, the maximum absorption wavelength was observed at 355 nm due to the TNBS-Na molecule (**Scheme 2-5(b)**). In the case of the APTES-TNP solution, the new band was observed at 420 nm due to the TNP derivative (**Scheme 2-5(c)**). According to the previous report [46], the absorption band was also observed at 420 nm when the amino group is present. Thus, the qualitative analysis of the surface of

the APTES-MTES-co-immobilized EHA nanoparticles was performed (**Figure 2-2(a-1)**). As a result, the absorption bands were also observed at 355 and 420 nm. **Figure 2-2(a-2)** shows the difference spectra of the UV-Vis diffuse reflection absorption spectra of the before and after TNBS-stained APTES-MTES-co-immobilized EHA nanoparticles and their deconvolution results. When comparing the area ratio (S_1/S_2), the S_1/S_2 value increased with increasing the modified APTES amount, indicating the functionalization of the amino group on the EHA nanoparticles (**Figure 2-2(b)**).

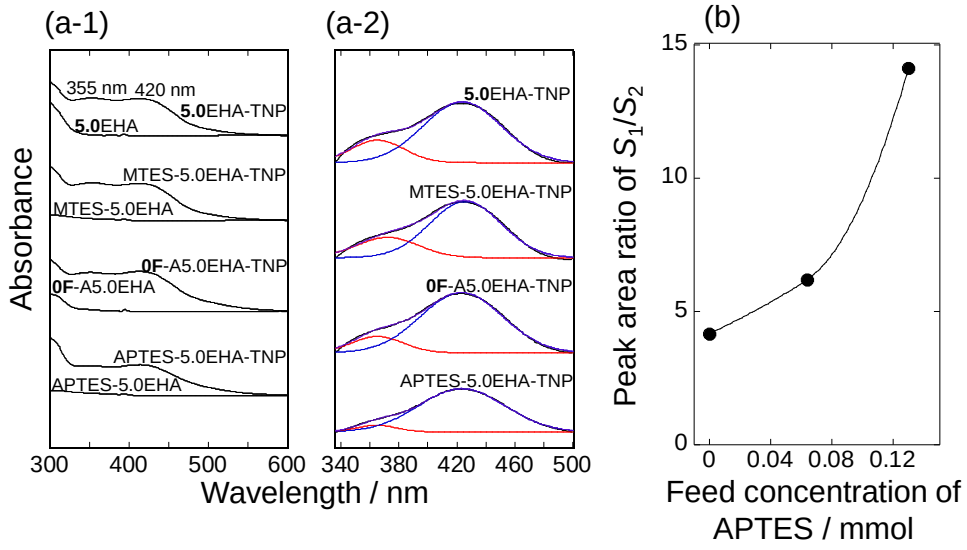

Figure 2-2. (a-1) UV-Vis diffuse reflection absorption spectra of the before and after TNBS-stained APTES-MTES-co-immobilized EHA nanoparticles, (a-2) difference spectra deconvolution result and (b) the change in the peak area ratio of S_1 (374–495 nm) to S_2 (333–379 nm).

Weight loss of **5.0**EHA, MTES-5.0EHA, **0F**-A5.0EHA and APTES-5.0EHA accompanying with the temperature change was observed by thermogravimetric differential thermal analysis (TG-DTA, Rigaku Co., Ltd. Thermo plus EVO2), and the amount of APTES and MTES on the EHA were evaluated. 10 mg of sample was introduced into a platinum sample pan and the temperature was changed from room temperature to 700 °C. (measurement atmosphere: air, heating rate: 10 °C/min, sampling time: 1 sec). **Figure 2-3(a)** exhibits the TG-DTA curves of the APTES-MTES-co-immobilized EHA nanoparticles. The weight loss with an endothermic peak was observed at around 60−80 °C in all the samples, suggesting to be due to the desorption of water on HA crystal surfaces [47]. In the EHA nanoparticle, the smaller weight loss with an exothermic peak was observed at 200−400 °C. The different loss degrees between the samples was dominantly attributed to the weight loss due to the oxidative decomposition of immobilized APTES and MTES. In the previous report [48], the weight loss of the APTES molecule was observed in the first step at around 80−160 °C for

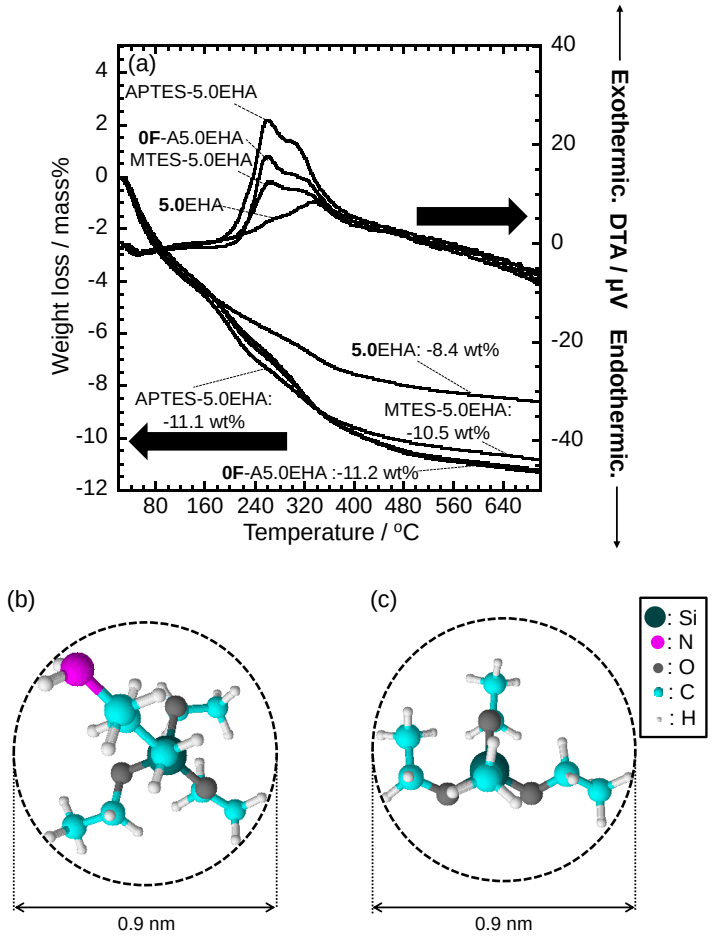

Figure 2-3. (a) TG-DTA curves of the APTES-MTES-co-immobilized **5.0**EHA nanoparticles. Chemical structures of (b) APTES and (c) MTES molecules at the 3-dimensional view.

the monomeric physical adsorption molecular state, in the second step at around 160−250 °C for the physical adsorption molecular state as polycondensation, in the third step at around 250−350 °C for the monomeric chemisorbed molecular state. The total weight loss rates with the temperature rise up to 700 °C was 8.4 wt% for **5.0**EHA, 10.5 wt% for MTES-5.0EHA, 11.2 wt% for **0F**-A5.0EHA and 11.1 wt% for APTES-5.0EHA. Only APTES or MTES exist in the APTES-5.0EHA or MTES-5.0EHA and the weight loss by the oxidative decomposition only APTES or MTES for APTES-5.0EHA and MTES-5.0EHA was calculated. As a result, the molecular occupancies of the immobilized APTES and MTES were estimated to be 111 and 108 %, respectively, clearly suggesting that the APTES and MTES molecules were completely covered over the **5.0**EHA nanoparticles. Therefore, the surface modification of APTES-MTES on the **5.0**EHA nanoparticles was successfully achieved for subsequently immobilizing FA-NHS. Here, the occupation molecular area of APTES or MTES ratio was assumed to be $0.45 \times 0.45 \times \pi$ nm^2 with spherical shape as shown in **Figure 2-3(b** and **c)**.

2.2.3.3 Analysis of the folate N-hydroxysuccinimidyl ester (FA-NHS)-immobilized nanoparticles

The prescribed amount of FA-NHS was dissolved in 10 mL of HCl aqueous solution (pH = 2) to prepare the calibration curve for the quantitative analysis. 10 mg of FA-NHS-immobilized **0F**-A5.0EHA were added to 10 mL of HCl aqueous solution (pH = 2) and were completely dissolved. The HCl aqueous solution (pH = 2) was placed in the reference cell for the UV-Visible spectral measurement, and the absorption spectra were measured to exhibit the maximum absorption wavelength of 321 nm and prepare the calibration curve as shown in **Figure 2-4(a)**. The correlation coefficient was 0.99974. The occupation molecular area of FA-NHS was assumed to be 1.1 × 1.5 nm^2 with rectangle shape shown in **Figure 2-4(b)**. The theoretical molecular occupancy of FA-NHS on **5.0**EHA was calculated by dividing the occupation molecular area of FA-NHS by the BET surface area. The resultant molecular occupancy areas of FA-NHS on **5.0**EHA and the intermolecular distance between FA-NHS molecules were calculated assuming monolayer-state adsorption from the above the theoretical occupancy of FA-NHS on **5.0**EHA.

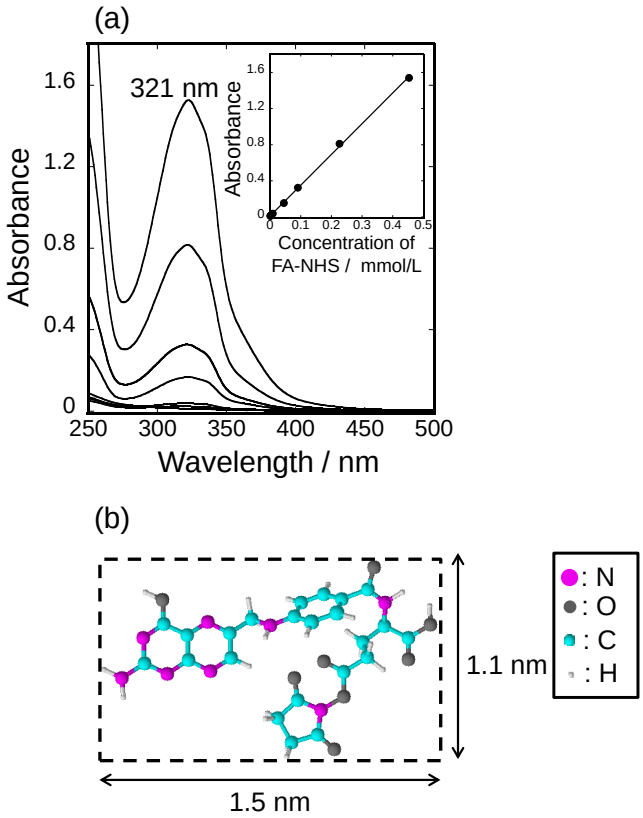

Figure 2-4. (a) UV-Vis absorption spectra of the FA-NHS solution at the pH of 2. (inset): the calibration curve between the FA-NHS concentration and absorbance (R^2= 0.99974). (b) Chemical structures of FA-NHS molecule at the 3-dimensional view.

The absorption spectra of the FA-NHS solutions (pH = 2, 6 and 7) with the concentration of 1.86 mM (1 mg/mL) were measured. In the reference cell, the HCl aqueous solution (pH = 2) for measuring the solution at pH = 2, ultrapure water for the solution at pH = 6, and PB for the solution at pH = 7 were used. For the comparison, the diffuse reflection absorption spectrum of FA-NHS powder (FA-NHS solid), **0F**-A5.0EHA and FA-NHS-immobilized nanoparticles were measured. The spectral measurement was carried out as same to the procedure mentioned in 2.2.3.2.

The luminescence decay curves were measured at room temperature with the FP-8500 fluorescence spectrometer. The samples were filled in a holder with sapphire window (diameter: φ 1 cm). The excitation was measured only at a wavelength of 464 nm from a Xe flash lamp (150 W), and the luminescence intensity decay was detected at the wavelength of 615 nm (i.e., $^5D_0 \rightarrow {}^7F_2$ transition). The intensity (I(t)) was fitted with a two-component exponential function as shown in **Eq. (8)** to calculate the luminescence lifetimes (τ_1, τ_2) in the decay process of each component.

$$I(t) = A_1\exp(-t / \tau_1) + A_2\exp(-t / \tau_2) \quad (8)$$

where the A_1 and A_2 are the constants expressing the mixture ratio of each component. The $I(t)$ is the luminescence intensity at the time of t (t = 0). The short-lived and long-lived components derived from EuTH alone and surface states are thought to be τ_1 and τ_2, respectively. For the EuTH, the one-component exponential function was applied and τ_1 was 0.450 ms.

The fluorescence microscopy (FM) images were obtained using the luminescence microscope (Olympus Co., Ltd., CKX41N-FL) mentioned in 2.2.3.1.

2.2.3.4 Characterization of the nanoparticles dispersed in phosphate buffer saline

In the evaluation of the nanoparticles, the size distribution was measured with the nanoparticle multi-analyzer (Izon Science, Co., Ltd., qNano), which is based on the electric resistance nanopulse method [49]. **5.0**EHA, **0F**-A5.0EHA, **5F**-A5.0EHA, **10F**-A5.0EHA and **100F**-A5.0EHA were ultrasonically dispersed in PBS at the particle concentration of 50 ng/mL for the particle size evaluation. Then, the dispersion solution was used at least contable 100 particles for the measurement. The average particle size (*Ave.*) and the coefficient of variation (*Cv.*) were calculated. Here, the current values were set to be 80 to 130 nA with the applied voltage of 0.6 V. As the calibration sample, the carboxylated polystyrene standard particles (Izon Science, Co., Ltd., CPC100) having the average diameter of 100 nm were placed in PBS at the concentration of 2×10^9 particles/mL. The *Ave.* value of the CPC100 particles at the manufacturing by the transmission electron microscope (TEM) observation was 114 nm with the *Cv.* of 21 %, and that by the qNano measurement was 126 nm with

the *Cv.* value of 13 %, suggesting that the particle sizes were almost same. According to the previous report on the histogram shapes of the particle size distributions with the various measurement methods [50], the shape by the qNano exhibited the good agreement with that by the TEM as compared with the case by a dynamic light scattering method [50]. The outline was shown in **Scheme 2-6**. V_0 indicates the power supply. Voltage (V) was applied to the conical pores. The resistance change (ΔR) can be expressed as **Eq. (9)** for the pores with a symmetrical length (L) in the z axis of the cylindrical polar coordinate system whose origin is located at one end of the pore.

$$\Delta R = \rho \int_0^L \frac{1}{A(z)} dz - R \tag{9}$$

where the electrolyte resistivity (ρ) was assumed to be homogeneous throughout the pores. $A(z)$ is the cross-sectional area of the pore and R is the pore resistance in the absence of clogging in the pores by the particles. This calculation can be contrasted with the two models developed for cylindrical pores [51,52]. Maxwell [51] and Lord Raleigh [52] developed a model of spherical particles and let ΔR be a linear function of particle volume. The measured resistance change (ΔR), the distance (l) from the pore opening to the particle, dimensions of pores (A, B and L) and the particle size (d) are related to ΔR and **Eq. (10)**.

$$\Delta R = \frac{4\rho d^3}{\pi D^4} \tag{10}$$

where D is the distance between the pores and is obtained from the following **Eq. (11)**.

$$D = A + l\left(\frac{B - A}{L}\right) \tag{11}$$

ΔR was measured via the change in the ion current time (t) according to **Eq. (12)**.

$$\Delta R = \left(\frac{V}{i_t} - \frac{V}{i_{bg}}\right) \tag{12}$$

The i_t is the current value at the time (t), and i_{bg} is the background current value in the absence of clogging in the hole by the particle. The particle size d can be obtained as in **Eq. (13)**, from the **Eq. (9)**, **(10)**, **(11)** and **(12)** [38,53].

$$d = \sqrt[3]{\frac{D^2 L \Delta R}{R}} \tag{13}$$

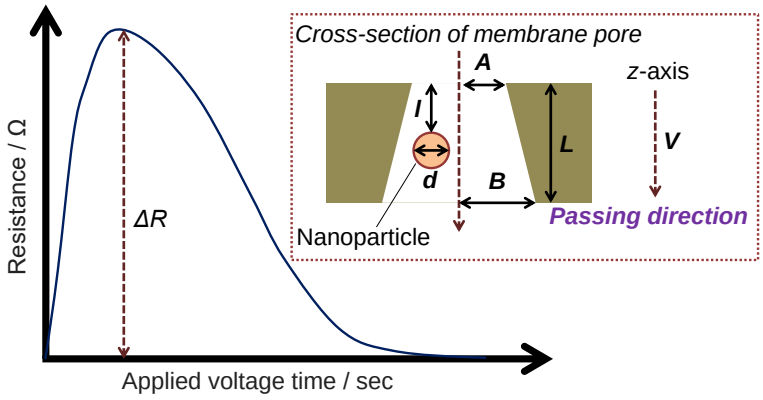

Scheme 2-6. Illustration of the resistive pulse curve to indicate the maximum resistance change (Δ*R*) from the baseline level with the applied voltage time. Inset: illustration of the cross-section of membrane pore structure with the passing of particle along with the axis of a conical pore.

0F-A5.0EHA, **5F**-A5.0EHA, **10F**-A5.0EHA and **100F**-A5.0EHA were ultrasonically dispersed in PBS at the particle concentration of 1.0 mg/mL for the evaluation of digital camera images with the UVA light irradiation to the nanoparticles. The excitation was measured at wavelength between 320–400 nm from a UVA lamp.

2.2.3.5 Cytotoxic evaluation of the nanoparticles against NIH3T3 fibroblasts

NIH3T3 fibroblast as the cell line was cultured in a plastic cell culture flask with the area of 75 cm^2 containing the 10 % FBS/DMEM (the solution containing the FBS in DMEM at 10 vol%).The cells were incubated at 37 °C in a humidified atmosphere of CO_2 (5 vol%). After the culture for 7 days, the cells were washed with 15 mL of PBS and treated with 1 mL of 0.05 w/v% trypsin-EDTA for 10 min, and the cells were dispersed in 15 mL of PBS and then re-dispersed in 15 mL of 10 % FBS/DMEM. The centrifugation and dispersion were carried out twice. The cell suspension in 10 % FBS/DMEM was seeded on the TCPS at the area density of 8000 cells/cm^2.

The sterilization treatment of the nanoparticles (**5.0**EHA, **0F**-A5.0EHA, **5F**-A5.0EHA, **10F**-A5.0EHA, **100F**-A5.0EHA and EuTH) were carried out with ethanol. In particular, 10 mg of the nanoparticles were treated by 10 mL of water/ethanol (50 vol%/50 vol%) and 10 mL of water/ethanol (30 vol%/70 vol%), and each treatment was performed for 1 h. Then, the nanoparticles were dispersed in 10 mL of 10 % FBS/DMEM, and centrifugation (4000 rpm, 2 min) was performed to be finally dispersed in 5 mL of 10 % FBS/DMEM.

At the cell culture time of 6 h, the nanoparticle dispersion solution was added to the cell surfaces at the final nanoparticle concentrations of 100 μg/mL and was incubated for the additional culture time of 66 h (i.e., total cell culture time: 72 h). At the culture times of 9, 12, 24, 48 and 72 h, the adhered cell densities of the living cells in PBS were evaluated. As a reference sample, the cells without addition of nanoparticles (sample name: **PS**) was evaluated. For the evaluation of the cell density, the adhered cells were washed twice with 1 mL of PBS in order to remove the non-bonded nanoparticles and non-adhered cells. After the washing, the cells were observed by an optical microscope to obtain the adhered cell density (cells/cm^2). The optical transmittance microscope images were obtained using the microscope (Olympus Co., Ltd., CKX41N-FL).

2.2.3.6 Evaluation of cytotoxicity and cell labeling ability against HeLa cancer cells by the nanoparticles

The evaluation of the cytotoxicity with the Eu(III) complex alone has been conducted, and the lethal concentration 50 (LC_{50}) value of the Eu(III) complexes containing the azaxanthane ligand was 175 μM, indicating the low cytotoxicity [54]. Here, the LC_{50} value was defined as the concentration to kill 50 % of a cell population after the incubation for 24 h. The lethal dose 50 (LD_{50}) value of the europium (III) oxide (CAS.No. 1308-96-9, Fuji Film Wako Pure Chemical Industries, Ltd.) was 5.0 mg/kg through an oral administration into rat. The europium (III) standard solution (Kishida Chemical Co., Ltd.) containing 96 wt% of water (CAS.No. 7732-18-5), 3.6 wt% of hydrogen chloride (CAS.No. 7647-01-0) and 0.24 wt% of europium (III) chloride hexahydrate (CAS.No. 13759-92-7) was 238 mg/kg through an oral administration into rat. Thus, the Eu(III) complexes can be seen as the non-cytotoxic substances, although the safety for the cellular labeling applications has being experimentally evaluated *in vitro* and *vivo* [11–15].

For evaluating the cellular ability under the more higher particle concentrations, Human (HeLa) cervical carcinoma cells (RCB0007) as the cell line, which were provided by the Riken BioResource center, was cultured in a plastic cell culture flask with the area of 75 cm^2 (BD Bioscience, USA.) containing the 10 % FBS/DMEM. The cells were incubated at 37 °C in a humidified atmosphere of CO_2 (5 vol%). After the culture for 7 days, the cells were washed with 15 mL of PBS and treated with 1 mL of 0.053M-ethylenediaminetetraacetate (0.053 M) containing trypsin (0.05 w/v%) (Trypsin-EDTA) for 10 min, and the cells were dispersed in 15 mL of PBS and then re-dispersed in 15 mL of 10 % FBS/DMEM. The centrifugation and dispersion were carried out twice. The cell suspension in 10 % FBS/DMEM was seeded on a commercially-available cell culture poly(styrene) dish (PS: BD Falcon™ Co., Ltd.) at the area density of 8000 cells/cm^2.

5F-A5.0EHA dispersion solution was prepared. The sterilization treatment of **5F**-A5.0EHA was carried out with ethanol. 10 mg of **5F**-A5.0EHA was treated by 10 mL of water/ethanol (50 vol%/50 vol%) and 10 mL of water/ethanol (30 vol%/70 vol%), and each treatment was performed for 1 h. Then, **5F**-A5.0EHA was dispersed in 10 mL of 10 % FBS/DMEM, and centrifugation (4000 rpm, 2 min) was performed to be finally dispersed in 5 mL of 10 % FBS/DMEM.

At the cell culture time of 6 h, the **5.0**EHA, **0F**-A5.0EHA, **5F**-A5.0EHA, **10F**- A5.0EHA, **100F**-A5.0EHA and EuTH dispersion solution was added to the cell surfaces and was incubated at the final nanoparticle concentrations of 100 μg/mL for the additional culture time for 66 h. At the additional culture times of 9, 12, 18, 42 and 66 h, the adhered cell densities, the luminescence intensities of the lyophilized cells, and the optical transmittance and FM images of the living cells in 1 mL of PBS were evaluated.

At the cell culture time of 6 h, the **5F**-A5.0EHA dispersion solution was added to the cell surfaces and was incubated at the final nanoparticle concentrations of 10, 50 and 100 μg/mL for the additional culture time for 66 h. At the additional culture times of 9, 12, 18, 42 and 66 h, the adhered cell densities, the luminescence intensities of the lyophilized cells, and the optical transmittance and FM images of the living cells in 1 mL of PBS were evaluated.

For the evaluation of the density, the adhered cells were washed twice with 1 mL of PBS in order to remove the surplus (i.e., non-bonded) particles and non-adhered cells. Thereafter, 0.1 mL of Trypsin-EDTA was placed in the PS and stand for 12 min at 37 ^{o}C to detach the cells from the PS surfaces. The cell suspension was subjected to the centrifugation (2000 rpm, 2 min), and 10 % FBS/DMEM was added to the cells. The cell suspension was placed in the disposable hemocytometer (C-Chip, model number: DHC-N01, Air Brown Co., Ltd.), and the number of cells was counted with the optical microscope. The optical transmittance microscope images were obtained using the microscope (Olympus Co., Ltd., CKX41N-FL). The average density of the cells (cells/cm^2) was calculated.

For the evaluation of the luminescence intensities, the adhered cells were washed twice with 1 mL of PBS. After the lyophilization of the adhered cells, the integrated areas in the wavelength range between 350–750 nm were measured on the FP-8500 spectrophotometer, which were excited by the wavelength of 464 nm for the monitored wavelengths between 600–635 nm.

The cells at the culture time of 60 h were densely packed each other and have the aggregation size more than 50 μm, which can be regarded as the tumorized cell spheres according to the previous report [55]. The labeling ability against these spheres was evaluated by the optical microscope and FM observation and luminescence intensity. At the cell culture time of 60 h, **5F**-A5.0EHA was added to the tumorized cell sphere surfaces. At the lapse of 1, 3, 6, 12 and 24 h from the addition, the

luminescence intensity of the lyophilized cells and were evaluated and the optical microscope and FM images of the living cells in 1 mL of PBS were observed based on the same procedure mentioned above.

2.3 Results and Discussion

2.3.1 Characterization of the Eu(III) complex-interacted nanoparticles

The resultant chemical composition, (Ca+K)/P molar ratio and the molar concentrations of Eu to (Eu+Ca) of EuTH of the EHA nanoparticles at different EuTH concentrations are summarized in **Table 2-2**. And the contained amount of EuTH, EuTH molecular area occupancy and intermolecular distance of EuTH of the EHA nanoparticles at different EuTH concentrations are shown in **Table 2-3**. The (Ca+K)/(P+C) molar ratio of **0**EHA was 1.62, indicating that Ca-deficient HA was synthesized. In **1.0**EHA, **2.5**EHA, **5.0**EHA and **10**EHA, the (Ca+K)/P molar ratio was 1.78–1.85, suggesting that carbonated HA were synthesized. The resultant concentrations of Eu to (Eu+Ca) in the nanoparticles were 1.05–9.82 mol%. As shown in **Figure 2-1(a)**, the UV-Vis absorption spectra of the EuTH solution exhibited the maximum absorption wavelength at 278 nm. The contained amount, the molecular occupancy of EuTH and the intermolecular distance between EuTH molecules varied with the feed concentration. Specifically, the actual molecular occupancy and the intermolecular distance between EuTH molecules were 1.02 % and 11.1 nm for **1.0**EHA, 1.77 % and 8.40 nm for **2.5**EHA, 2.97 % and 6.40 nm for **5.0**EHA, and 6.26 % and 4.74 nm for **10**EHA. Therefore, it was suggested that the EuTH amount contained on the nanoparticles can be controlled by the feed concentration.

Table 2-2. Resultant chemical composition, (Ca+K)/P molar ratio and the molar concentrations of Eu to (Eu+Ca) of the EHA nanoparticles with the different EuTH concentrations. The (Ca+K)/(P+C) molar ratio of **0**EHA was 1.62, indicating that Ca-deficient HA was synthesized. 0.9 mol% of CO_3^{2-} ion was contained in **0**EHA by FT-IR.

	Ca (mol%)	**K (mol%)**	**P (mol%)**	**(Ca+K)/P molar ratio**	**Concentration of Eu to (Eu+Ca) (mol%)**
1.0EHA	20.1	0.0621	11.1	1.82	1.05
2.5EHA	19.2	0.0665	10.8	1.78	2.80
5.0EHA	18.6	0.0547	10.5	1.78	5.62
10EHA	19.9	0.0757	10.8	1.85	9.82

Table 2-3. The contained amount of EuTH, EuTH molecular area occupancy and intermolecular distance of EuTH of the EHA nanoparticles with the different EuTH concentrations.

	Contained amount of EuTH (μmol/g of HA)	**EuTH molecular area occupancy (%)**	**Intermolecular distance between EuTH molecules (nm)**
1.0EHA	0.508	1.02	11.1
2.5EHA	1.55	1.77	8.40
5.0EHA	7.29	2.97	6.40
10EHA	11.3	6.26	4.74

Figure 2-5 shows the XRD patterns of the EuTH and EHA nanoparticles with the different EuTH concentrations. The patterns of the EHA nanoparticles are attributed to a single phase of HA (ICDD No. 00-009-0432) while no patterns ascribed to EuTH were observed in the nanoparticles.

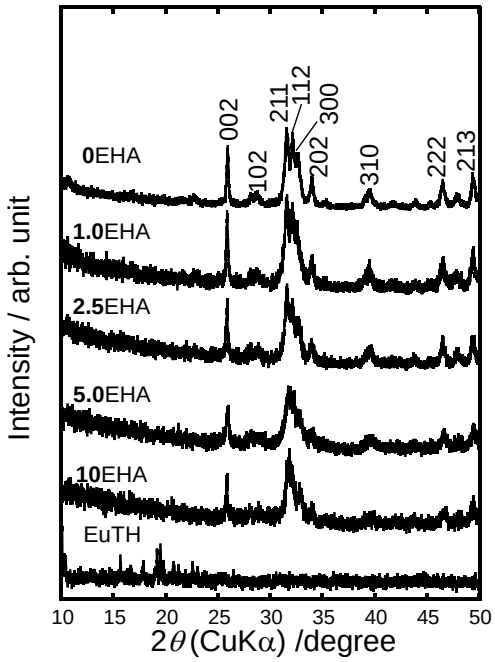

Figure 2-5. XRD patterns of the EHA nanoparticles with the different EuTH concentrations and EuTH alone.

Table 2-4 shows the crystalline sizes and ratio, and the zeta potential values of the EHA nanoparticles with the different EuTH concentrations. The crystallite size of D_{300} was similar irrespective of the EuTH concentration. In contrast, the **5.0**EHA had relatively smaller D_{002} than all the other samples, indicating the different crystal growth along with the *c*-axis direction. It was assumed that polycrystallization would occur in the particle through the altered interaction between the HA and

EuTH on the nanoparticle surfaces. The zeta potential values of the nanoparticles were –13 ~ –18 mV, which were lower than that of **0**EHA (approx. –2 mV). In the nanoparticles, many of the EuTH molecules exist on the HA via the interaction with the ligand and Ca ions at the crystal growth stage, indicating that the coverage of EuTH over the *a*–plane of HA resulted in the negatively-charged states. Furthermore, the zeta potential values of **5.0**EHA and **10**EHA were similar and were higher than those of **1.0**EHA and **2.5**EHA. Accordingly, the higher zeta potential values of **5.0**EHA and **10**EHA would be attributed to the EuTH molecules segregated on HA. Therefore, it was suggested that the present samples formed the different nanoparticle states depending on the EuTH concentration.

Table 2-4. The crystalline sizes and ratios, and the zeta potential values of the EHA nanoparticles with the different EuTH concentrations.

	Crystalline sizes and ratios			***Zeta potential (mV)***
	D_{002} **(nm)**	D_{300} **(nm)**	D_{002} / D_{300}	
0EHA	41±5	19±4	2.2	–2.3±1.7
1.0EHA	45±4	20±5	2.3	–13.1±1.4
2.5EHA	46±4	18±3	2.6	–13.7±1.8
5.0EHA	45±8	20±5	2.3	–17.7±1.4
10EHA	54±5	21±5	2.6	–16.7±0.71

Figure 2-6 shows TEM images of the nanoparticles (averaged *S* and *L* sizes, averaged *L/S* ratios and corresponding *Cv*. values are inserted). The nanoparticles exhibited a rod-like shape. **0**EHA, **1.0**EHA, **2.5**EHA and **5.0**EHA had a similar size which is also equivalent to the previously-synthesized HA nanoparticles with the size of 10–50 nm [56]. In particular, the particle size of **10**EHA was much longer than the other samples. Although the averaged *L* value of **10**EHA (92 nm) was clearly different from those of **0**EHA, **1.0**EHA, **2.5**EHA and **5.0**EHA (49−50 nm) (**Figure 2-6 (g−k)**), there was no difference between the average particle sizes of *S* with the EuTH concentration (**Figure 2-6 (g'−k')**). It was assumed that the segregated EuTH molecules selectively interacted with *a*-plane in the **10**EHA nanoparticle, so that the uncovered *c*-plane preferentially grew. The averaged *S* and *L* values of **0**EHA, **1.0**EHA, **2.5**EHA and **5.0**EHA were in agreement with the D_{300} and D_{002} values in **Table 2-4**, indicating the single crystalline states (**Figure 2-6 (f)**), and the averaged *L* values of **10**EHA were larger than the D_{002} values, indicating the polycrystalline states in the direction of the *c*-axis for **10**EHA (**Figure 2-6 (f)**). The *L*/*S* values of **0**EHA, **1.0**EHA, **2.5**EHA and **5.0**EHA were 2.5–2.9 and that of **10**EHA was 4.8 shown in **Figure 2-6 (l−p)**, which was higher than the reported values

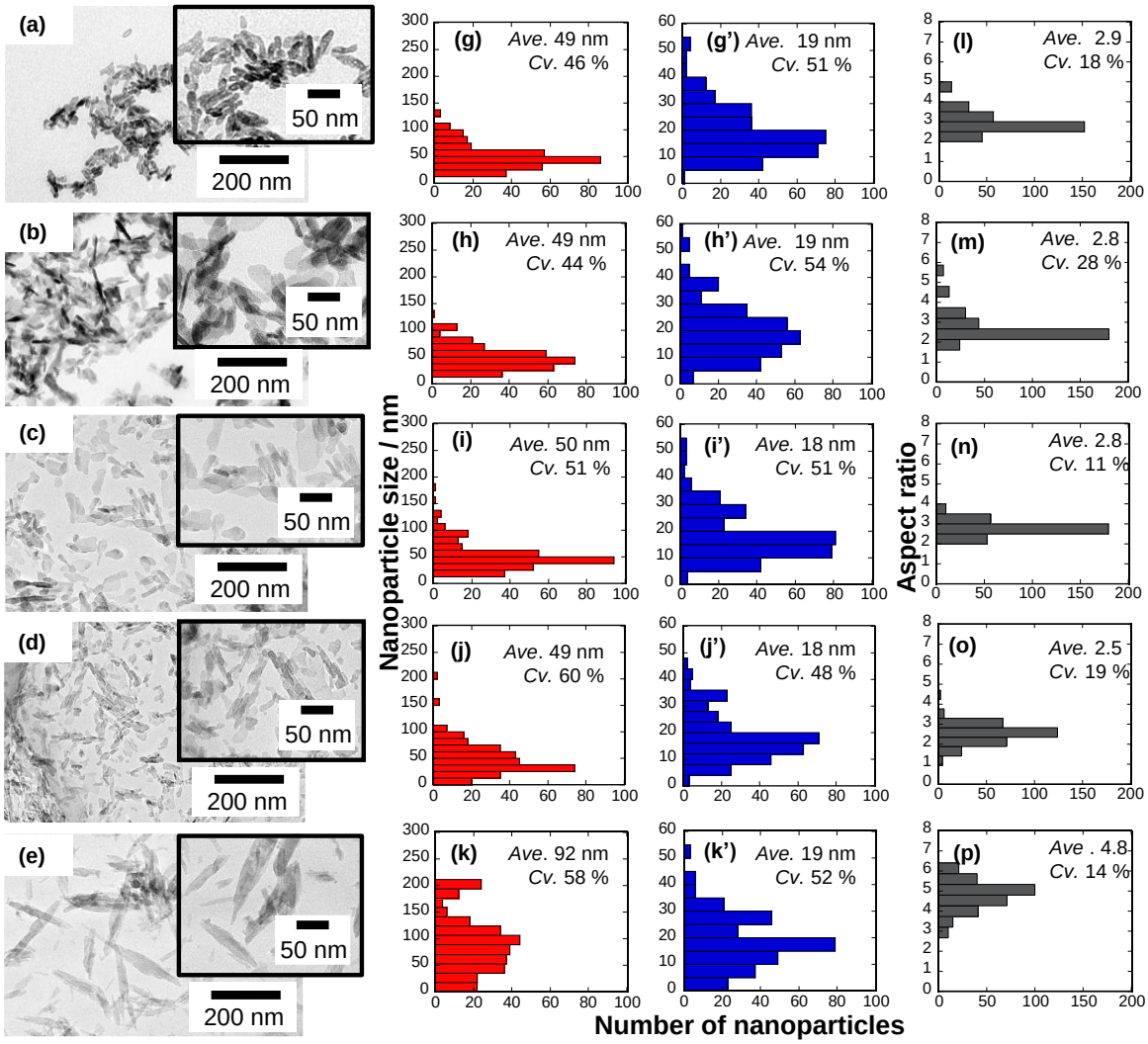

Figure 2-6. (a–e) TEM images of the ***X***EHA nanoparticles (inset: magnified images), illustration of the possible surface structures of the (f) ***X***EHA nanoparticles, (g–k) long-axis sizes and (g'–k') short-axis sizes of the particle shapes, and (l–p) aspect ratios ((a, g, g', l) **0**EHA, (b, h, h', m) **1.0**EHA, (c, i, i', n) **2.5**EHA, (d, j, j', o) **5.0**EHA, (e, k, k', p) **10**EHA).

of the HA nanoparticles (2.2–2.8) [24]. Therefore, the different morphologies of nanoparticles were

observed with the EuTH concentration. In particular, both the *L/S* value and the crystallite size ratio (D_{002}/D_{300}) showed the muximum value at **10**EHA. The segregated EuTH molecules covered over the *a*-plane and part of the *c*-plane in **10**EHA to induce an effective polycrystalization.

Figure 2-7(a) shows the dissolution rate of Ca^{2+} from the total Ca^{2+} content in the nanoparticles as a function of immersion time in PBS. The dissolution rate of Ca^{2+} from the total Ca^{2+} content in the nanoparticles was less than 2 wt% and the dissolution amount decreased as the EuTH

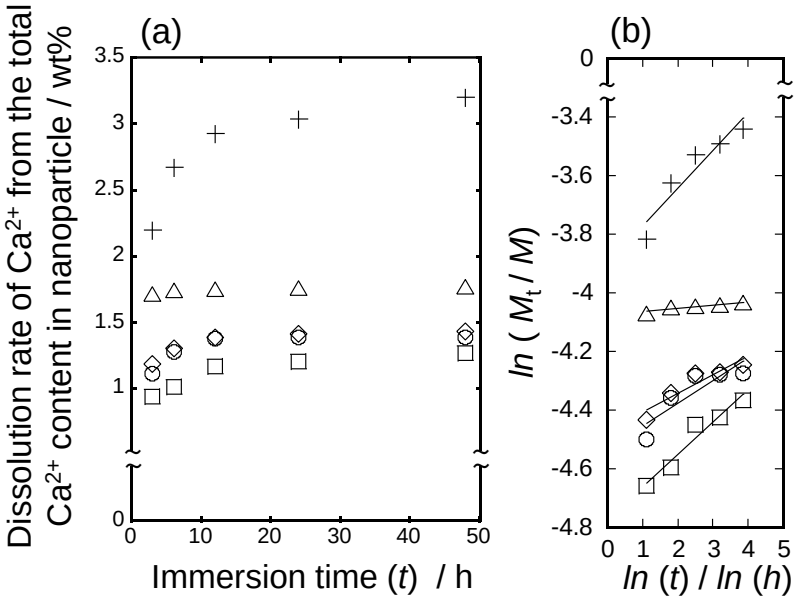

Figure 2-7. (a) Dissolution rate of Ca^{2+} from the total Ca^{2+} content in the nanoparticles ＋: **0**EHA, △: **1.0**EHA, ◇: **2.5**EHA, ○: **5.0**EHA, □: **10**EHA) with the immersion time in PBS. (b) Korsmeyer-Peppas plots calculated from the dissolved Ca^{2+} ratios with the immersion time in PBS.

concentration increased. The dissolution behavior agreed well with Korsmeyer-Peppas model that is expressed by the following form, **Eq. (14)** [57];

$$\ln(F) = \ln\left(\frac{Mt}{M}\right) = n\ln(Km \cdot t) \qquad (14)$$

where *F* is the fraction of the released Ca^{2+} at the time of *t* and can be represented by M_t/M. The *M* is the total amount of Ca^{2+} in the particulate form, and M_t is the amount of the released Ca^{2+}at the time of *t*. K_m is the kinetic constant that indicates the release rate and *n* is the diffusional exponent that depends on the release mechanism as well as the geometry of the system. Here, the low K_m values are the index of slow dissolution behavior and *n* depends on the physicochemical properties of the materials irrespective of the dissolution behavior. As previously reported on the radial diffusion from the cylindrical geometry, the *n* value for pure Fickian diffusion is 0.45. It is known that the value for

abnormal transport is more than 0.45, and that for Case II transport (e.g., polymer relaxation or swelling–controlled mechanism) is 0.89 [57]. In this study, the calculated *n* values were 0.13, 0.01, 0.06, 0.08 and 0.1 for **0**EHA, **1.0**EHA, **2.5**EHA, **5.0**EHA and **10**EHA, respectively, and the K_m values calculated from the plots in **Figure 2-7(b)** were 0.020, 0.017, 0.011, 0.010 and 0.0085 for **0**EHA, **1.0**EHA, **2.5**EHA, **5.0**EHA and **10**EHA, respectively. The nanoparticles were proved to show a very slow dissolution behavior, suggesting that the segregated EuTH molecules suppressed the Ca^{2+} dissolution. It is generally known that Ca^{2+} dissolution occurs from the *a*-plane of HA [58]. Therefore, it was suggested that EuTH existed on the *a*-plane of the nanoparticle and suppresses Ca^{2+} dissolution from the *a*-plane.

The chemical bonding states of the EHA nanoparticles were evaluated by FT-IR spectroscopy and the spectra are shown in the **Figure 2-8**. The absorption bands appeared at 1030–1090 cm^{-1} are attributed to the P–O stretching vibrations of phosphate groups in HA. The weak shoulder band at 960 cm^{-1}, which is attributed to the presence of HPO_4^{2-} ion in HA, resulted from v_1 symmetric P–O(H) stretching vibrations. The absorption band derived from CO_3^{2-} overlaps with the characteristic absorption band of EuTH and could not be confirmed at **1.0**EHA, **2.5**EHA, **5.0**EHA and **10**EHA. In

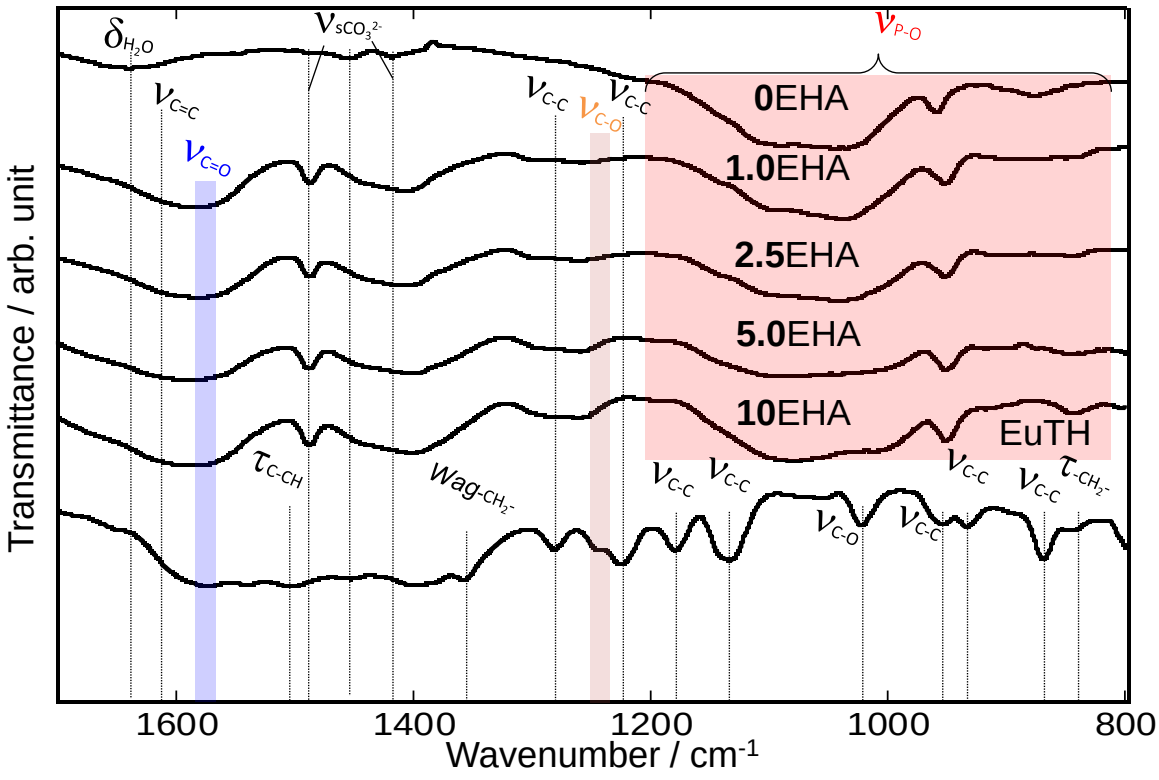

Figure 2-8. FT-IR spectra of the EHA nanoparticles with the different EuTH concentrations and EuTH alone.

the reference sample of EuTH (powder state), the absorption bands that appeared at 1574 cm^{-1} and 1247 cm^{-1} were attributed to C=O stretching and C−O stretching of EuTH shown in **Figure 2-8**. The several absorption bands that appeared at around 1653, 1500, 1356 and 1284 and 1230−1132 cm^{-1} are attributed to stretching vibration of C=C, twisting vibration of −C−CH, wagging vibration of $-CH_2-$ and stretching vibration of C−C, respectively. The characteristic bands of EuTH also appeared at around 1023, 1110, 954−868 and 839 cm^{-1}, which were attributed to stretching vibration of C−O, stretching vibration of C−C and twisting vibration of $-CH_2-$, respectively, and the absorption bands of EuTH were overlapped with those of EHA to be difficult to distinguish the absorption bands at similar wavenumber regions [59]. In the **1.0**EHA, **2.5**EHA, **5.0**EHA and **10**EHA, the absorption bands that appeared at around 1261−1239 cm^{-1} and 1585−1560 cm^{-1} were attributed to C−O stretching and C=O stretching of EuTH [59]. **Figure 2-9(a)** shows second derivative FT-IR spectra of the EHA nanoparticles and EuTH alone in the region 1261 to 1239 cm^{-1}. By the containing with EuTH, the C−O stretching mode was shifted to the higher energy region as compared to the case in the EuTH alone. The shift would be attributed to the interactions between the Ca site of HA and the Eu of the EuTH to alter the EuTH molecular state as shown in **Figure 2-9(b)**. In particular, when the bonding electron transferred to the C−O side of EuTH, shifted to the higher energy region as compared to the case of the EuTH alone [40]. Thus, since the bond between Eu and C−O weakened, it was suggested that Eu of EuTH was adsorbed on the Ca site [40]. **Figure 2-10(a)** shows second derivative FT-IR spectra of the EHA nanoparticles and EuTH alone in the region 1585 to 1560 cm^{-1}. The C=O stretching mode was shifted to the lower energy region as compared to the case in the EuTH alone. The shift would be attributed to the interactions between the C=O stretching mode and the Ca site of the HA structure [40,41] to alter the EuTH molecular state as shown in **Figure 2-10(b)**. In particular, when the bonding electron transferred to the Ca side of HA, shifted to the lower energy region as compared to the case of the EuTH alone [40,41]. Thus, since the bond between the Ca of HA and C=O formed, it was suggested that C=O stretching mode (ligand) of EuTH was adsorbed on the Ca site [40,41]. Judging from these results, EuTH was contained in HA, suggesting the interaction between the Ca site of HA and EuTH.

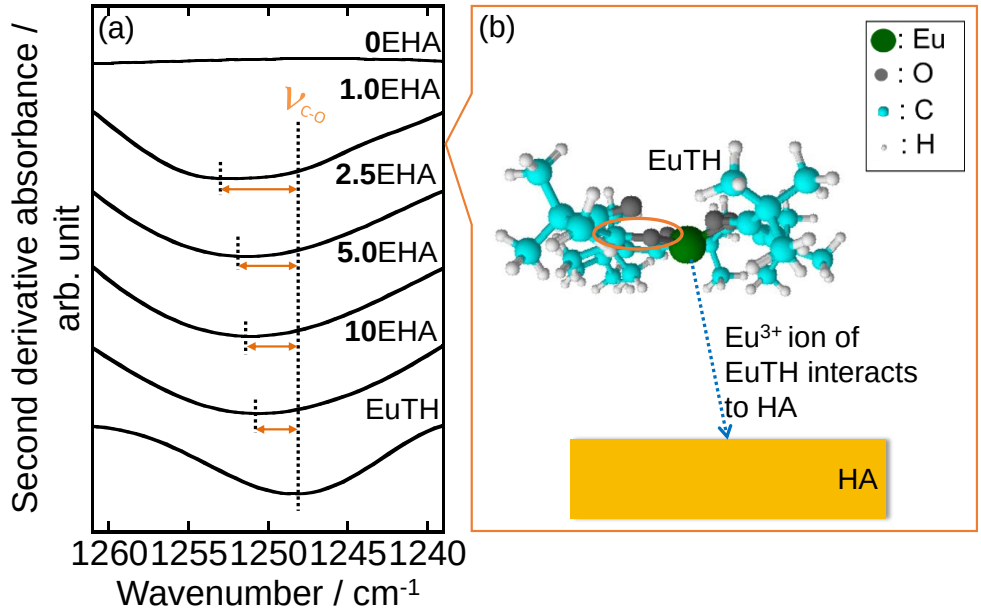

Figure 2-9. (a) Second derivative FT-IR spectra of the EHA nanoparticles and EuTH alone in the region between 1261 and 1239 cm^{-1}, which indicate the peak of C–O in EuTH, and (b) the possible interfacial interactions between C–O bonding (orange circle part) of EuTH and HA surface.

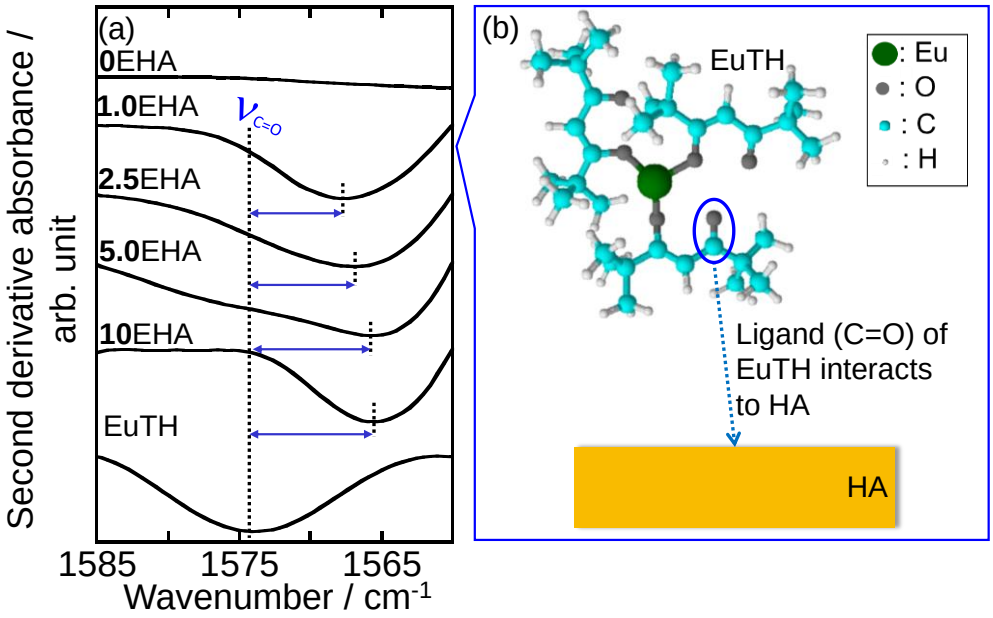

Figure 2-10. (a) Second derivative FT-IR spectra of the EHA nanoparticles and EuTH alone in the region between 1585 and 1560 cm^{-1}, which indicate the peak of C=O in EuTH, and (b) the possible interfacial interactions between C=O (blue circle part) of EuTH and HA surface.

Figure 2-11(a−e) shows the curve fitting and spectral separation results of the FT-IR deconvolution spectra for the P−O bonds of the EHA nanoparticle. The separated components of **Figure 2-11(a−e)** were assigned as shown in **Table 2-1**, which were described in the experimental

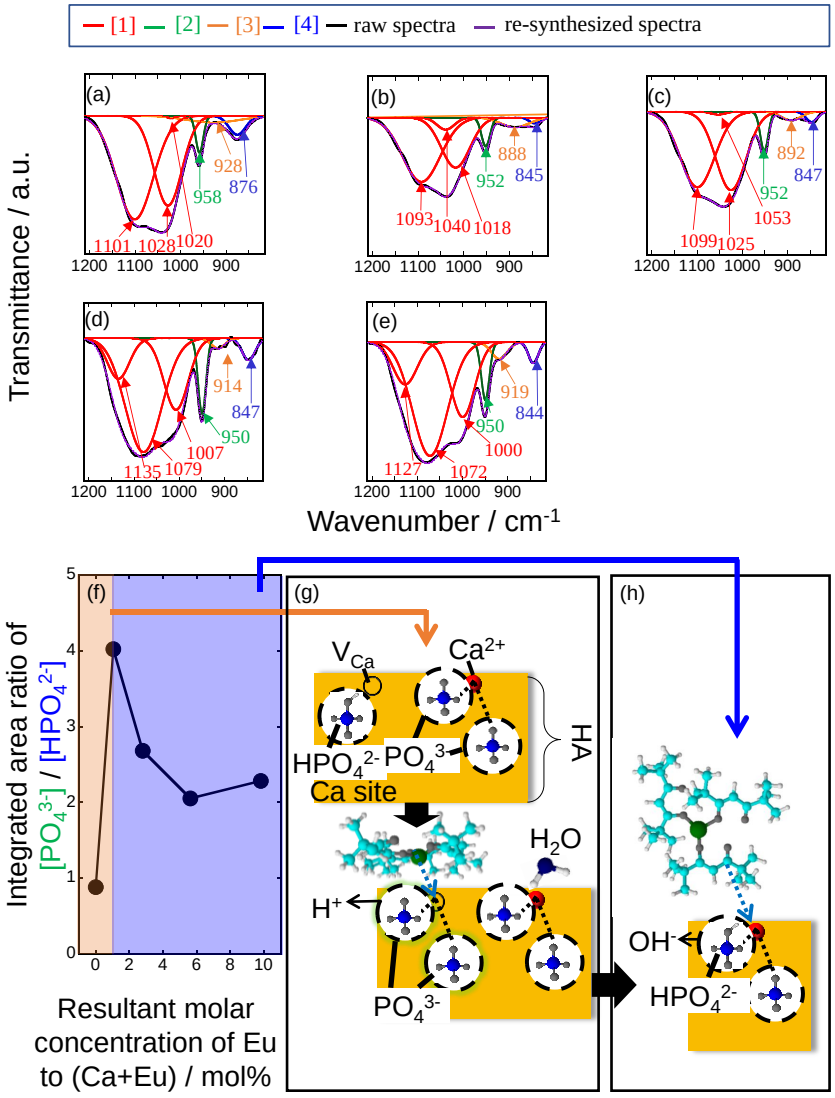

Figure 2-11. Curve fitting and spectral separation results of the FT-IR deconvolution spectra in the P–O absorption bands of (a) **0**EHA, (b) **1.0**EHA, (c) **2.5**EHA, (d) **5.0**EHA and (e) **10**EHA. The details of assignments were shown in **Table 2-1**. (f) Integrated area ratio of $[PO_4^{3-}]$ to $[HPO_4^{2-}]$ in the ***X***EHA nanoparticles. (g) and (h) shows the illustrations for the possible interfacial interactions between EuTH and HA at the orange and blue regions of (f), respectively.

section in detail. The spectral deconvolution was performed using only the P−O bond components. All the sample residuals were less than 3 % by the fitting. The component ratios of the peak areas [1a]−[1c] between the EHA nanoparticles were almost the same. Moreover, among the EHA nanoparticles, the component ratio of the area [2] and the area [4] ($[PO_4^{3-}]/[HPO_4^{2-}]$) were investigated

as shown in **Figure 2-11(f)**. The $[PO_4^{3-}]/[HPO_4^{2-}]$ ratio increased between the **0**EHA and **1.0**EHA, and had decreasing trend between the **1.0**EHA and **10**EHA. Since **0**EHA is Ca-deficient HA, it was expected to have the following composition formula (**Eq. (15).**) [60].

$$Ca_{10-x}(PO_4)_{6-x}(HPO_4)_x(OH)_{2-x} \quad (15)$$

As a result of interacting with Ca-deficient sites when EuTH was contained, the $[HPO_4^{2-}]$ decreased [60] as shown in **Figure 2-11(g)**. The decrease of $[HPO_4^{2-}]$ suggested that H^+ in HPO_4^{2-} was pulled out to become PO_4^{3-}. After that, as a result of the interaction of C=O in the EuTH ligand with Ca site, it is considered that the ratio of $[HPO_4^{2-}]$ increased in order to keep the charge of HA crystals neutral [61] as shown in **Figure 2-11(h)**. Therefore, it was suggested that EuTH induces different interactions depending on the state of the particle surface.

Figure 2-12(a) shows the excitation spectra of the EHA nanoparticles and EuTH. In the nanoparticles, all the peaks are attributed to *f*–*f* transitions within the $4f^6$ electron configuration, reflecting the electronic transitions of Eu^{3+} ion [62]. The excitation spectra for the EHA nanoparticles consist of several peaks, which are located at 363 nm ($^7F_0 \rightarrow {}^5D_4$), 383 nm ($^7F_0 \rightarrow {}^5G_4$), 394 nm ($^7F_0 \rightarrow {}^5L_6$), 464 nm ($^7F_0 \rightarrow {}^5D_2$) and 535 nm ($^7F_0 \rightarrow {}^5D_1$). The spectral shapes of the nanoparticles were similar irrespective of the EuTH concentration. When the coordination symmetry of the ligand becomes lower, the $^7F_0 \rightarrow {}^5L_6$ transition relatively becomes larger [63]. In this study, the symmetry in the nanoparticles were lower as compared with that in the EuTH alone. According to the previous report [64], the ligand absorption band of the EuTH in hexane is widely observed in the range of 322–649 nm, indicating that the ligand absorption band overlaps with that at the excitation wavelength of 464 nm in this study. In the solid state, the charge-transfer absorbance band was not detected because of the difficulty in obtaining the sufficient luminescence quality. In this study, the excitation spectra consist of the several peaks located at 464 nm ($^7F_0 \rightarrow {}^5D_2$) and 525–538 nm ($^7F_0 \rightarrow {}^5D_1$) for the EuTH in the solid state. In the case of the EuTH in ethanol, the $^7F_0 \rightarrow {}^5L_6$ transition newly appeared and the $^7F_0 \rightarrow {}^5D_1$ transition decreased, indicating the environmentally changed coordination structure of Eu^{3+} ion. The spectral shapes of the nanoparticles were different from that of the EuTH in the solid or solution state, suggesting that the EuTH in the nanoparticles had different ligand field symmetry.

To investigate the Eu ion environmental state, the luminescence spectra of the EHA nanoparticles and EuTH were measured as shown in **Figure 2-12(b)**. The luminescence exhibited red-color in the fluorescent microscope observation (**Figure 2-12(b): inset**). In the nanoparticles, all the peaks corresponded to the transitions from the metastable orbital singlet state of $^5D_0$ to the spin–orbital states of ^7F_J (J = 0, 1, 2, 3 and 4) of Eu^{3+} ion. These characteristic transitions are assigned to the $^5D_0$ to $^7F_0$ at 579 nm, $^7F_1$ at 590 nm, $^7F_2$ at 615 nm, $^7F_3$ at 653 nm and $^7F_4$ at 698 nm, respectively. As compared with the spectral shape of the EuTH in solid state, there are two distinct differences in

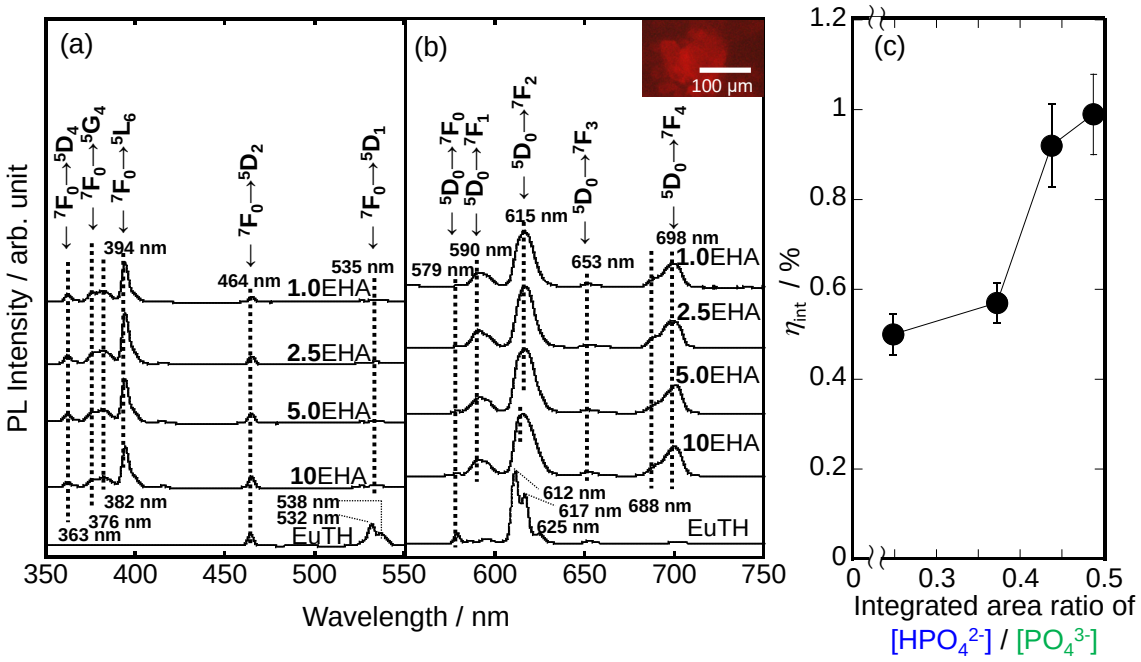

Figure 2-12. (a) excitation and (b) luminescence spectra of the EHA nanoparticles with the different EuTH concentrations and EuTH alone. The monitored luminescence and excitation wavelengths for the excitation and luminescence spectral measurements were 615 nm and 464 nm, respectively. Inset: representative fluorescence microscope image of **5.0**EHA. (c) η_{int} of the EHA nanoparticles. The monitored luminescence and excitation wavelengths for the excitation and luminescence spectral measurements were 615 nm and 464 nm, respectively.

the spectra of the nanoparticles; a new peak attributed to $^5D_0 \rightarrow {}^7F_1$ transition appeared and the spectral shape of $^5D_0 \rightarrow {}^7F_2$ transition (i.e., Stark splitting state) varied, leading to the color purity variation. The spectral broadening via the containing processes would be attributed to the modified symmetry of the Eu complex ligand by the inorganic-organic interactions. The $^5D_0 \rightarrow {}^7F_1$ and $^5D_0 \rightarrow {}^7F_2$ transitions were attributed to magnetic dipole and electric dipole transitions, respectively [45]. The electric-dipole transition is sensitive to the local structure surrounding the Eu^{3+} ion. The intensity of the magnetic dipole transition exhibits very little variation with the crystal field strength acting on the Eu^{3+} ion. Accordingly, the I_{590}/I_{615} ratio indicates the spatial symmetry of the Eu^{3+} ion site. For example, the lower value means the lower symmetry [65]. In the previous reports, the intensity ratios in the Eu^{3+}-doped niobium silicate glasses were 0.11–0.16 [45], and those in the Eu^{3+}-doped alkaline earth zinc phosphate glasses were 0.43–0.45 [65]. In this study, the I_{590}/I_{615} ratio of the nanoparticles has a small variation with the EuTH concentration. In particular, the I_{590}/I_{615} value was 0.27, 0.23, 0.19, 0.18 and 0.037 for **1.0**EHA, **2.5**EHA, **5.0**EHA, **10**EHA and EuTH, respectively. The value of the nanoparticle slightly decreased with increasing the EuTH concentration and is similar to those of the Eu^{3+}-doped glasses, indicating that the spatial symmetry of Eu^{3+} ion lowered by containing with

EuTH. Therefore, it was considered that the coordination environment of the Eu^{3+} ion in the present nanoparticles changed with the EuTH concentration.

Figure 2-12(c) shows the changes in the η_{int} of the nanoparticles. The η_{int} values of the nanoparticles increased more than 3 times at the excitation wavelength of 464 nm as compared with that of the EuTH and **5.0**EHA (0.98 %; highest), suggesting that such luminescence efficiency would be attributed to the change in the Eu ion coordination symmetric structure through the containing associated with the transition from single crystal to polycrystal.

Scheme 2-7 shows an illustration of the possible interface structures between HA and EuTH of the **5.0**EHA structural surface. Considering that the $[HPO_4^{2-}]$ increases or decreases when EuTH is present on the particle surface, EuTH may be present parallel and perpendicular to the particle surface. Specifically, when Eu^{3+} ion of EuTH interacts with the Ca-deficient site, EuTH exists parallel to the particle surface. When the C=O of the EuTH ligand interacts with the Ca site, EuTH exists perpendicular (or parallel) to the particle surface.

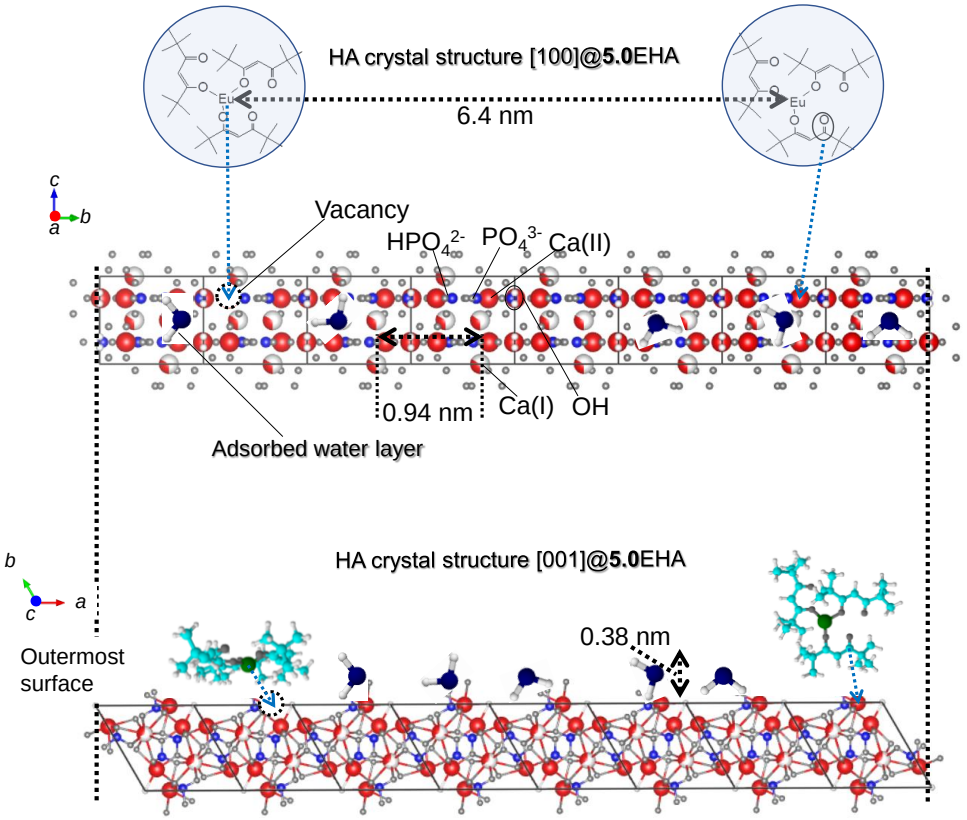

Scheme 2-7. Illustration of the possible interface structures between HA and EuTH of the **5.0**EHA structural surface. It is shown that the symmetry of EuTH is lowered by the interaction between the Eu^{3+} ion of EuTH and the Ca deficient site of HA and the ligand(C=O) of EuTH and the Ca^{2+} ion of HA.

2.3.2 Characterization of the FA-NHS-immobilized nanoparticles

Figure 2-13 shows resultant FA-NHS immobilization amount on the **0F**-A5.0EHA nanoparticle surface, and resultant FA-NHS molecular area occupancy and intermolecular distance with different FA-NHS immobilization amount on the **0F**-A5.0EHA nanoparticle surface. As shown in the **Figure 2-1(a)**, the UV-Vis absorption spectra of the FA-NHS solution (pH = 2) exhibited the maximum absorption wavelength at 322 nm. The immobilization amount and the molecular occupancy of FA-NHS varied with the feed concentration, and the actual molecular occupancy rate is clearly lower than the theoretical molecular occupancy rate. Specifically, the actual molecular occupancy and intermolecular distance between FA-NHS molecules were 3.5 % and 2.4 nm for **5F**-A5.0EHA, 4.3 % and 2.1 nm for **10F**-A5.0EHA, 6.0 % and 1.8 nm for **25F**-A5.0EHA, 10 % and 1.4 nm for **50F**-A5.0EHA, 13 % and 1.3 nm for **100F**-A5.0EHA, 29 % and 0.8 nm for **150F**-A5.0EHA, 37 % and 0.7 nm for **200F**-A5.0EHA and 47 % and 0.6 nm for **250F**-A5.0EHA. Therefore, it was suggested that the FA-NHS immobilization amount on the nanoparticles can be controlled by the feed concentration.

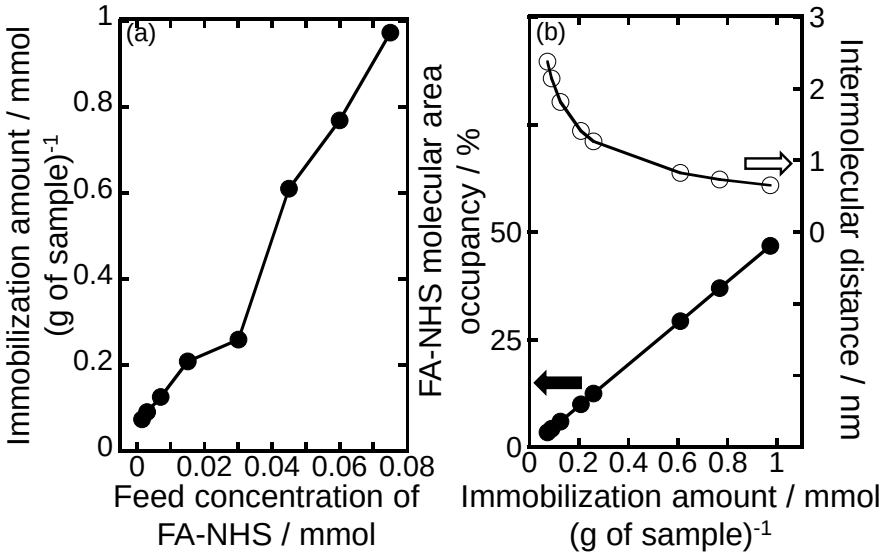

Figure 2-13. (a) Resultant FA-NHS immobilization amount on the **0F**-A5.0EHA nanoparticle surface. (b) Resultant FA-NHS molecular area occupancy and intermolecular distance with different FA-NHS immobilization amount on the **0F**-A5.0EHA nanoparticle surface.

Figure 2-14 shows the UV-Vis absorption spectra of the FA-NHS solutions at the different pH values and powder, and the UV-Vis diffuse reflection absorption spectra of the FA-NHS-immobilized **0F**-A5.0EHA. In **Figure 2-14(a)**, the FA-NHS powder had the broad spectral shape, which was different from that of the FA-NHS solution. In the absorption spectra of the FA-NHS solution, it was suggested that the state of FA-NHS varied depending on the pH value in the solution, and the maximum absorption wavelength was shifted to the longer region with increasing the pH value. The shift is attributed to the charged state of FA-NHS [34]. In the solution system, the FA-NHS molecule is totally positively-charged, as the proton approaches N atom of the pterin part at the pH of 2. At the pH of 6, the charge of the carboxyl group starts to be negatively-charged and the pterin moiety is positively-charged, and the molecule totally exhibits the positively-charged state. At the of pH of 7, the charge of the carboxyl group of FA-NHS is negatively-charged, and the molecule totally exhibits the negatively-charged state. In the diffuse reflection absorption spectra of the FA-NHS-immobilized **0F**-A5.0EHA nanoparticles (**Figure 2-14(b)**), the absorption bands derived from the Eu^{3+} ions were observed at 300 and 394 nm in **0F**-A5.0EHA, which was a white powder (**Figure 2-14(b) Inset**). In the FA-NHS-immobilized **0F**-A5.0EHA, which were yellow powders (**Figure 2-14(b) Inset**), the

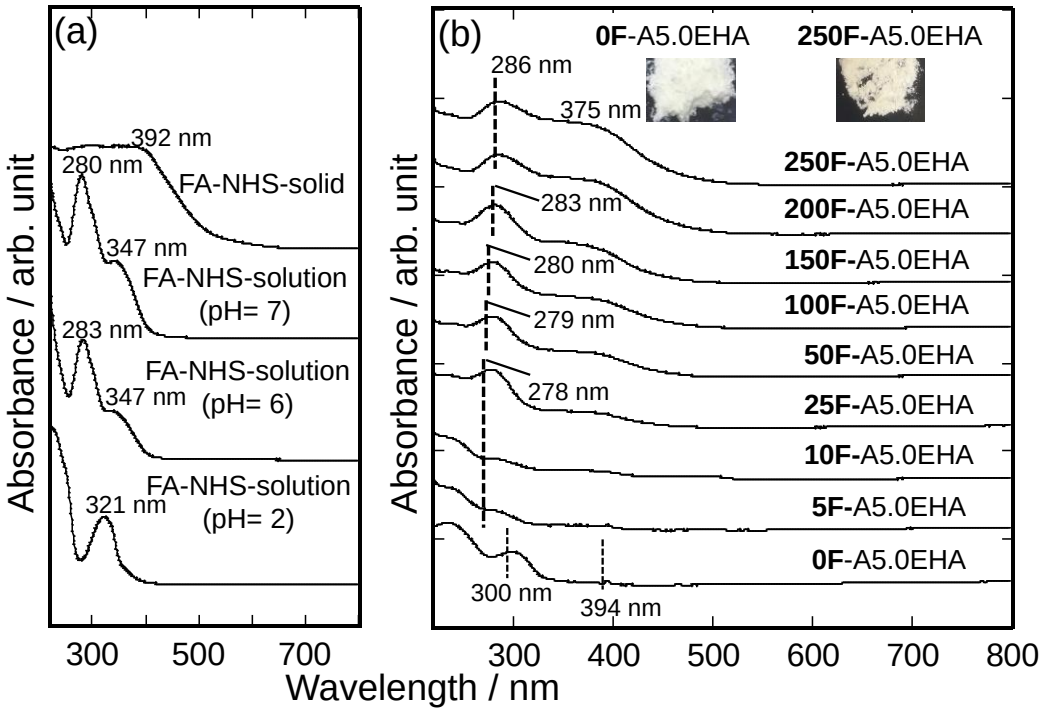

Figure 2-14. (a) UV-Vis absorption spectra of the FA-NHS solution at the different pH values and powder. (b) UV-Vis diffuse reflection absorption spectra of the FA-NHS-immobilized **0F**-A5.0EHA. Inset: representative photographs of the APTES-MTES-co-immobilized **5.0**EHA nanoparticles before and after the FA-NHS functionalization.

absorption of the Eu^{3+} ion was also observed, especially at 394 nm. By the immobilization of FA-NHS on the EHA nanoparticle, the absorption bands appeared at 278−286 nm. With increasing the immobilization amount of FA-NHS on the nanoparticles, the maximum absorption wavelength was red-shifted. The shift is similar to that case in the FA-NHS solution, suggesting the change of the charged state of the immobilized FA-NHS. When the amount of FA-NHS immobilization is smaller and larger, the FA-NHS molecular state is similar to that in the solution at the pH of 7 and 6, respectively, indicating the different charged states on the nanoparticles. Therefore, it was suggested that the charge state of FA-NHS molecule on the EHA nanoparticle changed with the immobilization amount of FA-NHS, which would be dominated by the interactions between the FA-NHS and nanoparticle as well as the intermolecular stacking.

The excitation and luminescence spectra and I and η_{int} value changes of the FA-NHS-immobilized nanoparticles, which were excited under the wavelengths of 464 nm were shown in **Figure 2-15**. In the excitation spectra of the FA-NHS-immobilized nanoparticles (**Figure 2-15(a)**), all the peaks were attributed to *f–f* transitions within the $4f^6$ electron configuration, reflecting the electronic transitions of the Eu^{3+} ion [62]. The excitation spectra for the EHA nanoparticles consisted of the several peaks, which are located at 363 nm ($^7F_0 \rightarrow {}^5D_4$), 383 nm ($^7F_0 \rightarrow {}^5G_4$), 394 nm ($^7F_0 \rightarrow {}^5L_6$), 464 nm ($^7F_0 \rightarrow {}^5D_2$) and 535 nm ($^7F_0 \rightarrow {}^5D_1$). The intensities at 464 nm was higher than the other peaks between visible light regions. In addition, the broad spectra were observed at around 500 nm. The spectral shapes among the FA-NHS-immobilized nanoparticles were almost same. Thus, it was suggested that there was no significant difference in the ligand field symmetry of the Eu^{3+} ion. **Figure 2-15(b)** exhibited the luminescence spectra of the FA-NHS-immobilized **0F**-A5.0EHA. The luminescence exhibited the red-color by the FM observation (**Figure 2-15(b) Inset**). All the peaks corresponded to the transitions from the metastable orbital singlet state of $^5D_0$ to the spin–orbital states of ^7F_J (J = 0, 1, 2, 3, 4) of the Eu^{3+} ion. These characteristic transitions were assigned to the $^5D_0$ to $^7F_0$ at 579 nm, $^7F_1$ at 590 nm, $^7F_2$ at 616 nm, $^7F_3$ at 653 nm and $^7F_4$ at 698 nm, respectively. In addition, the broad spectral peaks were newly observed at around 518 nm. These peaks were expressed by the FA-NHS immobilization. When the excitation light of 464 nm was applied to the FA-NHS solution (pH = 7), the luminescence peak was observed at around 550 nm. The luminescence was attributed to the charge transfer (CT) between S_1–S_0 of π-electrons, which were located on the conjugated system between pterin and imine parts of the FA-NHS molecule in the aqueous solution [34]. In the FA-NHS solid phase, the luminescence due to the CT between S_1–S_0 was observed at the shorter wavelength region at 440 nm under the excitation light at 369 nm was observed. From the above, it was suggested that the luminescence behavior of the immobilized FA-NHS molecules was

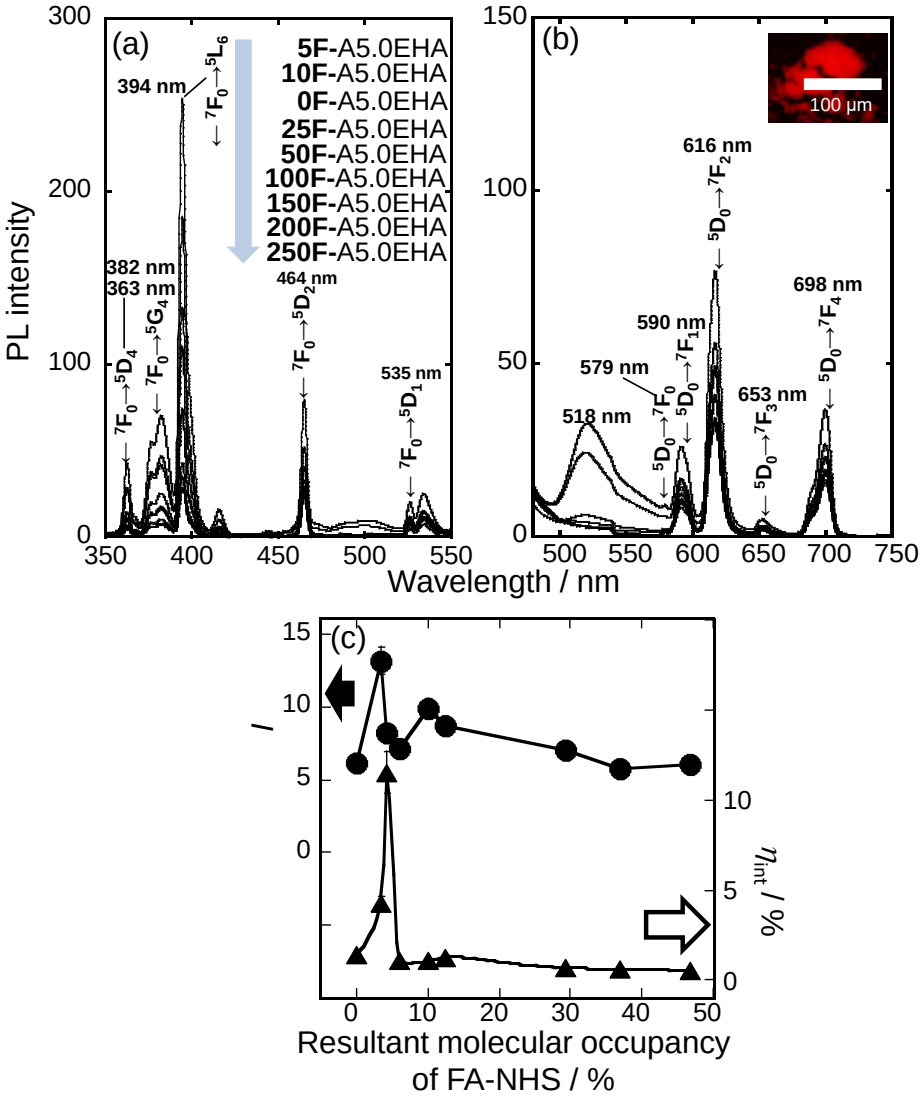

Figure 2-15. (a) Excitation and (b) luminescence spectra of the FA-NHS-immobilized **0F**-A5.0EHA nanoparticles. The monitored luminescence and excitation wavelengths for the excitation and luminescence spectral measurements were 615 nm and 464 nm, respectively. Inset: representative fluorescence microscope image of **5F**-A5.0EHA. (c) I and η_{int} value changes of the FA-NHS-immobilized **0F**-A5.0EHA nanoparticles, which were excited under the wavelengths of 464 nm.

close to the solution system. When the FA-NHS molecules on the **0F**-A5.0EHA are present at the low concentration (i.e., smaller FA-NHS intermolecular interactions), FA can exist as a monomer state that is close to the solution system. Accordingly, the FA monomer molecule stably exists on the **0F**-A5.0EHA to selectively interact with the EuTH molecule at the near-surfaces, so that the luminescence peak due to CT between EuTH–FA-NHS (monomer) was observed at 518 nm and red-shifted as compared with that of the solid phase of FA-NHS (440 nm). Thus, it was suggested that

the exciplex was formed between both molecules [66] and was the new excited state composed of two molecules, which was confirmed by the presence of the exciplex luminescence without the vibrating structure appearing at the longer wavelength region as compared with the case in the excited molecule alone [67]. **Figure 2-15(c)** showed the *I* and η_{int} value changes of the FA-NHS-immobilized **0F**-A5.0EHA. The highest *I* value of the immobilized **0F**-A5.0EHA was observed in **5F**-A5.0EHA, which had the molecular occupancy rate of the FA-NHS on the **0F**-A5.0EHA at 3 %. The *I* values of **5F**-A5.0EHA under the excitation at 464 nm was higher 2.1 times than those of the **0F**-A5.0EHA. It was suggested that the luminescence intensities derived from the Eu^{3+} ions would be enhanced by the formation of the exciplex. When the molecular occupancy rate of FA-NHS exceeded 5 %, the intensity became weak. With decreasing the distance between FA molecules, the states of the FA-NHS molecules on the **0F**-A5.0EHA would approach the solid phase to induce the energy transfer among the FA-NHS molecules. Accordingly, the luminescence intensity derived from Eu^{3+} ions decreased due to the change in the CT states. Therefore, the new luminescence band with accompanying exciplex formation between EuTH–FA-NHS was observed, and **5F**-A5.0EHA realized the maximum *I* value among all the samples. Moreover, **Figure 2-15(c)** exhibited the η_{int} values of the FA-NHS-immobilized nanoparticles. The **5F**-A5.0EHA with the molecular occupancy rate of FA-NHS at 5 % showed the best η_{int} value of 11.5 %. Therefore, when FA-NHS is immobilized on the **0F**-A5.0EHA with the molecular occupancy at 5 %, the higher η_{int} value was observed. Therefore, it was suggested that EuTH and FA-NHS can form exciplex [66,68,69] as shown in **Scheme 2-8**.

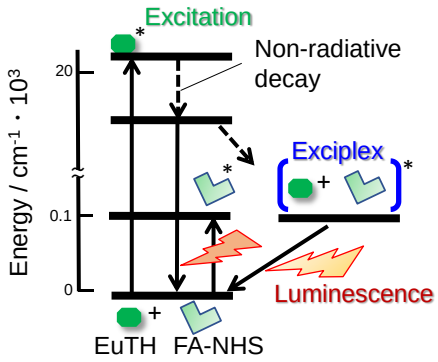

Scheme 2-8. Illustration of possible photofunctional interface between EuTH and FA-NHS.

The luminescence intensity decay plots and fitted curves of the **5.0**EHA, **0F**-A5.0EHA and FA-NHS-immobilized **0F**-A5.0EHA nanoparticles were shown in **Figure 2-16**. The EuTH exhibited the

first-order decay curve with the fluorescence lifetime at 0.37 ms. In the nanoparticle systems of **5.0**EHA, **0F**-A5.0EHA, **5F**-A5.0EHA, **10F**-A5.0EHA, **25F**-A5.0EHA, **50F**-A5.0EHA, **100F**-A5.0EHA, **150F**-A5.0EHA, **200F**-A5.0EHA and **250F**-A5.0EHA, the secondary decay curves were observed, and the τ_1 was 0.85, 1.27, 2.07, 2.01, 2.00, 2.01, 2.05, 1.92, 1.91 and 1.85 ms and the τ_2 was 0.99, 1.53, 2.13, 2.27, 2.12, 2.15, 2.27, 2.32, 2.10 and 2.58 ms, the τ_1/τ_2 ratio was 0.86, 0.83, 0.97, 0.88, 0.94, 0.94, 0.90, 0.83, 0.91 and 0.72, the A_1 was 0.93, 0.91, 0.76, 0.71, 0.74, 0.74, 0.75, 0.74, 0.68 and 0.75, and the A_2 was 0.07, 0.09, 0.24, 0.29, 0.26, 0.26, 0.25, 0.26, 0.32 and 0.25, respectively. As compared with the EuTH alone, the fluorescence lifetime was delayed by the nanoparticle. Furthermore, the FA-NHS immobilization delayed the fluorescence lifetimes (τ_1 and τ_2). Furthermore, it was found that the τ_1/τ_2 ratio tends to increase by the FA-NHS immobilization, suggesting that there is the interaction between the FA-NHS and EuTH. When there are hydrophobic groups around the luminescent species, the lifetime is relatively long [70]. Thus, it has been considered that A_1 and A_2 are caused by EuTH which exists parallel and perpendicular to the particle surface, respectively. The EuTH existing parallel to the particle surface is affected by the water existing on the particle surface and has a short lifetime. Therefore, the CT between EuTH (**5.0**EHA) and FA-NHS molecules, forming the exciplex between the molecules, delayed the fluorescence lifetime due to the appearance of the level derived from the exciplex.

Scheme 2-9 shows detailed illustration of the possible interface structures between EuTH (**5.0**EHA) and FA-NHS of the **5F**-A5.0EHA. **Scheme 2-10** shows detailed illustration of the possible interface structures between EuTH (**5.0**EHA) and FA-NHS of the **100F**-A5.0EHA. The distance between EuTH and FA-NHS in the scheme assumed that EuTH was at the center of the FA-NHS intermolecular distance. The EuTH was present at the Ca site and FA-NHS was bound to the OH site. The distance between the Ca site and the OH site is described as the distance between EuTH and FA-NHS. In **5F**-A5.0EHA, the FA-NHS intermolecular distance was longer than the FA-NHS molecular diameter (1.5 nm). Thus, FA-NHS molecular stacking is negligible. Furthermore, it was suggested that luminescence was achieved by charge transfer from EuTH to FA-NHS, suggesting that there is the interaction between the FA-NHS and EuTH. In **100F**-A5.0EHA, the FA-NHS intermolecular distance was shorter than the FA-NHS molecular diameter. Thus, it was considered that the stacking between FA-NHS molecules occurs. It was suggested that after charge transfer from EuTH to FA-NHS, it was deactivated by stacking between FA-NHS molecules.

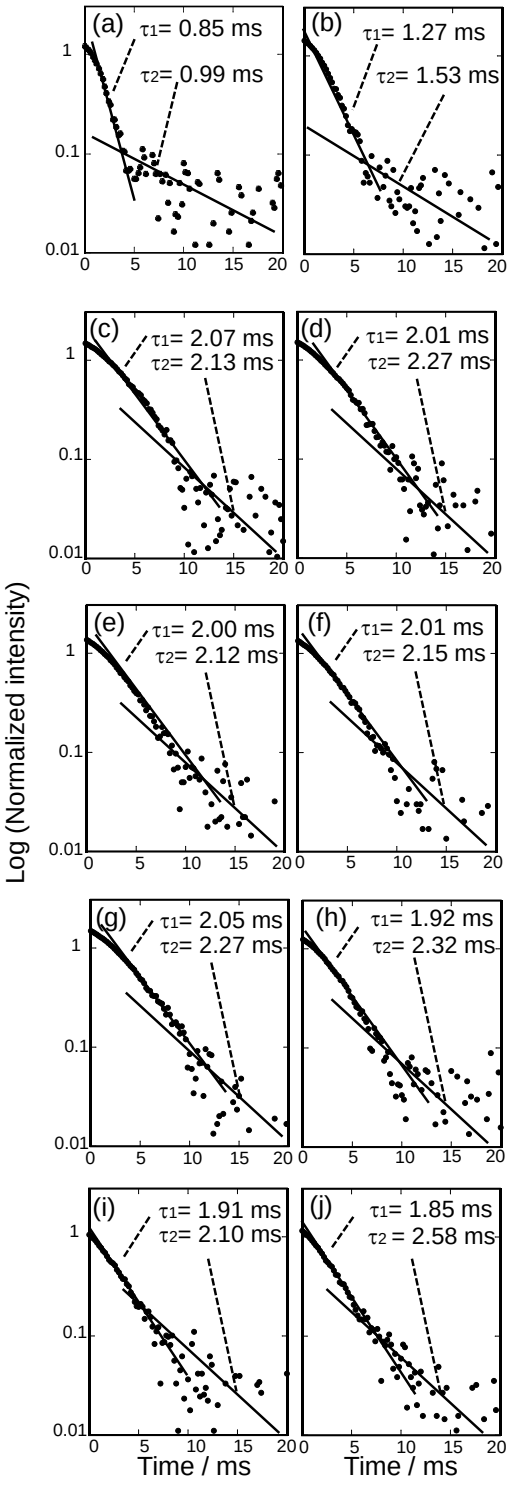

Figure 2-16. Luminescence intensity decay plots and fitted curves of the (a) **5.0**EHA, (b) **0F**-A5.0EHA, (c) **5F**-A5.0EHA, (d) **10F**-A5.0EHA, (e) **25F**-A5.0EHA, (f) **50F**-A5.0EHA, (g) **100F**-A5.0EHA, (h) **150F**-A5.0EHA, (i) **200F**-A5.0EHA, and (j) **250F**-A5.0EHA. The monitored luminescence and excitation wavelengths for the excitation and luminescence spectral measurements were 615 nm and 464 nm, respectively.

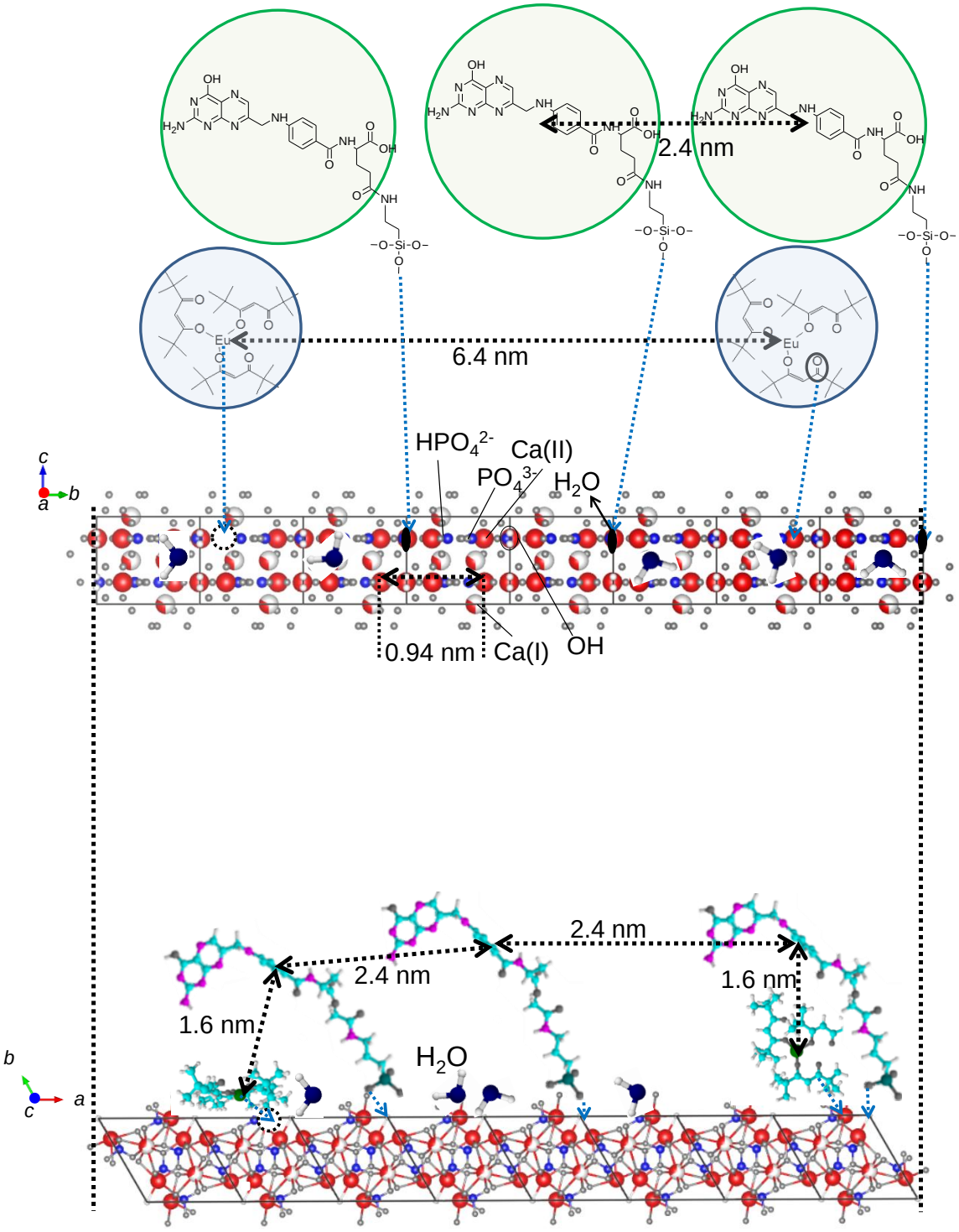

Scheme 2-9. Detailed illustration of the possible interface structures between EuTH (**5.0**EHA) and FA-NHS of the **5F**-A5.0EHA.

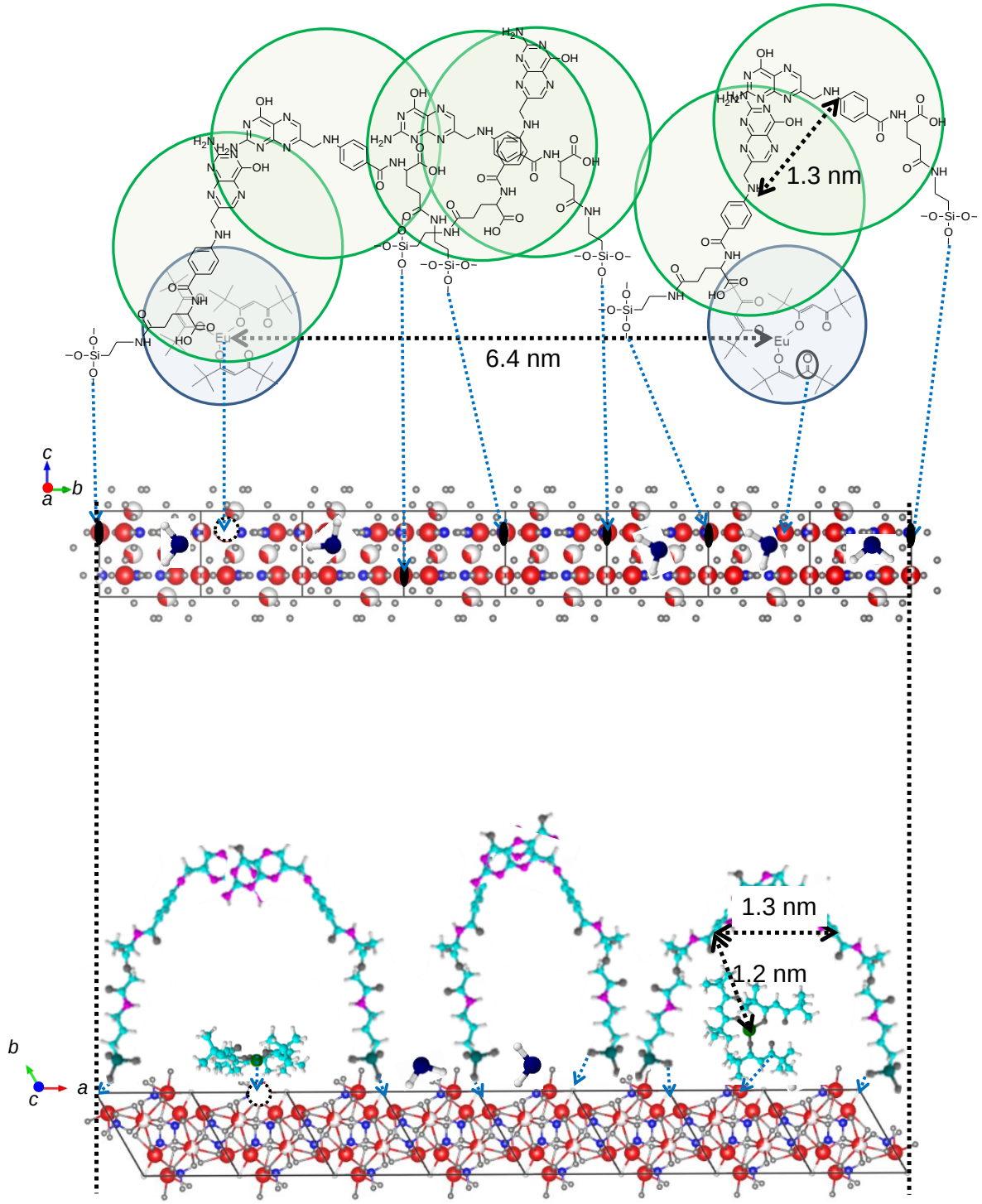

Scheme 2-10. Detailed illustration of the possible interface structures between EuTH (**5.0**EHA) and FA-NHS of the **100F**-A5.0EHA.

2.3.3 Size distributions of the nanoparticles in phosphate buffer saline

Figure 2-17(a-e) shows the particle size distributions of **5.0**EHA, **0F**-A5.0EHA, **5F**-A5.0EHA, **10F**-A5.0EHA and **100F**-A5.0EHA dispersed in PBS. The *Ave.* values were 148 nm for **5.0**EHA, 125 nm for **0F**-A5.0EHA, 122 nm for **5F**-A5.0EHA, 125 nm for **10F**-A5.0EHA and 115 nm for **100F**-A5.0EHA, respectively, and were smaller as compared with that of **5.0**EHA. In addition, the *Cv*

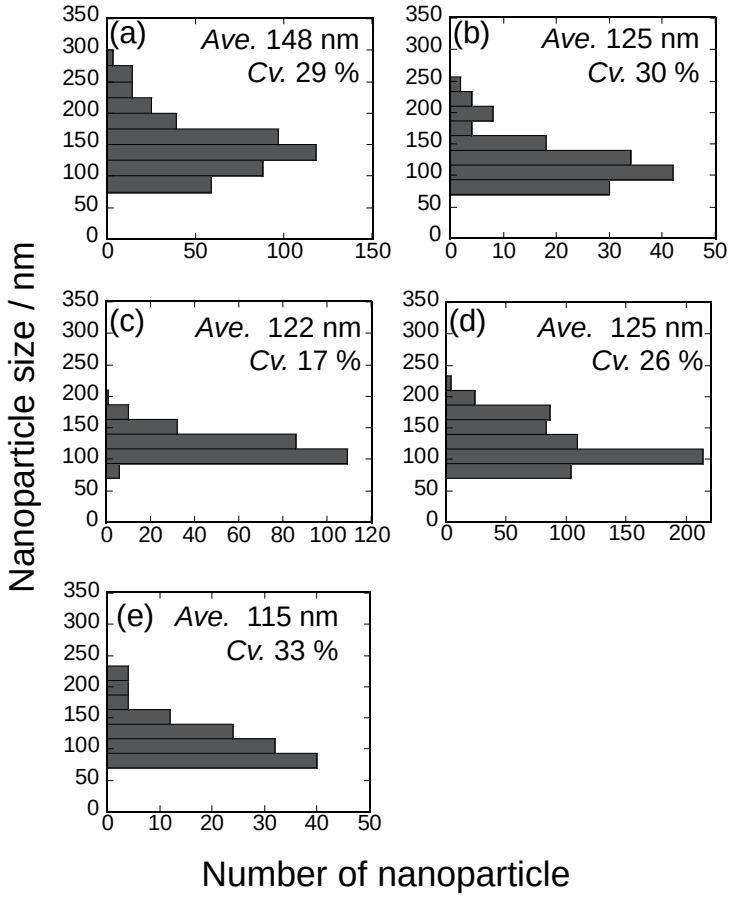

Figure 2-17. The particle size distributions of (a) **5.0**EHA, (b) **0F**-A5.0EHA, (c) **5F**-A5.0EHA, (d) **10F**-A5.0EHA and (e) **100F**-A5.0EHA dispersed in PBS (FA-NHS-immobilized **0F**-A5.0EHA nanoparticle concentrations : 50 ng/mL).

values of the **5F**-A5.0EHA and the **10F**-A5.0EHA were suppressed by the FA-NHS immobilization. Therefore, it was suggested that when FA-NHS was immobilized at the low concentration for **5F**-A5.0EHA, the nanoparticle dispersibility in PBS was improved by the positively-charged FA-NHS. From the above results, **5F**-A5.0EHA was used for the evaluation of the following cytotoxicity and cell labeling ability.

Figure 2-18(a) shows the dissolution rate of Ca^{2+} from the total Ca^{2+} content in the FA-NHS-immobilized nanoparticles as a function of immersion time in PBS. The dissolution rate of Ca^{2+} from the total Ca^{2+} content in the FA-NHS-immobilized nanoparticles was less than 0.5 wt% and the dissolution amount decreased as the FA-NHS concentration increased. **5.0**EHA showed about 1.3 wt% of Ca^{2+} dissolution. Therefore, it was confirmed that the Ca^{2+} dissolution was suppressed by the immobilization of APTES and FA-NHS on the nanoparticle surface. **Figure 2-18(b)** shows a digital camera images after the UVA light irradiation of the nanoparticles dispersed in PBS after the immersion time at 0 and 66 h. The red luminescence was confirmed from the dispersion.

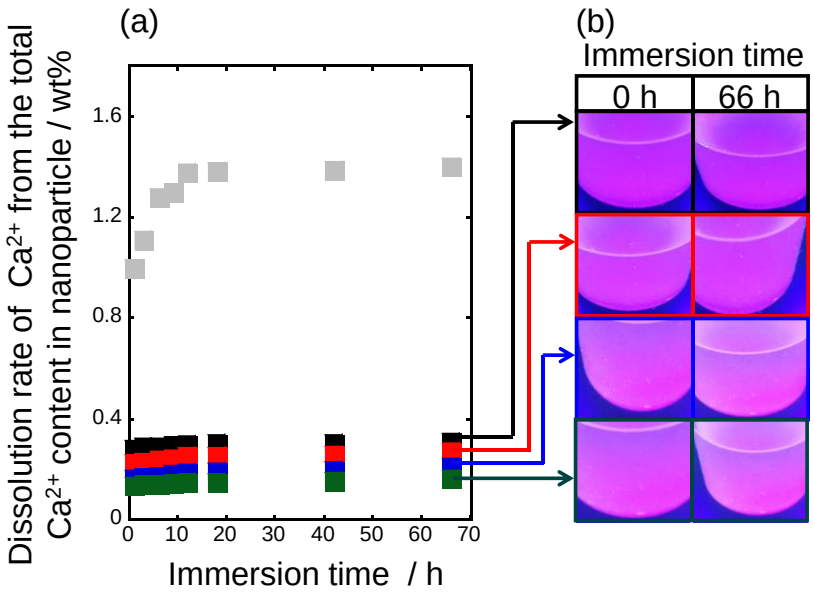

Figure 2-18. Dissolution rate of Ca^{2+} from the total Ca^{2+} content in the nanoparticles (■: **5.0**EHA, ■: **0F**-A5.0EHA, ■: **5F**-A5.0EHA, ■: **10F**-A5.0EHA, ■: **100F**-A5.0EHA) with the immersion time in PBS. (b) Digital camera images with the UVA light irradiation to the nanoparticles (**0F**-A5.0EHA, **5F**-A5.0EHA, **10F**-A5.0EHA and **100F**-A5.0EHA) dispersed in PBS (nanoparticle concentrations : 1.0 mg/mL) after the immersion time of 0 and 66 h.

2.3.4 Cytotoxicity of the nanoparticles against fibroblasts

The adhered fibroblast density changes in the reaction with the nanoparticles with the culture time are shown in **Figure 2-19(a)**. All the samples showed a linear increase with the culture time, and there was no significant difference between the samples. Therefore, the non-cytotoxic behaviors of the nanoparticles were elucidated. The optical transmittance images of the fibroblasts that reacted with the nanoparticles at the culture time of 72 h are shown in **Figure 2-19(b-h)**. The adherent cells spread, and the number of cells increased with the culture time. The nanoparticles on the cells could not be confirmed, so that the nanoparticles may interact with the cells at the dispersed state and be taken up by the cells. There were many fusiform cells and was no significant difference in the cellular shapes irrespective of the addition of the nanoparticles. Thus, the fibroblast affinity of the nanoparticles was confirmed.

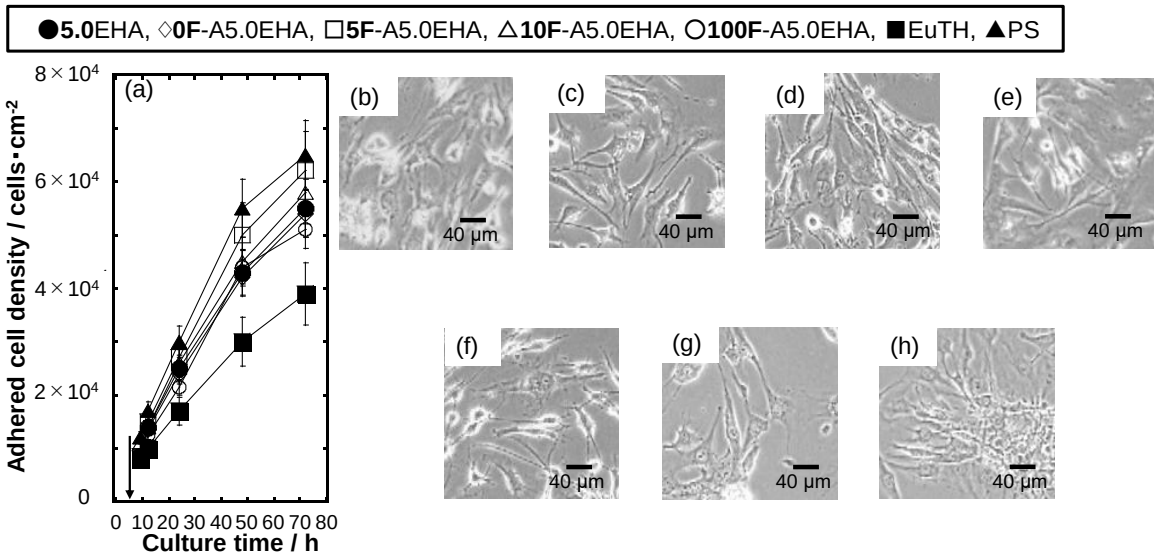

Figure 2-19. (a) Adhered fibroblast density changes in the reaction with **5.0**EHA, **0F**-A5.0EHA, **5F**-A5.0EHA, **10F**-EHA, **100F**-A5.0EHA and EuTH (particle concentration: 100 μg/mL) with the culture time. As the reference, the culture without adding was done on PS dish. Arrows in the figures indicate the addition timing of the nanoparticles at the culture time of 6 h. (c–h) Optical transmittance images of the fibroblasts reacted with the nanoparticles ((b) **5.0**EHA, (c) **0F**-A5.0EHA, (d) **5F**-A5.0EHA, (e) **10F**-A5.0EHA, (f) **100F**-A5.0EHA, (g) EuTH (particle concentration: 100 μg/mL) and (h) **PS**) at the culture time of 72 h.

2.3.5 Cytotoxicity and cell labeling ability of the nanoparticles against cancer cells

Figure 2-20(a) shows the adhered cell density changes in the reaction with **5.0**EHA, **0F**-A5.0EHA, **5F**-A5.0EHA, **10F**-A5.0EHA, **100F**-A5.0EHA and EuTH with the culture time from the particle addition point. As compared with the change in the EuTH alone, that in the EHA nanoparticles was higher, indicating the importance of the containing by HA for improving the cytocompatibility. The density in the FA-NHS-immobilized **0F**-A5.0EHA was higher than that in the **5.0**EHA and **0F**-A5.0EHA, suggesting the further improvement of cytotoxicity by the FA-NHS immobilization. In particular, **5F**-A5.0EHA exhibited no cytotoxicity as same to the reference PS dish. **Figure 2-20(b)** show the results of the integrated PL intensity changes of the cells in the reaction with **5.0**EHA, **0F**-A5.0EHA, **5F**-A5.0EHA, **10F**-A5.0EHA, **100F**-A5.0EHA and EuTH with the culture time from the particle addition point. The higher luminescence intensities of the cells were observed in **5F**-A5.0EHA under the excitation light of 464 nm, suggesting that the FA-NHS molecular occupancy would be the best for effectively binding to the folate molecule receptor on the cell membranes (i.e., targeting to the HeLa cells) [71]. Thus, we found the importance of the FA-NHS molecular occupancy on the nanoparticles. The lower luminescence intensity was observed in the case of **100F**-A5.0EHA, implying that the binding rate with the cells would be lower based on the aggregation between the FA-NHS molecules. **Figure 2-20 (c-h** and **c'-h')** showed the optical transmittance and FM images of the HeLa cells reacted with **5.0**EHA, **0F**-A5.0EHA, **5F**-A5.0EHA, **10F**-A5.0EHA, **100F**-A5.0EHA and EuTH at the culture time of 72 h. The cells reacted with **5.0**EHA and **0F**-A5.0EHA were in globular forms and those with the FA-NHS-immobilized EHA were tubular. The cells reacted with EuTH were in an extremely small form. The differences between the morphologies would be attributed to the cytotoxicity by the FA-NHS immobilization. The cellular luminescence was observed in the case of **5.0**EHA, **0F**-A5.0EHA, **5F**-A5.0EHA, **10F**-A5.0EHA and **100F**-A5.0EHA. In particular, the luminescence positions of **5F**-A5.0EHA, **10F**-A5.0EHA and **100F**-A5.0EHA at the cell surfaces were observed from the outsides, suggesting the binding to the cell surfaces. The FA-NHS-immobilized EHA provided the luminescence following the cellular shapes, suggesting the occurrence of the receptor-mediated binding between the nanoparticles and cells [71]. Therefore, **5F**-A5.0EHA is the most useful nanoparticles for HeLa cell labeling with no cytotoxicity.

Figure 2-21 showed the adhered HeLa cell density changes in the reaction with **5F**-A5.0EHA at the different nanoparticle concentrations with the culture time, and the integrated luminescence intensities of the HeLa cells reacted at the different concentrations. In the results of the cell density plotting vs. incubation time (**Figure 2-21(a)**), no significant difference between the samples was

observed with the incubation time. At the culture time of 72 h, the cell density was 82000 ± 8000 cells/cm^2 in 10 μg/mL, and 81000 ± 8200 cells/cm^2 in 50 μg/mL, and 83000 ± 7500 cells/cm^2 in 100 μg/mL. These results showed that no cytotoxicity behaviors were irrespective of the added nanoparticle concentration at the range between 10–100 μg/mL. **Figure 2-21(b)** showed the plotting of the integrated luminescence intensities of the cells taking in **5F**-A5.0EHA vs. incubation time. As the nanoparticle dispersion concentration increased, the binding amount of the nanoparticles in the cells increased to exhibit the intense luminescence intensity. At the culture time of 24 h, the luminescence intensity suddenly increased, suggesting that the FA molecular receptor on the cell was excessively expressed at the time to resultantly promote the binding between cells–nanoparticles [72]. Therefore, it was suggested that the nanoparticles were successfully bound with the cells with no cytotoxicity and the binding behavior was influenced by the nanoparticle concentration.

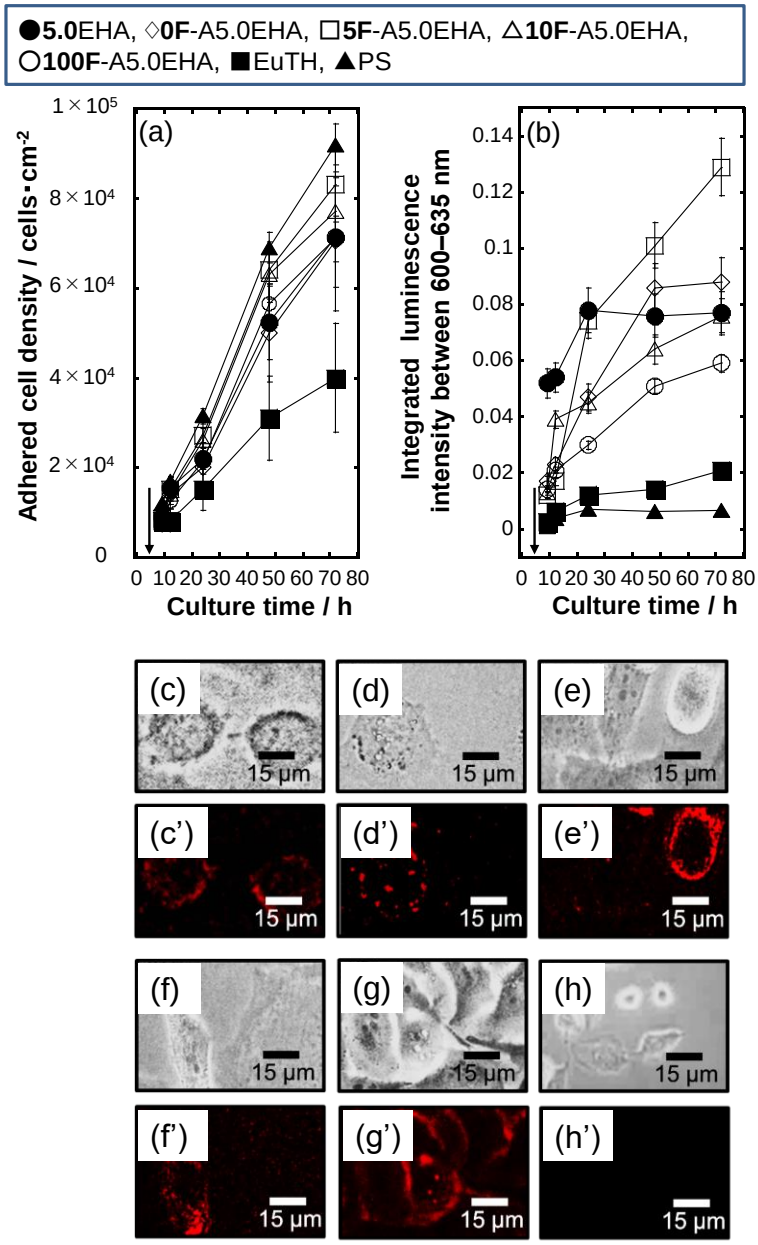

Figure 2-20. (a) Adhered cell density changes in the reaction with **5.0**EHA, **0F**-A5.0EHA, **5F**-A5.0EHA, **10F**-A5.0EHA, **100F**-A5.0EHA and EuTH (particle concentration: 100 μg/mL) with the culture time, and (b) the integrated luminescence intensity changes of the cells, which were excited by the light wavelength at 464 nm and monitored at the wavelengths between 600–635 nm. As the reference, the culture without adding was done on TCPS dish. Arrows in the figures indicate the addition timing of the nanoparticles at the culture time of 6 h. (c–h) Optical transmittance and (c'–h') fluorescence microscope images of the HeLa cells reacted with (c, c') **5.0**EHA, (d, d') **0F**-A5.0EHA, (e, e') **5F**-A5.0EHA, (f, f') **10F**-A5.0EHA, (g, g') **100F**-A5.0EHA and (h, h') EuTH (particle concentration: 100 μg/mL) at the culture time of 72 h.

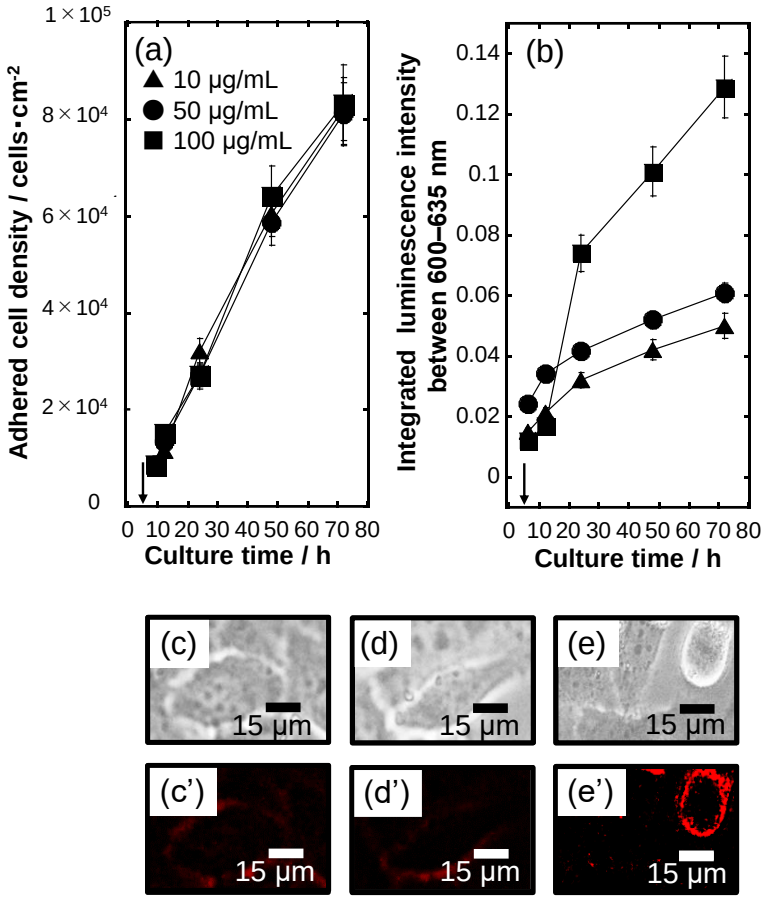

Figure 2-21. (a) Adhered HeLa cell density changes in the reaction with **5F**-A5.0EHA at the different nanoparticle concentrations with the culture time. (b) The integrated luminescence intensities at the wavelengths between 600–635 nm of the HeLa cells reacted with **5F**-A5.0EHA at the different concentrations, which were excited under the wavelengths at 464 nm. Arrows in the figures indicate the addition timing of the nanoparticles at the culture time of 6 h. (c–e) Optical transmittance and (a'–c' and d'–f') fluorescence microscope images of the HeLa cells reacted with **5F**-A5.0EHA at the different nanoparticle concentrations of (c, c') 10 μg/mL, (d, d') 50 μg/mL and (e, e') 100 μg/mL at the culture time of 72 h. (c'–e') FM images were the same positions to (c–e) the transmittance images.

Figure 2-21 (c-e and **c'-e')** showed the optical transmittance and FM images of the HeLa cells reacted with **5F**-A5.0EHA at the different nanoparticle concentrations of 10, 50 and 100 μg/mL at the total culture time of 72 h, which corresponds to the same state at the time of 72 h in **Figure 2-21(a** and **b)**. The enough luminescence for the FM observation was obtained at the culture time of 72 h, suggesting that the binding amount in the cells by the FA receptor overexpressed on the cell membrane was sufficient [73]. From the optical transmittance images, there was no significant difference of the cellular shapes and densities between the samples and many multilayered cells were observed. The cellular shapes were clearly followed by the FM images. In addition, the luminescence light from the cells was enhanced with increasing the nanoparticle dispersion concentration. Thus,

many nanoparticles would be taken into the cells at the concertation of 100 μg/mL to exhibit the efficient luminescent shapes.

Figure 2-22(A) showed the optical transmittance and FM images of the HeLa cells reacted with **5F**-A5.0EHA at the nanoparticle concentration of 100 μg/mL. The cells cultured at the time of 60 h

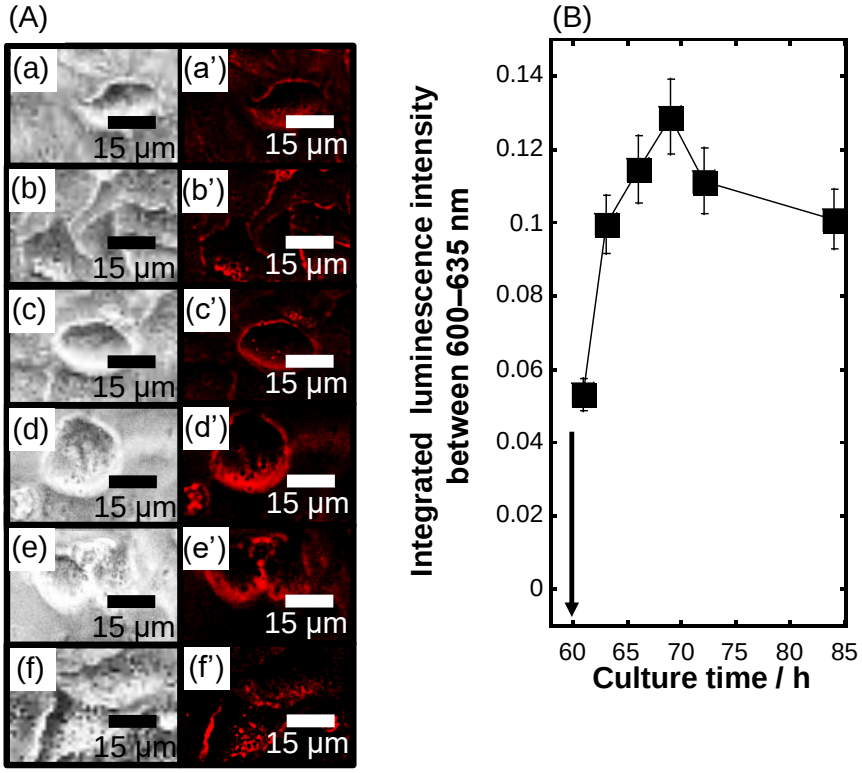

Figure 2-22. (A) Optical transmittance and fluorescence microscope images of the HeLa cells reacted with **5F**-A5.0EHA at the nanoparticle concentration of 100 μg/mL. (a–f) Optical transmittance and (a'–f') fluorescence microscope images. The addition timing was after the culture for 60 h, and the photographs were subsequently cultured at (a, a') 1, (b, b') 3, (c, c') 6, (d, d') 9, (e, e') 12 and (f, f') 24 h. (a'–f') FM images were the same positions as (a–f) the transmittance images. (B) Integrated luminescence intensities at the wavelengths between 600–635 nm of the HeLa cells reacted with **5F**-A5.0EHA, which were excited under the light wavelength at 464 nm. Arrows in the figures indicate the addition timing of the **5F**-A5.0EHA at the culture time of 60 h.

clearly exhibited the multilayered states, which were tumor cells and can be defined as sphere [55]. Accordingly, the addition timing was decided to be after the culture for 60 h, and the photographs were subsequent cultured at 1, 3, 6, 9, 12 and 24 h. At the 1 h after the **5F**-A5.0EHA addition, the cell labeling by following the cellular shapes was successfully achieved. With increasing the culture time, the contrast of the FM image was cleared until the 12 h after the **5F**-A5.0EHA addition. In the previous reports, the luminescence was observed from the tumorigenic cells in mice at the 6 h after the injection of indocyanine green-labeled polysarcosine particles [74]. The HeLa cell shapes have

also been visualized at the 4 h after the addition of the Fe_3O_4-mesoporous silica spheres modified with rhodamine B isothiocyanate [75]. Thus, it can be claimed that **5F**-A5.0EHA synthesized in this study can effectively bind with the HeLa cells to rapidly visualize the shapes.

Figure 2-22(B) exhibited the integrated luminescence intensities at the wavelengths between 600–635 nm from the HeLa cells reacted with **5F**-A5.0EHA (concentration:100 μg/mL), which were excited under the light wavelengths at 464 nm. The enhancement of the luminescence intensities was confirmed until the 12 h after the addition of **5F**-A5.0EHA. Then, the slight decrease in the intensities was observed. As the possible mechanism shown in **Scheme 2-11**, it is suggested that **5F**-A5.0EHA is bound to the cell membrane. when **5F**-A5.0EHA was reacted with the cells after the culture time of 60 h, the luminescence with following the cellular shapes could be observed for the 1 h after the nanoparticle addition. It indicating much faster cell labeling process for the spheres.

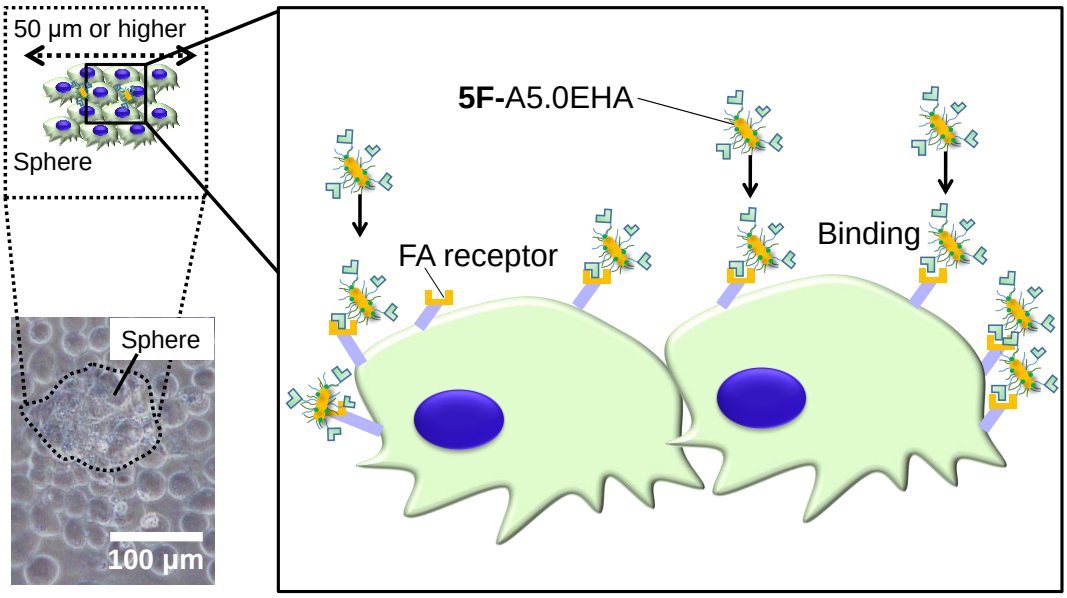

Scheme 2-11. Optical microscope image of the sphere formed by the cell culture at the 66h, and the illustration of the **5F**-A5.0EHA bounded to the FA receptor on sphere.

The importance of the photofunctional inorganic/organic interfacial structues based on the hydroxyapatite/8-hydroxyquinoline particles have already reported [25,26]. However, the interactions between the nanoparticles and the cells for the efficient incorporation of the particulate form and functions did not evaluated. In this study, the photofunctions based on the interfacial interactions between the FA-NHS molecules and EHA nanoparticles for preparing the novel inorganic-organic cell labeling nanomaterials were demonstrated.

Low molecular organic compounds can quickly be taken up by the cells as compared with the case in the particulate form. However, the rapid color degradation rate and short retention period of the compounds inside the cells are problems for cell labeling process. On the other hands, the uptakes of the HA particles with a size of 50–200 nm (concentration: 100 μg/mL) by the osteoblasts were reported, and those with the size of 80 nm were best [24]. The proliferation of the cells containing the particles exhibited the similar behavior to that without the particles. Accordingly, the HA particles as a drug delivery system has been reported [76], and the particulate form containing the other functional substances was important for the biomedical applications. The HA particles modified with the polymer containing fluorescein was reported [77], and the uptakes of the particles (concentration: 30 μg/mL) by mouse connective tissue derived cell lines occurred for the incubation time of 3 h. On the other hand, 2-methacryloyloxyethyl phosphorylcholine and itaconic acid were chemically modified on europium (III)-doped HA particles by an addition-fragmentation chain transfer polymerization method [78], and the uptakes of the particles (concentration: 100 μg/mL) by adenocarcinomic human alveolar basal epithelial cell lines occurred for the incubation time of 3 h. In this study, the visualization of the cancer cells by the FA-NHS-immobilized nanoparticles was achieved for the incubation time of 1 h, suggesting the rapid labeling of the cells.

2.4 Conclusion

The photofunctions based on the interfacial interactions between the FA-NHS molecules and EHA nanoparticles for preparing the novel inorganic/organic cell labeling nanomaterials were investigated. Specifically, the photofunctional interactions between the FA-NHS and EuTH were designed to provide “efficient luminescent ability including high η_{int}” as well as “rapid targeting to the cancer cells” in one particle.

The EHA nanoparticles by forming the HA under the existence of EuTH were synthesized. Then, the FA-NHS molecules as the targeting ligands for the HeLa cancer cells were successfully immobilized on the nanoparticles by the mediation of both APTES and MTES molecules. It was proposed here that the novel photofunctions could be changed by the FA-NHS molecular occupancy on the EHA. When the molecular occupancy ratio to the EHA surface is at around 3–5 %, the intense luminescence from the *f*-*f* transition of the Eu^{3+} ions as well as the charge transfer between the EuTH–FA-NHS was observed to efficiently exhibit the higher η_{int} values. Moreover, the effective dispersibility in PBS was confirmed by immobilizing the positively-charged FA-NHS. Thus, this is the first successful report to synthesize the inorganic/organic nanoparticle systems for controlling the interactions between EHA and FA-NHS.

The cytotoxicity against the NIH3T3 fibrobrasts was evaluated. The affinity and non-cytotoxicity between the nanoparticles and fibrobrasts were confirmed for 3 days. The cytotoxicity against the HeLa cells was also evaluated to verify whether the nanoparticles can be the candidate for rapid cell labeling. The affinity and non-cytotoxicity between the nanoparticles and cells were monitored for 3 days. The red luminescence from the cells could be observed. From the FM images, the label with following the cellular shapes was achieved by the additional culture time of 1 h after injecting the **5F**-A5.0EHA to the spheres, indicating the faster labeling process.

The achievement statuses for initial targets in ***Chapter 1*** were evaluated and achieved by this chapter as below.

I Extreme biosafety for normal cells

- ✓ The N_1/N_0 ratios by all the nanoparticles were more than 0.8.
- ✓ Average particle sizes in PBS were abuut 120 nm (coefficient of variation: 30 % or less)
- ✓ Excitation/luminescence light observation was in the visible region

II Efficient luminescence

- ✓ Strong luminescence intensity that can be visually confirmed
- ✓ Internal quantum efficiency: 11.5 %

III Construction of particle surface that is rapid binding with cancer cells and taken up into the cells at high concentration

- ✓ High concentration into the cell surfaces by the FA-NHS immobilization
- ✓ Short-term labeling of shperes at 1 h

IV Achievement of both cancer cell labeling and suppression of cell growth

Not achieved

In this chapter, the achievements other than IV were cleared. Thus, ***Chapter 3*** will aims to achieve all the targets in I–IV.

References

[1] L. Brannon-peppas, J.O. Blanchette, Nanoparticle and targeted systems for cancer therapy, Adv. Drug Deliv. Rev. 64 (2016) 206–212.

[2] A. Kumari, A. Sharma, U. Malairaman, R.R. Singh, Proficient surface modification of CdSe quantum dots for highly luminescent and biocompatible probes for bioimaging: A comparative experimental investigation, J. Lumin. 199 (2018) 174–182.

[3] L. Wang, W. Li, M. Li, Q. Su, Z. Li, D. Pan, M. Wu, Ultrastable amine, sulfo cofunctionalized graphene quantum dots with high two-photon fluorescence for cellular imaging, ACS Sustain. Chem. Eng. 6 (2018) 4711–4716.

[4] Z. Li, H. Miao, Y. Fu, Y. Liu, R. Zhang, B. Tang, Fabrication of $NaYF_4$:Yb,Er nanoprobes for cell imaging directly by using the method of hydrion rivalry aided by ultrasonic, nanoscale Res. Lett. 11 (2016) 1–10.

[5] A. Escudero, C. Carrillo-Carrión, M. V. Zyuzin, S. Ashraf, R. Hartmann, N.O. Núñez, M. Ocaña, W.J. Parak, Synthesis and functionalization of monodisperse near-ultraviolet and visible excitable multifunctional Eu^{3+}, Bi^{3+}:$REVO_4$ nanophosphors for bioimaging and biosensing applications, Nanoscale. 8 (2016) 12221–12236.

[6] M. Sołtys, J. Pisarska, M. Leśniak, M. Sitarz, W.A. Pisarski, Structural and spectroscopic properties of lead phosphate glasses doubly doped with Tb^{3+} and Eu^{3+} ions, J. Mol. Struct. 1163 (2018) 418–427.

[7] R. Vijayakumar, G. Venkataiah, K. Marimuthu, Structural and luminescence studies on Dy^{3+} doped boro-phosphate glasses for white LED's and laser applications, J. Alloys Compd. 652 (2015) 234–243.

[8] M.R. Rafiuddin, A.P. Grosvenor, Probing the effect of radiation damage on the structure of rare-earth phosphates, J. Alloys Compd. 653 (2015) 279–289.

[9] J. Gómez-Morales, C. Verdugo-Escamilla, R. Fernández-Penas, C.M. Parra-Milla, C. Drouet, F. Maube-Bosc, F. Oltolina, M. Prat, J.F. Fernández-Sánchez, Luminescent biomimetic citrate-coated europium-doped carbonated apatite nanoparticles for use in bioimaging: Physico-chemistry and cytocompatibility, RSC Adv. 8 (2018) 2385–2397.

[10] V.C. Costa, M.J. Lochhead, K.L. Bray, Fluorescence line-narrowing study of Eu^{3+}-doped sol−gel silica: effect of modifying cations on the clustering of Eu^{3+}, Chem. Mater. 8 (1996) 783–790.

[11] M.L.P. George, T. M.; Krishna, M. S.; Reddy, A lysosome targetable luminescent bioprobe based on a europium β-diketonate complex for cellular imaging applications, Dalt. Trans. 45 (2016) 18719–18729.

[12] M.L.P. Divya, V.; Sankar, V.; Raghu, K. G.; Reddy, A mitochondria-specific visible-light sensitized europium β-diketonate complex with red emission, Dalt. Trans. 42 (2013) 12317–12323.

[13] J. Wu, H. Liu, Y. Yang, H. Wang, M. Yang, A β-diketonate-europium(III) complex-based time-gatedluminescence probe for selective visualization of peroxynitrite in living cells, Opt. Mater. 77 (2018) 170–177.

[14] K. Singh, A. Goenka, S. Ganesh, A.K. Patra, Luminescent Eu III and Tb III complexes containing dopamine neurotransmitter : biological interactions, antioxidant activity and cellular-imaging studies, Eur. J. Inorg. Chem. (2018) 3942–3951.

[15] J.H.S.K. Monteiro, D. Machado, L.M. De Hollanda, M. Lancellotti, F.A. Sigoli, Selective cytotoxicity and luminescence imaging of cancer cells with a dipicolinato-based Eu III complex, 5125 (2017) 11818–11821.

[16] J.P. Fabiola Vázquez-Hernández, Salvador Mendoza-Acevedo, Claudia Oliva Mendoza-Barrera Mendoza-Álvarez, Julio Luna-Arias, Antibody-coupled hydroxyapatite nanoparticles as efficient tools for labeling intracellular proteins, Mater. Sci. Eng. C. 71 (2017) 909–918.

[17] X. Xiao, R. Liu, Q. Huang, Preparation and characterization of nano-hydroxyapatite/polymer composite scaffolds, J. Mater. Sci. Mater. Med. 19 (2008) 3429–3435.

[18] H.-W.J. Jeremy B. Vines, Dong-Jin Lim, Joel M. Anderson, Hydroxyapatite nanoparticle reinforced peptide amphiphile nanomatrix enhances the osteogenic differentiation of mesenchymal stem cells by compositional ratios, Acta Biomater. 8 (2012) 4053–4063.

[19] K. Shiba, S. Motozuka, T. Yamaguchi, N. Ogawa, Y. Otsuka, K. Ohnuma, T. Kataoka, M. Tagaya, Effect of cationic surfactant micelles on hydroxyapatite nanocrystal formation: An investigation into the inorganic-organic interfacial interactions, Cryst. Growth Des. 16 (2016) 1463–1471.

[20] A. Tesch, C. Wenisch, K.H. Herrmann, J.R. Reichenbach, P. Warncke, D. Fischer, F.A. Müller, Luminomagnetic Eu^{3+}- and Dy^{3+}-doped hydroxyapatite for multimodal imaging, Mater. Sci. Eng. C. 81 (2017) 422–431.

[21] A. Prichodko, F. Enrichi, Z. Stankeviciute, A. Benedetti, I. Grigoraviciute-Puroniene, A. Kareiva, Study of Eu^{3+} and Tm^{3+} substitution effects in sol–gel fabricated calcium hydroxyapatite, J. Sol-Gel Sci. Technol. 81 (2017) 261–267.

[22] Z. Liu, Q. Wang, S. Yao, L. Yang, S. Yu, X. Feng, F. Li, Synthesis and characterization of Tb^{3+}/Gd^{3+} dual-doped multifunctional hydroxyapatite nanoparticles, Ceram. Int. 40 (2014) 2613–2617.

[23] T. Honma, K. Toda, Z.-G. Ye, M. Sato, Concentration quenching of the Eu^{3+}-activated luminescence in some layered perovskites with two-dimensional arrangement, J. Phys. Chem. Solids. 59 (1998) 1187–1193.

[24] K. Deshmukh, M.M. Shaik, S.R. Ramanan, M. Kowshik, Self-activated fluorescent hydroxyapatite nanoparticles: A promising agent for bioimaging and biolabeling, ACS Biomater. Sci. Eng. 2 (2016) 1257–1264.

[25] Y. Matsuya, T.; Otsuka, Y.; Tagaya, M.; Motozuka, S.; Ohnuma, K.; Mutoh, Formation of stacked luminescent complex of 8-hydroxyquinoline molecules on hydroxyapatite coating by using cold isostatic pressing, Mater. Sci. Eng. C. 58 (2016) 127–132.

[26] S. Motozuka, M. Tagaya, An investigation into photofunctional interfaces of 8-hydroxyquinoline/hydroxyapatite hybrids, Opt. Mater. 66 (2017) 392–398.

[27] G.D. Venkatasubbu, S. Ramasamy, G.S. Avadhani, V. Ramakrishnan, J. Kumar, Surface modification and paclitaxel drug delivery of folic acid modified polyethylene glycol functionalized hydroxyapatite nanoparticles, Powder Technol. 235 (2013) 437–442.

[28] S.S. Syamchand, G. Sony, Fluorescein-labeled fluoroapatite nanocrystals codoped with Yb (III) and Ho (III) for trimodal (downconversion , upconversion and magnetic resonance) imaging of cancer cells, Microchim. Acta. 10 (2016) 3209–3219.

[29] S. Rehman, K. Khan, M. Mujahid, S. Nosheen, Synthesis of nano-hydroxyapatite and its rapid mediated surface functionalization by silane coupling agent, Mater. Sci. Eng. C. 58 (2016) 675–681.

[30] Y. Pan, F. Liu, D. Xu, X. Jiang, H. Yu, M. Zhu, Novel acrylic resin denture base with enhanced mechanical properties by the incorporation of PMMA-modified hydroxyapatite, Prog. Nat. Sci. Mater. Int. 23 (2013) 89–93.

[31] W. Sun, J. Fan, S. Wang, Y. Kang, J. Du, X. Peng, Biodegradable Drug-loaded hydroxyapatite nanotherapeutic agent for targeted drug release in tumors, ACS Appl. Mater. Interfaces. 10 (2018) 7832–7840.

[32] J.J. Turek, C.P. Leamon, P.S. Low, Endocytosis of folate-protein conjugates: ultrastructural localization in KB cells., J. Cell Sci. 106 (1993) 423–430.

[33] P. Martin, Acidic dissociation constants of folic acid, dihydrofolic acid, and methotrexate, J. J. Biological. Chem. 252 (1977) 3724–3728.

[34] A. Tyagi, A. Penzkofer, Fluorescence spectroscopic behaviour of folic acid, Chem. Phys. 367 (2010) 83–92.

[35] R. Weissleder, C.-H. Tung, U. Mahmood, A. Bogdanov, In vivo imaging of tumors with protease-activated near-infrared fluorescent probes, Nat. Biotechnol. 17 (1999) 375–378.

[36] Q. Wang, S.M. Cahill, M. Blumenstein, D.S. Lawrence, Self-reporting fluorescent substrates of protein tyrosine kinases, J. Am. Chem. Soc. 128 (2006) 1808–1809.

[37] S. Brunauer, P.H. Emmett, E. Teller, Adsorption of gases in multimolecular layers, J. Am. Chem. Soc. 60 (1938) 309–319.

[38] D. Kozak, W. Anderson, R. Vogel, S. Chen, F. Antaw, M. Trau, Simultaneous size and ζ-potential measurements of individual nanoparticles in dispersion using size-tunable pore sensors, ACS Nano. 6 (2012) 6990–6997.

[39] E.L.C.J. Blundell, R. Vogel, M. Platt, Particle-by-particle charge analysis of DNA-modified nanoparticles using tunable resistive pulse sensing, Langmuir. 32 (2016) 1082–1090.

[40] M. Kikuchi, S. Itoh, S. Ichinose, K. Shinomiya, J. Tanaka, Self-organization mechanism in a bone-like hydroxyapatite/collagen nanocomposite synthesized in vitro and its biological reaction in vivo, Biomaterials. 22 (2001) 1705–1711.

[41] K. Sato, Y. Kumagai, J. Tanaka, Apatite formation on organic monolayers in simulated body environment, J. Biomed. Mater. Res. 50 (2000) 16–20.

[42] S.Koutsopoulos, Synthesis and characterization of hydroxyapatite crystals: A review study on the analytical methods, J. Biomed. Mater. Res. 62 (2002) 600–612.

[43] A. Grunenwald, C. Keyser, A.M. Sautereau, E. Crubézy, B. Ludes, C. Drouet, Revisiting carbonate quantification in apatite (bio)minerals: A validated FTIR methodology, J. Archaeol. Sci. 49 (2014) 134–141.

[44] A. Mitsionis, T. Vaimakis, C. Trapalis, N. Todorova, D. Bahnemann, R. Dillert, Hydroxyapatite/titanium dioxide nanocomposites for controlled photocatalytic NO oxidation, Appl. Catal. B Environ. 106 (2011) 398–404.

[45] J. Wang, H. Song, X. Kong, H. Peng, B. Sun, B. Chen, J. Zhang, W. Xu, H. Xia, Fluorescence properties of trivalent europium doped in various niobate codoped glasses, J. Appl. Phys. 93 (2003) 1482–1486.

[46] R. Fields, Estimation of Amino Groups Using TNBS, Methods Enzymol. 25 (1972) 464–469.

[47] R.C. Ropp, M.A. Aia, Thermal analysis of phosphor raw materials, Anal. Chem. 34 (1962) 1288–1291.

[48] T. Fukuda, S. Fujii, Y. Nakamura, M. Sasaki, Mechanical properties of silica particle-filled styrene-butadiene rubber composites containing polysulfide-type silane coupling agents: Influence of loading method of silane, J. Appl. Polym. Sci. 130 (2013) 322–329.

[49] G.R. Willmott, R. Vogel, S.S.C. Yu, L.G. Groenewegen, G.S. Roberts, D. Kozak, W. Anderson, M. Trau, Use of tunable nanopore blockade rates to investigate colloidal dispersions, J. Phys. Condens. Matter. 22 (2010) 1–19.

[50] W. Anderson, D. Kozak, V.A. Coleman, Å.K. Jämting, M. Trau, A comparative study of submicron particle sizing platforms : Accuracy , precision and resolution analysis of polydisperse particle size distributions, J. Colloid Interface Sci. 405 (2013) 322–330.

[51] J.C. Maxwell, Summary for Policymakers, A Treatise Electr. Magn. 53 (1954) 1–30.

[52] L. Rayleigh, LVI. On the influence of obstacles arranged in rectangular order upon the properties of a medium, Philos. Mag. Ser. 5. 34 (1892) 481–502.

[53] R. Vogel, G. Willmott, D. Kozak, G.S. Roberts, W. Anderson, L. Groenewegen, B. Glossop, A. Barnett, A. Turner, M. Trau, Quantitative sizing of nano/microparticles with a tunable elastomeric pore sensor, Anal. Chem. 83 (2011) 3499–3506.

[54] C.P. Montgomery, B.S. Murray, E.J. New, R. Pal, D. Parker, Cell-penetrating metal complex optical Probes: Targeted and responsive systems based on lanthanide luminescence, Acc. Chem. Res. 42 (2009) 925–937.

[55] S. Yokoo, S. Yamagami, Y. Yanagi, S. Uchida, T. Mimura, T. Usui, S. Amano, Human corneal endothelial cell precursors isolated by sphere-forming assay, Investig. Opthalmology Vis. Sci. 46 (2005) 1626–1631.

[56] H. Luo, W. Li, D. Ji, G. Zuo, G. Xiong, Y. Zhu, L. Li, M. Han, C. Wu, Y. Wan, One-step exfoliation and surface modification of lamellar hydroxyapatite by intercalation of glucosamine, Mater. Chem. Phys. 173 (2016) 262–267.

[57] R. Machín, J.R. Isasi, I. Vélaz, Hydrogel matrices containing single and mixed natural cyclodextrins. Mechanisms of drug release, Eur. Polym. J. 49 (2013) 3912–3920.

[58] H. Aoki, Medical applications of hydroxyapatite, Ishiyaku Euro Am. (1994) 210.

[59] A.S. Borges, F. Fulgêncio, J.G. Da Silva, T.A. Ribeiro-Santos, R. Diniz, D. Windmöller, W.F. Magalhães, M.H. Araujo, Luminescence and positron spectroscopies studies of tris(2,2,6,6-tetramethyl-3,5-heptanedionate) europium(III) and terbium(III) complexes containing 2-pyrrolidone as coligand, J. Lumin. 205 (2019) 72–81.

[60] T. V. Safronova, V.I. Putlyaev, O.A. Avramenko, M.A. Shekhirev, A.G. Veresov, Ca-deficient hydroxyapatite powder for producing tricalcium phosphate based ceramics, Glas. Ceram. 68 (2011) 28–32.

[61] A. López-Macipe, J. Gómez-Morales, R. Rodríguez-Clemente, Nanosized hydroxyapatite precipitation from homogeneous calcium/citrate/phosphate solutions using microwave and conventional heating, Adv. Mater. 10 (1998) 49–53.

[62] M. Long, F. Hong, W. Li, F. Li, H. Zhao, Y. Lv, H. Li, F. Hu, L. Sun, C. Yan, Z. Wei, Size-dependent microstructure and europium site preference influence fluorescent properties of Eu^{3+}-doped $Ca_{10}(PO_4)_6(OH)_2$ nanocrystal, J. Lumin. 128 (2008) 428–436.

[63] S. Tanabe, T. Ohyagi, S. Todoroki, T. Hanada, N. Soga, Relation between the Ω6 intensity parameter of Er^{3+} ions and the 151Eu isomer shift in oxide glasses, J. Appl. Phys. 73 (1993) 8451–8454.

[64] M.T. Berry, P.S. May, H. Xu, Temperature dependence of the Eu^{3+} $^5D_0$ lifetime in europium tris(2,2,6,6-tetramethyl-3,5-heptanedionato), J. Phys. Chem. 100 (1996) 9216–9222.

[65] K. Jha, M. Jayasimhadri, Structural and emission properties of Eu^{3+}-doped alkaline earth zinc-phosphate glasses for white LED applications, J. Am. Ceram. Soc. 100 (2017) 1402–1411.

[66] Y. Seino, H. Sasabe, Y.J. Pu, J. Kido, High-performance blue phosphorescent OLEDs using energy transfer from exciplex, Adv. Mater. 26 (2014) 1612–1616.

[67] M.S. Walker, T.W. Bednar, R. Lumry, Exciplex studies. II. indole and indole derivatives, J. Chem. Phys. 47 (1967) 1020–1028.

[68] K. Binnemans, Interpretation of europium(III) spectra, Coord. Chem. Rev. 295 (2015) 1–45.

[69] J. Keizer, Nonlinear fluorescence quenching and the origin of positive curvature in Stern-Volmer plots, J. Am. Chem. Soc. 105 (1983) 1494–1498.

[70] R.M. Supkowski, W.D.W. Horrocks, On the determination of the number of water molecules, q, coordinated to europium(III) ions in solution from luminescence decay lifetimes, Inorganica Chim. Acta. 340 (2002) 44–48.

[71] M. Fenech, The role of folic acid and Vitamin B12 in genomic stability of human cells, Mutat. Res. 475 (2001) 57–67.

[72] R.I. Pinhassi, Y.G. Assaraf, S. Farber, M. Stark, D. Ickowicz, S. Drori, A.J. Domb, Y.D. Livney, Arabinogalactan - folic acid - drug conjugate for targeted delivery and target-activated release of anticancer drugs to folate receptor-overexpressing cells, Biomolecules. 11 (2010) 294–303.

[73] D. Feng, Y. Song, W. Shi, X. Li, H. Ma, Distinguishing folate-receptor-positive cells from folate-receptor-negative cells using a fluorescence off-on nanoprobe, Anal. Chem. 85 (2013) 6530–6535.

[74] K. Sano, M. Ohashi, K. Kanazaki, A. Makino, N. Ding, J. Deguchi, Y. Kanada, M. Ono, H. Saji, Indocyanine green-labeled polysarcosine for in vivo photoacoustic tumor imaging, bioconjug. Chem. 28 (2017) 1024–1030.

[75] Y. Zhu, T. Ikoma, N. Hanagata, S. Kaskel, Rattle-type Fe_3O_4@SiO_2 hollow mesoporous spheres as carriers for drug delivery, Small. 6 (2010) 471–478.

[76] D. Placente, L.A. Benedini, M. Baldini, J.A. Laiuppa, Multi-drug delivery system based on lipid membrane mimetic coated nano- hydroxyapatite formulations, Int. J. Pharm. 548 (2018) 559–570.

[77] J. Chen, M. Liu, Q. Huang, R. Jiang, H. Huang, F. Deng, A novel strategy for fabrication of fl uorescent hydroxyapatite based polymer composites through the combination of surface ligand exchange and self- catalyzed ATRP, Mater. Sci. Eng. C. 92 (2018) 518–525.

[78] C. Heng, X. Zhou, X. Zheng, M. Liu, Y. Wen, H. Huang, Surface grafting of rare-earth ions doped hydroxyapatite nanorods (HAp : Ln (Eu/Tb)) with hydrophilic copolymers based on ligand exchange reaction : Biological imaging and cancer treatment, Mater. Sci. Eng. C. 91 (2018) 556–563.

Chapter 3

Synthesis of Luminescent Hydroxyapatite Nanoparticles Coordinated with Citric Acid for Their Bifunctional Cell Labeling and Cytostatic Properties

Chapter 3

Synthesis of Luminescent Hydroxyapatite Nanoparticles Coordinated with Citric Acid for Their Bifunctional Cell Labeling and Cytostatic Properties

3.1 Introduction

Luminescent nanoparticles have been attracted as good candidates for use in the biomedical labeling nanomaterials with the detection of the light emission, which provides enough fluorescence contrast for visualizing specific cells [1]. The physicochemical properties of the nanoparticles can be easily changed by the surface functional groups to achieve the efficient nanoparticle uptakes by the living cells so that the practical applications as one nanoparticle having the biomedical multi-functions of both labeling and drug delivery carrier [2]. Since it is possible to impart the other functions for achieving the multi-functional particles, it is important to design as nanoparticle shapes. As the luminescent inorganic nanoparticles for the cell labeling, semiconductor quantum dots (QDs) [3–5], dye-doped mesoporous silica nanoparticles [6,7] and fluorescent nanodiamonds [8,9] have been proposed so far. The semiconductor QDs (e.g., CdS semiconductor QDs [3]) exhibit the high luminescence intensity among the inorganic nanoparticles, and the excited electrons in the conduction band recombine with the holes to provide the highly efficient emission. However, the inclusion of biotoxic elements in the nanoparticles is a problem for the safety of the cells. The dye-doped mesoporous silica nanoparticles can provide the luminescence by the charge transfer between the molecules, where the mesoporous silica act as the host matrix for the stable luminescence [6].

However, there are problems of the luminescence decrease due to the dye degradation and the lower luminescent efficiency due to the dye−silanol interactions. The fluorescent nanodiamonds used as the specifically-targeted probes for labeling the transferrins through their receptors, which were over-expressed on cancer cells, have been studied [8]. The nitrogen-vacancy centers, which were generated with high-energy electron or ion bombardment for the nitrogen-rich type Ib nanodiamonds, result in bright fluorescence. However, the luminescence was obtained by high-energy laser irradiation (e.g., Ar-ion laser, 20 μW, excitation wavelength at 514 nm) [8]. Therefore, it is necessary to synthesize the luminescent nanoparticles for solving the above problems and to impart a therapeutic ability to the labeling [10].

The lanthanide (Ln: Tb, Eu, etc.) ion-doped hydroxyapatite (HA: $Ca_{10}(PO_4)_6(OH)_2$), exhibits a long fluorescence lifetime and sharp luminescence peak shape, has been studied [11,12]. There are two types of calcium (Ca) sites in the HA crystalline structure, which can be substituted with the Ln ions [11–14]. In particular, four columnar Ca (i.e., Ca (I) site) is aligned with the parallel to the *c* axis, and six screw axis Ca (i.e., Ca (II) site) surrounding the *c* axis [15]. The Ln ion alone has insufficient light absorption capability due to the forbidden intra-configuration *f-f* transitions, and the spectral shape depends on the structure of the electronic environment [14,16]. As the host, the HA provides a flexible crystal lattice for substituting with the dopant ions [13], which provides detectable and stable luminescence in the matrix. The basic study on the HA nanoparticles doped with lower cytotoxic europium (III) (Eu^{3+}) ions (Eu:HA) has been reported [12,14]. Eu:HA is easy to be synthesized and provide the stable red luminescence. As compared to the conventional luminescent nanoparticles, the Eu^{3+} ion in HA nanoparticles provides excellent features for cell labeling applications. However, the doping amount of the Eu^{3+} ion is limited because of the luminescence quenching due to the energy transfer between the adjacent ions [17]. Therefore, it is thought that the main trials for Eu:HA nanoparticles are to improve the luminescence internal efficiency (η_{int}), luminescence intensity and labeling ability of the cells.

The hybrids of the HA with organic polymeric molecules have been synthesized in the utilization of artificial bones based on inorganic/organic interactive functions [18,19]. In our group, the HA bound to a photofunctional low molecular weight compound of 8-hydroxyquinoline (8Hq) was reported as the luminescent nanoparticle applications [20–22]. In particular, the 8Hq molecules were chemically bonded to the Ca^{2+} ions on the HA by applying mechanical forces. The photofunction of the hybrids was investigated by evaluating the light absorption and luminescence with the metal-ligand charge transfer complex formation. Fluorescent HA-amino acid hybrids were synthesized to reveal the effect of pressure during cold isostatic pressing on the microstructures and luminescent properties [23], suggesting that the pressure increased the luminescence intensity of the hybrids. In

Chapter 2, the Eu^{3+} complex-interacted HA (EHA) was studied for the synthesis of luminescent nanoparticles. As a result, the nucleation and particle growth of HA on the electronic localization on the Eu^{3+} complex molecule occurred. The EHA nanoparticles exhibited the luminescence based on the inorganic/organic photofunctional interfaces between ligand of EuTH and HA, indicating the possibility of the improvement of the photofunction of Eu^{3+} ions in the HA by the organic molecular interactions. Moreover, folate N-hydroxysuccinimidyl ester (FA-NHS) was immobilized on the EHA nanoparticles. As a result, the charge transfer between the EHA nanoparticles and FA-NHS was successfully achieved, leading to the photofunctional inorganic/organic interfaces between EHA and FA-NHS. Therefore, it is proposed in the present paper that the construction of the interface state of the Eu^{3+} ions on the HA surfaces with organic molecule can improve the η_{int} and luminescence intensity, and the labeling ability of the cells.

The citric acid (Cit) is known to form chelates with the metal ions in an aqueous solution [24–27]. For example, the Cit can form the chelate with Ca^{2+} ion based on the binding affinity between Cit and Ca^{2+} ion at about 2.0×10^4 M^{-1} [27]. Cit molecule forms the chelate with Ca^{2+} ion or iron (II) (Fe^{2+}) ion in the increase in the Cit amount at the acidic biological fluid inside the cancer cells and inhibits the action of proteins (e.g., iron-binding protein 1) involved in the cancer cell growth and antioxidant enzymes [28], resulting in the suppression of the cancer cell growth to finally induce the cell death. In particular, the chelate complex with Cit was formed with the Fe^{2+} ion to resultantly deplete Fe^{2+} ion states in the cytoplasm and inhibit the growth of the cells [29]. In normal cells (e.g., prostatic epithelium cells) [30], it is known to be no effect of the addition of Cit on the cellular activity. The interactions between the Cit and Ca ions in HA (e.g., Eu^{3+} ions doped in HA) can be caused by the chemical bonding. Accordingly, the Eu^{3+} ion doped into the Ca sites in the HA can form the inorganic/organic interfacial interactions between Cit and Eu:HA, leading to the biomedical nanoparticles containing the luminescent photofunction as well as the suppression of the cancer cell growth. It proposed that the bifunctional properties of the labeling of the cancer cell as well as the suppression of the cell growth could simultaneously be achieved by designing the nanoparticle structures. Therefore, it is important to elucidate the interactions between Cit and Eu:HA, and it is suggested that the control of the spatial arrangement of the Eu^{3+} ions in Eu:HA would change the coordination environment of oxygen around the Eu^{3+} ions to resultantly enhance the luminescence efficiency. When the Eu^{3+} complex is interacted with the HA surfaces, there is a limit to the asymmetry around the Eu^{3+} ions. It was suggested that the coordination of the Cit molecule with respect to the Eu^{3+} ion on the Eu:HA surfaces would lead to the construction of an effective asymmetric environment that achieves strong luminescence properties.

In this study, it aimed to achieve the efficient luminescence ability including the η_{int} based on the photofunctional interfaces between the Cit and Eu:HA in the nanoparticles, and investigate the Cit effect on the suppression of the HeLa (Human Cervical Carcinoma) cell line growth. In particular, the Eu:HA nanoparticles were synthesized in the presence of the Cit, and the Cit molecules would be coordinated with the Eu:HA (Cit/Eu:HA) nanoparticles and the physicochemical properties based on the inorganic (Eu:HA)/organic (Cit) interfacial interactions in the nanoparticles were elucidated. The FA-NHS was immobilized on the Cit/Eu:HA nanoparticles to resultantly enhance the uptake efficiency of the nanoparticles into the HeLa cells, and the cytocompatibility using HeLa cells and NIH3T3 fibroblasts and their cell labeling properties were evaluated to investigate the effect of the nanoparticles on the suppression of the HeLa cell growth by the Cit molecules (**Scheme 3-1**).

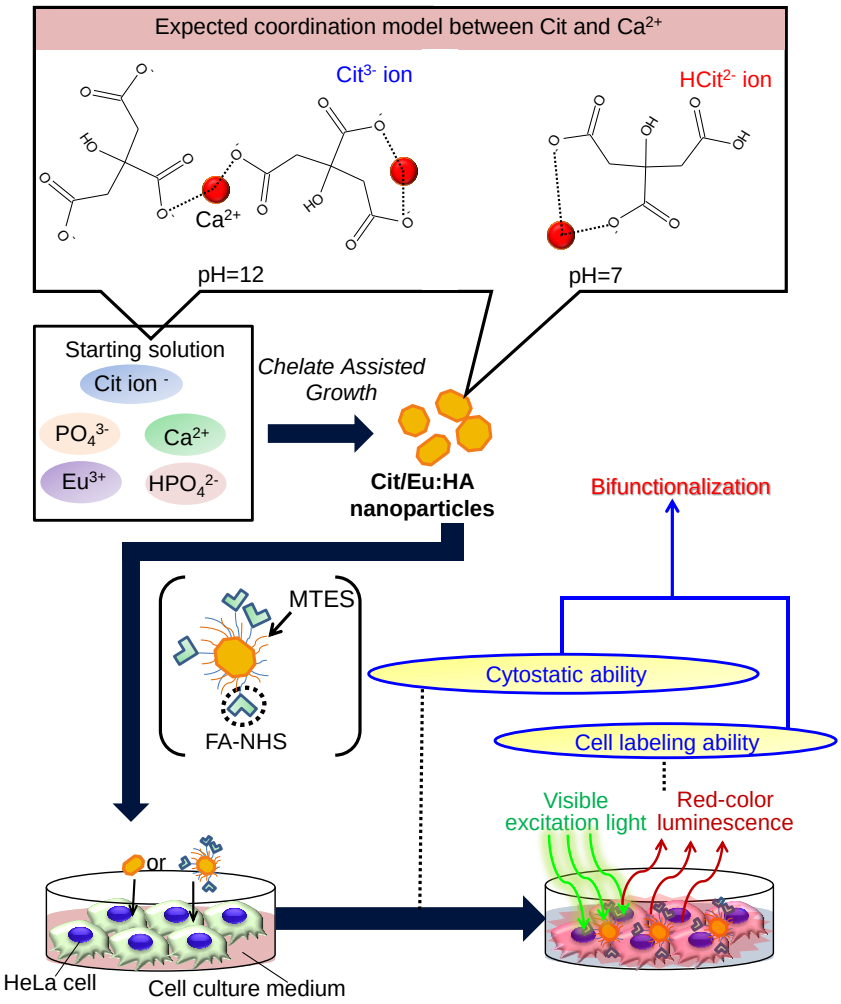

Scheme 3-1. Illustration of the preparation of the Cit/Eu:HA nanoparticles and their cytostatic suppuration and cell labeling ability based on the inorganic/organic coordinated functions. At pH = 12, citric acid exists in water in the dissociated state of Cit^{3-}, and at pH = 7, it exists in the dissociated state of Cit^{3-} and $HCit^{2-}$. At pH = 7, 60 % of Cit^{3-} and 40 % of $HCit^{2-}$ are exists in water, respectively.

3.2 Experimental Section

3.2.1 Chemicals

Citric acid (Cit), dipotassium hydrogen phosphate (K_2HPO_4), tetramethylammonium hydroxide (TMAOH), calcium chloride dehydrate ($CaCl_2 \cdot 2H_2O$), ethanol, dimethyl sulfoxide (DMSO), phosphate buffer (PB: pH = 7, phosphate ion concentration = 0.1 M), hydrochloric acid (HCl: 1 N) and trypsin (0.05 w/v%)-ethylenediaminetetraacetate (0.053 M) (trypsin-EDTA) were purchased from Wako Chemical Co. Ltd. Europium (III) chloride hexahydrate ($EuCl_3 \cdot 6H_2O$), 3-aminopropyltriethoxysilane (APTES: $H_2N(CH_2)_3Si(OC_2H_5)_3$) and methyltriethoxysilane (MTES: $CH_3Si(OC_2H_5)_3$) were purchased from Tokyo Chemical Industry Co., Ltd. FA-NHS was purchased from Fuji Molecular Planning Co., Ltd. Phosphate buffered saline (PBS: pH = 7) with the ions (K^+: 4.15 mM, Na^+: 153 mM, HPO_4^{2-}: 9.57 mM, Cl^-: 139.57 mM) was purchased from DS pharma biomedical Co., Ltd. Fetal bovine serum (FBS) were purchased from Sigma-Aldrich Co. Ltd (catalog number: 172012). Dulbecco's minimum essential medium (DMEM) was purchased from Thermo Fisher Scientific Inc. Penicillin-Streptomycin was purchased from Life Technologies Co., Ltd. Human cervical carcinoma HeLa cells (RCB0007) and fibroblast NIH3T3 cells (RCB1862) were provided by the Riken BioResource Center. All the chemicals were used as received without further purification. A plastic cell culture flask with the area of 75 cm^2 (BD Bioscience, USA.) and tissue culture poly(styrene) dish (TCPS: BD Falcon™ Co., Ltd.) were used for the cell culture. Cit quantification kit (R-Biopharm AG, Enzytec^{TM} Citric Acid) was also purchased and used for the Cit concentration measurement in the Cit/Eu:HA nanoparticles. Carboxylated polystyrene standard particles (Izon Science, Co., Ltd., CPC100) having the average diameter of ca. 126 nm with the coefficient of variation value of 13 % were purchased for particle distribution measurement.

3.2.2 Materials and preparation

50 mL of ultrapure water containing 6 mmol of K_2HPO_4 and Cit (0, 12, 20, 24 and 36 mmol) were vigorously stirred and the pH was adjusted to be 12 by adding TMAOH. 30 mL of an aqueous solution containing 19.5 mmol of $CaCl_2 \cdot 2H_2O$ and 0.5 mmol of $EuCl_3 \cdot 6H_2O$ was added to the K_2HPO_4/Cit aqueous solution at the dropping rate of 1 mL/min. Then, the precursor solution was refluxed at 40 °C for 3 h. **Scheme 3-2(a)** shows dissociated state in solution at the different pH (pK_{a1}= 3.12, pK_{a2}= 4.76, pK_{a3} = 6.39). The precipitation products were washed once with ethanol and ultrapure water, and dried at 100 °C for 1 day. Here, the feed Eu concentration of Eu to (Ca+Eu) was 2.5 mol% and fixed in this study, and the sample was abbreviated as Cit/Eu:HA. It has been confirmed that when the feed Eu concentration of Eu to (Ca+Eu) was 2.5 mol%, good luminescence properties

were exhibited [48]. The molar ratio of Ca to P was fixed at 1.67. Here, the sample name was called as ***X***Cit/Eu:HA (***X*** = the resultant amount of Cit as shown in **Table 3-1** described in 3.3.1). In particular, the resultant amounts of Cit were 0, 0.99, 1.06, 1.13 and 1.24 mmol/(g of HA) and the samples were named as **0**, **1**, **2**, **3** and **4**Cit/Eu:HA, respectively (**Table 3-1**). As a reference sample, the compounds were prepared without K_2HPO_4 by the same method mentioned above. The sample was named as Cit/EuCa. 50 mL of ultrapure water containing 20 mmol of Cit (pH= 12) and 30 mL of an aqueous solution containing 19.5 mmol of $CaCl_2 \cdot 2H_2O$ and 0.5 mmol of $EuCl_3 \cdot 6H_2O$ were used for Cit/EuCa.

For the cell culture experiment, APTES and MTES were immobilized on **4**Cit/Eu:HA according to ***Chapter 2***. **4**Cit/Eu:HA (200 mg) was dispersed in 20 mL of ethanol and the pH was adjusted to be 12 by adding TMAOH. APTES (0.0225 mmol) and MTES (0.0225 mmol) were added to the **4**Cit/Eu:HA-dispersed solution and stirred at 40 °C for 1 h. The solid product was washed with ethanol and dried at 65 °C for 1 day to obtain the APTES-MTES-modified **4**Cit/Eu:HA. The occupation molecular area of APTES or MTES ratio was assumed to be $0.45 \times 0.45 \times \pi$ nm^2 as the spherical shape, and the theoretical occupancy with the modification on the **4**Cit/Eu:HA based on the Brunauer-Emmett-Teller (BET) [31] surface area (77 ± 8 m^2/g) of the **4**Cit/Eu:HA was determined to be 125 %, when all the feed molecules are immobilized on the **4**Cit/Eu:HA. Just for the reference, the BET surface area of the **0**Cit/Eu:HA was 100 ± 11 m^2/g.

FA-NHS was immobilized on the APTES-MTES-modified **4**Cit/Eu:HA according to ***Chapter 2***. APTES-MTES-modified **4**Cit/Eu:HA (140 mg) was mechanically dispersed into the mixture solution of 12 mL of DMSO and 25 mL of PB containing 486 nmol of FA-NHS, and the solution was stirred at 40 °C for 3 h. The solid products were washed with ethanol and lyophilized and the sample name is called as **FA4**Cit/Eu:HA. The occupation molecular area of FA-NHS was assumed to be 1.1×1.5 nm^2 as the rectangle shape, and the theoretical occupancy of the immobilized FA-NHS on the APTES-MTES- modified **4**Cit/Eu:HA was determined to be 5 % when all the feed molecules of FA-NHS is immobilized on APTES-MTES-modified **4**Cit/Eu:HA.

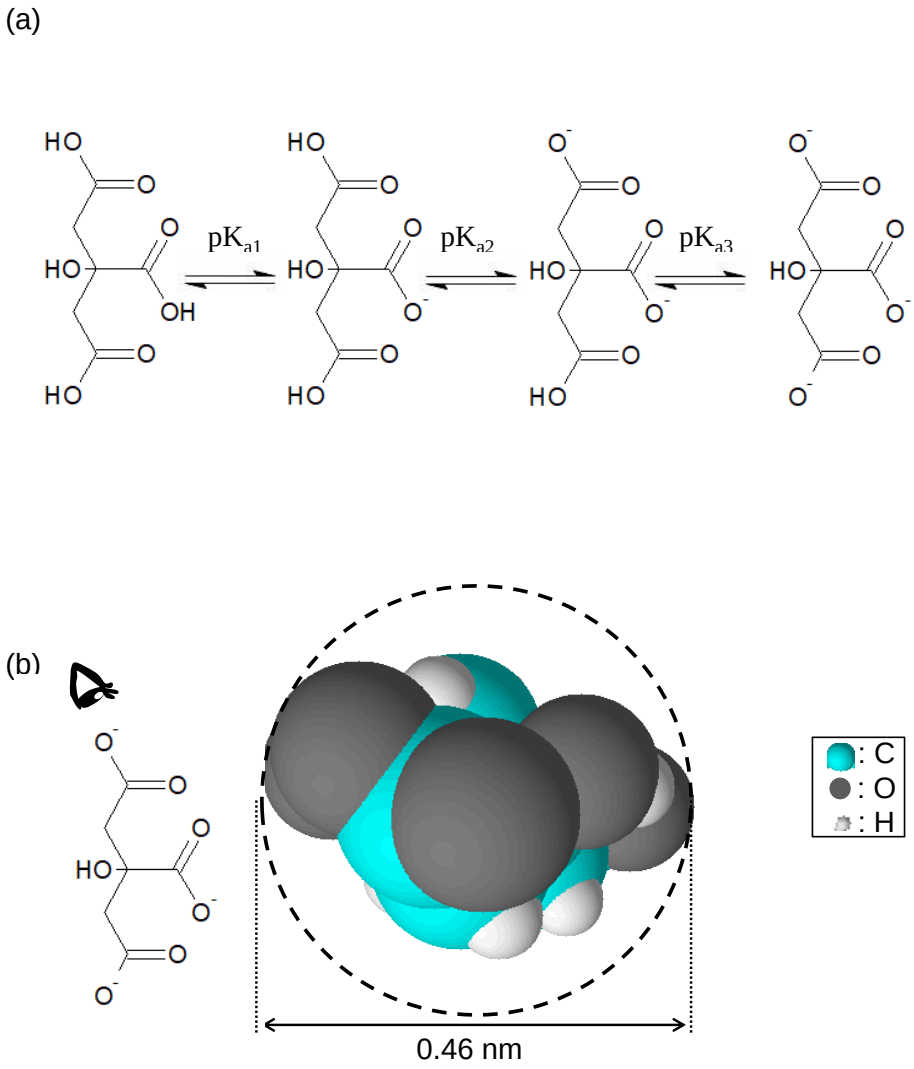

Scheme 3-2. (a) Dissociated state in solution at the different pH (pK$_{a1}$= 3.12, pK$_{a2}$= 4.76, pK$_{a3}$ = 6.39) and (b) chemical structures of Cit molecule at the 3-dimensional view. The illustration on the left of the 3-dimensional view of Cit molecule shows the line of sight in the 2-dimensional view corresponding to the 3-dimensional view.

3.2.3 Characterization

3.2.3.1 Characterization of europium(III) ion-doped hydroxyapatite nanoparticles coordinated with citric acid

The coordinated amount of Cit with HA was obtained by dissolving Cit/Eu:HA in 10 mL of HCl aqueous solution (pH = 2) to prepare the calibration curve for the quantitative analysis. 10 mg of Cit/Eu:HA was added to 10 mL of HCl aqueous solution (pH = 2) to be completely dissolved. The HCl aqueous solution was placed in the reference cell for the UV-Visible spectral spectrophotometer (V-750, JASCO Co., Ltd.) measurement, and the absorption maxima were observed at the wavelength of 210 nm, which was attributed to the absorption of carboxy group in Cit. The calibration curve was shown in **Figure 3-1** and the correlation coefficient was 0.99949. The occupation molecular area of Cit was assumed to be $0.23 \times 0.23 \times \pi$ nm^2 as the spherical shape **(Scheme 3-2(b))**, and was calculated the concentration at which the theoretical occupancy of Cit on Eu:HA is 100 %. The resultant contained amounts of Cit on Eu:HA were measured, and the resultant molecular occupancy areas of Cit on Eu:HA were calculated assuming monolayer-state adsorption from the above the theoretical occupancy of Cit on Eu:HA. The BET surface area was determined through nitrogen (N_2) adsorption and desorption instrument according to ***Chapter 2***. **Figure 3-2** shows N_2 adsorption and desorption isotherms of the **0**Cit/Eu:HA, **1**Cit/Eu:HA, **2**Cit/Eu:HA, **3**Cit/Eu:HA and **4**Cit/Eu:HA, and their BET

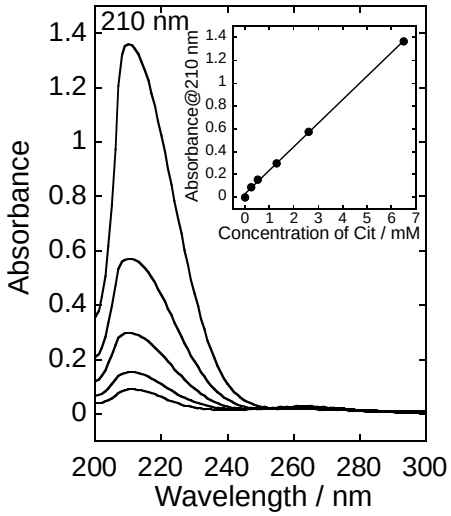

Figure 3-1. UV-Vis absorption spectra of the Cit aqueous solution at the pH of 2. (inset): the calibration curve between the Cit concentration and absorbance (R^2= 0.99871). The amount of the coordinated Cit was also confirmed by the commercially-available quantification kit, which was consistent with the result determined by the UV-Vis absorption spectra.

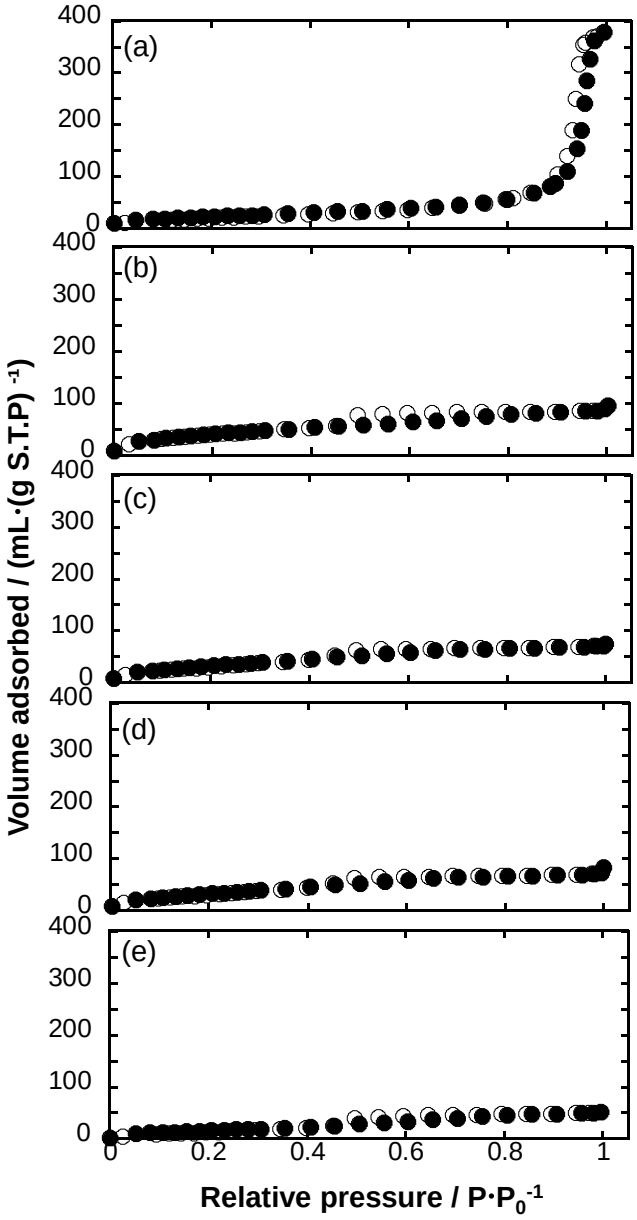

Figure 3-2. N_2 adsorption (closed circles) and desorption (open circles) isotherms of the (a) **0**Cit/Eu:HA, (b) **1**Cit/Eu:HA, (c) **2**Cit/Eu:HA, (d) **3**Cit/Eu:HA and (e) **4**Cit/Eu:HA, and their BET surface areas were 100 ± 11, 171 ± 14, 121 ± 23, 104 ± 11 and 77 ± 8 m^2/g, respectively.

surface areas were 100 ± 11, 171 ± 14, 121 ± 23, 104 ± 11 and 77 ± 8 m^2/g, respectively. **Scheme 3-3** shows the distance between Ca sites on *a*-plane and *c*-plane of HA. For the *a*-plane, the average value of 0.82 nm between 0.94 nm and 0.68 nm was used as the distance between Ca sites. For the *c*-plane, the 0.94 nm was used as the distance between Ca sites. The black double-headed arrow indicates the distance between the Ca sites. The green double-headed arrow indicates the distance

between the Ca site and the phosphate site. The distance between the Ca site and the phosphate site was about 0.33−0.37 nm. Since this distance is shorter than the molecular diameter of Cit, the distance between Cit molecules depends on the distance between Ca sites. In this chapter, the Cit intermolecular distance is assumed to be the same as the Ca site distance.

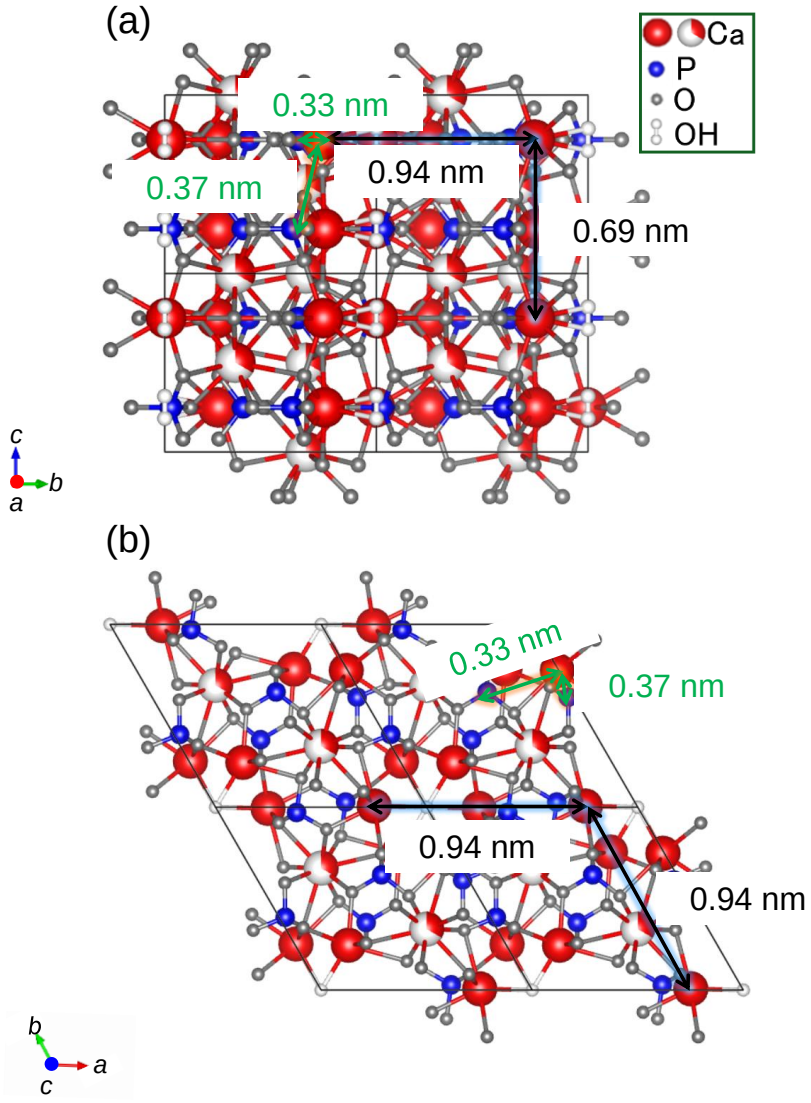

Scheme 3-3. Distance between Ca sites on (a) *a*-plane and (b) *c*-plane of HA. For *a*-plane, the average value of 0.82 nm between 0.94 nm and 0.68 nm was used as the distance between Ca sites. The black double-headed arrow indicates the distance between the Ca sites. The green double-headed arrow indicates the distance between the Ca site and the phosphate site. For *c*-plane, the 0.94 nm was used as the distance between Ca sites.

The elemental compositions were characterized by an X-ray fluorescence analysis (XRF: ZSX Primus II, Rigaku Co., Ltd.) according to ***Chapter 2***.

Zeta potential measurements of the Cit/Eu:HA nanoparticles dispersed in PBS at the particle concentration of 50 ng/mL were performed at room temperature using the nanoparticle multi-analyzer (qNano, Izon Science, Co., Ltd.) according to ***Chapter 2***.

Infrared spectra were recorded on a Fourier transform infrared spectrometer (FT-IR; JASCO Co., Ltd., FT/IR-4600) as the background of KBr in the range between 2000–800 cm^{-1} with an accumulation times of 128 and the spectral resolution of 2 cm^{-1} according to ***Chapter 2***. Furthermore, the carbonation amount (mass %CO_3) of the nanoparticles was calculated according to ***Chapter 2***.

In order to analyze the bonding states of C=O stretching vibration of carboxylate ion (COO^-) in Cit/Eu:HA structure [18,32], the peak position of C=O (COO^-) stretching vibration was examined by the second derivative FT-IR spectra. The baseline was drawn in the range between 1662 and 1645 cm^{-1} according to ***Chapter 2***.

In order to analyze the P–O bonding states in a HA structure [33], the peak position of the P–O stretching vibration was examined. The baseline was drawn in the range between 1132 and 1078 cm^{-1}, and the peak shift from 1103 cm^{-1} was evaluated by the coordination with Cit.

In order to analyze the P–O bonding component, the P–O bonding states of Cit/Eu:HA nanoparticles were investigated by the FT-IR spectral deconvolution technique at the wavenumber regions between 817–1210 cm^{-1} according to ***Chapter 2***. The P–O stretching band was deconvoluted into six components at the absorption peak bands of 1103–1083, 1039–1029, 1032–997, 958–951, 903–881 and 866–842 cm^{-1}. All the residual values by the deconvolutions were less than 3 %. From the separated spectra, the ratio of the mono-component area was calculated.

The charge transfer states of the Eu–O bonding were evaluated by a photoluminescence excitation spectrum. The excitation spectra were recorded on FP-8500 spectrophotometer (PL: JASCO Co., Ltd.) with the monitored luminescence wavelengths at 615 nm, which were excited by a Xe lamp (atmosphere: air, excitation /detection slit sizes: 2.5 nm / 2.5 nm, measure time: 0.1 s, step width: 1.0 nm, sample weight: 20 mg, shape: pellet).

X-ray diffraction (XRD) patterns were recorded with a powder X-ray diffractometer (Rigaku Co., Ltd., Smart Lab) according to ***Chapter 2***. According to Scherer's equation (K=0.9), the crystallite sizes were estimated from the half width of the 002 and 300 diffractions to be D_{002} and D_{300}, and the ratio (D_{002}/D_{300}) was calculated.

The morphologies were observed on the carbon-coated Cu grid using a transmission electron microscope (TEM: JEOL Co., Ltd., JEM-2100F) at an accelerating voltage of 200 kV, and the short-axis sizes (S), long-axis sizes (L) and aspect ratio (L/S) distributions in the Cit/Eu:HA nanoparticle

shapes were calculated by counting 300 particles, and the average (*Ave.*) and coefficient of variation (*Cv.*) values were calculated.

The detailed surface structural layers of the nanoparticles were observed on the carbon-coated Cu grids using two TEMs (JEOL Co., Ltd., JEM1230, 100 eV or JEOL Co., Ltd., JEM-2200FS, 200 eV). In the images, the surface structural layers were defined and binarized using options in the software (Microsoft Power Point 2016). The black and white values were defined as 0 and 255. The binarization was conducted at the position between 100 and 200 to evaluate the surface structural layers.

The photoluminescence properties were evaluated by luminescence spectroscopy and microscopy according to ***Chapter 2***. The excitation and luminescence spectra were recorded on the FP-8500 spectrophotometer with the monitored luminescence and excitation wavelengths at 615 nm and 464 nm, respectively. All the spectra were recorded under the same condition.

The integrated luminescence intensities centered at the peak tops due to the $^5D_0 \rightarrow {}^7F_2$ transition (between 600–635 nm) under the excitation wavelengths at 464 nm were calculated, and the integrated luminescence intensity (I) per 1 mol of the amount of Eu^{3+} ion was calculated according to ***Chapter 2***.

The fluorescence microscopy (FM) images were obtained using the luminescence microscope (Olympus Co., Ltd., CKX41N-FL) according to ***Chapter 2***.

The internal quantum efficiency (η_{int}) was measured using an integrating sphere (ISF-834; internal diameter: φ 60 mm) according to ***Chapter 2***.

3.2.3.2 Characterization of the nanoparticles in phosphate buffer saline

4CitEu:HA was ultrasonically dispersed in PBS at the particle concentration of 1.0 mg/mL for the evaluation of digital camera images with the UVA light irradiation to the nanoparticles according to ***Chapter 2***.

The size distributions of the nanoparticles (**0**Cit/Eu:HA, **1**Cit/Eu:HA, **2**Cit/Eu:HA, **3**Cit/Eu:HA, **4**Cit/Eu:HA and **FA4**Cit/Eu:HA) were measured with the electric resistance nanopulse method, which was demonstrated as the product name of qNano according to ***Chapter 2***. The Cit/Eu:HA nanoparticles were ultrasonically dispersed in PBS at the particle concentration of 50 ng/mL for the particle size evaluation. Then, the dispersion solution was used at least countable 100 particles for the measurement to calculate the *Ave.* and the *Cv.* values. Here, the current values were set to be 80 to 120 nA with the applied voltage of 0.49 V. As the calibration sample, the CPC100 were placed in PBS at the concentration of 2×10^9 particles/mL.

3.2.3.3 Cytotoxic evaluation of the nanoparticles against NIH3T3 fibroblasts

NIH3T3 fibroblast as the cell line was cultured in a plastic cell culture flask with the area of 75 cm^2 containing the 10 % FBS/DMEM (the solution containing the FBS in DMEM at 10 vol%). The cells were incubated at 37 °C in a humidified atmosphere of CO_2 (5 vol%). After the culture for 7 days, the cells were washed with 15 mL of PBS and treated with 1 mL of 0.05 w/v% trypsin-EDTA for 10 min, and the cells were dispersed in 15 mL of PBS and then re-dispersed in 15 mL of 10 % FBS/DMEM. The centrifugation and dispersion were carried out twice. The cell suspension in 10 % FBS/DMEM was seeded on the TCPS at the area density of 8000 cells/cm^2.

The sterilization treatment of the Cit/Eu:HA nanoparticles (**0**Cit/Eu:HA, **1**Cit/Eu:HA, **4**Cit/Eu:HA and **FA4**Cit/Eu:HA) was carried out with ethanol. In particular, 10 mg of the Cit/Eu:HA nanoparticles were treated with 10 mL of water/ethanol (50 vol%/50 vol%) and 10 mL of water/ethanol (30 vol%/70 vol%), and each treatment was performed for 1 h. Then, the Cit/Eu:HA nanoparticles were dispersed in 10 mL of 10 % FBS/DMEM, and centrifugation (4000 rpm, 2 min) was performed to be finally dispersed in 5 mL of 10 % FBS/DMEM.

At the cell culture time of 6 h, the Cit/Eu:HA nanoparticle dispersion solution was added to the cell surfaces at the final nanoparticle concentrations of 100 μg/mL and was incubated for the additional culture time of 66 h (i.e., total cell culture time: 72 h). At the culture times of 9, 12, 24, 48 and 72 h, the adhered cell densities of the living cells in PBS were evaluated. As a reference sample, the cells without addition of nanoparticles (sample name: **PS**) was evaluated. For the evaluation of the cell density, the adhered cells were washed twice with 1 mL of PBS to remove the non-bonded nanoparticles and non-adhered cells. After the washing, the cells were observed by an optical microscope to obtain the adhered cell density (cells/cm^2). The optical transmittance microscope images were obtained using the microscope (Olympus Co., Ltd., CKX41N-FL).

3.2.3.4 Evaluation of cell labeling and cytostatic ability of the nanoparticles against HeLa cancer cells

The HeLa cancer cells were cultured and seeded and their reaction with the Cit/Eu:HA nanoparticles was evaluated based on the same method for the fibroblasts mentioned above. At the cell culture time of 6 h, the Cit/Eu:HA nanoparticle dispersion solution was added to the cell surfaces and was incubated at the final nanoparticle concentrations of 100 μg/mL for the additional culture time of 66 h. At the culture times of 9, 12, 24, 48 and 72 h, the adhered cell densities were evaluated by the optical microscope of the living cells in 1 mL of PBS based on the same method of the

fibroblasts mentioned above. The optical transmittance microscope images and the FM images were obtained using the above microscope and the luminescence microscope under the same condition, respectively.

The luminescence intensities of the lyophilized cells were measured. In particular, the adhered cells were washed twice with 1 mL of ultrapure water. After the lyophilization of the adhered cells, the integrated luminescence spectral areas at the wavelengths between 600–635 nm were measured on the FP-8500 spectrophotometer under the excitation wavelength of 464 nm.

The HeLa cells at the culture time of 60 h were densely-packed with each other and had an aggregation size of more than 50 μm, which were tumor cells and can be defined as tumorized spheres according to the previous report [34]. For the demonstration of the biomedical applications, the labeling ability against the tumorized spheres was evaluated. At the cell culture time of 60 h, the **FA4**Cit/Eu:HA nanoparticles were added to the tumorized spheres at the final nanoparticle concentrations of 100 μg/mL. At the lapse of 1, 3, 6, 12 and 24 h from the nanoparticle addition, the tumorized sphere density, shape and labeling of the living cells, and the luminescence intensity of the lyophilized cells and were evaluated according to the same procedure mentioned above.

3.3 Results and Discussion

3.3.1 Characterization of the nanoparticles

Table 3-1 indicates the resultant chemical composition, (Ca+Eu+K)/P molar ratio and the molar concentration of Eu to (Eu+Ca)) of the Cit/Eu:HA nanoparticles. **Table 3-2** indicates the resultant coordinated amount of Cit, Cit molecular area occupancy and the zeta potential values of the Cit/Eu:HA nanoparticles. The feed (Eu+Ca+K)/P molar ratio of the nanoparticles was 2.06–2.16, which was higher than that of the feed (Eu+Ca+K)/P ratio at 1.67, whereas that of **0**Cit/Eu:HA was 1.67 and was the same as the feed ratio. The concentration of the Eu to (Eu+Ca) was 2.3–3.3 mol%, and the values were irrespective of the synthetic condition. When the Cit molecule was coordinated with the HA phase, the atom content of Ca decreased and that of Eu was constant, suggesting the substitution of Ca^{2+} with Eu^{3+} ion. Furthermore, that of P decreased with decreasing the atom content of Ca and that of C also increased. It was suggested that the increase in the C atom content indicates the Cit existence as well as the carbonate ion inclusion in the nanoparticles. Moreover, It is also possible that Cit was substituted with PO_4^{3-} or HPO_4^{2-} because the concentration of P was reduced by the coordination of Cit [35]. For the possibility of the Cit existence, when the feed concentration of Cit was higher, the ions (i.e., Ca^{2+}, Eu^{3+} ions) in the Ca sites would interact with the Cit molecules on

Table 3-1. Resultant chemical composition, (Ca+Eu+K)/P molar ratio and the molar concentration of Eu to (Eu+Ca) of the Cit/Eu:HA nanoparticles.

Sample name	Ca (mol%)	Eu (mol%)	K (mol%)	P (mol%)	(Ca+Eu+K)/ P molar ratio	Concentration of Eu to (Eu+Ca) (mol %)
0Cit/Eu:HA	18.7	0.584	0.692	11.6	1.67	3.0
1Cit/Eu:HA	15.6	0.544	1.16	8.13	2.06	2.3
2Cit/Eu:HA	15.4	0.367	1.62	8.14	2.09	2.7
3Cit/Eu:HA	16.0	0.376	1.92	8.33	2.15	2.3
4Cit/Eu:HA	15.0	0.423	2.02	7.88	2.16	3.3

Table 3-2. Resultant coordinated amount of Cit, Cit molecular area occupancy and the zeta potential values of the Cit/Eu:HA nanoparticles.

Sample name	Resultant coordinated amount of Cit / mmol·(g of HA)$^{-1}$	Cit molecular area occupancy (%)	Zeta potential (mV)
0Cit/Eu:HA	0	-	–10.2 ± 7.5
1Cit/Eu:HA	0.99	42.8	–25.0 ± 11
2Cit/Eu:HA	1.06	61.4	–28.9 ± 4.1
3Cit/Eu:HA	1.13	80.6	–27.1 ± 15
4Cit/Eu:HA	1.24	117	–37.6 ± 11

the nanoparticle surfaces to form the preferential chelate complex. For the possibility of the carbonate ion inclusion, taking into account the higher (Eu+Ca)/P values, the B-type carbonate HA would be formed due to the charge compensation with the substitution of the Ca^{2+} with trivalent Eu^{3+} ion [14,36–38]. Therefore, the Eu^{3+} ion was substituted with the Ca^{2+} ion of HA and the Cit molecules interact with the Ca^{2+} and Eu^{3+} ions in the Ca sites. The resultant coordinated amount of Cit varied with the feed concentration. In particular, the resultant coordinated amounts of Cit and the Cit molecular area occupancy were 0, 0.99, 1.06, 1.13 and 1.24 mmol·(g of HA)$^{-1}$ and 0, 42.8, 61.4, 80.6 and 117 % for **0**Cit/Eu:HA, **1**Cit/Eu:HA, **2**Cit/Eu:HA, **3**Cit/Eu:HA and **4**Cit/Eu:HA, respectively. Also, the Cit content in the Cit/Eu:HA nanoparticles was confirmed using the Cit quantification kit. The zeta potential value of the previously-reported HA nanoparticles was about −4 mV [39]. **0**Cit/Eu:HA exhibited a higher value at −10.2 mV, suggesting the larger proportion of PO_4^{3-} to HPO_4^{2-} ions at the phosphate sites (i.e., rich in PO_4^{3-}) in the crystal structure. The zeta potential values of the **1**Cit/Eu:HA, **2**Cit/Eu:HA, **3**Cit/Eu:HA and **4**Cit/Eu:HA nanoparticles were about −25.0, −28.9, −27.1 and −37.6 mV, respectively, and were changed to be negative with increasing the coordinated amount of Cit, which were lower than that of **0**Cit/Eu:HA. Considering that the Cit molecules interact

with the Ca^{2+} ions and Eu^{3+} ions in the **1**Cit/Eu:HA, **2**Cit/Eu:HA, **3**Cit/Eu:HA and **4**Cit/Eu:HA nanoparticle surface layers, the Cit molecules would exist over the Ca ion sites on the Eu:HA and the surfaces were negatively-charged.

The FT-IR spectra of the Cit/Eu:HA nanoparticles measured in the range of 2000−800 cm^{-1} were shown in **Figure 3-3**. In the spectrum of **0**Cit/Eu:HA, the O−H bending vibration of H_2O and

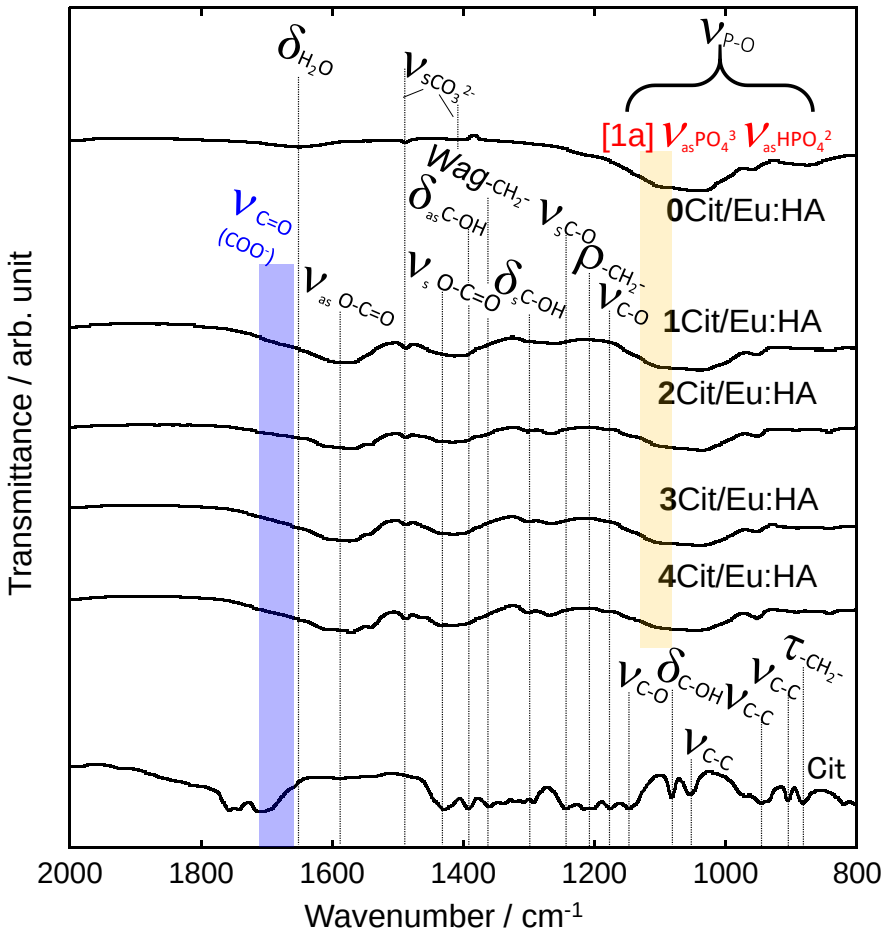

Figure 3-3. (a) FT-IR spectra of the the Cit/Eu:HA nanoparticles and Cit.

stretching vibration of carbonate ion (CO_3^{2-}) band ($\nu_s(CO_3^{2-})$) were observed at around 1650 cm^{-1} and 1485 cm^{-1}, respectively. The several absorption bands that appeared at around 1100−1000 cm^{-1} were attributed to triply degenerated asymmetric stretching mode (ν_3) of P−O ($\nu_{as}PO_4^{3-}$, $\nu_{as}HPO_4^{2-}$). Especially, the weak shoulder band at around 960 cm^{-1} resulted from nondegenerated symmetric stretching mode (ν_1) of P−O bond ($\nu_sPO_4^{3-}$). The weak shoulder band at around 860 cm^{-1} resulted from symmetric stretching mode (ν_5) of P−O(H) of HPO_4^{2-} group ($\nu_sHPO_4^{2-}$). These results indicated the formation of HA in **0**Cit/Eu:HA [40,41].

In the reference sample of Cit (powder state), the absorption bands appeared at 1657 cm^{-1} were attributed to C=O stretching of carboxylate ion [42]. The adsorption bands at around 1590 and 1530 cm^{-1}, corresponding to asymmetric O−C=O stretching vibrations of carboxylate ion, and the adsorption band at around 1430 cm^{-1}, corresponding to symmetric O−C=O stretching vibration [43]. The several absorption bands appeared at around 1400, 1360, 1291, 1245 and 1206 cm^{-1} are attributed to asymmetric bending vibration of C−OH, wagging vibration of $-CH_2-$, symmetric bending vibration of C−OH, symmetric stretching vibration of C−O and rocking vibrations of $-CH_2-$, respectively [42]. The characteristic bands of Cit also appeared at around 1171−1141, 1110, 1085−905 and 880 cm^{-1}, which were attributed to stretching vibration of C−O, bending vibration of C−OH, stretching vibration of C−C and twisting vibration of $-CH_2-$, respectively, and the absorption bands of Cit were overlapped with those of Eu:HA to be difficult to distinguish the absorption bands at similar wavenumber regions.

At about 860 cm^{-1}, there are bending mode of the CO_3^{2-} ion group and stretching mode of the CO_3^{2-} ion group in addition to weak shoulder band at around 860 cm^{-1} resulted from symmetric stretching mode (ν_5) of P−O(H) of HPO_4^{2-} group ($\nu_s HPO_4^{2-}$). The existence of CO_3^{2-} ion in these samples, the bending mode of the CO_3^{2-} ion group and stretching mode of the CO_3^{2-} ion group may appear at 870 and 860 cm^{-1}, respectively [40]. The contained amount of CO_3^{2-} ion in the Cit/Eu:HA nanoparticles were estimated from the FT-IR spectra as the background of the spectrum shape of the KBr alone [44]. Based on the FT-IR spectra in **Figure 3-3**, the peak areas were calculated after a preliminary baseline correction of the complete 4000–400 cm^{-1} spectrum. As the vibrational domains were retained for the analysis, both the stretching vibration of $\nu_s(CO_3^{2-})$ for carbonate ions and ν_1 and ν_3 of the P−O bonds were simply used. In particular, the integration of the $\nu_s(CO_3^{2-})$ band was performed at the wavenumbers between 1502–1475 cm^{-1}, and that of ν_1 and ν_3 by the P−O bond contributions was integrated at the wavenumbers between 1205–930 cm^{-1}. By the calculation based on the previous report [44], the contained amount of CO_3^{2-} ions was 0.18, 0.41, 0.44, 0.46 and 0.61 wt % for **0**Cit/Eu:HA, **1**Cit/Eu:HA, **2**Cit/Eu:HA, **3**Cit/Eu:HA and **4**Cit/Eu:HA, respectively. Thus, the contained amount of CO_3^{2-} ion in the Cit/Eu:HA nanoparticles increased with increasing the coordinated amount with Cit. The error range of amount of CO_3^{2-} ion in the previous report for CO_3^{2-} ion-containing HA synthesized at 20, 22, 37, 50 and 70 °C exhibited ± 0.5 wt% [44]. Therefore, it was suggested that the included amount of CO_3^{2-} ion of this study was very small and could be regarded for the characterization of the Cit/Eu:HA nanoparticles.

Figure 3-4(a) shows the second derivative FT-IR spectra of the Cit/EuHA nanoparticles and Cit alone in the region 1662 to 1645 cm^{-1}. In the **1**Cit/Eu:HA, **2**Cit/Eu:HA, **3**Cit/Eu:HA and **4**Cit/Eu:HA, the absorption bands appeared at around 1653 cm^{-1} and were attributed to C=O stretching vibration

of carboxylate ion (COO^-) [42]. By the coordination, the C=O stretching mode was shifted to the lower energy region as compared to the case in the Cit alone. The shift would be attributed to the

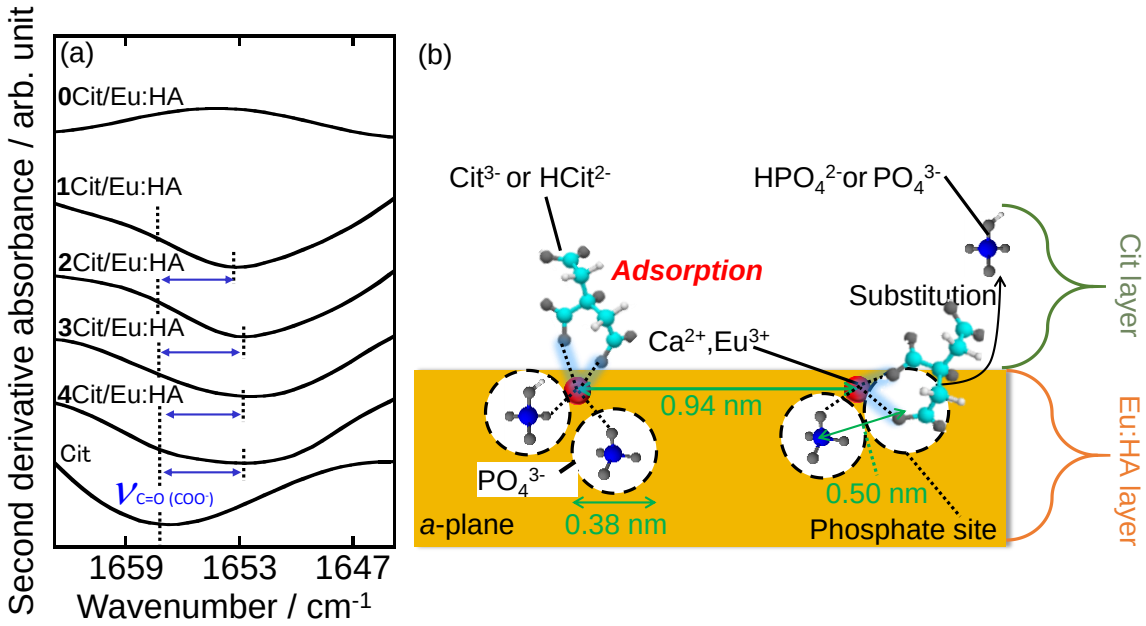

Figure 3-4. (a) Second derivative FT-IR spectra of the Cit/Eu:HA nanoparticles and Cit alone in the region between 1662 and 1645 cm^{-1}, which indicates the peak band of C=O (COO^-) of Cit, and (b) the possible interfacial interactions between C=O (COO^-) (blue part) of Cit and Eu:HA surface.

interactions between the carboxylate ion of Cit and the Ca site of the HA structure [18,32] to alter the Cit molecular state as shown in **Figure 3-4(b)**. In particular, it has been known that the C=O stretching mode position due to the Cit monomer sate appeared at the lower energy side as compared with the case in the C=O stretching due to the dimer state [42]. Moreover, when the bonding electron transferred to the Ca side of Eu:HA, shifted to the lower energy region as compared to the case of the Cit alone [18,32]. Thus, since the bond between the Ca^{2+} or Eu^{3+} ion of Eu:HA and C=O formed, it was suggested that C=O stretching mode of Cit was adsorbed on the Ca site [18,32]. Accordingly, it was suggested that the monomer component ratio of Cit increased by the coordination based on the fix due to the interaction with the Ca site on the HA structure.

The spectral shape change of the absorption band due to ν_3 of the P−O bond with increasing the coordinated amount of Cit was investigated as follows. The peak shape was broadened and shifted to the lower wavenumber region with the coordination. As shown in **Figure 3-5(a)**, the peak shift degree of the Cit/Eu:HA nanoparticles with the coordination was 3 cm^{-1}. In particular, the peak maxima of the HA and **0**Cit/Eu:HA were observed at 1103 cm^{-1}, and those of **1**Cit/Eu:HA, **2**Cit/Eu:HA, **3**Cit/Eu:HA and **4**Cit/Eu:HA were observed at 1106 cm^{-1}. Based on the previous report [33], the

spectral shape change indicates that the Cit molecule enhances the structural disorder of the Eu:HA nanoparticles and polycrystallizes the surface layers. Thus, it was suggested that the atomic structures on the Eu:HA layer were disordered by increasing the liquid-solid interface by the interaction between the Cit and the Ca site of Eu:HA as shown in **Figure 3-5(b)**.

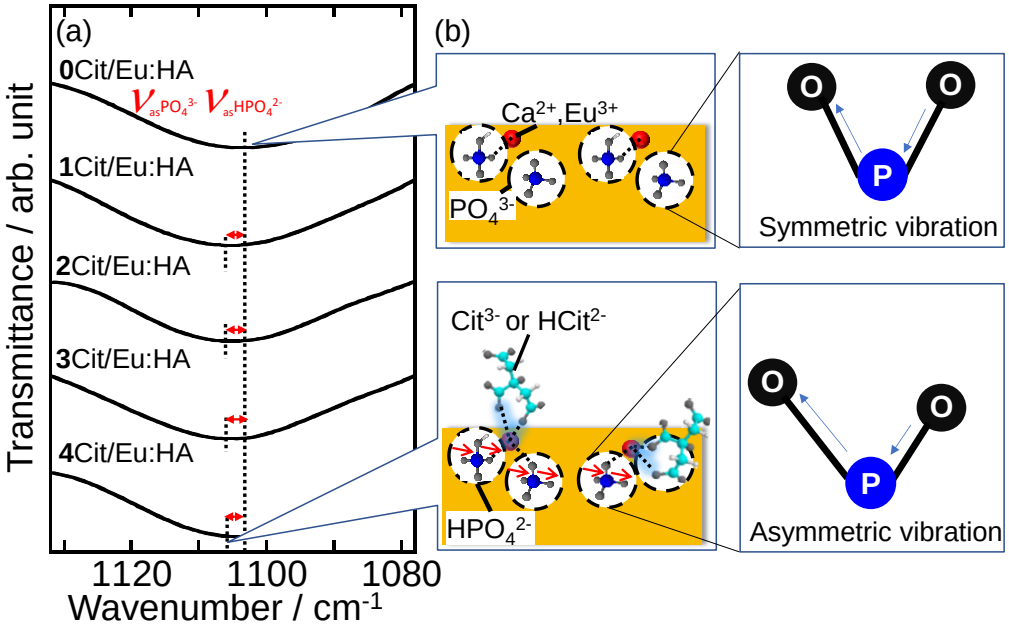

Figure 3-5. (a) FT-IR spectra of the Cit/Eu:HA nanoparticles in the region between 1132 and 1078 cm^{-1}, which indicates the peak band due to asymmetric stretching mode, $\boldsymbol{n}_{3a}$, of the P−O bond in the HA strucure, and (b) the possible asymmetric vibration generated by the interactions between C=O (COO^-) of Cit and P−O of Eu:HA surface.

Figure 3-6(a−e) showed the curve fitting and spectral separation results of the FT-IR deconvolution spectra for the P−O bonds of the HA and Cit/Eu:HA nanoparticles. The separated components of **Figure 3-6(a−e)** were assigned as shown in ***Chapter 2***, which were described in the experimental section in detail. Since the lower content of carbonate ion in the Cit/Eu:HA nanoparticles can be disregard in this study, the spectral deconvolution was performed using only the P−O bond components. All the sample residuals were less than 3.5 % by the fitting. From the deconvolution spectral areas, the component ratios were represented in **Figure 3-6(f)**. The component ratios of the peak areas [1a]−[1c] of the **1**Cit/Eu:HA, **2**Cit/Eu:HA, **3**Cit/Eu:HA and **4**Cit/Eu:HA nanoparticles were higher than those of the HA and **0**Cit/Eu:HA, suggesting that the atomic structures of the Eu:HA surface layer would be disordered. Here, the ratio of area [2] was irrespective of the presence of Cit. Among the **1**Cit/Eu:HA, **2**Cit/Eu:HA, **3**Cit/Eu:HA and **4**Cit/Eu:HA nanoparticles, the component ratio of area [4] increased with the increasing the coordinated amount of Cit, and that of **1**Cit/Eu:HA, **2**Cit/Eu:HA, **3**Cit/Eu:HA and **4**Cit/Eu:HA was 1.1, 1.9, 2.0 and 2.1 %, respectively,

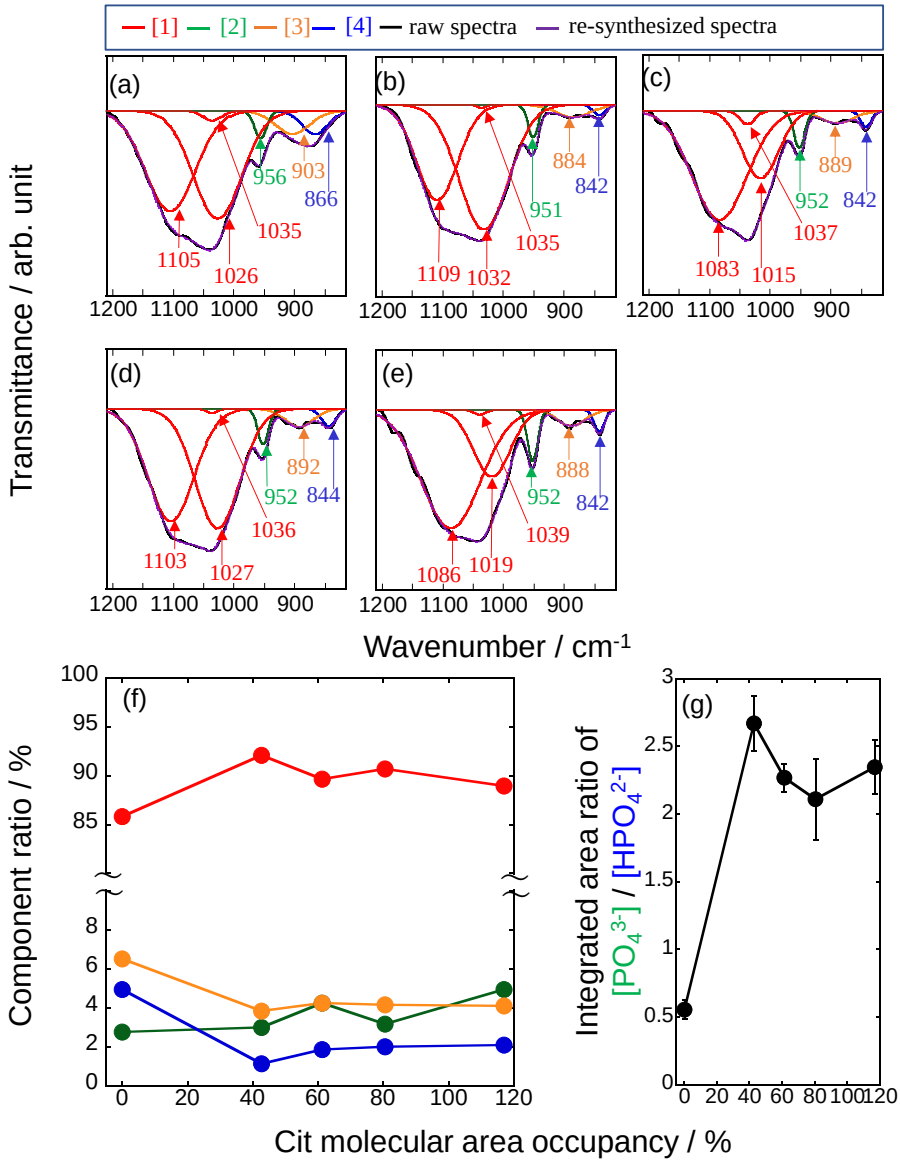

Figure 3-6. Curve fitting and spectral separation results of FT-IR deconvolution spectra in the P–O absorption bands of (a) **0**Cit/Eu:HA, (b) **1**Cit/Eu:HA, (c) **2**Cit/Eu:HA, (d) **3**Cit/Eu:HA and (e) **4**Cit/Eu:HA. From the deconvolution spectral areas, the component ratios were represented in (f). The details of assignments in (f) were shown in ***Chapter 2***. (g) Integrated area ratio of $[PO_4^{3-}]/[HPO_4^{2-}]$ of Cit/Eu:HA nanoparticles.

indicating the increase in the ratio of HPO_4^{2-} by the coordination. Moreover, among the Cit/Eu:HA nanoparticles, the component ratio of the area [2] and the area [4] ($[PO_4^{3-}]/[HPO_4^{2-}]$) were investigated as shown in **Figure 3-6(g)**. The $[PO_4^{3-}]/[HPO_4^{2-}]$ ratio increased between the **0**Cit/Eu:HA and **1**Cit/Eu:HA, and had a decreasing trend between the **1**Cit/Eu:HA and **4**Cit/Eu:HA. Since **0**Cit/Eu:HA is Ca-deficient HA, it is expected to have the following composition formula [45].

$$Ca_{10-x}Eu_x(PO_4)_{6-x}(HPO_4)_x(OH)_{2-x} \quad (1)$$

When substituting [HPO_4^{2-}] with Cit ion, [HPO_4^{2-}] may decrease [35]. After that, as a result of the interaction of C=O in Cit with the Ca site, it is considered that [HPO_4^{2-}] increased in order to keep the charge of HA crystals neutral [46]. The decrease of [HPO_4^{2-}] suggested that H^+ in HPO_4^{2-} was pulled out to become PO_4^{3-}. Thus, it was found that the Cit molecular coordination altered the bonding state between the Ca and the phosphate sites in the Eu:HA structure to increase the ratio of HPO_4^{2-} in the Eu:HA and subsequently disorder the surface atomic structures.

Figure 3-7 indicated the excitation spectra of the Cit/Eu:HA nanoparticles in the wavelength region between 200−350 nm. The charge transfer (CT) transition band [39] of the Eu−O bond was observed at around 232 nm for **0**Cit/Eu:HA and at around 235−237 nm for the **1**Cit/Eu:HA, **2**Cit/Eu:HA, **3**Cit/Eu:HA and **4**Cit/Eu:HA nanoparticles. The CT transition band was red-shifted by the coordination with Cit. Here, it has been reported that the CT transition band is closely related to the covalent bond degree between the O and Eu atoms [39]. In particular, the decrease in the energy state of electron transfer from O to Eu by the coordination with Cit represents the increase in the covalent bonding degree. Thus, it was suggested that the bonding states between the Eu and O atoms were changed due to the increase of the HPO_4^{2-} ratio by the coordination with Cit.

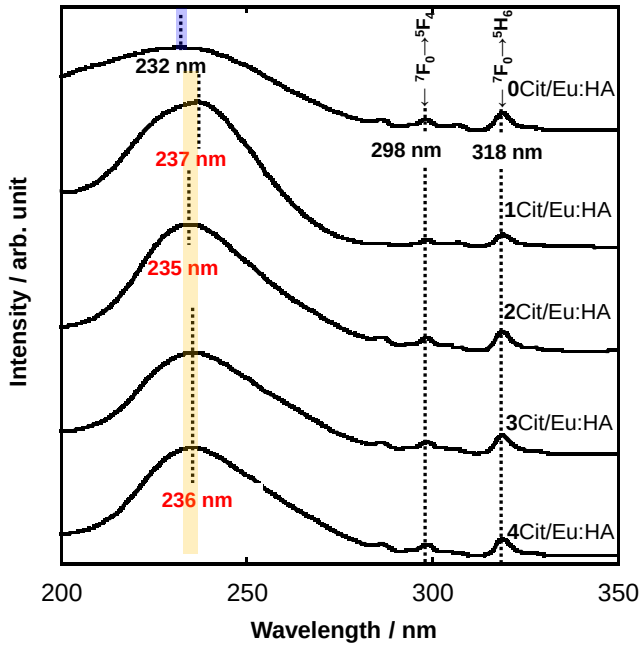

Figure 3-7. Excitation spectra of the Cit/Eu:HA nanoparticles in the wavelength region between 200−350 nm. The monitored luminescence wavelength for the measurement was 615 nm.

Scheme 3-4 showed an illustration of the possible coordinated structures of the Cit coordinated on the Eu:HA crystal structural surfaces. **0**Cit/Eu:HA has calcium deficient sites. The Cit may substitute HPO_4^{2-} in Eu:HA when it first interacts with Eu:HA. The decrease in the energy state of electron transfer from O to Eu by the substitution with Cit represents the increase in the covalent bonding degree. As the result, the Cit molecule enhances the structural disorder of the Eu:HA nanoparticles and polycrystallizes the surface layers to be amorphous state at the near-surface layer. Then, it is suggested that Cit adsorbs to the Ca site on the Eu:HA. As a result of the interaction of C=O in Cit with Ca site, it is considered that [HPO_4^{2-}] increased in order to keep the charge of HA crystals neutral [46].

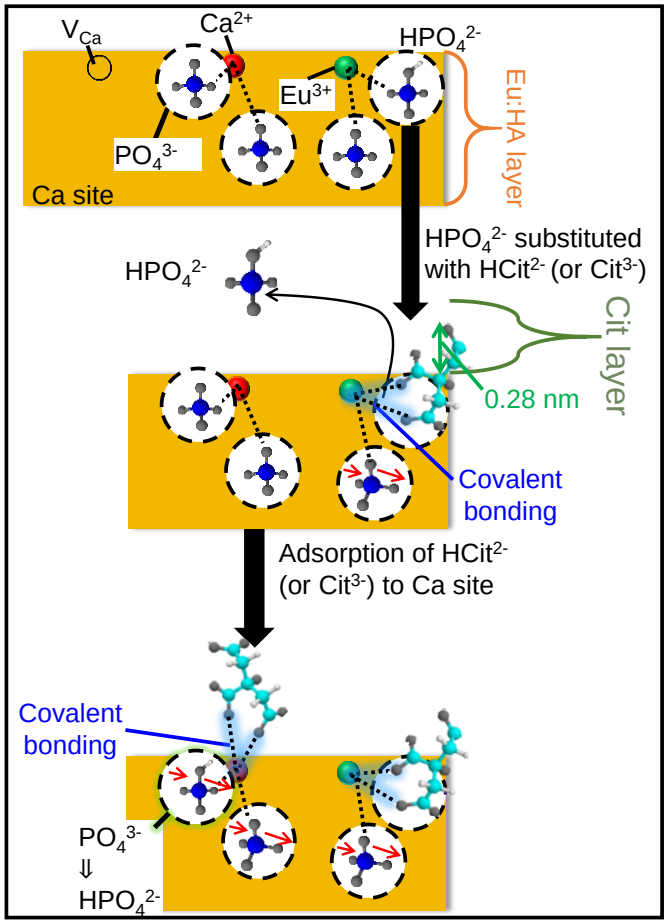

Scheme 3-4. Illustration of the possible coordinated structures of the Cit coordinated on the Eu:HA crystal structural surfaces. Cit chelate formation increases the covalent bond ratio.

The XRD patterns of the Cit/Eu:HA nanoparticles with the different Cit concentrations and Cit were shown in **Figure 3-8**. The patterns of the Cit/Eu:HA nanoparticles were attributed to a single phase of HA (ICDD No. 00-009-0432) with no diffraction patterns of Cit. The Cit/Eu:HA nanoparticles (**1**Cit/Eu:HA, **2**Cit/Eu:HA, **3**Cit/Eu:HA and **4**Cit/Eu:HA) exhibited the lower HA

crystalline states as compared with the case in **0**Cit/Eu:HA. The crystallite sizes of both D_{002} and D_{300} were reduced by bonding with the Cit (**Table 3-3**). In particular, the D_{002} and D_{300} of **0**Cit/Eu:HA were 36 nm and 14 nm, and the smaller D_{002} and D_{300} of the Cit/Eu:HA nanoparticles were 16−18 nm and 2.9−4.6 nm. Therefore, the Cit molecules interacted with the Eu:HA nanoparticle surfaces sterically hindered the nanoparticle growth by the inorganic/organic interactions.

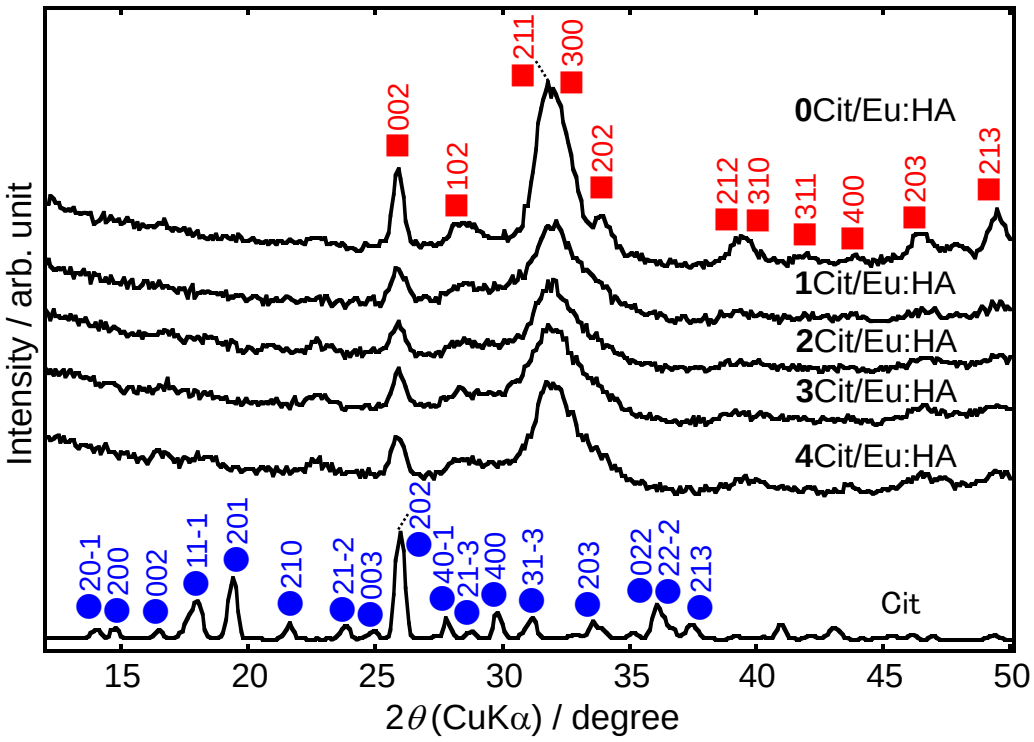

Figure 3-8. XRD patterns of the Cit/Eu:HA nanoparticles and Cit alone. ■ and ● are the diffraction patterns of HA and Cit, respectively.

Table 3-3. The crystalline sizes and ratios of the Cit/Eu:HA nanoparticles with the different Cit concentrations.

Sample name	***Crystalline sizes and ratios***		
	D_{002} **(nm)**	D_{300} **(nm)**	D_{002} / D_{300}
0Cit/Eu:HA	41	18	2.3
1Cit/Eu:HA	16	4.3	3.7
2Cit/Eu:HA	16	2.9	5.5
3Cit/Eu:HA	16	2.7	5.9
4Cit/Eu:HA	18	4.6	3.9

In the following, the analysis of the spectral peak due to $^5D_0 \rightarrow {}^7F_0$ transition was performed to evaluate the existing states of Eu^{3+} ions in the Ca sites of HA. Although the $^5D_0 \rightarrow {}^7F_0$ transition of Eu^{3+} ion is parity-forbidden, which can be partially permitted when the Eu^{3+} ion is occupied in one of the C_s, C_1, C_2, C_3, C_4, C_6, C_{2v}, C_{3v} and C_{6v} environmental sites and the $^5D_0 \rightarrow {}^7F_0$ transition can be resultantly observed [16]. As shown in **Figure 3-7**, the luminescence spectra due to the $^5D_0 \rightarrow {}^7F_0$ transition of the Cit/Eu:HA nanoparticles were separated and fitted to the characteristic luminescence peaks attributed to the different substitution of Eu^{3+} ions into the Ca(I) and Ca(II) sites of HA [14]. Here, the substitution of Eu^{3+} into Ca (II) site and Ca (I) sites provides the luminescence peak tops at 574 and 577 nm, respectively, which was elucidated by the analytic comparison of the $^5D_0 \rightarrow {}^7F_0$ transition areas with the ratio of the Eu^{3+} ions in the Ca (I) and Ca (II) sites [14,47]. The luminescence spectra of **0**Cit/Eu:HA, **1**Cit/Eu:HA, **2**Cit/Eu:HA, **3**Cit/Eu:HA and **4**Cit/Eu:HA in **Figure 3-9(a−e)** exhibited the peak tops at 574.4, 575.0, 574.9, 574.6 and 574.6 nm for the Ca(II) site, and at 578.6, 578.7, 578.8, 578.8 and 578.8 nm for the Ca(I) site, respectively, which were almost same to those in the previous reports [14] and were slightly red-shifted by the coordination with Cit, suggesting that

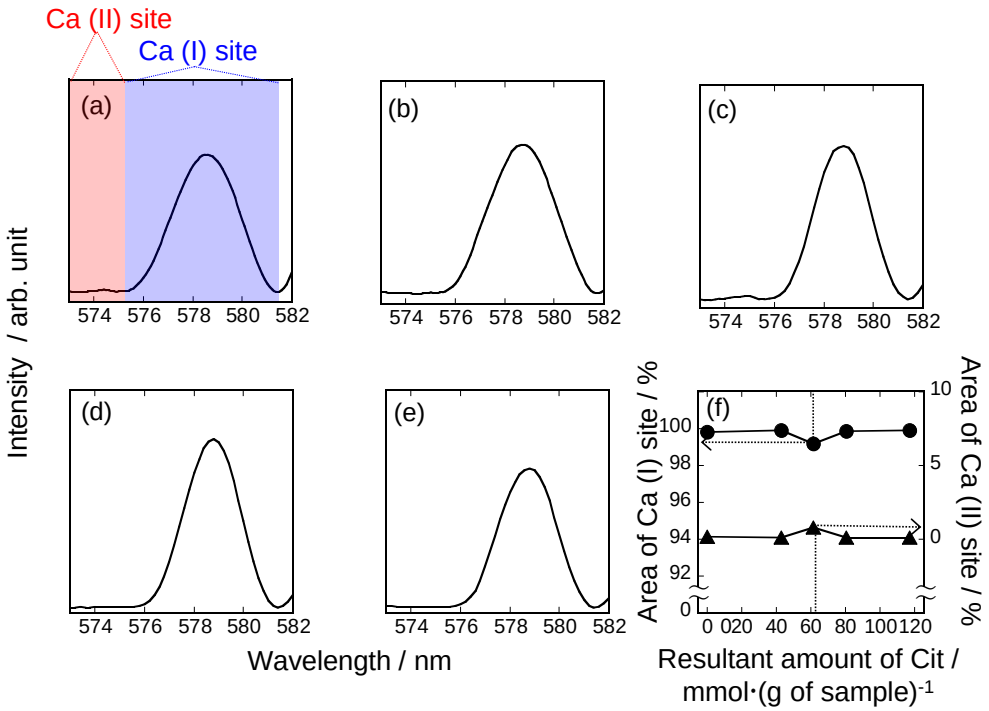

Figure 3-9. Luminescence spectra of (a) **0**Cit/Eu:HA, (b) **1**Cit/Eu:HA, (c) **2**Cit/Eu:HA, (d) **3**Cit/Eu:HA and (e) **4**Cit/Eu:HA in the wavelength region between 573−582 nm for investigating the Ca sites by the substitution of Eu^{3+} with Ca^{2+} ions. In particular, the luminescence wavelength regions of the Ca(II) and Ca(I) sites at the wavelength regions between 573−575 nm and 575−581 nm, respectively, were calculated by the peak separation technique under the monitored excitation wavelength at 464 nm to obtain (f) the separated peak area of Ca(I) and Ca(II) sites with the coordinated Cit amount.

the Ca site environment occupied by Eu^{3+} ions in Cit/Eu:HA nanoparticles was partially changed by the coordination. The integrated intensity areas due to the Ca(I) and Ca(II) sites of **0**Cit/Eu:HA, **1**Cit/Eu:HA, **2**Cit/Eu:HA, **3**Cit/Eu:HA and **4**Cit/Eu:HA were about 99 % and 1 %, respectively (**Figure 3-9(f)**), indicating the preferential substitution into Ca(I) site by the coordination with Cit. The Eu:HA nanoparticles calcined at 750 ℃ exhibited the preferential substitution into the Ca(I) site [14]. The Eu:HA nanoparticles synthesized at the room temperature in the presence of cetyltrimethylammonium bromide. The integrated intensity area due to the Ca(I) and Ca(II) sites of nanoparticles was about 82 % and 18 %, respectively [48]. Thus, the presence of the coordinated organic molecules with HA may change the selective substitution into Ca(I) site irrespective of the coordinated Cit amount.

Figure 3-10 showed the TEM images of the Cit/Eu:HA nanoparticles, and their average *S* and *L* size and *L*/*S* ratio distributions. **0**Cit/Eu:HA exhibited the rod-like particle shapes, and **1**Cit/Eu:HA, **2**Cit/Eu:HA, **3**Cit/Eu:HA and **4**Cit/Eu:HA exhibited the spherical particle shapes. The average *L* and *S* values of **0**Cit/Eu:HA were 48 and 18 nm, respectively (**Figure 3-10(f** and **f')**), and those of **1**Cit/Eu:HA, **2**Cit/Eu:HA, **3**Cit/Eu:HA and **4**Cit/Eu:HA were 16–20 nm and 9.4–12 nm, respectively (**Figure 3-10(g−j** and **g'−j')**). The shapes and sizes of the **0**Cit/Eu:HA were almost the same to the case in the synthetic HA nanoparticles at about 10–50 nm [49] and 20–100 nm [50], which were longer than those of **1**Cit/Eu:HA, **2**Cit/Eu:HA, **3**Cit/Eu:HA and **4**Cit/Eu:HA. The average *L* and *S* values of **0**Cit/Eu:HA were almost matched to the D_{002} and D_{300} values in **Table 3-3** and the average *L*/*S* value of **0**Cit/Eu:HA was almost matched to the D_{002}/D_{300} values, suggesting the single crystal in a nanoparticle of **0**Cit/Eu:HA. On the other hand, the average *L* values of **1**Cit/Eu:HA, **2**Cit/Eu:HA, **3**Cit/Eu:HA and **4**Cit/Eu:HA were almost matched to the D_{002} values, and the average *S* values were larger 3 times than the D_{300} values, suggesting a polycrystalline state along with the *a*-axis direction. The average *L*/*S* value decreased by the coordination with Cit. A rational synthesis method for mesoporous Mg–Al mixed metal oxides has been demonstrated using Mg-Al monodispersed layered double hydroxide nanoparticles stabilized with tris(hydroxymethyl)aminomethane tripod ligand as a building block [51]. The morphologies of the nanoparticles were successfully controlled by the coordination of the carboxylate ion of tris(hydroxymethyl)aminomethane ligand. The coordination of tris(hydroxymethyl)aminomethane tripod ligand achieved the morphological control of the nanoparticles, suggesting the possibility of nanoparticle shape control by the coordination of organic molecules. In this study, the Cit molecules selectively interact with the *a*-plane (Ca site) on the Cit/Eu:HA, and then gather and grow based on the Cit molecular aggregative interactions (e.g., dimer formation) to polycrystallize in the nanoparticle by binding along with the *a*-axis direction. Thus, the

interactions of Cit as an organic molecule and Eu:HA as an inorganic matrix were thought to be important for achieving luminescence properties.

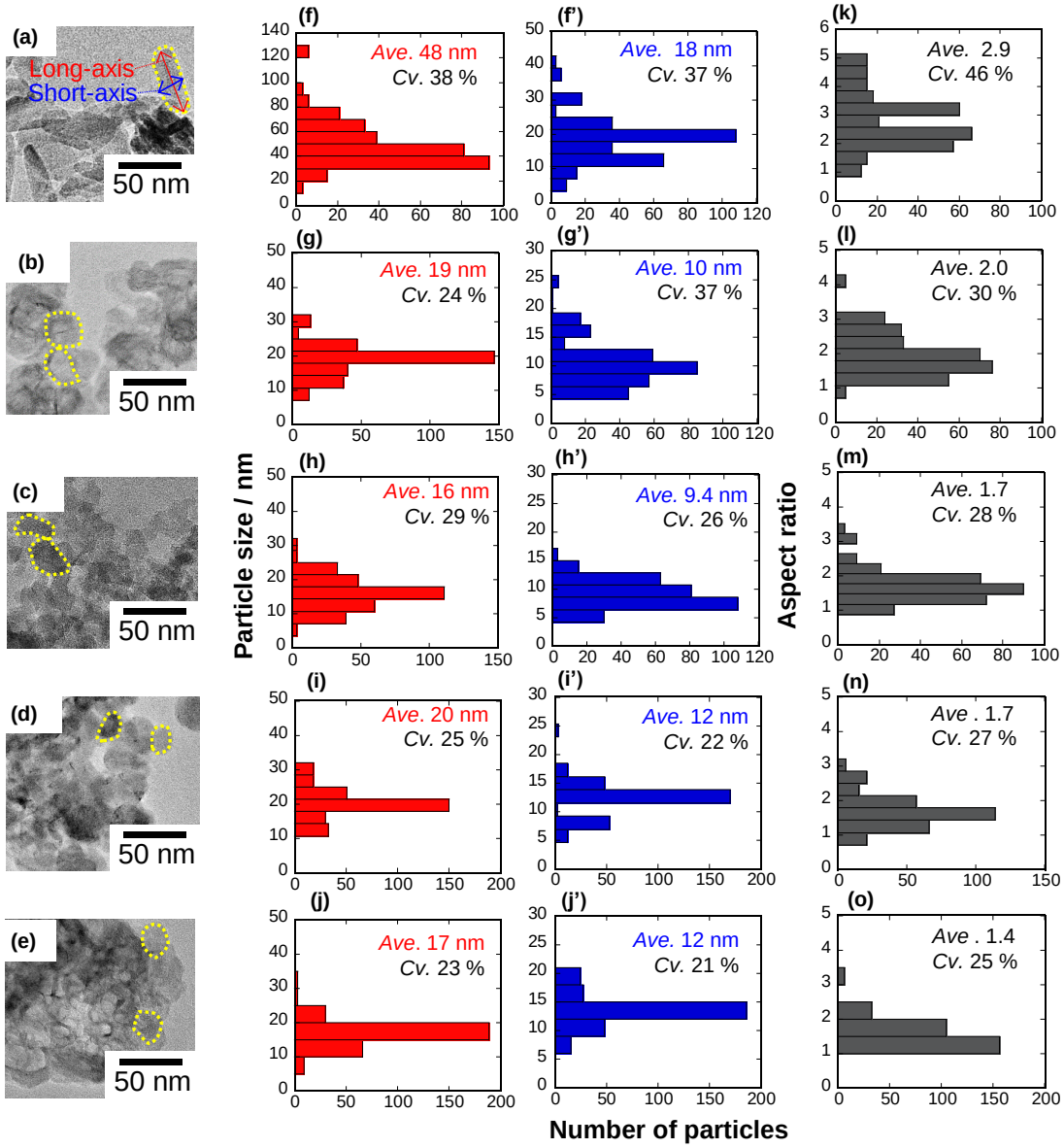

Figure 3-10. (a–e) TEM images of the nanoparticles and (f–j) long-axis sizes and (f'–j') short-axis sizes of the particle shapes, and (k–o) aspect ratios ((a, f, f', k) **0**Cit/Eu:HA, (b, g, g', l) **1**Cit/Eu:HA, (c, h, h', m) **2**Cit/Eu:HA, (d, i, i', n) **3**Cit/Eu:HA and (e, j, j', o) **4**Cit/Eu:HA). The yellow dotted circles in the TEM images indicate the nanoparticle shapes.

Figure 3-11 indicated the magnified TEM images at the near surfaces of **0**Cit/Eu:HA, **1**Cit/Eu:HA, **2**Cit/Eu:HA, **3**Cit/Eu:HA and **4**Cit/Eu:HA. At the near surfaces of **0**Cit/Eu:HA, the HA atomic structures were uniform and ordered. In the case of **1**Cit/Eu:HA, **2**Cit/Eu:HA, **3**Cit/Eu:HA and **4**Cit/Eu:HA nanoparticles, the structures at the near-surface layers with the thickness of about

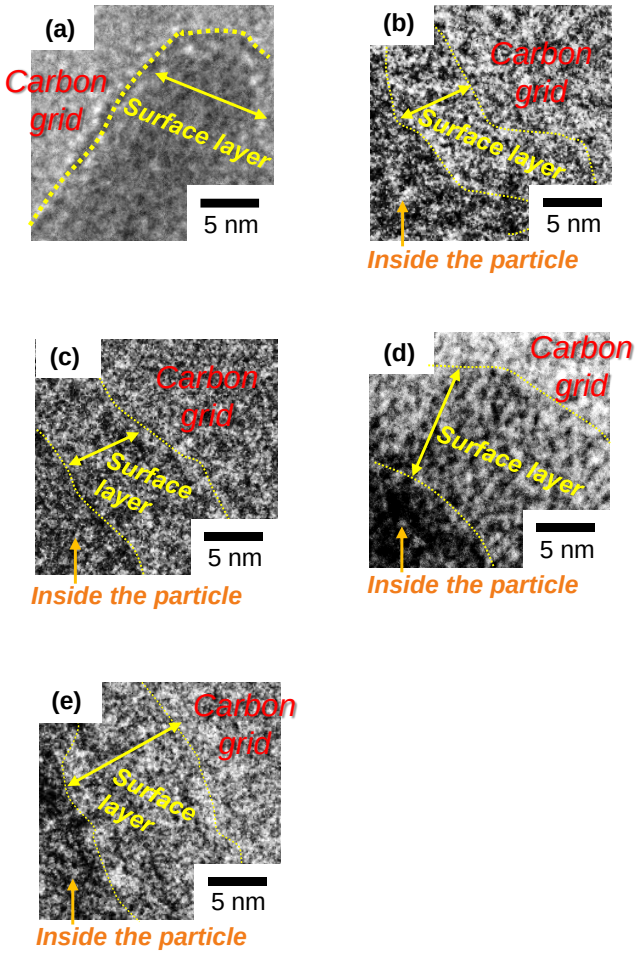

Figure 3-11. (a−e) TEM images of the surface structural layers of the Cit/Eu:HA nanoparticles ((a) **0**Cit/Eu:HA, (b) **1**Cit/Eu:HA, (c) **2**Cit/Eu:HA, (d) **3**Cit/Eu:HA and (e) **4**Cit/Eu:HA). Although the TEM images were acquired while minimizing the damage of the nanoparticle structures by the electron beam.

3−8 nm was different from those of the inner, suggesting the disordering of the surface atomic structures by the coordination with Cit. From the result of the XRD patterns (**Figure 3-8**), the inside and near surfaces of the nanoparticles would be HA crystalline phase and an amorphous calcium phosphate-containing Cit molecules, respectively. Furthermore, the zeta potential values of the nanoparticles were changed to be negative with increasing the coordinated amount of Cit (**Table 3-2**). From the FT-IR results (**Figure 3-4** and **Figure 3-5**), the Cit molecules enhanced the structural disordering of the nanoparticles [33], and the atomic structures at the Eu:HA surface layers become the disordering. Therefore, it was suggested that the Cit molecules existed on the surface of the nanoparticles, even though the TEM images should be acquired while minimizing the electron beam damages. In the future, a detailed surface analysis will be carried out to understand the atomic disordering mechanism. Therefore, the disordered surface structures at the near surfaces of **1**Cit/Eu:HA, **2**Cit/Eu:HA, **3**Cit/Eu:HA and **4**Cit/Eu:HA nanoparticles were successfully observed.

Figure 3-12 showed the FT-IR spectra of the ***X***Cit/Eu:HA and Cit/EuCa and a detailed illustration of the possible coordinated structures of the Cit on the Eu:HA crystal structural surfaces. The characteristic bands of Cit/EuCa also appeared at around 950−920, 880 and 885 cm^{-1}, which were attributed to stretching vibration of C−C, twisting vibration of $-CH_2-$ and stretching vibration of C−C, respectively, and the absorption bands of Cit/EuCa were overlapped with those of Eu:HA, as shown in **Figure 3-12(a)**. Therefore, it is possible that a compound similar to Cit/EuCa was formed on Eu:HA as shown in **Figure 3-12(b)**, and indicated the illustration of the possible coordinated structures of the Cit molecules coordinated on the Eu:HA nanoparticle surfaces. As the expected Eu:HA nanoparticle state, the *S* and *L* values along with the *a*- and *c*-axis directions were about 18 and 48 nm, respectively. Taking into account the crystallite sizes (D_{002} and D_{300}) estimated by the XRD result, the Eu:HA nanoparticle was a single crystal. The TEM images of the near-surface layers of the nanoparticles (**Figure 3-11**) revealed the homogeneous atomic arrangement. From the result of FT-IR spectra, the presence of PO_4^{3-} and HPO_4^{2-} in the Eu:HA were confirmed. In the charge compensation process, the Eu^{3+} ion substitution into the Ca site induces one vacancy inside the site [15,52], and the unstable vacancy was compensated by the HPO_4^{2-} ion generated at the phosphate site for achieving the electrical neutrality in the crystal. Thus, the increase in the defects in the structure of nanoparticle induced the change in the environmental phosphate ion state around Eu^{3+} ion into an asymmetry. As the result, it was suggested that the environmental coordination structures around Eu^{3+} ions in the Ca(I) site became the low symmetry.

For the expected Cit/Eu:HA nanoparticle state, the *S* and *L* values along with the *a*- and *c*-axis directions were about 9–12 and 16–20 nm, respectively, and these values mismatch with the D_{002} and D_{300} values estimated by the XRD patterns, suggesting the polycrystalline state in one particle. The surface structural layers of the nanoparticles in TEM images (**Figure 3-11**) suggested the formation of the surface layer based on the low crystalline calcium phosphate, which would be attributed to the atomic disordering by the Cit coordination. By the Cit molecules preferentially included in the surface layer, the Cit/Eu:HA nanoparticles provided the negatively-charged state. From the results on the FT-IR spectra, the presence of PO_4^{3-} and HPO_4^{2-} ions were confirmed and the proportion of PO_4^{3-} and HPO_4^{2-} increased and decreased by the coordination with Cit, respectively, and the spectral shape changes indicated that the coordinated Cit molecules enhanced the structural disordering of phosphate site in the Eu:HA nanoparticles [33]. The Eu^{3+} ions in the Ca(I) site interacted with the phosphate site ions, and the covalent bond ratio at the interface increased due to the chelate formation [39] between Cit and Eu^{3+}according to the excitation spectral result (i.e., the CT transition band of the Eu−O bond change). As a result, the symmetry coordination structure of the Ca(I) site would be lowered by the coordination with Cit, leading to the enhanced luminescence efficiency. Thus, it was suggested that

the low symmetry of the coordination structure for the Ca (I) site was an important factor for achieving an enhanced luminescence efficiency.

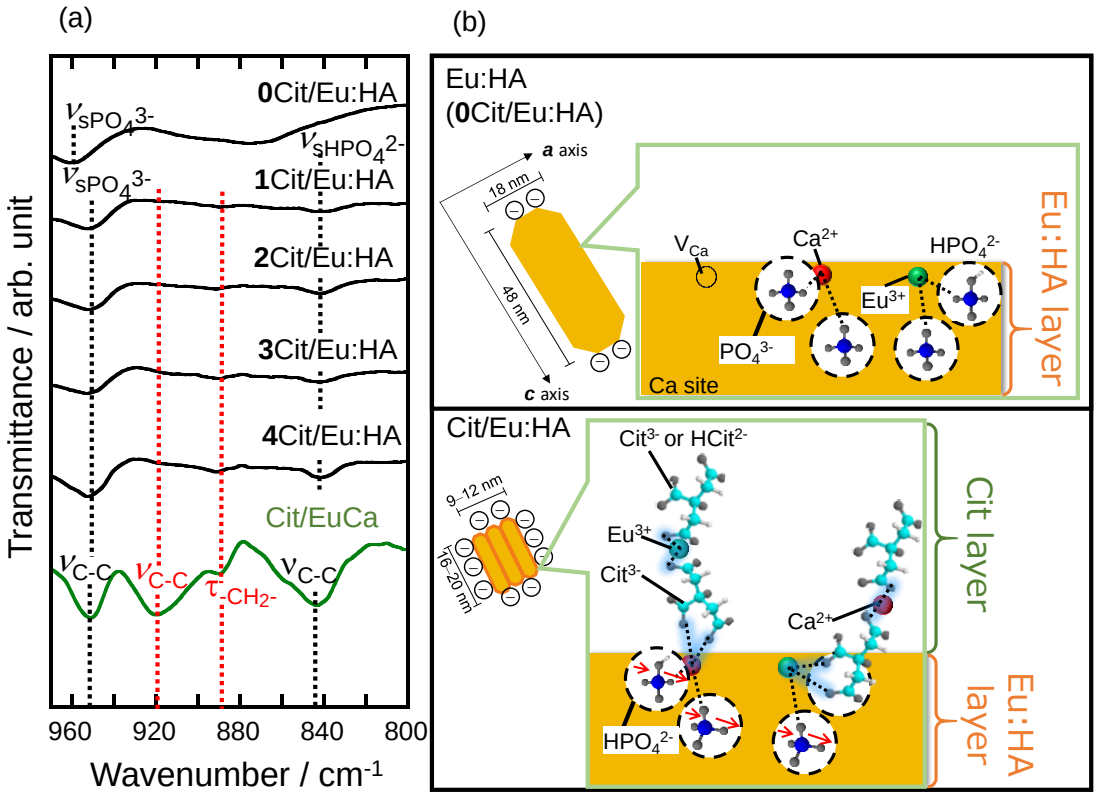

Figure 3-12. (a) FT-IR spectra of the ***X***Cit/Eu:HA and Cit/EuCa. (b) Detailed illustration of the crystalline sizes of Eu:HA nanoparticles and the possible coordination structures of the Cit on the surfaces.

Figure 3-13 showed the number of Cit layer and the maximum thickness of Cit layer of ***X***Cit/Eu:HA nanoparticle, and the average thickness change of Cit and Eu:HA layer by TEM with the maximum thickness of Cit layer, and the detailed illustration of the possible coordinated structures by substitution, adsorption and multi-layer formation of the Cit on the Eu:HA crystal structural surfaces. The number of Cit layer and the maximum thickness of Cit layer of ***X***Cit/Eu:HA nanoparticle increased linearly with the increase of the Cit molecular occupancy as shown in **Figure 3-13(a)**. The average thickness change of Cit and Eu:HA layer by TEM was almost proportional as shown in **Figure 3-13(b)**. It was suggested that the region where the layer was observed by TEM was a layer containing both the Cit and the amorphous Eu:HA near-surface layer. Considering the size of the Cit molecule, it was suggested that all the region (i.e., surface structural layers) observed by TEM was mainly derived from the amorphous state of Eu:HA. Thus, as shown in **Figure 3-13(c)**, The Cit may be substituted with HPO_4^{2-} in Eu:HA, when it first interacts with Eu:HA. The decrease in the

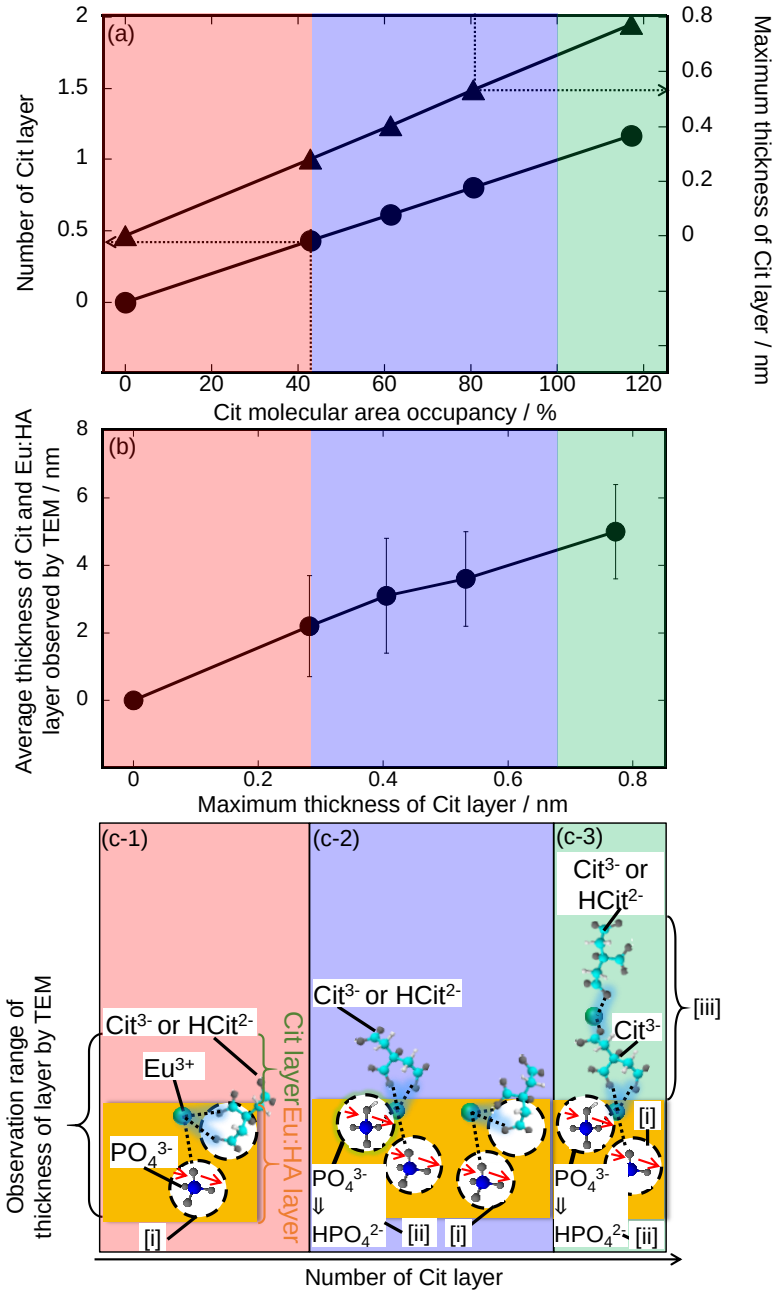

Figure 3-13. (a) Number of Cit layer and maximum thickness of Cit layer on ***X***Cit/Eu:HA nanoparticle. (b) Average thickness change of the Cit and Eu:HA layers observed by TEM with the maximum thickness of Cit layer. (c) Detailed illustrations of the possible coordination structures by (c-1) substitution, (c-2) adsorption and (c-3) multilayer formation of the Cit on the Eu:HA surfaces, which were totally investigated by the above results. The red, blue and green regions in the figures indicate the possible regions of substitution, adsorption and multilayer formation, respectively.

energy state of electron transfer from O to Eu by the substitution with Cit represents the increase in the covalent bonding degree ([i] in **Figure 3-13(c)**). As the result, the Cit molecule enhances the structural disorder of the Eu:HA nanoparticles and polycrystallizes the surface layers to be amorphous

state. Then, it is suggested that Cit adsorbs to the Ca site on the Eu:HA. After that, as a result of the interaction of C=O in Cit with Ca site, it is considered that the ratio of [HPO_4^{2-}] increased in order to keep the charge of HA crystals neutral [46] ([ii] in **Figure 3-13(c)**). The decrease of [HPO_4^{2-}] suggested that H^+ in HPO_4^{2-} was pulled out to become PO_4^{3-}. Then, the compound similar to Cit/EuCa was formed on Eu:HA to be the multilayer-state ([iii] in **Figure 3-13(c)**).

The excitation and luminescence spectra, I and η_{int} value changes of the Cit/Eu:HA nanoparticles were shown in **Figure 3-14**. In the excitation spectra of the Cit/Eu:HA nanoparticles (**Figure 3-14(a)**), all the peaks could be attributed to the f–f transitions within the $4f^6$ electron configuration, reflecting the electronic transitions of the Eu^{3+} ion [16]. The excitation spectra for the Cit/Eu:HA nanoparticles consisted of several peaks, which were located at 363 nm ($^7F_0 \rightarrow {}^5D_4$), 383 nm ($^7F_0 \rightarrow {}^5G_4$), 394 nm ($^7F_0 \rightarrow {}^5L_6$), 464 nm ($^7F_0 \rightarrow {}^5D_2$) and 535 nm ($^7F_0 \rightarrow {}^5D_1$), and the spectral shapes among the Cit/Eu:HA nanoparticles were almost same. In the visible light range (400–550 nm) and the UVA range (315–400 nm), the most PL intense band assigned to the excitation from the ground $^7F_0$ to the $^5D_2$ level and $^7F_0$ to the $^5L_6$ are located at 464 nm, so that the wavelengths were used to excite the Eu^{3+} ions in the following.

Figure 3-14(b) exhibited the luminescence spectra of the Cit/Eu:HA nanoparticles under the excitation wavelength at 464 nm. The luminescence exhibited the red-color digital camera image by the UVA light irradiation of the **4**Cit/Eu:HA (**Figure 3-14(b) Inset**). All the peaks corresponded to the transitions from the metastable orbital singlet state of $^5D_0$ to the spin–orbital states of ^7F_J (J = 0, 1, 2, 3, 4) of the Eu^{3+} ion. These characteristic transitions were assigned to the $^5D_0$ to $^7F_0$ at 579 nm, $^7F_1$ at 590 nm, $^7F_2$ at 615 nm (for **0**Cit/Eu:HA) or 617 nm (for **1**Cit/Eu:HA, **2**Cit/Eu:HA, **3**Cit/Eu:HA and **4**Cit/Eu:HA), $^7F_3$ at 653 nm and $^7F_4$ at 698 nm, respectively. The observation of $^5D_0 \rightarrow {}^7F_0$ transition at 579 nm implied that the Eu^{3+} ion is thought to be abundant at the Ca (I) site [14]. The spectral shape of the $^5D_0 \rightarrow {}^7F_2$ transition (i.e., Stark splitting state [16,53]) were compared among **0**Cit/Eu:HA and **1**Cit/Eu:HA, **2**Cit/Eu:HA, **3**Cit/Eu:HA and **4**Cit/Eu:HA were changed. This would be attributed to the change in the coordination space symmetry of Eu^{3+} ion by the coordination with Cit. Here, the $^5D_0 \rightarrow {}^7F_1$ (between 583−603nm) and $^5D_0 \rightarrow {}^7F_2$ (between 603−636nm) transitions can be attributed to magnetic dipole and electric dipole transitions, respectively [54]. The integrated luminescence intensities of the $^5D_0 \rightarrow {}^7F_1$ and $^5D_0 \rightarrow {}^7F_2$ were I_{590} and I_{615}, respectively. The intensity of the magnetic dipole transition exhibits very little variation with the crystal field strength acting on the Eu^{3+} ion. The electric-dipole transition is sensitive to the local structure surrounding the Eu^{3+} ion. Accordingly, the relative peak intensity ratio (i.e., I_{590}/I_{615}) indicates the spatial symmetry of the Eu^{3+} ion site [55], and the I_{590}/I_{615} values under an excitation wavelength of 464 nm were measured to be 0.38, 0.41, 0.40, 0.37 and 0.36 for **0**Cit/Eu:HA, **1**Cit/Eu:HA, **2**Cit/Eu:HA, **3**Cit/Eu:HA and

4Cit/Eu:HA, respectively. Among the **1**Cit/Eu:HA, **2**Cit/Eu:HA, **3**Cit/Eu:HA and **4**Cit/Eu:HA, the value slightly decreased with increasing the coordinated amount of Cit. It was indicated that the spatial symmetry of Eu^{3+} ion was lowered with the coordination amount with Cit, indicating the coordination environment (i.e., symmetry) change of the Eu^{3+} ion in the Cit/Eu:HA nanoparticles by the coordination.

Figure 3-14(c) showed the I and η_{int} value changes of the Cit/Eu:HA nanoparticles under the excitation at 464 nm. The highest I value in the Cit/Eu:HA nanoparticles was observed in **4**Cit/Eu:HA. The I values of **4**Cit/Eu:HA under the excitation at 464 nm were higher 3 times than those of the **0**Cit/Eu:HA. Moreover, the **4**Cit/Eu:HA exhibited the best η_{int} values of 12.5 % under the excitation at 464 nm, and the η_{int} values of **4**Cit/Eu:HA were higher 4 times than those of the **0**Cit/Eu:HA, which are best values in the previously-reported luminescent HA systems. For example, the Eu^{3+} ion-doped HA nanoparticles exhibited the efficient η_{int} values of 2.1 % under the excitation wavelength of 393 nm [38]. The enhanced luminescence intensity would be attributed to the change in the disordering of the atomic structures at the Eu:HA surface layer to lower the spatial symmetry of Eu^{3+} ion by the coordination of Cit molecules to the Eu:HA. The coordination of Cit molecules to the Eu:HA lowered the Eu^{3+} spatial symmetry and permitted the *f-f* transition with the chelate formation between Cit and Eu^{3+} [56], and achieved the distance between the Eu^{3+} ions that do not cause concentration quenching and suppressed the deactivation due to the resonance energy transfer to water molecules, suggesting the enhanced luminescence. Therefore, the luminescence enhancement with the coordination was successfully elucidated, and **4**Cit/Eu:HA exhibited the highest η_{int} value in the previous reports. As the expected Eu:HA nanoparticle state, there are two types of Ca sites, which are Ca(I) with C_3 symmetry surrounded by 9 oxygen atoms and Ca(II) with C_s symmetry surrounded by 7 oxygen atoms [57]. From the analytical result of the luminescence spectral peak due to $^5D_0 \rightarrow {}^7F_0$ transition, the Eu^{3+} ions were preferentially present in the Ca(I) site. It has been reported that the bond distance between Ca(I) site–O and Ca(II) site–O were 0.2553 and 0.2459 nm, respectively [14]. The distance between Ca(I) site–O atom is longer than that between Ca(II) site–O atom, suggesting that the concentration quenching between the Eu^{3+} ions would be suppressed by the substitution into Ca(I) site to resultantly provide the efficient luminescence. Therefore, the luminescence of the substituted Eu^{3+} ion in HA would be affected by the environmental phosphate ion type and the special symmetry in the Ca site to totally provide the negatively-charged surface property. For the expected Cit/Eu:HA nanoparticle state, the Eu^{3+} ions in the Ca(I) site interacted with the phosphate site ions, and the covalent bond ratio at the interface increased due to the chelate formation [39] between Cit and Eu^{3+}according to the excitation spectral result (i.e., the CT transition band of the Eu−O bond change). As a result, the symmetry coordination structure of the Ca(I) site would be lowered by the coordination with Cit,

leading to enhanced luminescence efficiency. Thus, it was suggested that the low symmetry of the coordination structure for the Ca (I) site was an important factor for achieving an enhanced luminescence efficiency.

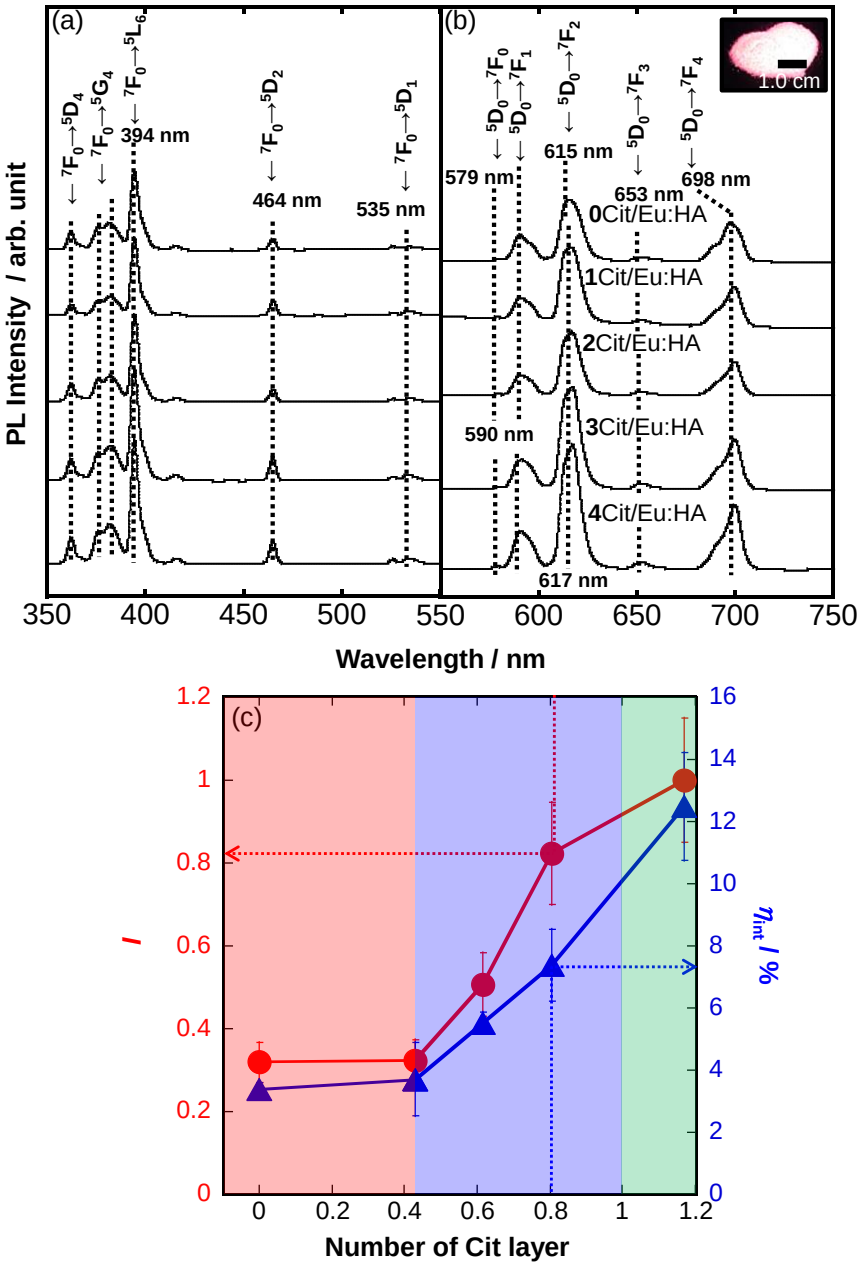

Figure 3-14. (a) Excitation and (b) luminescence spectra of the Cit/Eu:HA nanoparticles. The monitored luminescence and excitation wavelengths for the excitation and luminescence spectral measurements were 615 or 617 nm and 464 nm, respectively. Inset: digital camera image after the UVA light irradiation of the **4**Cit/Eu:HA. (c) *I* and η_{int} value changes of the Cit/Eu:HA nanoparticles, which was excited under the wavelengths of 464 nm. Here, the red, blue and green regions in the figures indicate the possible regions of substitution, adsorption and multilayer formation, respectively.

3.3.2 Size distributions of the nanoparticles in phosphate buffer saline

Figure 3-15 shows the digital camera image before and after the UVA light irradiation of the **4**Cit/Eu:HA dispersed in PBS (**Figure 3-15(a-1** and **a-2)**), and particle size distributions of **0**Cit/Eu:HA, **1**Cit/Eu:HA, **2**Cit/Eu:HA, **3**Cit/Eu:HA, **4**Cit/Eu:HA and **FA4**Cit/Eu:HA nanoparticles dispersed in PBS (**Figure 3-15(b-g)**), and the *Ave.* and *Cv.* value changes with the coordinated Cit amount (**Figure 3-15(h)**). Red luminescence was confirmed from the dispersion. The *Ave.* and *Cv.* values were 113 nm and 29 % for **0**Cit/Eu:HA, 83 nm and 9.9 % for **1**Cit/Eu:HA, 84 nm and 7.2 % for **2**Cit/Eu:HA, 65 nm and 7.8 % for **3**Cit/Eu:HA, and 90 nm and 7.7 % for **4**Cit/Eu:HA. The *L/S* distribution of the **0**Cit/Eu:HA based on the TEM observation result indicated the bimodal, suggesting that **0**Cit/Eu:HA had an anisotropic nanoparticle shape. Thus, the aggregation form of **0**Cit/Eu:HA dispersed in PBS also exhibited the bimodal distribution that was analyzed by the electric resistance nanopulse method in this study, which was reflected to the primary nanoparticle shapes of **0**Cit/Eu:HA. Here, this electric resistance nanopulse method was able to obtain a result following the aspect ratios of the nanoparticle by TEM [58]. The *Cv.* values of **1**Cit/Eu:HA, **2**Cit/Eu:HA, **3**Cit/Eu:HA and **4**Cit/Eu:HA were significantly suppressed by the coordination with Cit to be monodispersed sate in PBS. Therefore, the Cit/Eu:HA nanoparticles dispersibility in PBS was improved by the coordination of the negatively-charged Cit molecules. The uptake of the HA particles with a size of 50−200 nm (concentration: 100 μg/mL) by the osteoblasts has been investigated, and those with the size of 80 nm exhibited the best uptake efficiency without the cytotoxic proliferation behavior [50]. From the viewpoint of the particle sizes, the Cit/Eu:HA nanoparticles synthesized in this study are thought to be suitable for uptake efficiency and non-cytotoxicity. In particular, **4**Cit/Eu:HA exhibited the highest I and η_{int} values among the Cit/Eu:HA nanoparticles, and **4**Cit/Eu:HA and FA-NHS-immobilized **4**Cit/Eu:HA (**FA4**Cit/Eu:HA) were mainly used in the following experiment.

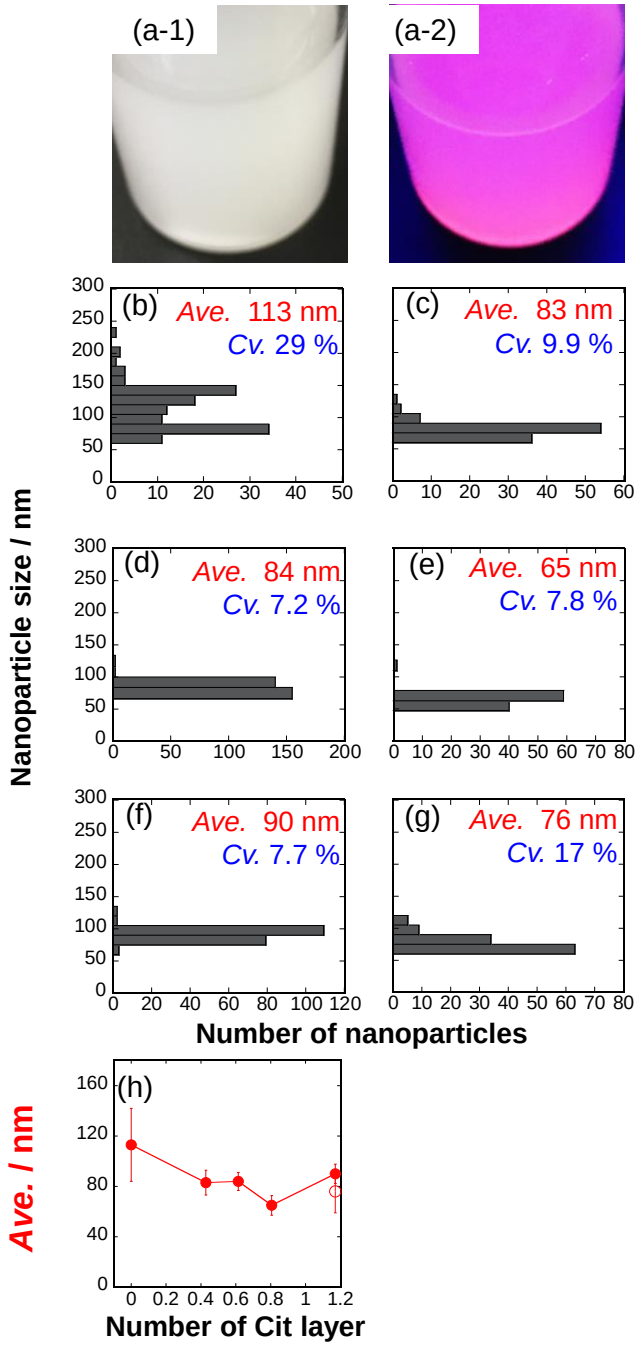

Figure 3-15. Digital camera image (a-1) before and (a-2) after the UVA light irradiation of the **4**Cit/Eu:HA dispersed in PBS (nanoparticle concentrations : 1.0 mg/mL). Particle size distributions of (b) **0**Cit/Eu:HA, (c) **1**Cit/Eu:HA, (d) **2**Cit/Eu:HA, (e) **3**Cit/Eu:HA, (f) **4**Cit/Eu:HA and (g) **FA4**Cit/Eu:HA dispersed in PBS (Cit/Eu:HA nanoparticle concentration: 50 ng/mL), and (h) the *Ave*. value changes with the coordinated Cit amount. ○ show the *Ave*. value for **FA4**Cit/Eu:HA .

3.3.3 Cytotoxicity of the nanoparticles

The adhered fibroblast density changes in the reaction with the Cit/Eu:HA nanoparticles with the culture time were shown in **Figure 3-16(A)**. All the samples showed a linear increase with the

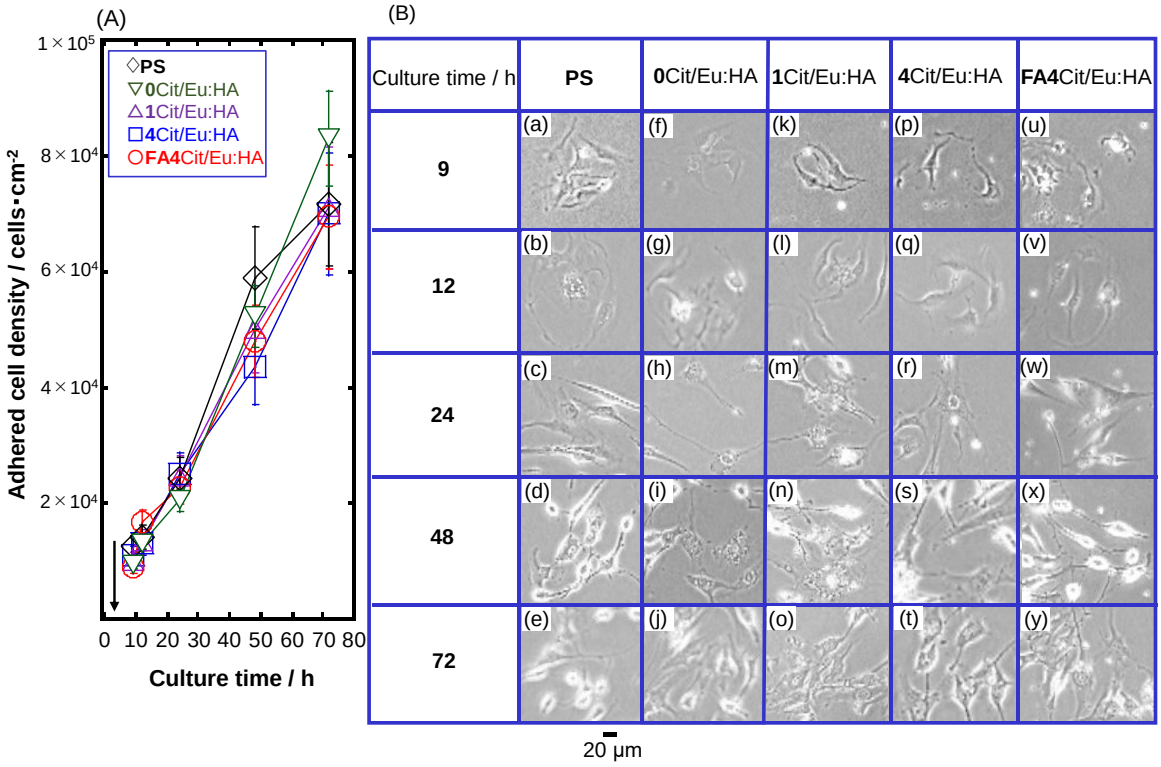

Figure 3-16. (A) Adhered fibroblast density changes in the reaction with the Cit/Eu:HA nanoparticles with the culture time (Cit/Eu:HA nanoparticle concentration: 100 μg/mL). The arrow in the figure indicates the Cit/Eu:HA nanoparticles addition point at the culture time of 6 h. (B) (a–y) Optical transmittance images of the fibroblasts reacted with the Cit/Eu:HA nanoparticles ((a–e) **PS**, (f–j) **0**Cit/Eu:HA, (k–o) **1**Cit/Eu:HA, (p–t) **4**Cit/Eu:HA and (u–y) **FA4**Cit/Eu:HA) for the culture time of 72 h.

culture time, and there was no significant difference between the samples. At the culture time of 72 h, the cell density of **PS**, **0**Cit/Eu:HA, **1**Cit/Eu:HA, **4**Cit/Eu:HA and **FA4**Cit/Eu:HA were 71600 ± 11000, 83000 ± 8000, 71000 ± 11000, 70000 ± 10500 and 69500 ± 9000 cells/cm^2, respectively. Therefore, non-cytotoxic behaviors of the Cit/Eu:HA nanoparticles were elucidated. The optical transmittance images of the fibroblasts reacted with the Cit/Eu:HA nanoparticles for the culture time of 72 h were shown in **Figure 3-16(B)**. The adherent cells spread, and the number of cells increased with the culture time. The nanoparticles on the cells could not be confirmed, so that the nanoparticles may interact with the cells at the dispersed state and be taken up by the cells. There were many fusiform cells and was no significant difference in the cellular shapes irrespective of the addition of the nanoparticles. Thus, the fibroblast affinity of the nanoparticles was confirmed.

3.3.4 Cell labeling and cytostatic ability of the nanoparticles against cancer cells

Figure 3-17(A) shows the adhered HeLa cell density changes in the reaction with the Cit/Eu:HA nanoparticles with the culture time. All the samples induced an increase of cell density with the culture time. In particular, the **1**Cit/Eu:HA, **4**Cit/Eu:HA and **FA4**Cit/Eu:HA increased moderately with the culture time, and these slopes of the growth line curves were smaller than those of **PS** and **0**Cit/Eu:HA. A significant difference between the samples was observed with culture time. At the culture time of 72 h, the cell densities with interacting **PS**, **0**Cit/Eu:HA, **1**Cit/Eu:HA, **4**Cit/Eu:HA and **FA4**Cit/Eu:HA were 88000 ± 13000, 76000 ± 7500, 45000 ± 6700, 46000 ± 6900 and 35000 ± 4500 cells/cm^2, respectively. The Cit/Eu:HA nanoparticles (**1**Cit/Eu:HA, **4**Cit/Eu:HA and **FA4**Cit/Eu:HA) exhibited the lower cell densities, indicating that the suppression of the HeLa cell growth was started at the time of 18 h after the addition of the nanoparticles. It was supposed that the coordinated Cit molecules effectively form the chelate with Ca^{2+} ion or Fe^{2+} ion at the acidic biological fluid inside the HeLa cells with the dissolving of the HA host matrix, and inhibit the action of the proteins (e.g, iron-binding protein 1) involved in the cell growth and antioxidant enzymes [28]. Furthermore, it was suggested that the interactions between Fe^{2+} ions and Cit ions depleted Fe^{2+} ion concentration in the cytoplasm, leading to cell death [29]. And, it has been also reported that the glycolytic system of the cell is inhibited to suppress cell proliferation [59]. Therefore, it was suggested that the suppression of the HeLa cell growth (i.e., the cytostatic property) was achieved by the interactions with the Cit/Eu:HA nanoparticles.

Figure 3-17(B) indicates the integrated luminescence intensity changes of the HeLa cells reacted with the Cit/Eu:HA nanoparticles under the excited wavelength at 464 nm with the culture time. The adhered cells were washed twice with PBS to remove the non-bonded nanoparticles and non-adhered cells. After the washing, the integrated luminescence intensity of the adhered cells with interacting the Cit/Eu:HA nanoparticles was evaluated and increased with the culture time, indicating that the binding and uptake of the nanoparticles by the cells occurred to exhibit the intense luminescence intensity. In particular, the luminescence intensity from the cells reacted with the **FA4**Cit/Eu:HA greatly increased at the culture time of 24–48 h. It was suggested that the FA molecular receptor on the cells was excessively expressed to resultantly promote the binding between cells and **FA4**Cit/Eu:HA and the uptake finally occurred [60]. The cells interacted with **FA4**Cit/Eu:HA showed the highest luminescence intensity, even although the cell density for the case in **FA4**Cit/Eu:HA was lower than that for the case in the other samples, suggesting that the cell−nanoparticle interactive uptakes proceeded efficiently. Therefore, the Cit/Eu:HA nanoparticles were successfully reacted with

the HeLa cells and the red-color luminescence from the cells could be observed while suppressing the HeLa cell growth, indicating the bifunctional labeling and cytostatic property of the HeLa cells.

The optical transmittance and FM images of the HeLa cells reacted with the Cit/Eu:HA nanoparticles for the culture time of 72 h were shown in **Figure 3-17(C)**. From the optical transmittance images, the adherent cells spread and the number of cells increased with the culture time. There were no significant difference in the cellular shapes and many elongated and spindle-shaped cells were observed, and the FM images along with the cellular shapes were clearly observed. Until the 3 h after the addition of the Cit/Eu:HA nanoparticles, the FM images were unclear, and those at the 6 h after the addition were clear. The Cit/Eu:HA nanoparticles may interact safely with the cells and be taken up by the cells for 6 h. Additionally, the luminescence intensity from the cells was enhanced by the coordination with Cit. In particular, the cells interacted with the **FA4**Cit/Eu:HA exhibited the strongest luminescence. The luminescence of **FA4**Cit/Eu:HA was apparently observed from the inside/outside of the cellular surfaces, suggesting that the nanoparticles were partially taken up into the cellular insides. Then, the achievement of the cell growth suppression may also be an evidence against the presence of **FA4**Cit/Eu:HA inside the cell. The efficient luminescence from the cells by the FM observation was obtained at the culture time of 72 h, suggesting that the binding and uptake efficiency against the cells through the FA receptor overexpressed on the surfaces was sufficient [60]. Thus, the Cit/Eu:HA nanoparticles could be reacted with the HeLa cells to exhibit the appropriate cellular shapes.

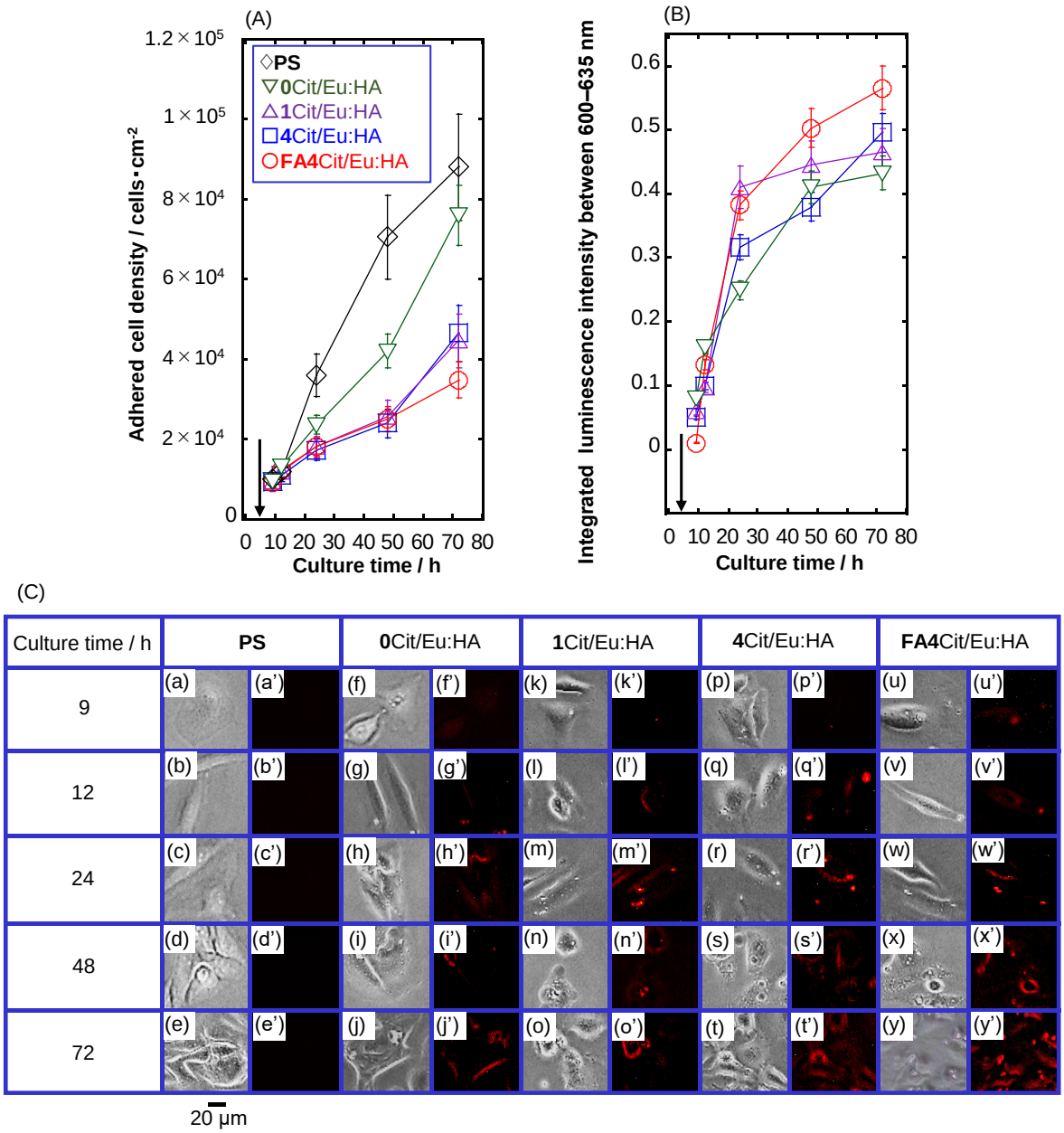

Figure 3-17. (A) Adhered HeLa cell density changes in the reaction with the Cit/Eu:HA nanoparticles with the culture time (Cit/Eu:HA nanoparticles concentration: 100 μg/mL). (B) The integrated luminescence intensity changes at the wavelengths between 600–635 nm of the HeLa cells reacted with the Cit/Eu:HA nanoparticles under the excited wavelength at 464 nm with the culture time. Here, the integrated luminance intensity from TCPS alone was subtracted from those of the Cit/Eu:HA nanoparticles. Arrows in the figures indicate the addition timing of the Cit/Eu:HA nanoparticles at the culture time of 6 h. (C) Optical transmittance and FM images of the HeLa cells reacted with the Cit/Eu:HA nanoparticles. (a–e, f–j, k–o, p–t and u–y) Optical transmittance and (a'–e', f'–j', k'–o', p'–t' and u'–y') FM images of the HeLa cells reacted with the Cit/Eu:HA nanoparticles ((a–e, a'–e') **PS**, (f–j, f'–j') **0**Cit/Eu:HA, (k–o, k'–o') **1**Cit/Eu:HA, (p–t, p'–t') **4**Cit/Eu:HA and (u–y, u'–y') **FA4**Cit/Eu:HA) for the culture time of 72 h. The images of (a'–y') were same positions to those of (a–y).

Scheme 3-5 showed the illustration of the cytostatic mechanism by Cit. **FA4**Cit/Eu:HA binds to the folic acid receptor located on the cell membrane and is taken up by endocytosis. When it becomes an acidic environment in the lysosome (endosome), Fe^{3+} ions are then dissociated into Fe^{2+} ions. It then forms the chelate complex with the Cit dissolved from **FA4**Cit/Eu:HA, depletes Fe^{2+} ions in the cytoplasm, and inhibits the growth of the cells [29]. The binding affinity between citric acid and Fe^{2+} ion is about 5.0×10^{19} M^{-1} [26], and the binding affinity between citric acid and Ca^{2+} ion is about 2.0×10^{4} M^{-1} [27]. In the cells, the stable chelates are formed between the Fe^{2+} ions and citric acid to successfully induce the cytostatic property.

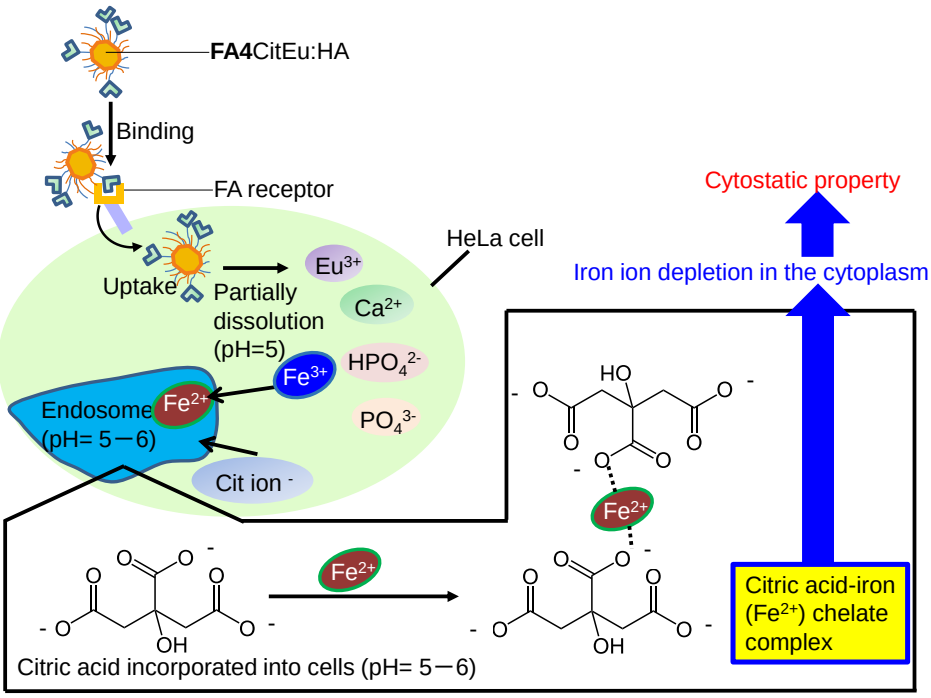

Scheme 3-5. Illustration of cytostatic mechanism by Cit ion. In details, the Cit and Fe^{2+} ions can form a chelate complex, and the depletion of the Fe^{2+} ions in the cytoplasm can suppress the cancer cell proliferation. The binding affinity between Cit and Fe^{2+} is about 5.0×10^{19} M^{-1}, and the binding affinity between Cit and Ca^{2+} is about 2.0×10^{4} M^{-1}, indicating that the stable chelates are formed between Cit and Fe^{2+} in the HeLa cells.

The **FA4**Cit/Eu:HA, which provided the preferential bifunctional of the labeling and cytostatic property of the HeLa cells, was added to the cells after the culture time of 60 h. **Figure 3-18(A)** shows the adhered HeLa cell density changes in the reaction with the Cit/Eu:HA nanoparticles with the culture time. The cells cultured for 60 h clearly exhibited the elongated and spindle-shaped states, which were tumor cells and can be defined as spheres [34]. In the application for the cell labeling nanoparticles, the evaluation against the spheres is important. In the following, the cytostatic property and cell labeling ability against the spheres were evaluated using **FA4**Cit/Eu:HA. The **FA4**Cit/Eu:HA induced the lower sphere growth behavior than the case in the **PS** with culture time. In particular, the

suppression of the sphere growth clearly began to be at the time of 12 h after adding **FA4**Cit/Eu:HA. Thus, it was confirmed that the coordinated Cit molecules could significantly contribute to the sphere growth suppression.

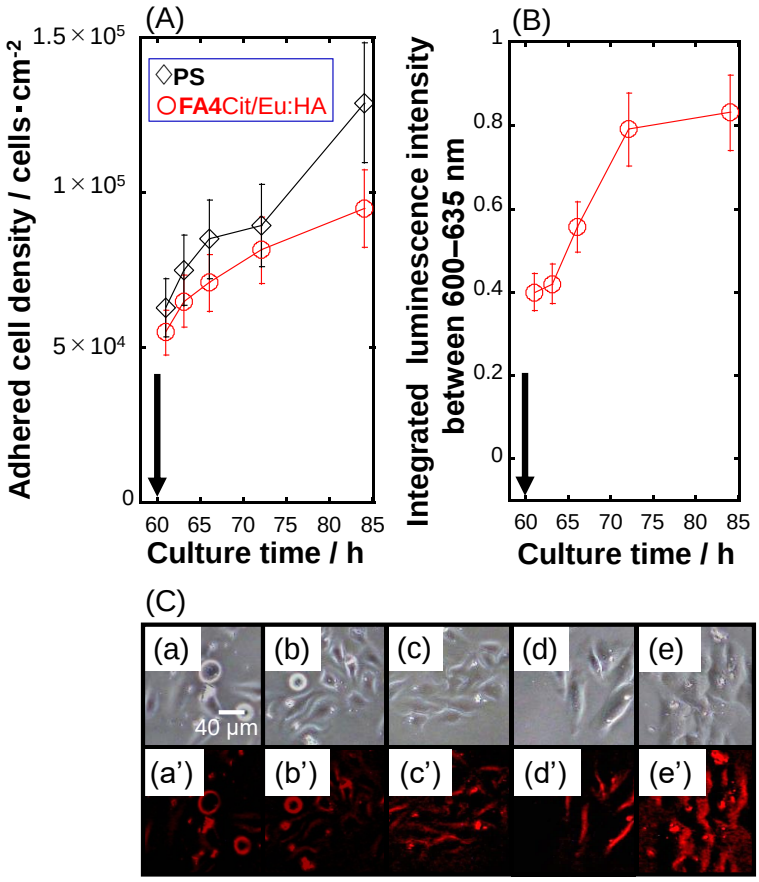

Figure 3-18. (A) Adhered HeLa cell density changes in the reaction with the Cit/Eu:HA nanoparticles with the culture time from the Cit/Eu:HA nanoparticles addition point at the culture time of 60 h (Cit/Eu:HA nanoparticles concentration: 100 μg/mL). (B) The integrated luminescence intensity change at the wavelengths between 600–635 nm of the HeLa cells reacted with **FA4**Cit/Eu:HA under the excited wavelength at 464 nm. Here, the integrated luminance intensity from TCPS alone was subtracted from those of the Cit/Eu:HA nanoparticles. Arrows in the figures indicate the addition timing of the Cit/Eu:HA nanoparticles at the culture time of 60 h. (C) Optical transmittance (a–e) and (a'–e') FM images of the HeLa cells reacted with **FA4**Cit/Eu:HA. The photographs were subsequent cultured at (a, a') 1, (b, b') 3, (c, c') 6, (d, d') 12 and (e, e') 24 h, indicating the culture times of 61, 63, 66, 72 and 84 h. The images of (a'–e') were same positions to those of (a–e).

Figure 3-18(B) exhibits the integrated luminescence intensity change of the spheres reacted with **FA4**Cit/Eu:HA under the excited wavelength at 464 nm. The cells reacted with **FA4**Cit/Eu:HA increased with the culture time, and the luminescence intensity was enhanced at the time of 12 h after the addition of the nanoparticles and those were suppressed at the time of 24 h. For the possible

mechanism, the **FA4**Cit/Eu:HA was incorporated inside the sphere by the efficient binding/uptake rout based on the sphere−nanoparticle interactions and transported into the intracellular endosome and lysosome, where the pH value was 6.0−6.5 and 4.0−5.5, respectively [61], suggesting that the **FA4**Cit/Eu:HA would be dissolved in the endosome and lysosome to slightly suppress the intensity enhancement at the time of 24 h.

The optical transmittance and FM images of the spheres that reacted with **FA4**Cit/Eu:HA are shown in **Figure 3-18(C)**. From the optical transmittance images, the adherent spheres spread and the size of spheres increased with the culture time. At the time of 1 h after the **FA4**Cit/Eu:HA addition, the cell labeling with following the cellular shapes was successfully achieved, suggesting that the **FA4**Cit/Eu:HA would exist along with the cellular shapes. The labeling contrast was enhanced until the time of 24 h after the nanoparticle addition, indicating that the **FA4**Cit/Eu:HA may interact safely with the spheres with the culture. Therefore, **FA4**Cit/Eu:HA was effectively reacted with the spheres after the culture time of 60 h, and the luminescent labeling with following the cellular shapes could be observed at the time of 1 h after the nanoparticle addition, indicating the speedy cell labeling process with cytostatic property for the spheres. In particular, the sphere growth began to be suppressed at the time of 12 h after the nanoparticle addition.

3.4 Conclusion

The efficient luminescence ability in the application for HeLa cell label including the higher η_{int} based on the photofunctional interfaces between the Cit and Eu:HA in the nanoparticles was achieved, and the Cit molecular effect on the suppression of the HeLa cell line growth was investigated. In particular, the Eu:HA nanoparticles were successfully synthesized in the presence of the Cit, and the Cit molecules coordinated with the Eu:HA nanoparticles and the physicochemical properties based on the Eu:HA/Cit interfacial interactions in the nanoparticles were elucidated. It was suggested that the monomer component ratio of Cit increased by the coordination based on the interaction with the Ca site on the HA structure. Accordingly, the monomeric Cit molecular coordination altered the bonding state between the Ca and the phosphate sites in the Eu:HA structure to increase the ratio of HPO_4^{2-} in the Eu:HA and subsequently disorder the surface atomic structures on the Eu:HA surface layer. Furthermore, it was suggested that the bonding states between the Eu and O atoms were changed due to the increase of the HPO_4^{2-} ratio by the coordination with Cit. The Cit molecules interacted with the Eu:HA nanoparticle surfaces sterically hindered the nanoparticle growth by the inorganic/organic interactions to form the spherical shape of Eu:HA nanoparticles. Considering that the Cit molecules interact with the Ca^{2+} ions and Eu^{3+} ions in the Cit/Eu:HA nanoparticle surface

layers, the Cit molecules would exist over the Ca ion sites on the Eu:HA to exhibit the negatively-charged property. The spatial symmetry of Eu^{3+} ion was lowered with the coordination amount with Cit, indicating the coordination environment change of the Eu^{3+} ion in the Cit/Eu:HA nanoparticles by the coordination. The luminescence enhancement with the coordination was successfully elucidated. In fact, the low symmetry of the coordination structure for the Ca (I) site was an important factor for achieving the enhanced luminescence efficiency. Furthermore, the FA-NHS was immobilized on the Cit/Eu:HA nanoparticles to resultantly enhance the uptake efficiency of the nanoparticles into the HeLa cells, and the cytocompatibility using NIH3T3 fibroblasts and cell labeling properties of HeLa cells were evaluated. As a result, non-cytotoxic behaviors of the Cit/Eu:HA nanoparticles were elucidated. Moreover, it was suggested that the suppression of the HeLa cell growth was achieved by the interactions with the Cit/Eu:HA nanoparticles. The Cit/Eu:HA nanoparticles were successfully reacted with the HeLa cells and the red-color luminescence from the cells could be achieved while suppressing the HeLa cell growth, indicating the bifunctional cell labeling and cytostatic property. The Cit/Eu:HA nanoparticles could be reacted with the HeLa cells to exhibit the appropriate cellular shapes, and the coordinated Cit molecules could significantly contribute to the sphere growth suppression. In particular, **FA4**Cit/Eu:HA was effectively reacted with the spheres after the culture time of 60 h, and the luminescent labeling with following the cellular shapes could be achieved at the time of 1 h after the nanoparticle addition, indicating the rapid labeling process with cytostatic property for the spheres.

The achievement statuses for initial targets in ***Chapter 1*** were evaluated and achieved by this chapter as below.

I Extreme biosafety for normal cells

- ✓ The N_1/N_0 ratios by all the nanoparticles were more than 0.8
- ✓ Average particle sizes in PBS were abuut 90 nm (coefficient of variation: 30 % or less)
- ✓ Excitation/luminescence light observation was in the visible region

II Efficient luminescence

- ✓ Strong luminescence intensity that can be visually confirmed
- ✓ Internal quantum efficiency: 12.5 %

III Construction of particle surface that is rapid binding with cancer cells and taken up into the cells at high concentration

- ✓ High concentration into the cell surfaces by the FA-NHS immobilization
- ✓ Short-term labeling of spheres at 1 h

IV Achievement of both cancer cell labeling and suppression of cell growth

- ✓ Growth suppression while labeling cells: N_1/N_0 ratios of **4**Cit/Eu:HA and

FA4 Cit/Eu:HA nanoparticles were 0.5

In this chapter, all the targets of I–IV were achieved.

References

[1] P. Sharma, S. Brown, G. Walter, S. Santra, B. Moudgil, Nanoparticles for bioimaging, Adv. Colloid Interface Sci. 123–126 (2006) 471–485.

[2] S.T. Selvan, T.T.Y. Tan, D.K. Yi, N.R. Jana, Functional and multifunctional nanoparticles for bioimaging and biosensing, Langmuir. 26 (2010) 11631–11641.

[3] K. Shivaji, S. Mani, P. Ponmurugan, C.S. De Castro, M. Lloyd Davies, M.G. Balasubramanian, S. Pitchaimuthu, Green-synthesis-derived CdS quantum dots using tea leaf extract: antimicrobial, bioimaging, and therapeutic applications in lung cancer cells, ACS Appl. Nano Mater. 1 (2018) 1683–1693.

[4] Y. Wang, R. Hu, G. Lin, I. Roy, K.T. Yong, Functionalized quantum dots for biosensing and bioimaging and concerns on toxicity, ACS Appl. Mater. Interfaces. 5 (2013) 2786–2799.

[5] S. Kang, K.M. Kim, K. jung, Y. Son, S. Mhin, J.H. Ryu, K.B. Shim, B. Lee, H.S. Han, T. Song, Graphene oxide quantum dots derived from coal for bioimaging: facile and green approach, Sci. Rep. 9 (2019) 1–7.

[6] W.-H. Zhang, X.-X. Hu, X.-B. Zhang, Dye-doped fluorescent silica nanoparticles for live cell and in vivo bioimaging, nanomaterials. 6 (2016) 81–97.

[7] J.E. Lee, N. Lee, H. Kim, J. Kim, S.H. Choi, J.H. Kim, T. Kim, I.C. Song, S.P. Park, W.K. Moon, T. Hyeon, Uniform mesoporous dye-doped silica nanocrystals for simultaneous enhanced magnetic resonance imaging, fluorescence imaging, and drug delivery, J. Am. Chem. Soc. 132 (2010) 552–557.

[8] M.F. Weng, S.Y. Chiang, N.S. Wang, H. Niu, Fluorescent nanodiamonds for specifically targeted bioimaging: Application to the interaction of transferrin with transferrin receptor, Diam. Relat. Mater. 18 (2009) 587–591.

[9] N. Prabhakar, J.M. Rosenholm, Nanodiamonds for advanced optical bioimaging and beyond, Curr. Opin. Colloid Interface Sci. 39 (2019) 220–231.

[10] Ł. Lamch, A. Pucek, J. Kulbacka, M. Chudy, E. Jastrzębska, K. Tokarska, M. Bułka, Z. Brzózka, K.A. Wilk, Recent progress in the engineering of multifunctional colloidal nanoparticles for enhanced photodynamic therapy and bioimaging, Adv. Colloid Interface Sci. 261 (2018) 62–81.

[11] Y. Jiménez-Flores, M. Suárez-Quezada, J.B. Rojas-Trigos, L. Lartundo-Rojas, V. Suárez, A. Mantilla, Characterization of Tb-doped hydroxyapatite for biomedical applications: optical properties and energy band gap determination, J. Mater. Sci. 52 (2017) 9990–10000.

[12] G. Zeng, M. Liu, C. Heng, Q. Huang, L. Mao, H. Huang, J. Hui, F. Deng, X. Zhang, Y. Wei, Surface polyPEGylation of Eu^{3+} doped luminescent hydroxyapatite nanorods through the combination of ligand exchange and metal free surface initiated atom transfer radical polymerization, Appl. Surf. Sci. 399 (2017) 499–505.

[13] M. Šupová, Substituted hydroxyapatites for biomedical applications: A review, Ceram. Int. 41 (2015) 9203–9231.

[14] M. Long, F. Hong, W. Li, F. Li, H. Zhao, Y. Lv, H. Li, F. Hu, L. Sun, C. Yan, Z. Wei, Size-dependent microstructure and europium site preference influence fluorescent properties of Eu^{3+}-doped $Ca_{10}(PO_4)_6(OH)_2$ nanocrystal, J. Lumin. 128 (2008) 428–436.

[15] M. Jiang, J. Terra, A.M. Rossi, M.A. Morales, E.M. Baggio Saitovitch, D.E. Ellis, Fe^{2+}/Fe^{3+} substitution in hydroxyapatite: Theory and experiment, Phys. Rev. B - Condens. Matter Mater. Phys. 66 (2002) 1–15.

[16] K. Binnemans, Interpretation of europium(III) spectra, Coord. Chem. Rev. 295 (2015) 1–45.

[17] T. Honma, K. Toda, Z.-G. Ye, M. Sato, Concentration quenching of the Eu^{3+}-activated luminescence in some layered perovskites with two-dimensional arrangement, J. Phys. Chem. Solids. 59 (1998) 1187–1193.

[18] M. Kikuchi, S. Itoh, S. Ichinose, K. Shinomiya, J. Tanaka, Self-organization mechanism in a bone-like hydroxyapatite/collagen nanocomposite synthesized in vitro and its biological reaction in vivo, Biomaterials. 22 (2001) 1705–1711.

[19] F. Nudelman, K. Pieterse, A. George, P.H.H. Bomans, H. Friedrich, L.J. Brylka, P.A.J. Hilbers, G. De With, N.A.J.M. Sommerdijk, The role of collagen in bone apatite formation in the presence of hydroxyapatite nucleation inhibitors, Nat. Mater. 9 (2010) 1004–1009.

[20] Y. Matsuya, T.; Otsuka, Y.; Tagaya, M.; Motozuka, S.; Ohnuma, K.; Mutoh, Formation of stacked luminescent complex of 8-hydroxyquinoline molecules on hydroxyapatite coating by using cold isostatic pressing, Mater. Sci. Eng. C. 58 (2016) 127–132.

[21] S. Motozuka, M. Tagaya, An investigation into photofunctional interfaces of 8-hydroxyquinoline/hydroxyapatite hybrids, Opt. Mater. 66 (2017) 392–398.

[22] T. Matsuya, S. Morakul, Y. Otsuka, K. Ohnuma, M. Tagaya, S. Motozuka, Y. Miyashita, Y. Mutoh, Visible light-induced antibacterial effects of the luminescent complex of hydroxyapatite and 8-hydroxyquinoline with gray titania coating, Appl. Surf. Sci. 448 (2018) 529–538.

[23] S. Morakul, Y. Otsuka, A. Nararya, M. Tagaya, S. Motozuka, K. Ohnuma, Y. Miyashita, Y. Mutoh, Effects of compression on orientation of ligands in fluorescent complexes between hydroxyapatite with amino acids and their optical properties, J. Mech. Behav. Biomed. Mater. 88 (2018) 406–414.

[24] B. Müller, Citric acid as corrosion inhibitor for aluminium pigment, Corros. Sci. 46 (2004) 159–167.

[25] C.J. Dodge, A.J. Francis, Photodegradation of a ternary iron(III)-uranium(VI)-citric acid complex, Environ. Sci. Technol. 36 (2002) 2094–2100.

[26] J.L. Pierre, I. Gautier-Luneau, Iron and citric acid: A fuzzy chemistry of ubiquitous biological relevance, BioMetals. 13 (2000) 91–96.

[27] A. De Robertis, A. Gianguzza, S. Sammartano, Solubility of some calcium-carboxylic ligand complexes aqueous solution, Talanta. 42 (1995) 1651–1662.

[28] S. Johnson, Do mitochondria regulate cellular iron homeostasis through citric acid and haem production? Implications for cancer and other diseases, Med. Hypotheses. 60 (2003) 106–111.

[29] H.C. Hann HW, Stahlhut MW, Effect of iron and desferoxamine on cell growth and in vitro ferritin synthesis in human hepatoma cell lines, Hepatology. 11 (1990) 566–569.

[30] M.E. Mycielska, A. Patel, N. Rizaner, M.P. Mazurek, H. Keun, A. Patel, V. Ganapathy, M.B.A. Djamgoz, Citrate transport and metabolism in mammalian cells: Prostate epithelial cells and prostate cancer, BioEssays. 31 (2009) 10–20.

[31] S. Brunauer, P.H. Emmett, E. Teller, Adsorption of Gases in Multimolecular Layers, J. Am. Chem. Soc. 60 (1938) 309–319.

[32] K. Sato, Y. Kumagai, J. Tanaka, Apatite formation on organic monolayers in simulated body environment, J. Biomed. Mater. Res. 50 (2000) 16–20.

[33] X. Wang, A. Klocke, B. Mihailova, L. Tosheva, U. Bismayer, New insights into structural alteration of enamel apatite induced by citric acid and sodium fluoride solutions, J. Phys. Chem. B. 112 (2008) 8840–8848.

[34] S. Yokoo, S. Yamagami, Y. Yanagi, S. Uchida, T. Mimura, T. Usui, S. Amano, Human corneal endothelial cell precursors isolated by sphere-forming assay, Investig. Opthalmology Vis. Sci. 46 (2005) 1626–1631.

[35] M.R.T. Filgueiras, D. Mkhonto, N.H. de Leeuw, Computer simulations of the adsorption of citric acid at hydroxyapatite surfaces, J. Cryst. Growth. 294 (2006) 60–68.

[36] A. Nikolaev, I. Kolesnikov, O. Frank-Kamenetskaya, M. Kuz'mina, Europium concentration effect on characteristics and luminescent properties of hydroxyapatite nanocrystalline powders, J. Mol. Struct. 1149 (2017) 323–331.

[37] R.L. Yang, Y.J. Zhu, F.F. Chen, L.Y. Dong, Z.C. Xiong, Luminescent, fire-resistant, and water-proof ultralong hydroxyapatite nanowire-based paper for multimode anticounterfeiting applications, ACS Appl. Mater. Interfaces. 9 (2017) 25455–25464.

[38] A. Escudero, M.E. Calvo, S. Rivera-Fernández, J.M. de la Fuente, M. Ocaña, Microwave-assisted synthesis of biocompatible europium-doped calcium hydroxyapatite and fluoroapatite luminescent nanospindles functionalized with poly(acrylic acid), Langmuir. 29 (2013) 1985–1994.

[39] T. Igarashi, M. Ihara, T. Kusunoki, K. Ohno, Relationship between optical properties and crystallinity of nanometer Y_2O_3:Eu phosphor, Appl. Phys. Lett. 76 (2000) 1549–1551.

[40] S.Koutsopoulos, Synthesis and characterization of hydroxyapatite crystals: A review study on the analytical methods, J. Biomed. Mater. Res. 62 (2002) 600–612.

[41] A. Mitsionis, T. Vaimakis, C. Trapalis, N. Todorova, D. Bahnemann, R. Dillert, Hydroxyapatite/titanium dioxide nanocomposites for controlled photocatalytic NO oxidation, Appl. Catal. B Environ. 106 (2011) 398–404.

[42] L. Bichara, H. Lanús, E.G. Ferrer, M.B. Gramajo, S.A. Brandan, Vibrational study and force field of the citric acid dimer based on the SQM methodology, Adv. Phys. Chem. 2011 (2011) 1–10.

[43] A.S. Tselesh, Anodic behaviour of tin in citrate solutions: The IR and XPS study on the composition of the passive layer, Thin Solid Films. 516 (2008) 6253–6260.

[44] A. Grunenwald, C. Keyser, A.M. Sautereau, E. Crubézy, B. Ludes, C. Drouet, Revisiting carbonate quantification in apatite (bio)minerals: A validated FTIR methodology, J. Archaeol. Sci. 49 (2014) 134–141.

[45] T. V. Safronova, V.I. Putlyaev, O.A. Avramenko, M.A. Shekhirev, A.G. Veresov, Ca-deficient hydroxyapatite powder for producing tricalcium phosphate based ceramics, Glas. Ceram. 68 (2011) 28–32.

[46] A. López-Macipe, J. Gómez-Morales, R. Rodríguez-Clemente, Nanosized hydroxyapatite precipitation from homogeneous calcium/citrate/phosphate solutions using microwave and conventional heating, Adv. Mater. 10 (1998) 49–53.

[47] M.E. Fleet, X. Liu, Y. Pan, Site preference of rare earth elements in hydroxyapatite [$Ca_{10}(PO_4)_6(OH)_2$], J. Solid State Chem. 149 (2000) 391–398.

[48] T. Kataoka, K. Shiba, M. Tagaya, Preparation of europium(III)-doped hydroxyapatite nanocrystals in the presence of cationic surfactant, Colloid Interface Sci. Commun. 13 (2016) 1–5.

[49] H. Luo, W. Li, D. Ji, G. Zuo, G. Xiong, Y. Zhu, L. Li, M. Han, C. Wu, Y. Wan, One-step exfoliation and surface modification of lamellar hydroxyapatite by intercalation of glucosamine, Mater. Chem. Phys. 173 (2016) 262–267.

[50] Z. Shi, X. Huang, Y. Cai, R. Tang, D. Yang, Size effect of hydroxyapatite nanoparticles on proliferation and apoptosis of osteoblast-like cells, Acta Biomater. 5 (2009) 338–345.

[51] Y. Oka, Y. Kuroda, T. Matsuno, K. Kamata, H. Wada, A. Shimojima, K. Kuroda, Preparation of mesoporous basic oxides through assembly of monodispersed Mg–Al layered double hydroxide nanoparticles, Chem. A Eur. J. 23 (2017) 9362–9368.

[52] R.D.S. Santos, M.V.D.S. Rezende, Atomistic simulation of intrinsic defects and trivalent and tetravalent ion doping in hydroxyapatite, Adv. Condens. Matter Phys. 2014 (2014) 1–8.

[53] K.P. Zhuravlev, V.I. Tsaryuk, V.A. Kudryashova, Photoluminescence of europium and terbium trifluoroacetylacetonates. Participation of LMCT state in processes of the energy transfer to Eu^{3+} ion, J. Fluor. Chem. 212 (2018) 137–143.

[54] J. Wang, H. Song, X. Kong, H. Peng, B. Sun, B. Chen, J. Zhang, W. Xu, H. Xia, Fluorescence properties of trivalent europium doped in various niobate codoped glasses, J. Appl. Phys. 93 (2003) 1482–1486.

[55] K. Jha, M. Jayasimhadri, Structural and emission properties of Eu^{3+}-doped alkaline earth zinc-phosphate glasses for white LED applications, J. Am. Ceram. Soc. 100 (2017) 1402–1411.

[56] A. Heller, A. Barkleit, H. Foerstendorf, S. Tsushima, K. Heim, G. Bernhard, Curium(III) citrate speciation in biological systems: A europium(III) assisted spectroscopic and quantum chemical study, Dalt. Trans. 41 (2012) 13969–13983.

[57] A. Fihri, C. Len, R.S. Varma, A. Solhy, Hydroxyapatite: A review of syntheses, structure and applications in heterogeneous catalysis, Coord. Chem. Rev. 347 (2017) 48–76.

[58] W. Anderson, D. Kozak, V.A. Coleman, Å.K. Jämting, M. Trau, A comparative study of submicron particle sizing platforms : Accuracy, precision and resolution analysis of polydisperse particle size distributions, J. Colloid Interface Sci. 405 (2013) 322–330.

[59] J.G. Ren, P. Seth, H. Ye, K. Guo, J.I. Hanai, Z. Husain, V.P. Sukhatme, Citrate suppresses tumor growth in multiple models through inhibition of glycolysis, the tricarboxylic acid cycle and the IGF-1R pathway, Sci. Rep. 7 (2017) 1–13.

[60] D. Feng, Y. Song, W. Shi, X. Li, H. Ma, Distinguishing folate-receptor-positive cells from folate-receptor-negative cells using a fluorescence off-on nanoprobe, Anal. Chem. 85 (2013) 6530–6535.

[61] Y. Wang, C. Wang, Y. Li, G. Huang, T. Zhao, X. Ma, Z. Wang, B.D. Sumer, M.A. White, J. Gao, Digitization of endocytic pH by hybrid ultra-pH-sensitive nanoprobes at single-organelle resolution, Adv. Mater. 29 (2017) 1–9.

Chapter 4

Summary

Chapter 4

Summary

Various types of the cell labeling nanoparticles that label cancer cells have been developed for the non-cytotoxicity visualization. In luminescent materials for safely visualizing cancer cells, there was a problem of attenuation of luminescence intensity at observation and toxicity to the cells. In order to solve these problems, this thesis focuses on the photofunctionalization and surface functionalization of hydroxyapatite (HA), which is the main component of hard tissue, and applied it as a nanoparticle for cell labeling.

In ***Chapter 1***, "*General Introduction*", the problems of cell labeling technology were explained by giving examples of conventional cell labeling nanomaterials. Furthermore, the photophysical chemistry properties of Eu (III) ion were described. Moreover, HA is one of the excellent inorganic hosts to overcome the barriers based on its high biocompatibility, and it is present as a main component of hard tissues *in vivo*, making it possible to be utilized as a cell labeling nanomaterials. When aiming at the cell labeling application of HA, it is important to bind a functional molecule with HA in the nucleation process and to synthesize as a form of nanoparticle. Accordingly, the importance of the Ca site of HA and the inorganic/organic interface structure between HA and functional molecules to realize photofunctionalization and cell selectivity *in vivo* were proposed, and the control of the surface state was outlined. Then, focusing on the inorganic/organic interface between photofunctional HA and functional molecules, the strategy for photofunctionalization of HA was proposed. Furthermore, It described cell binding (ligand) molecule immobilization technology to particle surfaces for specific binding or uptake to cancer cells and the importance of coordination of functional molecules that suppress cancer cell growth to photofunctional HA, and showed the significance and purpose of this study.

In ***Chapter 2***, "*Synthesis of Luminescent Europium(III) Complex-interacted Hydroxyapatite Nanoparticles and Their Rapid Cell Labeling by Folic Acid Immobilization*", tris(2,2,6,6-tetramethyl-3,5- heptanedionato)europium(III) (EuTH) complex-interacted HA nanoparticles (EHA) were synthesized. The EHA nanoparticles containing 5.0 mol% of EuTH relative to calcium ion had a primary particle size that can be easily taken up by HeLa cells. Then, the folic acid

derivative (folate N hydroxysuccinimidyl ester (FA-NHS)) as the targeting ligand for the HeLa cells was immobilized on the EHA. When the molecular occupancy of FA-NHS to the EHA surfaces is at around 3−5%, the intense luminescence from the *f*−*f* transition of the Eu^{3+} ions as well as the charge transfer between the EuTH and FA-NHS was observed to exhibit higher quantum efficiency. Moreover, effective dispersibility in phosphate-buffered saline was confirmed with immobilizing the positively charged FA-NHS. The cytotoxicity against the NIH swiss mouse embryo-derived (NIH3T3) fibroblasts was evaluated. The cell labeling property against the human cervical cancer-derived (HeLa) cells was evaluated. The affinity and non-cytotoxicity between the FA-NHS-immobilized EHA nanoparticles and NIH3T3 fibroblasts were monitored for 3 days. Red luminescence from the HeLa cells could be observed, and the labels with following the cellular shapes were achieved by an additional culture time of 1 h after injecting the FA-NHS-immobilized EHA nanoparticles to the tumorized cells, indicating the rapid cell labeling process.

In ***Chapter 3***, "*Synthesis of Luminescent Hydroxyapatite Nanoparticles Coordinated with Citric Acid for Their Bifunctional Cell Labeling and Cytostatic Properties*", luminescent nanoparticles based on photofunctional interfaces between the citric acid (Cit) molecules and europium(III) ion (Eu^{3+})-doped HA (Eu:HA) to provide bifunctional cell labeling and cytostatic property was synthesized. In particular, the Eu:HA nanoparticles were synthesized in the presence of Cit, and the Cit molecules were coordinated with the Eu:HA nanoparticles (Cit/Eu:HA). It was suggested that the Cit molecules that interacted with the Eu:HA nanoparticle surfaces sterically hindered the nanoparticle growth. Moreover, it was demonstrated that the interactions of Cit and Eu:HA were important for achieving the efficient photoluminescence properties. Moreover, the efficient luminescence ability including the internal quantum efficiency for HeLa cell labeling was achieved, and simultaneously, the Cit molecular effect on the suppression of the HeLa cell line growth was investigated. The luminescence enhancement of the nanoparticles with the coordination of Cit was successfully elucidated. In particular, the low symmetry of the coordination structure for the Eu^{3+} ion at the Ca(I) site provided the enhanced luminescence efficiency. Furthermore, the FA-NHS was immobilized on the Cit/Eu:HA nanoparticles to enhance the uptake efficiency of the nanoparticles into the HeLa cells. Then, the cytotoxicity against the NIH3T3 fibroblasts was evaluated. Moreover, the cell labeling property was evaluated to investigate the effect of the nanoparticles on the HeLa cell growth suppression by the Cit molecules. The affinity and non-cytotoxicity between the nanoparticles and NIH3T3 fibroblasts were monitored for 3 days. HeLa cell growth suppression was achieved by the interactions with the Cit/Eu:HA nanoparticles. Furthermore, the Cit/Eu:HA nanoparticles reacted with the cells to exhibit red-color luminescence from the cells while suppressing HeLa cell growth, indicating the bifunction of cell labeling and

cytostatic property in one particle. The Cit/Eu:HA nanoparticles were effectively reacted with the tumorized cells after a culture time of 60 h to exhibit the luminescent labeling with following the cellular shapes. Furthermore, the cytostatic property of the tumor cells were observed.

As conclusive viewpoints, the rapid cell labeling and cytostatic properties through specific uptake into cancer cells using the interfacial interactions between HA and functional molecules were successfully achieved. The achievement statuses by this study were described as compared with initial targets in ***Chapter 1*** and previously-reported statuses in **Table 4-1**.

For the future applications, it will be an additional requirement to evaluate the influence of nanoparticles in co-culturing between normal and cancer cells,. For *in vivo* use based on the highly-selective targeting for cancer cells, the enhanced permeability and retention (EPR) effect in addition to the immobilization of cancer cell-binding molecules will be an important topic. Accordingly, it is necessary to control the particle size of the nanoparticles to about tens to hundreds of nanometers. Further studies are important to develop theranostic nanoparticles with fluorescence and therapeutic properties toward future applications in such a field as biomedicine. In order to synthesis novel theranostic nanoparticle, one of the keys would be to control interfacial interactions between HA and functional molecules. To explore the combination of HA and various functional molecules will lead to a large number of multifunctional HA nanoparticles that advance the frontier technologies of bio-related fields.

Table 4-1. Requirements and targets in this study, and the achievement statuses by the previously-reported cell labeling nanoparticles and those by this study.

Requirements	Targets in this study	Achievement statuses by the previously-reported cell labeling nanoparticles	Achievement statuses by this study
I Extreme biosafety for normal cells	✓ The ratio of N_1 (which means the normal cell adhesion density with adding nanoparticles at the culture time of 24 h) to N_0 (which means the normal cell adhesion density without adding nanoparticles at the culture time of 24 h) **) (N_1/N_0) is 0.7 or more**	N_1/N_0 ratio is 0.7 or more (in the case of Eu:HA)	The N_1/N_0 ratios by all the nanoparticles were more than 0.8
	✓ Average particle size of **20–200 nm** in biological fluid (coefficient of variation: **30 % or less**)	Average particle sizes of Eu:HA were about 100 nm in PBS (coefficient of variation: 30 % or less)	Average particle sizes in PBS were abuut 90 nm (coefficient of variation: 30 % or less)
	✓ **Excitation/luminescence visible light at 400–800 nm region in the observation**	Luminescence observation of Eu:HA with visible light irradiation	Excitation/luminescence light observation was in the visible region
II Efficient luminescence	✓ Strong luminescence intensity that can be **visually confirmed**	Strong luminescence by semiconductor quantum dots	Strong luminescence intensity that can be visually confirmed
	✓ Internal quantum efficiency of **more than 7 %**	Internal quantum efficiency of 10 % or more by semiconductor quantum dots	Internal quantum efficiency: 12.5 %
III Construction of particle surface that is rapid binding with cancer cells and taken up into the cells at high concentration	✓ High concentration of binding and uptake into cells by **immobilization of cell-binding molecules**	Achievable by functionalizing the surface silanol groups of mesoporous silica	High concentration into the cell surfaces by the FA-NHS immobilization
	✓ Short-term labeling of tumor cells **within 3 h after the adding nanoparticles**	Not achieved	Short-term labeling of spheres at 1 h
IV Achievement of both cancer cell labeling and suppression of cell growth	✓ **Growth suppression (N_1/N_0 ratio of 0.7 or less) while labeling cancer cells**	Not achieved	Growth suppression while labeling cells: N_1/N_0 ratios of **4**Cit/Eu:HA and **FA4**Cit/Eu:HA nanoparticles were 0.5

Achievement List

Publication Papers

1. Takuya Kataoka, Sadaki Samitsu, Mitsuhiro Okuda, Daisuke Kawagoe, Motohiro Tagaya, "Highly Luminescent Hydroxyapatite Nanoparticles Hybridized with Citric Acid for Their Bifunctional Cell-Labeling and Cytostatic Suppression Properties", ***ACS Applied Nano Materials***, 3, 241–256 (2020).
2. Takuya Kataoka, Shigeaki Abe, Motohiro Tagaya, "Surface-engineered Design of Efficient Luminescent Europium(III) Complex-based Hydroxyapatite Nanocrystals for Rapid HeLa Cancer Cell Imaging", ***ACS Applied Materials & Interfaces***, 11, 8915–8927 (2019).
3. Takuya Kataoka, Shigeaki Abe, Motohiro Tagaya, "Synthesis of Europium(III) Complex-Based Hydroxyapatite Nanocrystals for Biolabeling Applications", ***Key Engineering Materials***, 782, 41–46 (2018).
4. Takuya Kataoka, Kota Shiba, Motohiro Tagaya, "An Investigation into Nanohybrid States of Europium (III) Complex with Hydroxyapatite Nanocrystals", ***Optical Materials***, 84, 252–258 (2018).

Other Related Publication Papers and Patents

1. Takuya Kataoka, Kota Shiba, Motohiro Tagaya, "Design of Hydroxyapatite-Based Multifunctional Nanoparticles for Cell Labelling and Cell Growth Inhibition", ***Regenerative Medicine Frontiers***, 2020, e200001/pp. 1–27 (2019).
2. Takuya Kataoka, Kenji Shinozaki, Shigeaki Abe, Motohiro Tagaya, "Preparation of Calcium Phosphate Nanoparticles Hybridized with Europium(III) Complex for Novel Luminescent Organic-Inorganic Systems", ***Journal of Physics and Chemistry of Solids***, 122, 218–226 (2018).
3. Takuya Kataoka, Kota Shiba, Motohiro Tagaya "Preparation of Europium(III)-Doped Hydroxyapatite Nanocrystals in the Presence of Cationic Surfactant", ***Colloid and Interface Science Communications***, 13, 1−5 (2016).

Presentation in International Conference and Symposium

1. Takuya Kataoka, Daisuke Kawagoe, Motohiro Tagaya, "Design of Photoluminescent Hydroxyapatite Nanoparticles Interacting Citric acid and Their Cell-labeling and Cytostatic Suppression Functions." [Presentation No. STI-3-3] **STI-gigaku**, 2019 年 11 月 (Niigata, Japan).
2. Takuya Kataoka, Motohiro Tagaya, "Synthesis of Europium(III) Complex-based Hydroxyapatite Nanocrystals for Biolabeling Applications." [Presentation No. P-39] ***30th Symposium and Annual***

Meeting of the International Society for Ceramics in Medicine － Bioceramics 30, 2018 年 10 月 (Nagoya, Japan).

3. Shigeaki Abe, Takuya Kataoka, Motohiro Tagaya, “Photoluminescent and biocompatible property of folic acid derivative immobilized apatite/Eu-complex hybrid particles for biomedical tool.” [Session: TS04. Nanobiotechnology & Nanomedicine, Presentation No. P1804_0366] ***NANO KOREA 2018***, 2018 年 7 月 (Korea).
4. Takuya Kataoka, Liyin Wang, Yuri Maruko, Kouhei Kobayashi, Motohiro Tagaya, “Preparation of Hybrid Luminescent Mesoporous Silica Particles with Calcium Phosphate.” [Session: Nanocomposite and Hybrid Materials, presentation No. P26] ***The International Symposium on the Science of Engineering Ceramics (EnCera 2016)***, 2016 年 5 月 (Niigata, Japan).